

61  
SAI-84/1589

AD A142526

Q AND ITS EFFECT ON SHORT  
PERIOD P WAVES FROM EXPLOSIONS  
IN CENTRAL ASIA

by  
THOMAS C. BACHE

Semi-Annual Technical Report

SCIENCE APPLICATIONS, INC.  
1200 Prospect St.  
P.O. Box 2351  
La Jolla, CA 92038

Sponsored by:  
Defense Advanced Research Projects Agency  
DARPA Order No. 4858  
Monitored by Defense Nuclear Agency  
Under Contract No. DNA001-83-C-0383

APRIL 1984

DTIC FILE COPY

The views and conditions contained in the document are those of the author and should not be interpreted as necessarily representing the official policies, expressed or implied, of the Defense Advanced Research Projects Agency or the U.S. Government

DARPA Order No. 4858  
Program Code No. 3D60  
Program Element Code 61101E

This document has been approved  
for public release and sale; its  
distribution is unlimited.

Amount of Contract \$149,679  
Contract No. DNA001-83-C-0383  
Principle Investigator and Telephone No.  
Dr. Thomas C. Bache 011-44-7356-4111  
Extension 5873

84 06 22 01

Q AND ITS EFFECT ON SHORT  
PERIOD P WAVES FROM EXPLOSIONS  
IN CENTRAL ASIA

by  
THOMAS C. BACHE

Semi-Annual Technical Report

SCIENCE APPLICATIONS, INC.  
1200 Prospect St.  
P.O. Box 2351  
La Jolla, CA 92038

Sponsored by:  
Defense Advanced Research Projects Agency  
DARPA Order No. 4858  
Monitored by Defense Nuclear Agency  
Under Contract No. DNA001-83-C-0383

APRIL 1984

The views and conditions contained in the document are those of the author and should not be interpreted as necessarily representing the official policies, expressed or implied, of the Defense Advanced Research Projects Agency or the U.S. Government

DARPA Order No. 4858  
Program Code No. 3D60  
Program Element Code 61101E

Amount of Contract \$149,679  
Contract No. DNA001-83-C-0383  
Principle Investigator and Telephone No.  
Dr. Thomas C. Bache 011-44-7356-4111  
Extension 5873

This document has been approved  
for public release and sale; its  
distribution is unlimited.

DTIC  
ELECTE  
S JUN 25 1984 D  
A

## ABSTRACT

A detailed model for the attenuation of high frequency (1-8Hz) P waves is developed for the paths from the Soviet test site in eastern Kazakhstan to the sites of the four 20-element United Kingdom arrays. These short period arrays (Scotland, India, Canada and Australia) have been operated in an essentially constant configuration since the mid-1960's and are very well suited to high frequency spectral analyses. Event P wave spectra are computed by summing the power spectra (corrected for the noise power) from individual array elements, and the interpretation is based on very smooth average path spectra obtained by stacking spectra from many similar events. Effects of source differences, especially corner frequency variations, can be seen and taken into account. The attenuation model includes contributions from both intrinsic absorption and scattering. The absorption Q dominates at low frequencies and is strongly dependent on frequency on this band. The preferred model has  $t^* = 0.6$  seconds at long period and frequency dependence characterized by a half-amplitude value ( $\tau_M$ ) of 0.05 to 0.1 seconds. The scattering is represented by an essentially frequency-independent  $t^*$  of about 0.1 seconds and has an important effect above 2.5 Hz. Differences in the phase spectrum for these two mechanisms for attenuation are important. A key conclusion is that regional attenuation variations are not represented very well by fitting frequency-independent  $t^*$  operators to P wave spectra in the 0.5 - 3.0 Hz band. Source spectrum variations can have a large biasing effect, as can the effect of frequency dependence of Q. The Q will be seriously overestimated if frequency dependence is present, but not included in the model.



Accession For	
NTIS GRAAI	
DTIC TAB	
Unreduced	
Classification	
<i>Follow on file</i>	
By _____	
Distribution/ _____	
Availability Codes	
Dist	Avail and/or Special
A1	

## TABLE OF CONTENTS

I	INTRODUCTION AND SUMMARY	1
	1.1    Background and Summary	2
	1.2    Objective and Approach	2
	1.3    Method	3
	1.4    Attenuation from E. Kazakh to the UK Array Stations	3
	1.5    Additional Results	5
II	UNITED KINGDOM ARRAY DATA	7
III	SHAGAN RIVER - TWO DISTINCT TEST SITES?	31
IV	SIGNAL SPECTRUM AND $t^*$ ESTIMATION FROM ARRAY DATA	39
	4.1    Introduction	39
	4.2    Signal Spectrum Estimation	40
	4.3 $t^*$ Estimation from Signal Spectra	55
V	SEISMIC NOISE CHARACTERISTICS OF THE UK ARRAYS FROM 0.5 TO 8 Hz	59
VI	AN ATTENUATION MODEL FOR E KAZAKH TO THE UK ARRAY STATIONS	71
	6.1    Introduction	71
	6.2    Spectra for GBA	71
	6.3    Attenuation from E Kazakh to the UK Array Stations	77
	6.4    Synthetic Seismograms	94
VII	SPECTRA FOR SALMON AND THE AMCHITKA AND FRENCH SAHARA EVENTS	99
	7.1    Introduction	99
	7.2    SALMON and the Amchitka Events	99
	7.3    French Sahara Events	102
VIII	ACKNOWLEDGEMENTS	105
IX	REFERENCES	107
	APPENDIX A - WAVEFORMS FOR SEMIPALATINSK EXPLOSIONS	111
	APPENDIX B - GBA SPECTRUM CALCULATIONS	155
	APPENDIX C - SPECTRA FOR EAST KAZAKH EXPLOSIONS	167

## I. INTRODUCTION AND SUMMARY

### 1.1 BACKGROUND

Despite much effort, there remains an inadequate quantitative understanding of the effect of attenuation and its regional variations on the amplitude of short period P waves. Until very recently, this attenuation has always been represented by a Q which is independent of frequency. However, it has become increasingly clear that there must be some frequency dependence that causes the effective Q at long periods (greater than 10 seconds) to be much smaller than that at high frequencies (greater than 3 Hz). But how the Q varies between the two and how much effect this frequency-dependence has in the 0.5-2.0Hz band where P wave amplitudes are measured is not known.

There are several reasons why a solution to this problem remains illusive. The most important is that the data are inadequate; the illuminating characteristics are obscured by noise and path effects. Another reason is that there is a strong tradeoff between source and attenuation effects in this band; most of the events that provide the best data have their corner frequency within or very near the 0.5-2.0 Hz band.

In understanding the attenuation at these high frequencies, it is not enough to consider only the amplitude attenuation. The effects on the phase spectrum (dispersion) can also be important. As has been pointed out many times, very effectively in a recent paper by Richards and Menke (1983), there are differences between the phase effects of attenuation due to intrinsic absorption and that due to scattering. Understanding these differences and properly accounting for them is important to explain key characteristics of observed P wave signals.

## 1.2 OBJECTIVE AND APPROACH

The objective of this study is to develop the kind of detailed understanding of attenuation needed to confidently assess the effect of its frequency dependence, mechanism and regional variation on short period P waves. The key is to have adequate data, and these are provided by recordings of underground explosions made by the four 20-element United Kingdom arrays. The data base is described in detail in Section II where we note that these arrays provide a uniform and consistent source of data for events (including earthquakes) occurring since 1966. Because of the array design and instrument response, these data are uniquely suited to high frequency spectral analyses.

The analysis is based on the characteristics of the P wave spectra of underground nuclear explosions, and data are available for nearly all underground nuclear test sites ever used. However, in this study we focus on the major Soviet test site in eastern Kazakhstan, and therefore on the attenuation in Central Asia. A few results for some important U.S. (outside Nevada) and French (Sahara) tests are also briefly discussed.

While not directly related to our primary focus on attenuation, we also discuss in Section III the observation that the Shagan River test site seems to divide into two separate and distinct sites. This is based on the fact that events in the northeast half of the site write seismograms that are distinctly and consistently different from the seismograms written by events in the southwest half. Later, in Section VI, we see that the spectra for these two areas are also different in a way that suggests that the source corner frequency is systematically different (for roughly the same yield). This supports the conclusion that the waveform differences are due to site geology and is consistent with the hypothesis that the events in the southwest occur in a less competent or weaker material.

### 1.3 METHOD

The technique for estimating the spectrum is described in Section IV. Each element of the arrays is processed separately, first computing energy density spectra for very short (typically 2.5 sec.) time windows chosen to isolate the first-arriving P-wave. The power spectrum of a noise window just before the signal is subtracted and the final event spectrum is computed from the average of these over the array. These array spectra are much smoother and simpler than single sensor spectra, and for many events are confidently determined to 8 Hz. The next step is to stack these spectra for similar events. The stacked spectra are very smooth and are shaped by only the average source spectrum and attenuation. Comparing different classes of events, the source effects can be identified and their influence suppressed. Thus our analysis results in smooth and consistent spectra whose shape is dominated by the effect of attenuation.

A remarkable feature of the spectra is that they all lie very close to the same straight line above 2.5 Hz. This result depends on the accuracy of the calculations at frequencies (>4 Hz) above those where almost all previous work has concentrated. Further, we are aware that other systems (e.g., NORSAR and the SRO) cannot give accurate spectra above 3 or 4 Hz because of discretization errors arising from the gain ranging used in the digitization (e.g. Bungum, 1983). Thus, we have spent considerable effort to develop confidence in the accuracy of our results at 4-8 Hz. One important part of this effort was a study of the characteristics of the noise at the U.K. arrays and the results of this study are described in Section V.

### 1.4 ATTENUATION FROM E. KAZAKH TO THE UK ARRAY STATIONS

We have developed a clear, consistent and rather detailed model for attenuation between 1 and 8 Hz on these four paths. A key feature of the model is that it separates the effect of attenuation due to intrinsic absorption from that due to scattering. The latter is represented by a frequency-

independent (over this band) Q that gives a  $t^*$  of about 0.1 seconds. It is likely that the attenuation on every path, no matter what the intrinsic absorption, includes a scattering contribution of at least this size. On these particular paths the intrinsic absorption has a frequency dependence that has a strong effect on the spectrum between 1 and 4 Hz. The intrinsic absorption is not the same for all four paths, some (rather small) differences can be seen. The preferred model for the paths to GBA (India) and WRA (Australia) has a long period  $t^*$  of 0.6 seconds and frequency dependence characterized by a half amplitude ( $\tau_m$ ) value of 0.05 seconds. For EKA (Scotland) the  $\tau_m$  appears to be somewhat larger, the best estimate is 0.1 seconds. The attenuation to YKA (Canada) appears to be intermediate between that for the GBA and EKA paths. Spectra were also computed for Pcp phases recorded at GBA and show that the attenuation is slightly greater than for P.

The constant  $t^*$  part of the model is dominant at high frequencies and the evidence that the mechanism is scattering seems quite clear. First, we find that the spectrum is the same above 2.5 Hz for all classes of events and all stations, and essentially falls along a constant  $t^*$  line. Second, the coda has more high frequency than the initial P wave. Third, synthetic seismograms will only match the data if the attenuation at high frequencies causes dispersion and pulse broadening much greater than that expected for intrinsic attenuation.

Inference of attenuation at the lower frequencies (1 - 3Hz) requires correction for the source. We cannot be sure we have been completely successful in doing so, but are able to see the effect of source corner frequency on the spectrum and base our results on events for which it is least. These are large ( $m_b > 6.0$ ) events in the southwest portion of the Shagan River test site.

The accuracy of our model is verified by comparison of synthetic and observed seisograms. We see that to improve the synthetics we must:

1. Introduce a Q model which has the proper phase spectrum for the scattering contribution.
2. Introduce a  $pP$  reflection coefficient which is frequency-dependent and smaller than the elastic.

Finally, one of the key conclusions of this work is that the effect of regional attenuation variations on magnitude is not represented very well by differences in the frequency-independent  $t^*$  that fit P wave spectra in the 0.5 - 3.0 Hz band. Source spectrum variations can have a large biasing effect, and there must be frequency dependence on this band. We have inverted the frequency-dependent  $t^*$  inferred for these four paths to determine a Q model for  $f > 1$  Hz for central Asia. This model appears to be a consistent high frequency extension of the worldwide absorption band Q model of Anderson and Given (1982), but has much lower Q than would be obtained if the frequency-dependence were ignored.

#### 1.5 ADDITIONAL RESULTS

We also discuss in Section VII the available P wave spectra for SALMON, the Amchitka events and the French Sahara events. The data are sparse and the interpretation difficult. The major point is that it will be necessary to account for the source to understand the attenuation effect, and this has not yet been done. For SALMON and two of the three teleseismic paths from Amchitka, there is no obvious evidence for significant attenuation differences with respect to E. Kazakh; for one path (Amchitka to WRA) the attenuation is clearly greater. For French Sahara events a similar mixed picture emerges, with some indications of greater attenuation, but other evidence that it is not much different than for E Kazakh.

The next step is to study spectra for NTS events, which are numerous enough that we can hope to separate source and attenuation effects. Certainly the NTS spectra appear to be quite different on initial review. Perhaps the insight gained in interpreting them will also help fit the Amchitka and French Sahara spectra into a coherent picture of regional attenuation variations and their effect on body wave magnitude.

## II UNITED KINGDOM ARRAY DATA

In the mid-1960's the United Kingdom deployed four arrays which have now been operated with essentially constant characteristics for nearly two decades. Important characteristics of the arrays are listed in Table 1 and the locations are mapped in Figure 1.

The configuration of each array is shown in Figure 2. The seismometer response has been carefully determined and checked over the years by the Blacknest staff and is very well known up to 10 Hz and beyond. It varies slightly among the stations and there have been some changes over the years, but all this information is included in the software used to read the data tapes and prepare them for processing. The amplitude responses are plotted in Figure 3. On the right side the response for digital recording is compared to the response of several other widely used instruments. Note that the UK seismometers respond like other short period seismometers at low frequencies, but are much more sensitive to high frequencies.

The standard processing applied to the UK array data includes simple delay-and-sum beamforming. For underground explosions we know the event locations, and simply use the slowness from the J-B tables to form the beam. More accurate slowness estimates and station corrections cannot make any significant improvement on the beam because of the size of the arrays and relative simplicity of the site geology. The data quality obtainable for an early low signal/noise event (SALMON) is illustrated in Figure 4. All data are carefully examined to identify faulty channels (eg R10 and B8). Also, the spectral processing described later is a sensitive indicator of high frequency system noise, and is used to identify faulty data.

It is necessary to discard all overloaded channels. We know that 5 volts is the maximum signal allowed by the instrumentation, so the data processing software marks all channels where this level has been reached. We also know that the instrument response must become non-linear at some point as the 5 volt level is approached. We took a cautious approach and

TABLE 1  
United Kingdom Arrays

<u>Station</u>	<u>Code</u>	<u>Location</u>	<u>Element Spacing (km)</u>	<u>Maximum Element Spacing (km)</u>	<u>Date Operational</u>	<u>Date or Digital Recording</u>
Eskdalemuir Scotland	EKA	55°19'59"N 3°09'33"W	0.9	9.8	17 May 196?	14 Nov 1983
Yellowknife Canada	YKA	62°29'34"N 114°36'17"W	2.5	22.5	26 Nov 196?	-
Gauribidanur India	GBA	13°36'15"S 77°26'10"E	2.5	32.0	1 Feb 1966*	4 Mar 1979
Warramunga Australia	WRA	19°56'39"S 142°20'27"E	2.5	26.3	1 Mar 1966*	7 Jun 1977

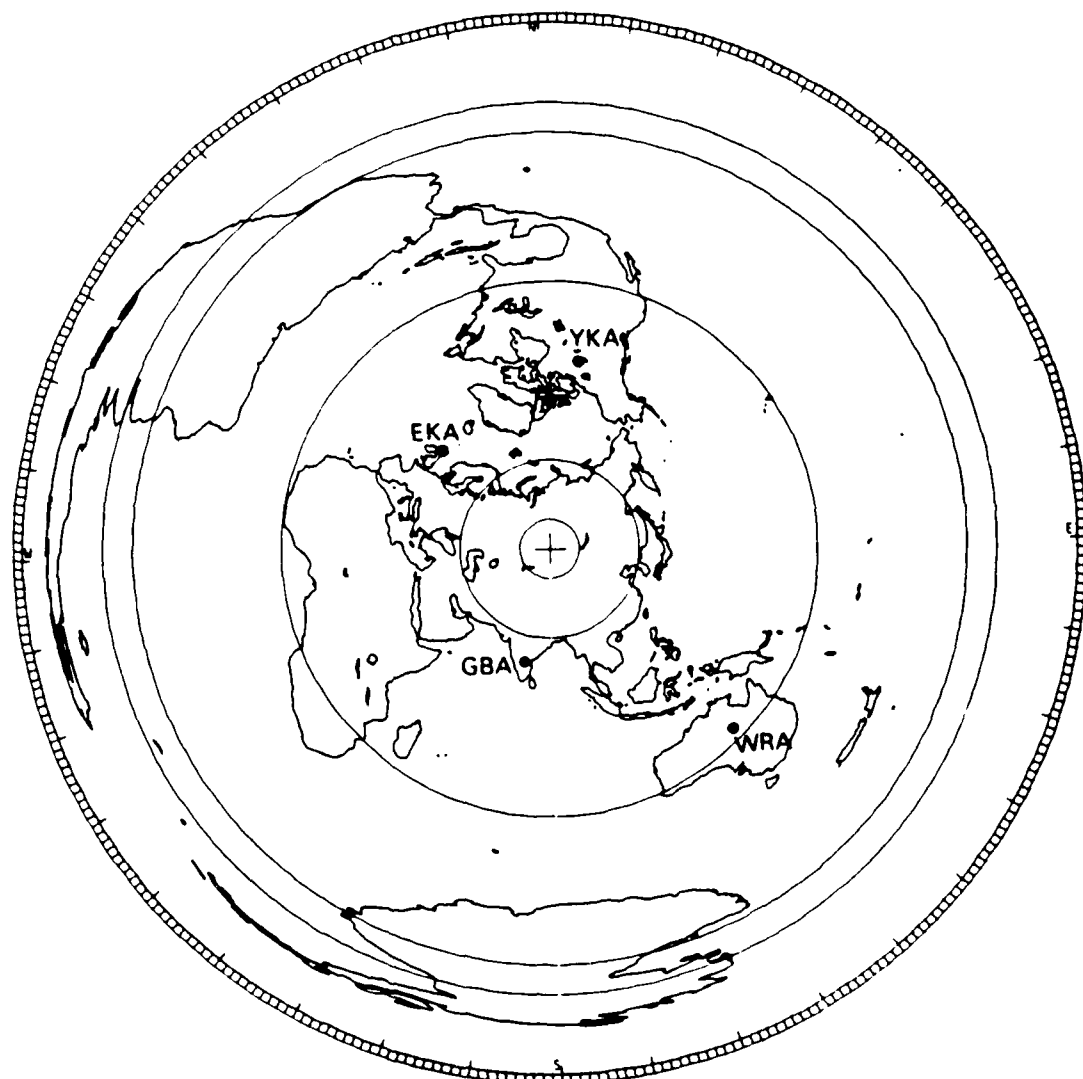


Figure 1 The UK array locations are plotted on an azimuthal great circle projection centred at 50°N 79°E. All stations are between the circular lines indicating ranges of 30° and 90°.

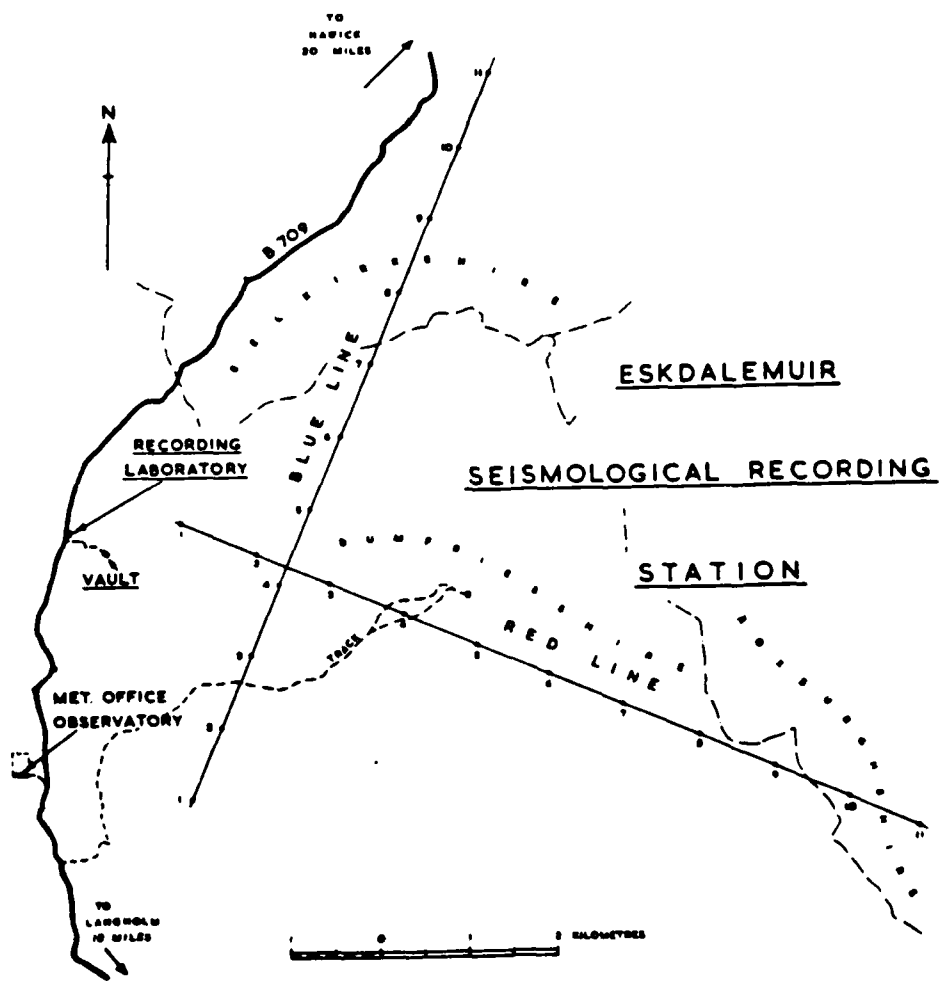
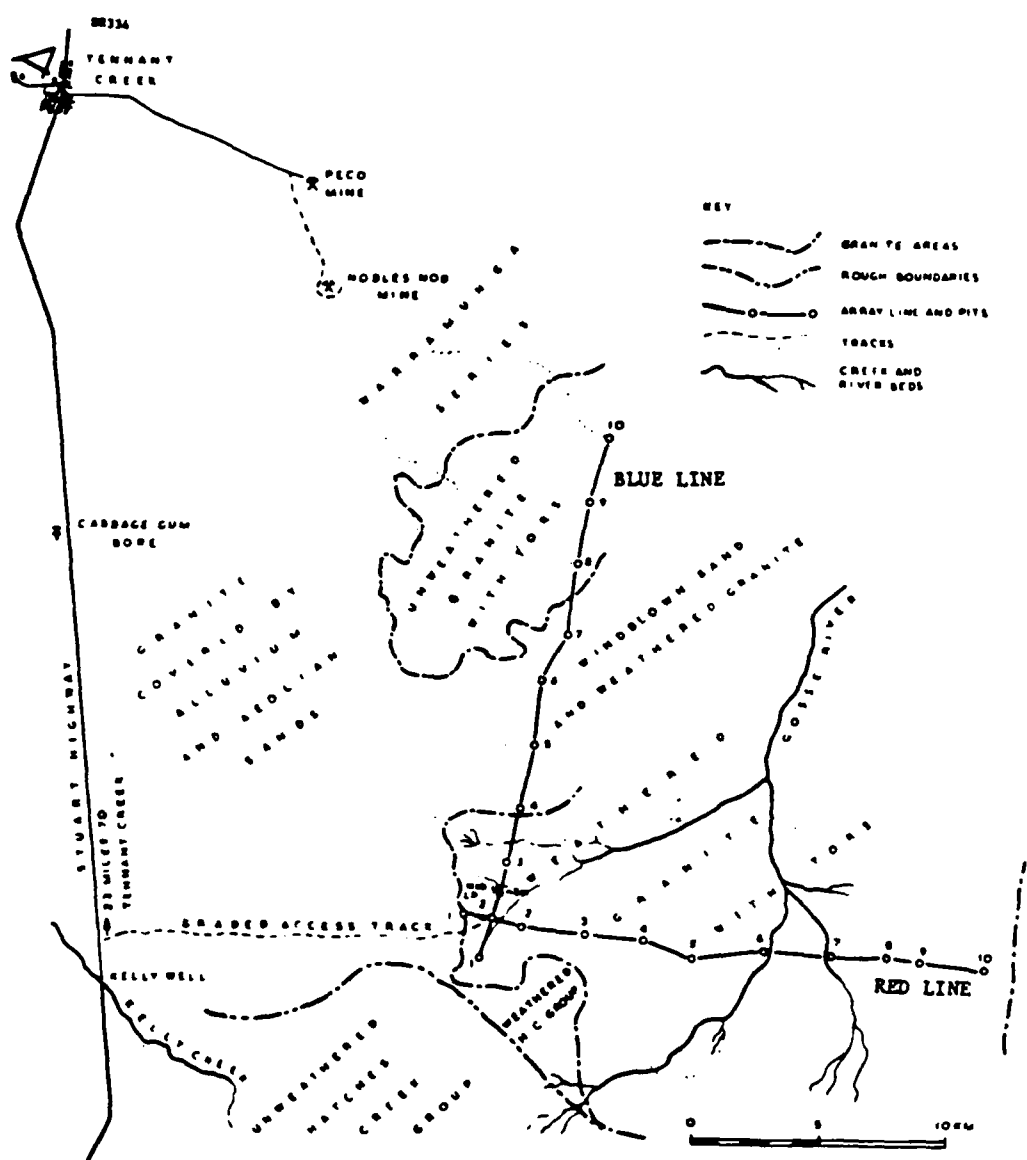
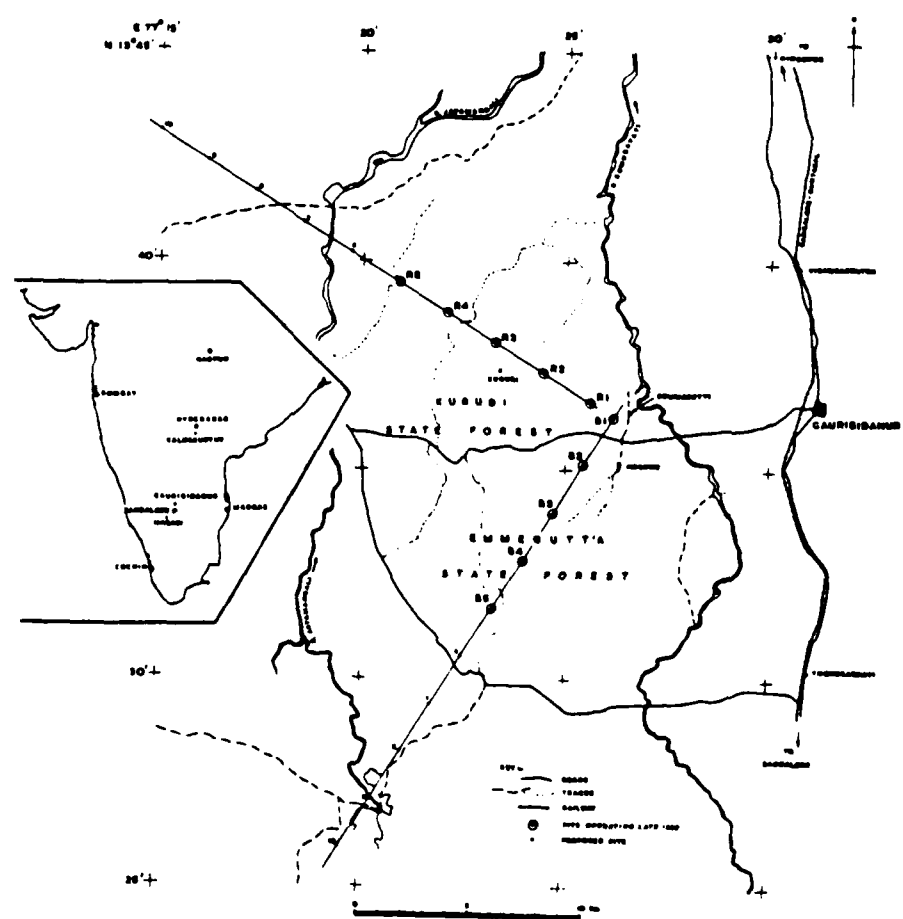


Figure 2 The geometry of the four "K" arrays is sketched



MAP OF TENNANT CREEK SHOWING THE ARRAY AND LOCAL SURFACE GEOLOGY

Figure 2 (continued)



SKETCH MAP OF THE GAURIBIDANUR ARRAY

Figure 2 (continued)

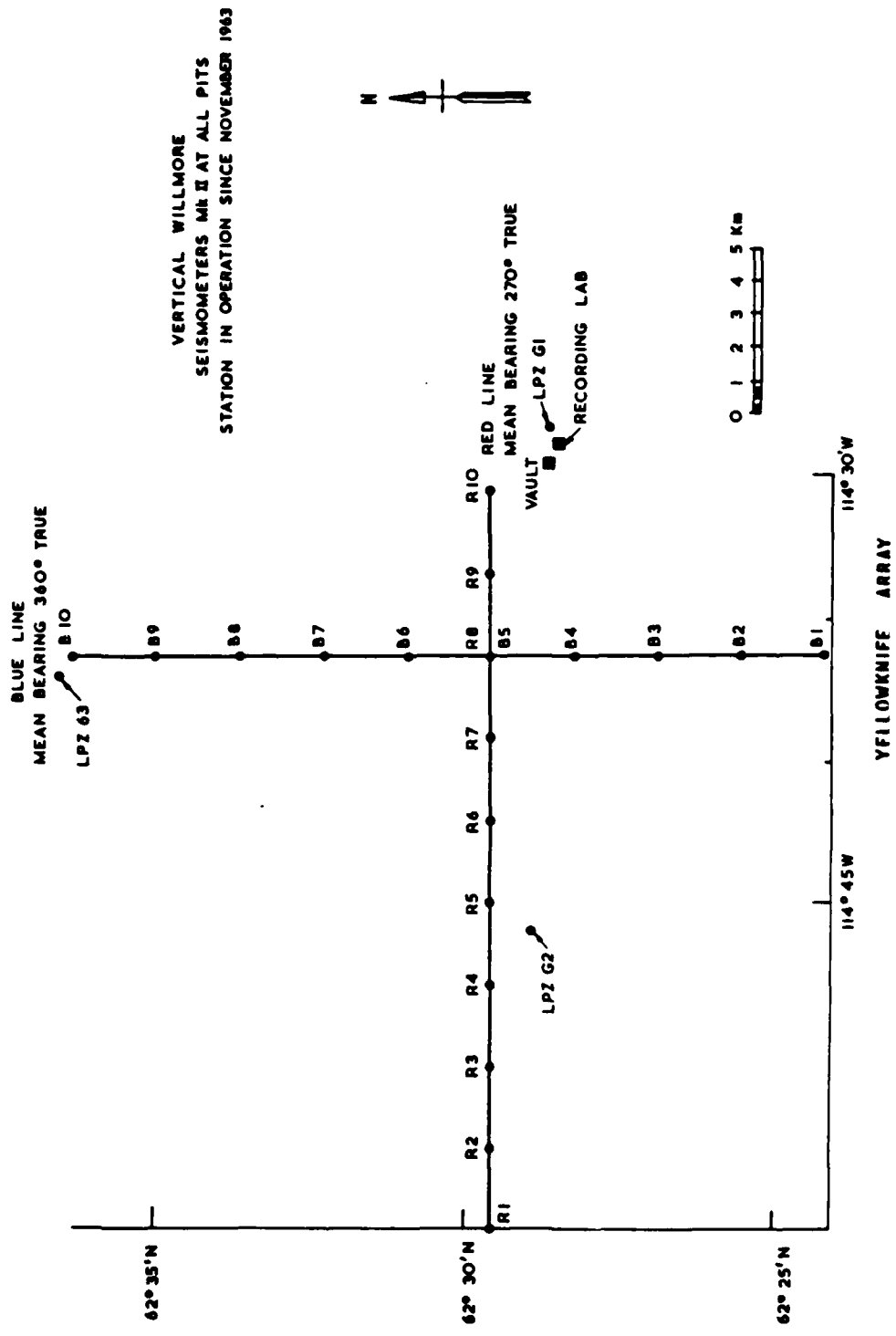


Figure 2 (continued)

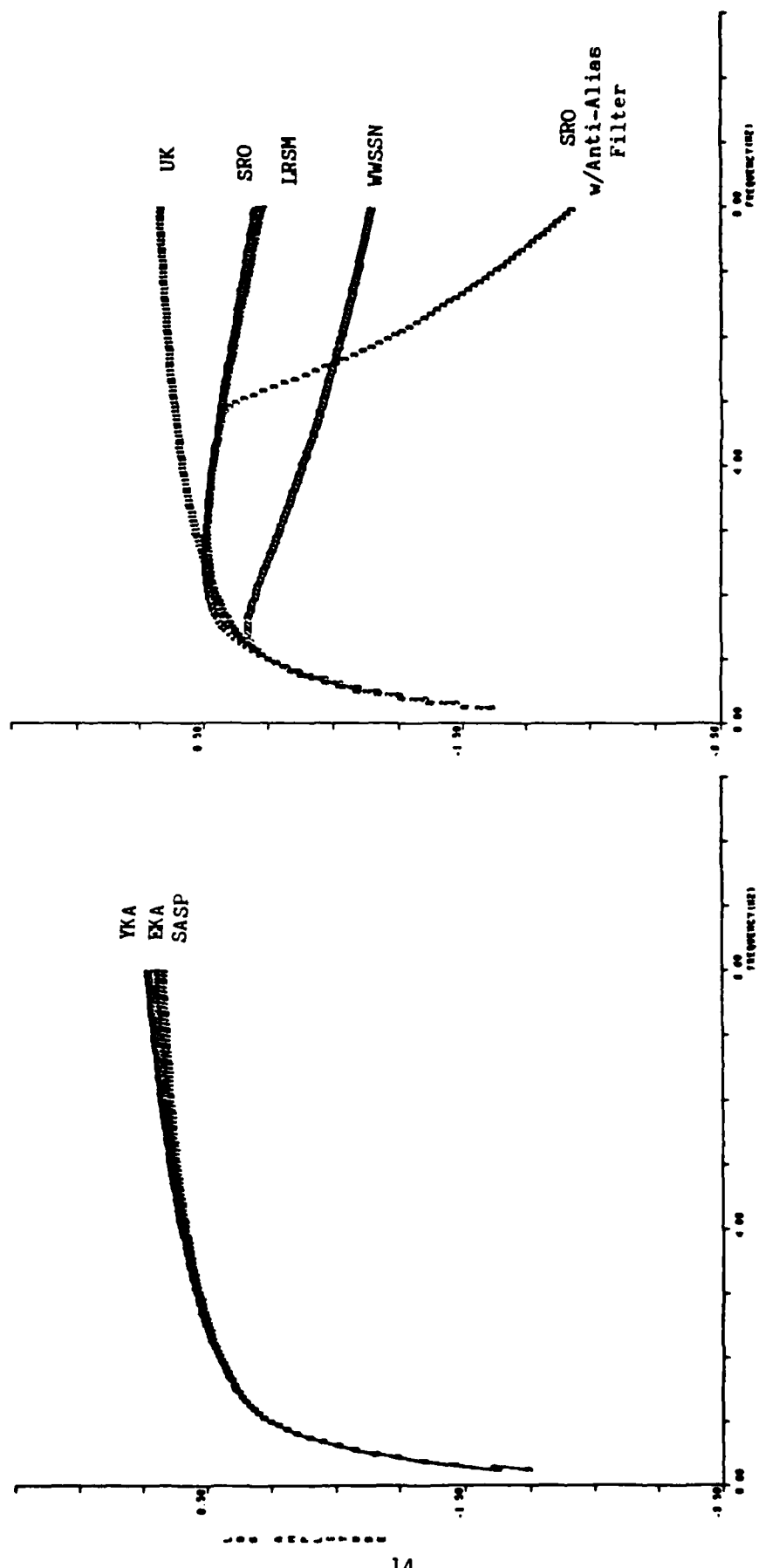


Figure 3 The instrument amplitude responses are plotted for the UK arrays. The analog recording response is nearly identical for EKA, GKA and WRA. The SASP is the response when digital recording is used and it is compared to the response of several other short period seismometer systems.

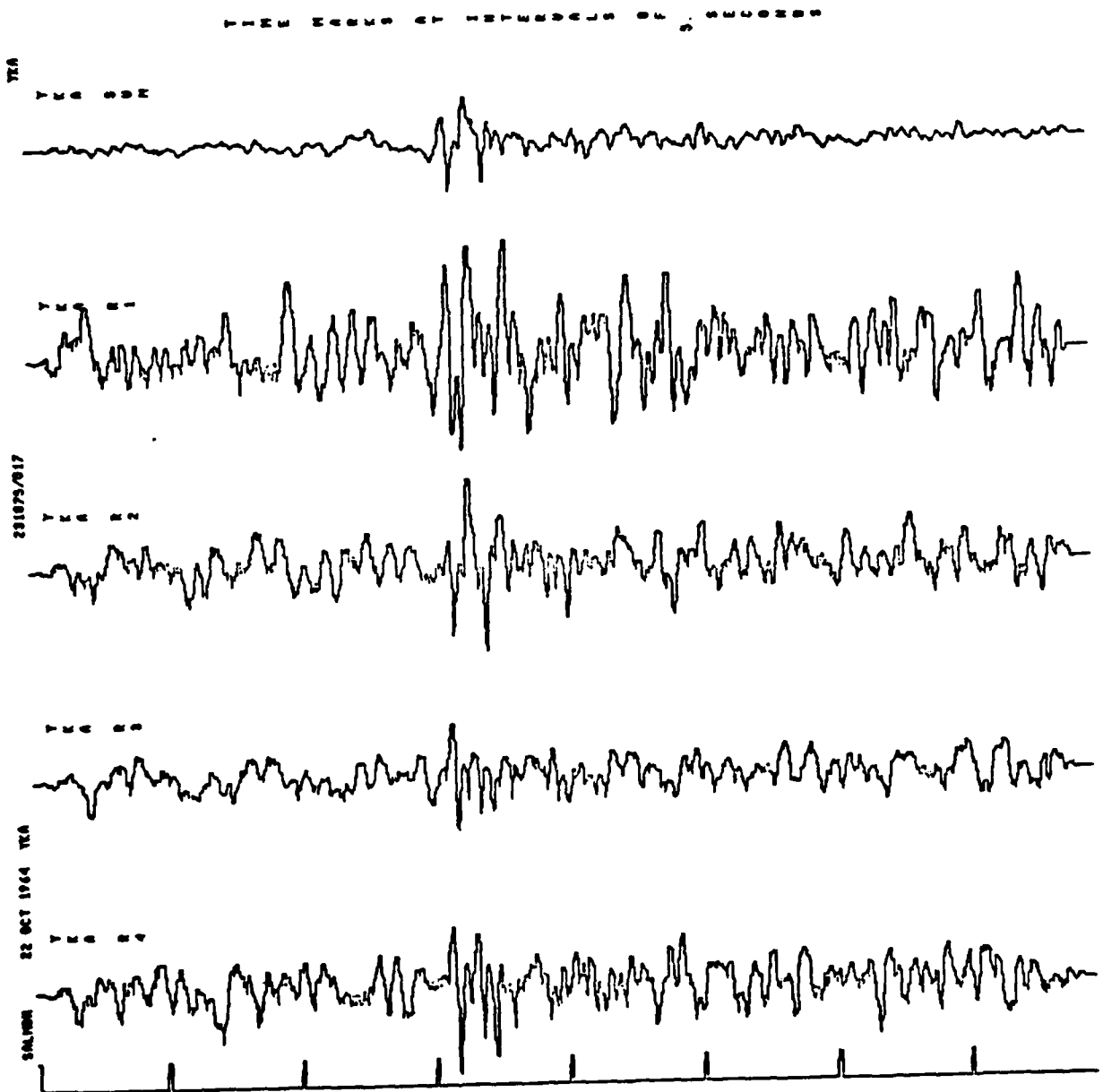


Figure 4 The YKA data for the SALMON (22 October 1964) beam sum (SUM) and individual array elements are plotted. The channels marked with an asterisk are faulty and were not included in the sum.

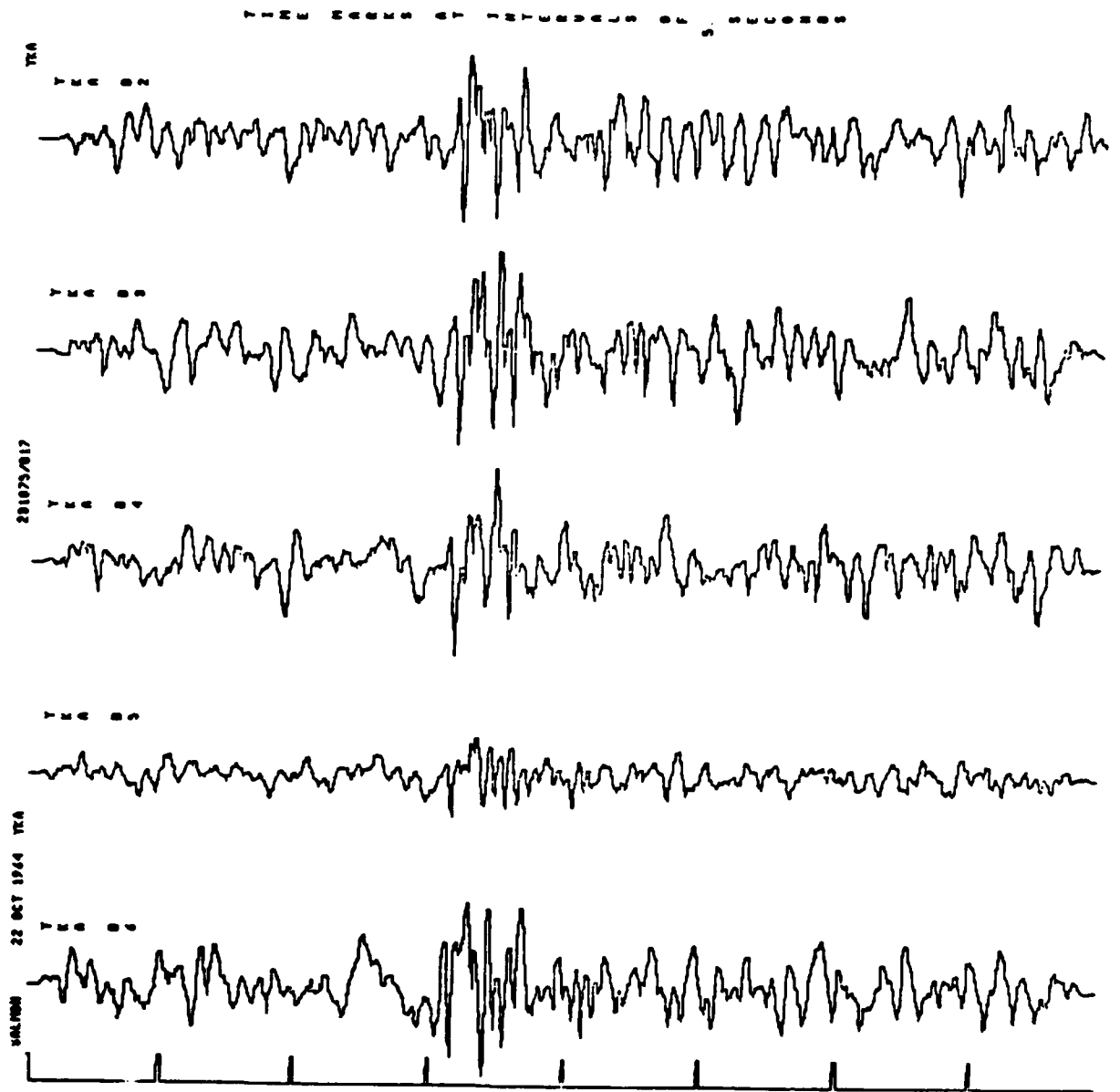


Figure 4 (continued)

THESE RECORDS OF EXTRATERRESTRIAL ORIGIN

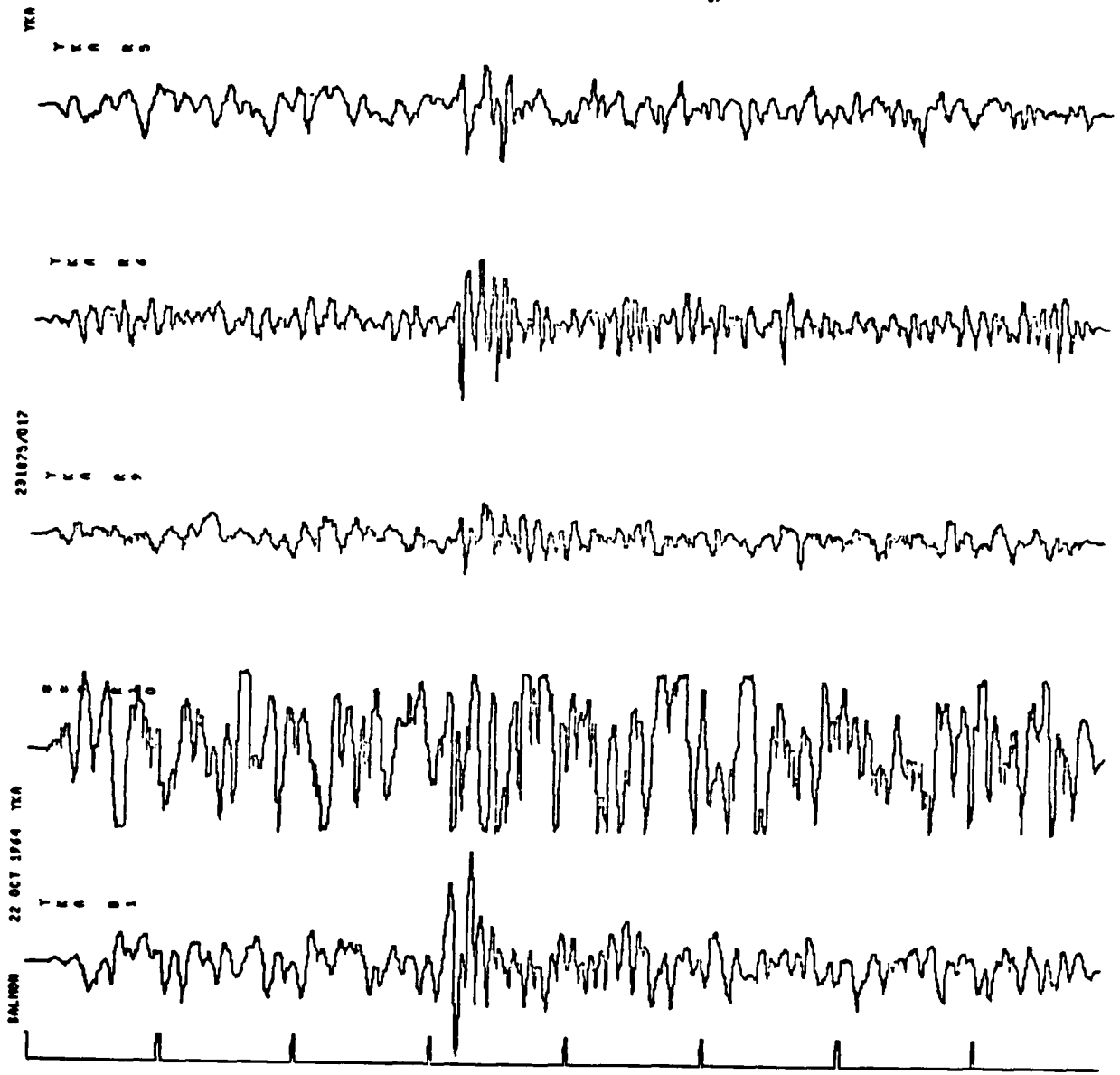
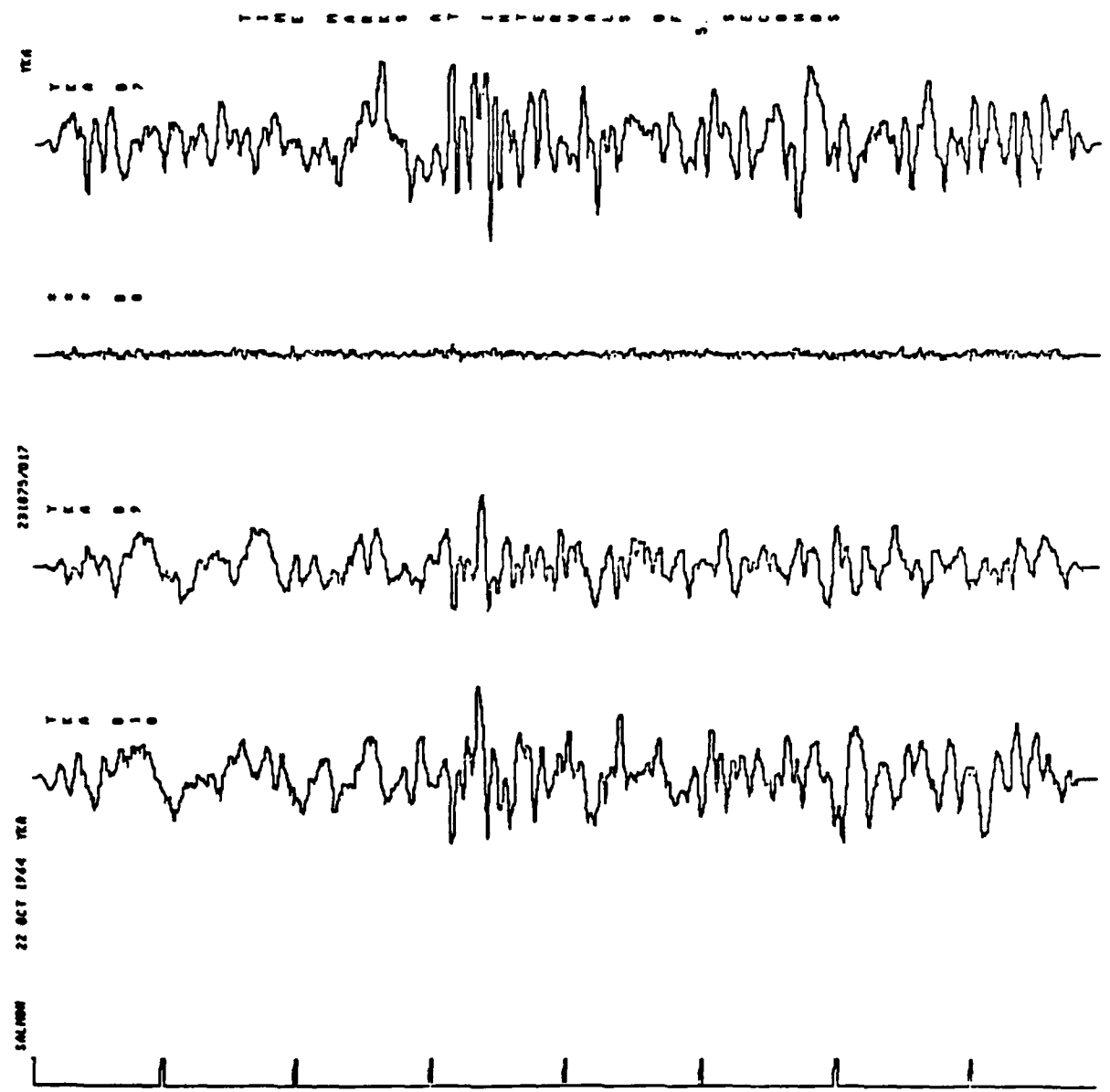


Figure 4 (continued)



**Figure 4 (continued)**

designed the software to mark all channels where the signal has exceeded 90% of the clipping level, that is, 4.5 volts, and did not use these channels in any of the subsequent analysis. The process is illustrated for a large event at EKA in Figure 5.

A very difficult fault to identify is the presence of small electronic spikes. Undetected, these will exaggerate the high frequency content of the signal. We try to eliminate their effect by looking at the spectrum of every signal and noise window processed, then deleting channels that show any unusual high frequency behaviour. This information is then included in the data base for future researchers.

The epicentral distance of the four UK stations from test sites of principal concern is listed in Table 2. Only stations in the 20-90° window are suitable for studying the characteristics of teleseismic P, with stations beyond 30° being preferred. Thus, for eastern Kazakhstan all four stations are at excellent distances while two or three stations are at suitable ranges for other test sites. Those data that have been carefully prepared for detailed analysis (as of 1 March 1984) are listed in Tables 3-7. The data collection and quality control effort is continuing and is expected to continue throughout the current contract.

For each event the ISC (or PDE when ISC is unavailable)  $m_b$  is listed. Also listed for the E Kazakh events is an  $m_b$  computed by P Marshall and colleagues at Blacknest using a least squares method (Douglas, 1966) for estimating station corrections that give the minimum variance  $m_b$ . See Marshall *et al* (1984) for details on these  $m_b$ .

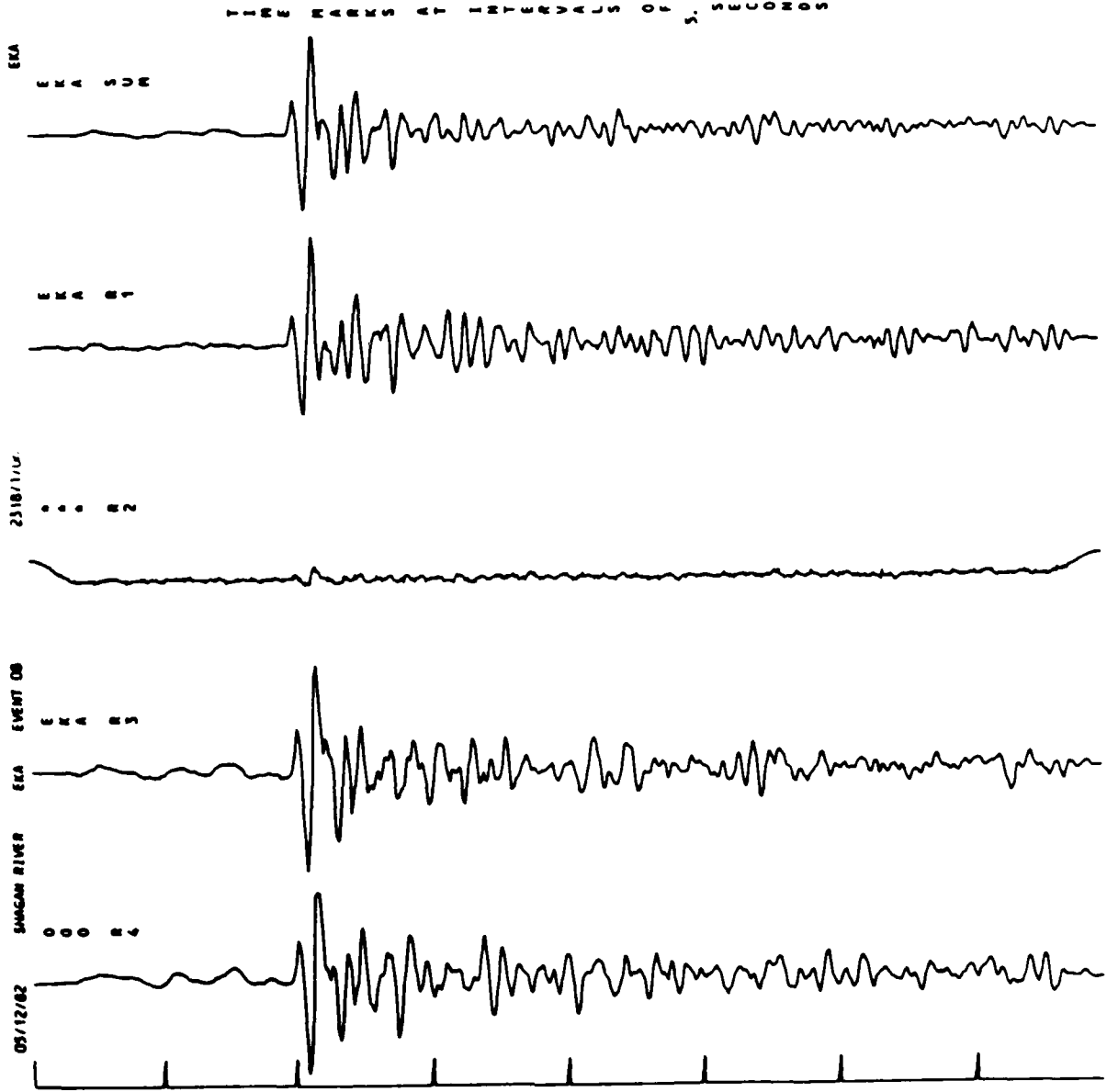


**Figure 5** The EKA data are plotted for the 5 May 1982 Shagan River explosion. The channels marked '0' are overloaded, while those marked 'C' have peak motions greater than 90% of the system maximum. Only R1, R3, S4 and S6 are included in the beam sum.

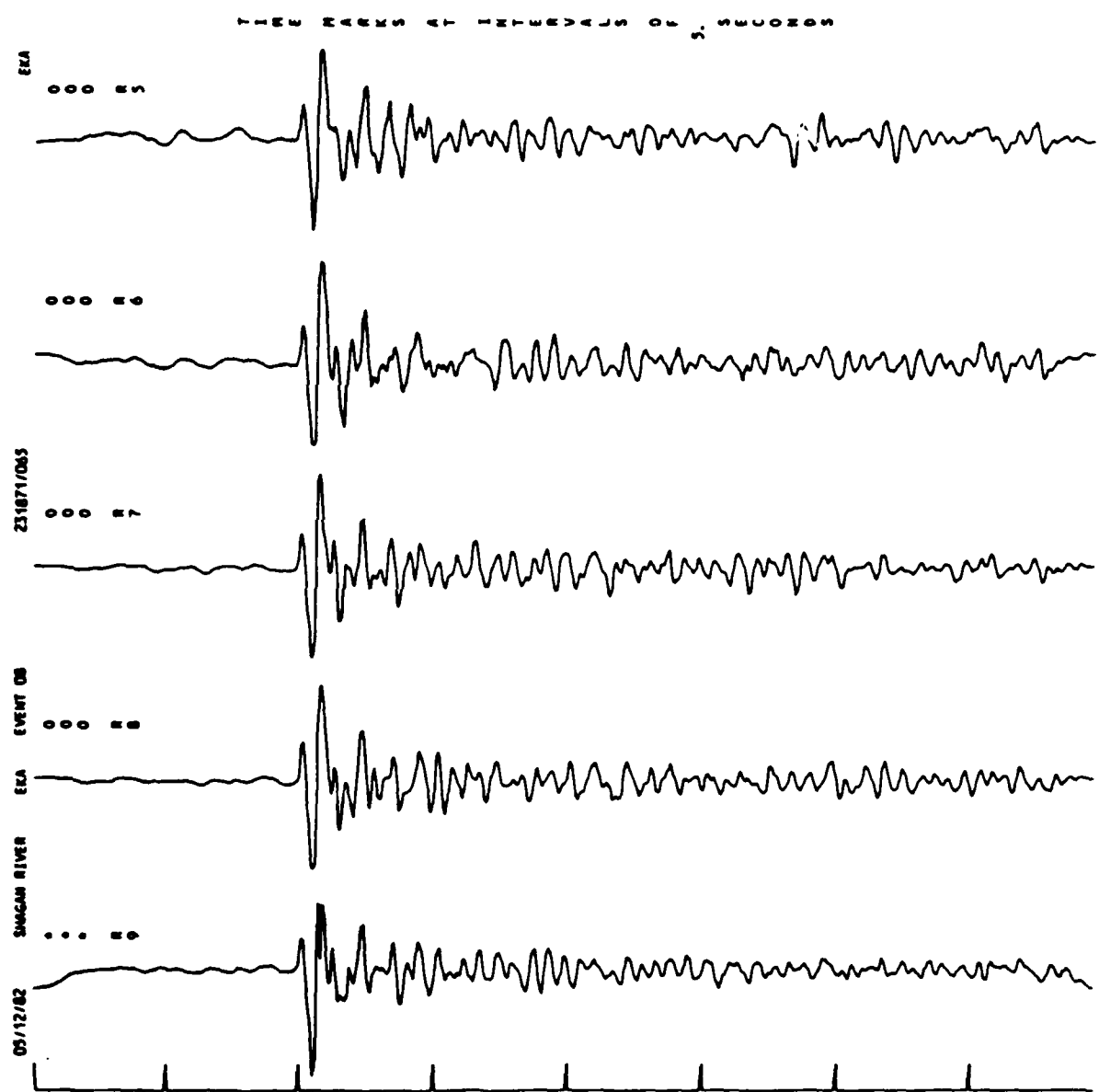


Figure 5 (continued)

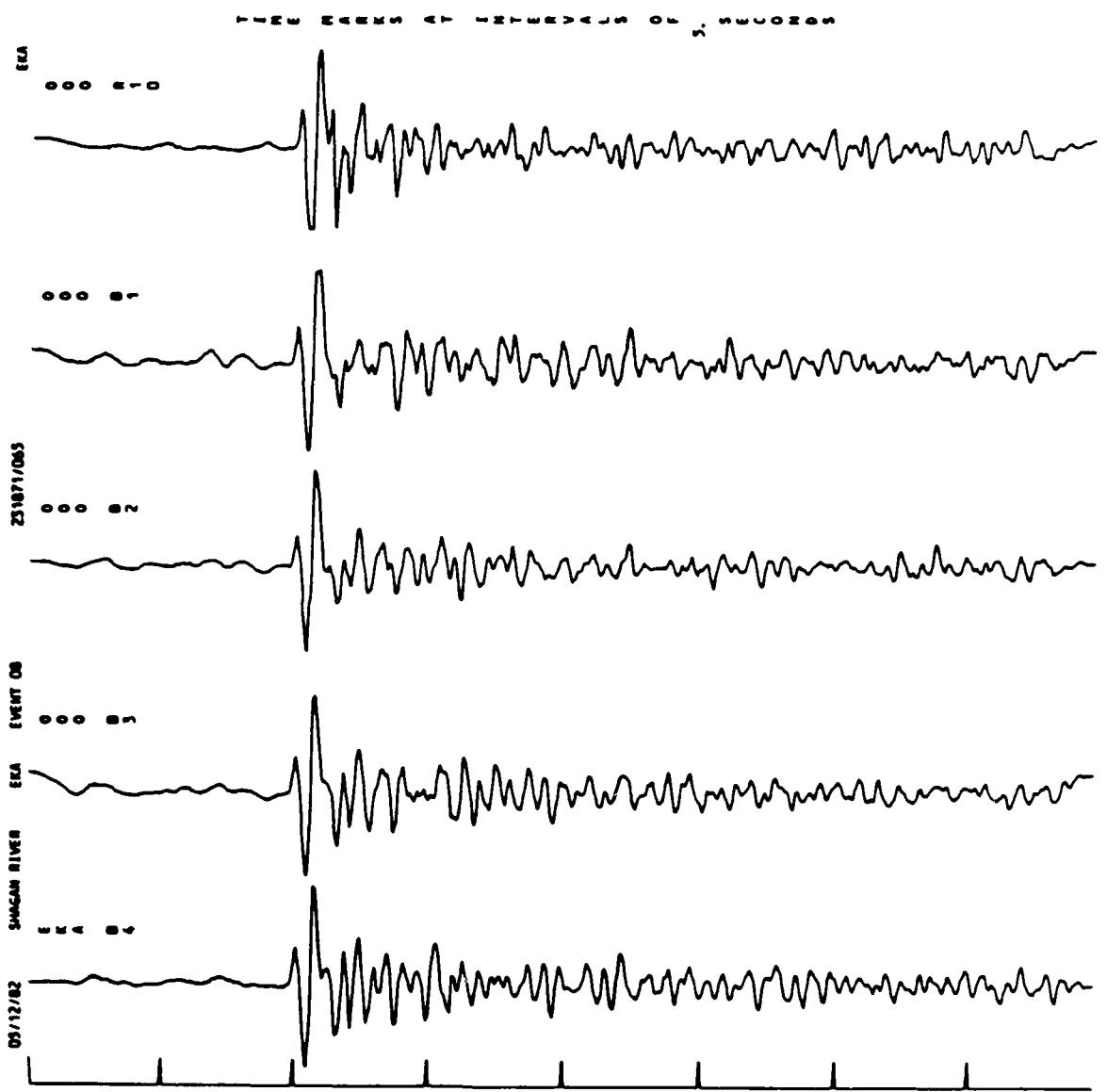


Figure 5 (continued)

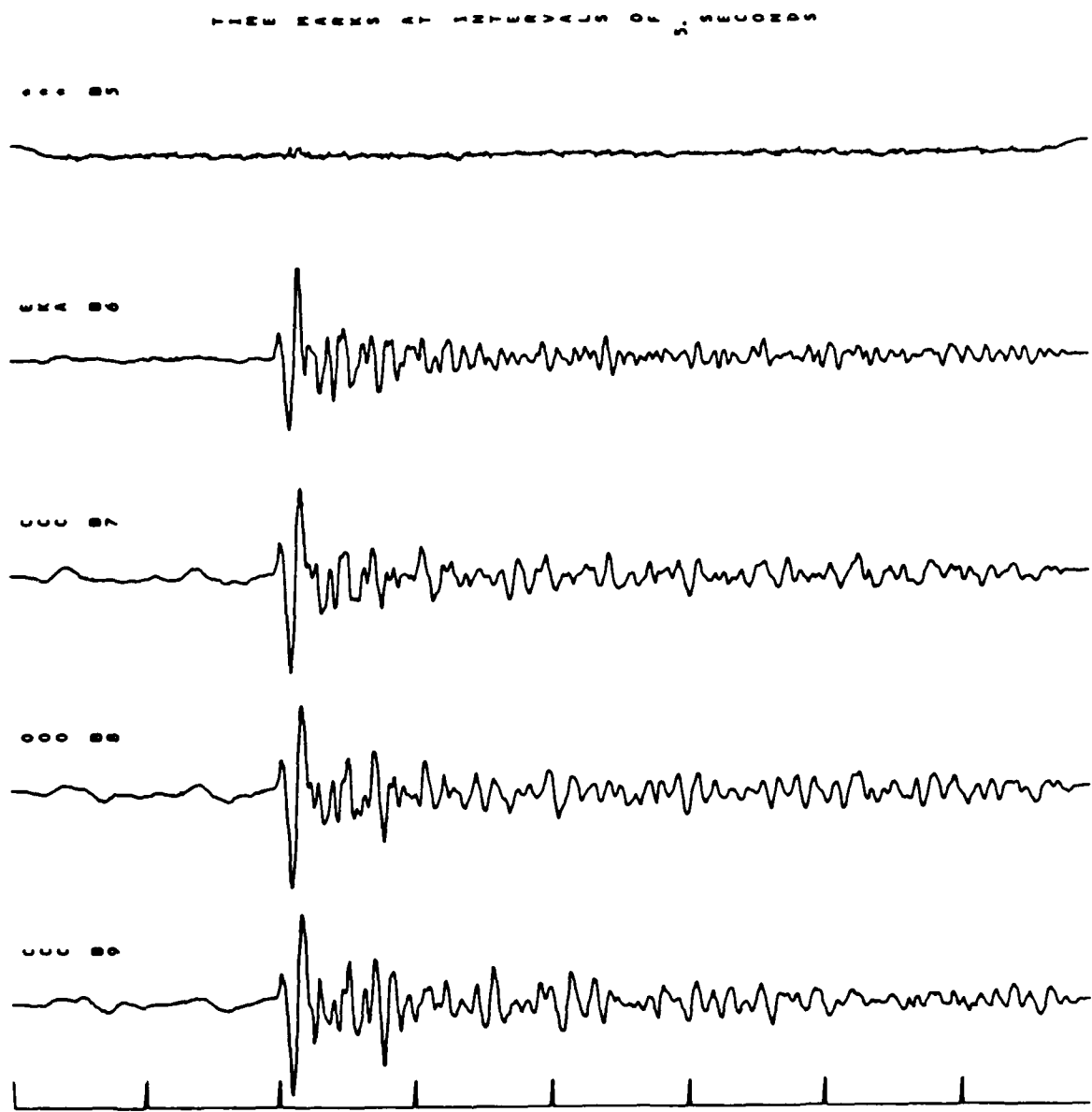


Figure 5 (continued)

Table 2

Epicentre Distance to Major Test Sites

Test Site	EKA	GBA	WRA	YKA
E Kazakhstan	47.1	36.2	85.4	67.5
NTS	71.7	128.1	117.2	25.5
French Sahara	31.7	68.6	not operating	81.3
French Mururoa	133.2	144.5	80.0	86.3
Novaya Zemlya	28.9	61.4	106.3	44.0
N Caspian	32.2	41.9	102.0	69.2

Table 3

Degelen Explosions

Date	ISC/PDE* m <sub>b</sub>	Blacknest m <sub>b</sub>	EKA	GBA	WRA	YKA
18-12-66	5.8		O	O	O	O
26-02-67	6.0		A	O	X	O
25-04-71	5.9	6.00	O	O	O	O
30-12-71	5.7	5.80	A	A	O	O
20-02-75	5.7	5.73	A	X	X	A
29-03-77	5.4		A	A	X	A
30-07-77	5.1	5.09	A	A	A	A
26-03-78	5.6	5.62	X	A	A	A
22-04-78	5.3	5.29	A	A	A	A
28-07-78	5.7	5.68	A	A	A	O
15-10-78	5.2	5.11	A	A	X	A
31-10-78	5.2	5.20	A	A	A	A
06-05-79	5.2	5.18	A	A	A	A
31-05-79	5.3	5.22	A	A	A	A
18-10-79	5.2	5.18	A	A	A	A
22-05-80	5.5	5.48	A	A	A	A
31-07-80	5.3	5.29	A	A	A	A
19-02-82	5.4*		A	A	X	A

Key: A - Available for processing

O - All channels overloaded

X - Data unusable or unavailable

? - Not now available, but may be recoverable

N - Too small to be seen

Table 4  
Shagan River Explosions

Date	ISC/PDE* m <sub>D</sub>	Blacknest m <sub>D</sub>	EKA	GBA	WRA	YKA#
15-01-65	5.8		A	X	X	O
19-06-68	5.4		A	A	X	O
30-11-69	6.0		A	X	A	X
30-06-71	5.4*	5.29	A	A	X	A
10-02-72	5.4	5.37	A	X	A	X
2-11-72	6.1		O	O	O	O
10-12-72	6.0		A	O	A	O
23-07-73	6.1	6.18	O	O	O	O
14-12-73	5.8	5.82	A	X	A	O
31-05-74	5.9	5.83	A	O	X	O
16-10-74	5.5	5.47	A	A	X	O
27-12-74	5.6	5.50	A	A	X	O
27-04-75	5.6	5.56	A	A	X	O
30-06-75	5.0	4.63	A	A	X	A
29-10-75	5.8	5.74	A	A	A	?
25-12-75	5.7	5.70	A	O	A	O
21-04-76	5.3		A	A	?	A
09-06-76	5.3	5.12	A	A	X	A
04-07-76	5.8	5.81	A	O	X	O
28-08-76	5.8	5.82	A	A	X	O
23-11-76	5.8	5.87	A	A	X	O
07-12-76	5.9	5.90	A	O	X	O
29-05-77	5.8	5.77	A	O	X	A
29-06-77	5.3	5.22	A	A	A	A
05-09-77	5.8	5.74	A	O	A	O
30-11-77	6.0		A	O	X	O
11-06-78	5.9	5.86	A	O	A	VBB
05-07-78	5.8	5.83	A	O	?	O
29-08-78	5.9		A	O	A	VBB
15-09-78	6.0	5.99	A	O	A	VBB
04-11-78	5.6	5.56	A	A	A	VBB
29-11-78	6.0		A	O	X	O

\*A broad-band velocity instrument is operated at low-gain.  
The notation VBB indicates that the array data are clipped,  
but this single element is available.

Table 4 Continued

Date	ISC/PDE* mb	Blacknest mb	EKA	GBA	WRA	YKA
01-02-79	5.4	5.38	A	A	X	O
23-06-79	6.2	6.22	A	O	O	O
07-07-79	5.8	5.83	A	X	X	VBB
04-08-79	6.1	6.16	A	A	A	VBB
18-08-79	6.1	6.12	A	A	A	VBB
28-10-79	6.0	5.96	A	O	A	O
02-12-79	6.0	6.01	A	O	A	O
23-12-79	6.2	6.18	A	X	O	O
25-04-80	5.5	5.50	X	A	A	A
12-06-80	8.0	5.59	?	A	A	VBB
29-06-80	5.7	5.74	A	X	A	VBB
14-09-80	6.2	6.21	O	A	O	O
12-10-80	5.9	5.90	A	A	A	VBB
14-12-80	5.9	5.95	A	A	A	O
27-12-80	5.9	5.88	A	A	A	X
29-03-81	5.6*	5.61	A	A	X	O
22-04-81	5.9*	6.05	A	A	A	O
27-05-81	5.4*	5.46	X	A	?	VBB
13-09-81	6.0*	6.18	A	A	A	VBB
18-10-81	6.0*	6.11	A	A	A	VBB
29-11-81	5.6*	5.73	A	A	A	VBB
27-12-81	6.2*	6.31	O	A	O	O
25-04-82	6.1*		X	A	A	X
04-07-82	6.1*		X	A	X	O
31-08-82	5.4*		A	A	A	A
05-12-82	6.1*		A	?	A	VBB
26-12-82	5.7*		A	A	A	VBB

Table 5  
French Explosions

Date	Sahara	ISC $M_D$	EKA	GBA	WRA	YKA
18-03-63	Emerald		A	X		A
20-10-63	Rubis		A	X		A
01-12-65	Tourmaline		A	X		A
02-07-65	Saphir		A	X		O
16-02-66	Grenat		A	A		A
Date	Mururoa	ISC $M_D$	EKA	GBA	WRA	YKA
26-11-75					A	A
11-07-76		5.0			X	A
19-02-77		5.2			X	A
19-03-77		5.8			X	O
06-07-77		5.2			A	A
22-03-78		4.8			A	A
19-07-78						A
26-07-78					N	A
30-11-78		5.8			A	O
17-12-78					N	A
19-12-78		4.9			A	A
09-03-79					A	A
24-03-79		4.9			A	A
29-06-79		5.4			A	A
25-07-79		6.0				O
22-11-79					N	A
23-02-80					N	A
03-03-80					N	A
23-03-80		5.7			A	A
01-04-80		5.1			A	A
04-04-80		4.5			N	A
16-06-80		5.4			A	A
21-06-80					N	A
06-07-80		4.6			N	A
19-07-80		5.8			?	O
03-12-80		5.6			?	X
06-03-81					A	A
28-03-81					A	A
08-07-81					A	A
03-08-81					A	A
08-12-81					A	A

Table 6  
NTS Explosions

Date	Name	M <sub>D</sub>	EKA	YKA
	YUCCA FLAT			
17-12-70	Carpetbag	5.8	X	O
27-09-77	Bulkhead	5.7	N	A
25-05-77	Crewline	5.3	A	A
19-08-77	Scantling	5.5	X	A
14-12-77	Parallones	5.7	A	A
12-07-78	Lowball	5.6	A	A
27-09-78	Draughts	5.0	N	A
27-09-78	Rummy	5.8	A	O
18-11-78	Quargel	5.1	A	A
06-09-78	Hearts	5.8	A	O
05-08-82	Atrisco	5.6*	A	A
	PAHUTE MESA			
30-06-66	Halfbeak		A	
20-12-66	Greeley		A	
14-05-75	Tybo	5.9	A	O
03-06-75	Stilton	5.8	A	X
19-06-75	Mast	5.9	A	O
26-06-75	Camembert	6.1	A	O
28-10-75	Kasseri	6.2	A	O
03-01-76	Muenster	6.2	A	O
12-02-76	Fontina	6.1	A	O
14-02-76	Cheshire	5.8	A	
09-03-76	Estuary	5.8	A	
14-03-76	Colby	6.2	A	O
17-03-76	Pool	6.0	A	O
11-04-78	Backbeach	5.7	A	A
03-08-78	Panir	5.6	A	A
26-04-80	Colwick	5.5	A	A
06-06-81	Harzer	5.6	A	A

Table 7  
US Explosions - Non-NTS Tuff/Rhyolite

Date	Name	mb	EKA*	YKA
22-10-64	Salmon		N	A
29-10-65	Longshot		A	A
02-06-66	Piledriver		A	O
19-01-68	Faultless		A	O
02-10-69	Milrow		SM	
06-11-71	Cannikin		SM	

\*A single low-gain channel is indicated by SM.

### III SHAGAN RIVER - TWO DISTINCT TEST SITES?

A remarkable feature of the Shagan River data (see Appendix A for the array beam seismograms for all events) recorded at the UK arrays is the way the waveforms consistently fall into two classes. For example, at EKA the waveforms for many events are quite simple, while others exhibit a consistent type of complexity. It is easy to recognise the two types and separate the events into Class 1, characterised by simple waveforms, and Class 2. Some typical events in each class are shown in Figure 6. This would not be especially noteworthy, except that the Class 1 and Class 2 events also write distinctly different seismograms at GBA and WRA, in Figure 7. At GBA the Class 1 events write very simple seismograms, while the Class 2 events show a strong interference shortly after the second peak. At WRA Class 1 events write seismograms with little energy after the second peak, while Class 2 events are characterized by complex signals that continue for several cycles. At YKA the array data are too sparse to tell whether a similar separation occurs. However, the single channel velocity broad-band data do not seem to separate into two classes. This may indicate that the waveform dichotomy does not occur at all azimuths, or (less likely) that array beaming to remove near receiver effects is necessary to bring out the differences.

For the three stations where the separation into two classes is clear, the waveform classification for 57 Shagan River events is summarised in Table 8. Fifteen of these were observed at only one station, while 29 are observed at two and 13 at all three stations. Of the latter 42 events, the classification is ambiguous for only three. Thus, the waveform complexity for Class 2 events must be due to something about the source and/or its vicinity.

We note from the summary at the end of Table 8 that while the Class 2 events have generally smaller  $m_b$ , there is too much overlap to attribute the waveform differences to source size. The examples in Figure 6 and 7 also demonstrate this point. The explanation almost certainly must be in systematically different source coupling and/or near source geology.

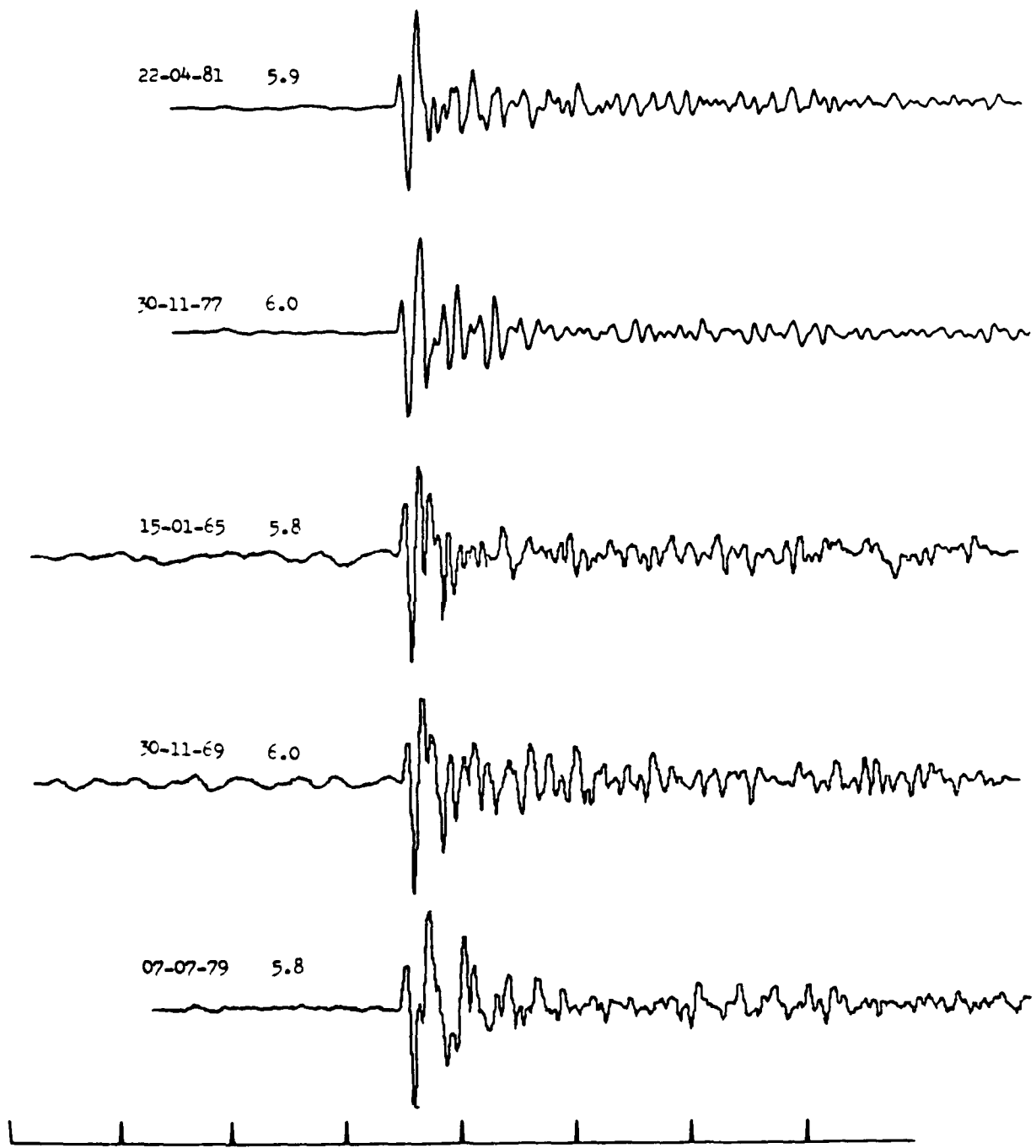


Figure 6 The EKA seismograms (beammed array sum) are plotted for two Class 1 and three Class 2 Shagan River events. The  $m_b$  are indicated for each event.

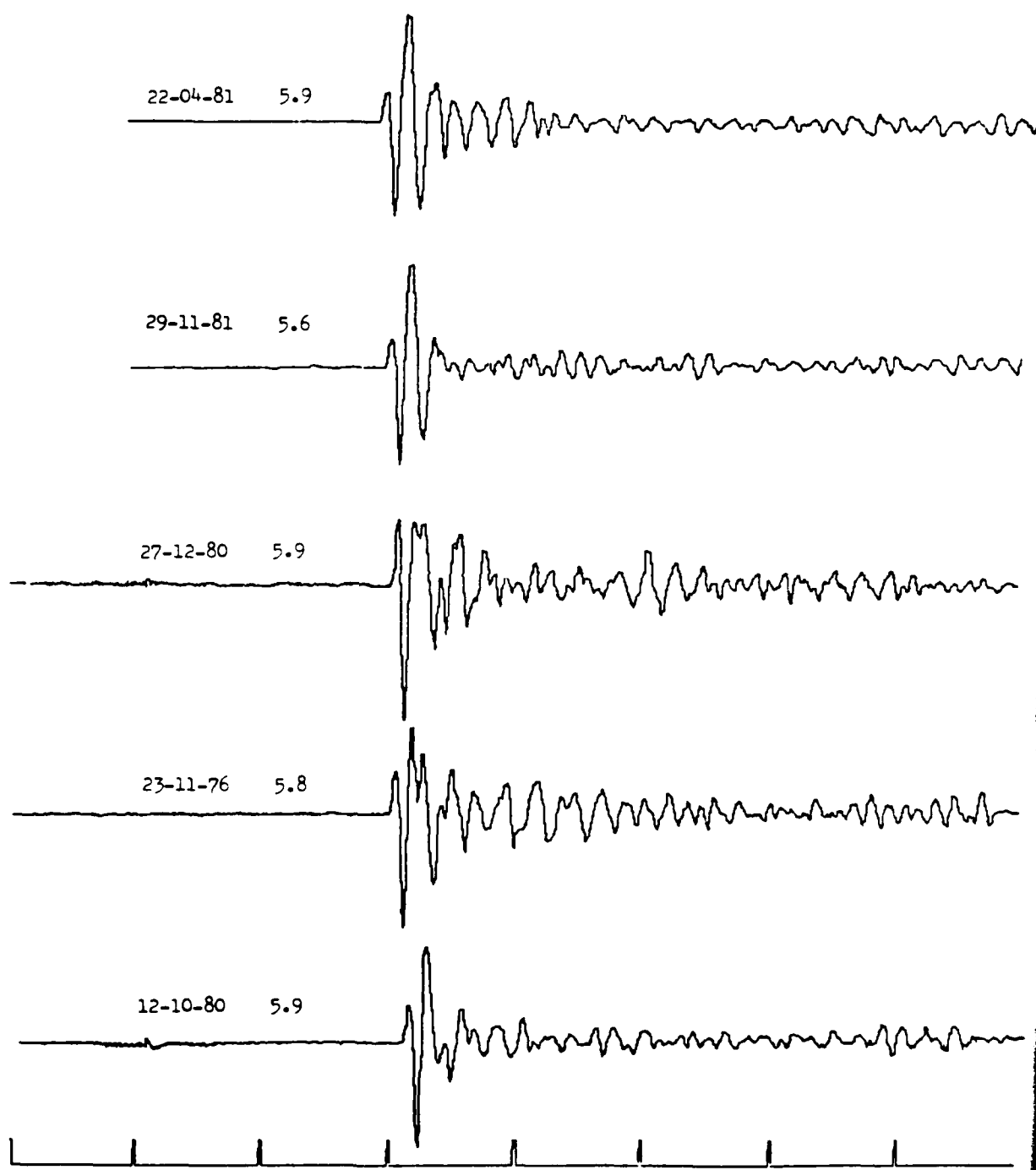


Figure 7(a) Two Class 1 and three Class 2 seismograms are plotted for GBA.

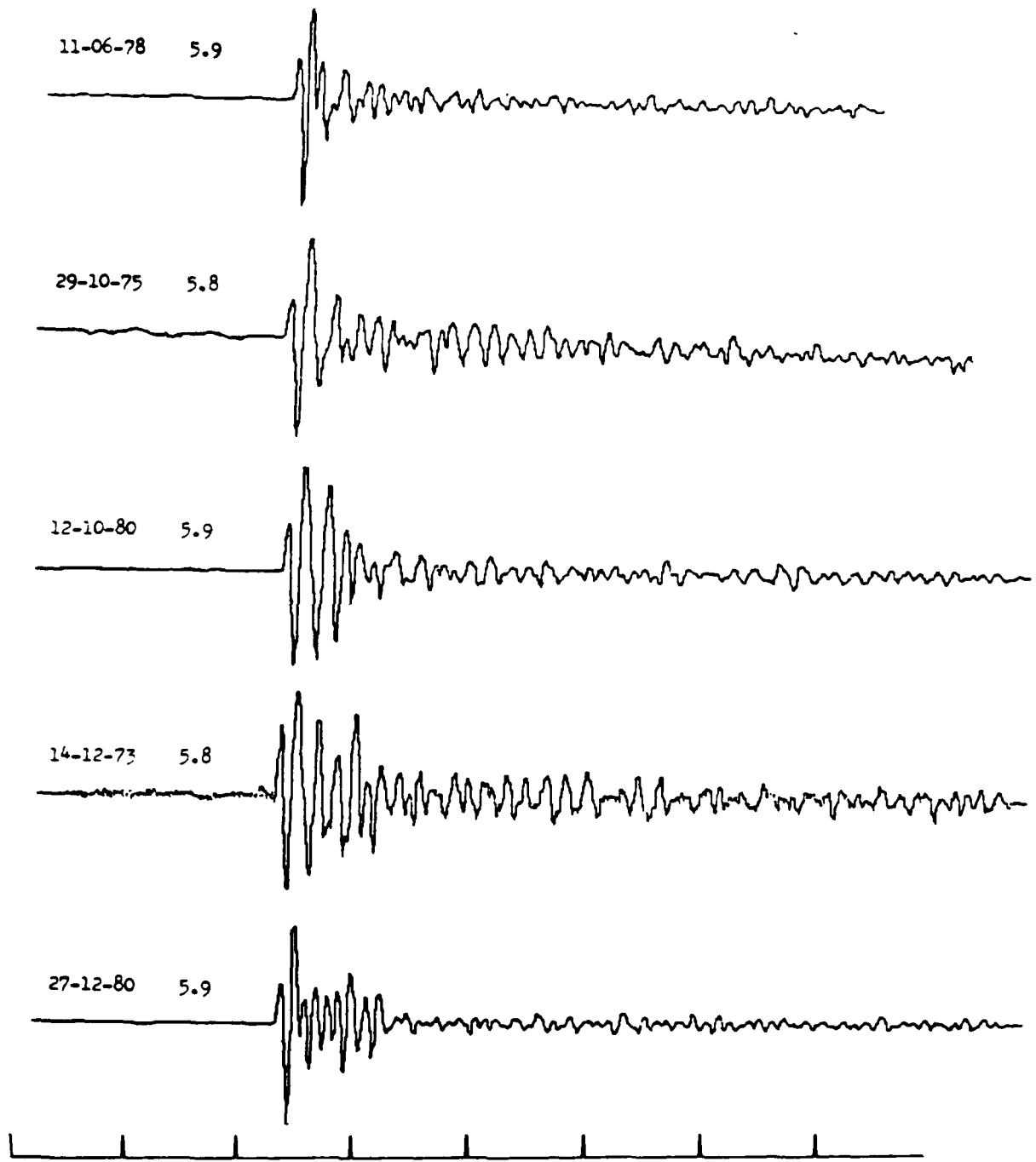


Figure 7(b) Two Class 1 and three Class 2 seismograms are plotted for WRA.

TABLE 8  
Waveform Classification for Shagan River Explosions

<u>Date</u>	<u>m<sub>b</sub></u>	<u>Class*</u>	<u>EKA</u>	<u>GBA</u>	<u>WRA</u>
15.01.65	5.8	'2'	2	X	X
19.06.68	5.4	'2'	2	X	X
30.11.69	6.0	'2'	2	X	X
30.06.71	5.4	2	2	2	X
10.02.72	5.4	2	2	X	2
10.12.72	6.0	2	2	X	2
14.12.73	5.8	2	2	X	2
31.05.74	5.9	'1'	1	X	X
16.10.74	5.5	2	2	2	X
27.12.74	5.6	2	2	2	X
27.04.75	5.6	2	2	2	X
30.06.75	5.0	2	2	2	X
29.10.75	5.8	?	1	2	X
25.12.75	5.7	2	2	2	X
21.04.76	5.3	'2'	2	X	X
09.06.76	5.3	2	2	2	X
04.07.76	5.8	'1'	1	X	X
23.11.76	5.8	2	2	2	X
07.12.76	5.9	'1'	1	X	X
29.05.77	5.8	'1'	1	X	X
29.06.77	5.3	2	2	2	2
05.09.77	5.8	2	2	2	2
30.11.77	6.0	'1'	1	X	X
11.06.78	5.9	1	1	X	1
05.07.78	5.8	'1'	1	X	X
29.08.78	5.9	?	2	2	2
15.09.78	6.0	1	1	X	1
04.11.78	5.6	2	2	2	2
29.11.78	6.0	'1'	1	X	X
01.02.79	5.4	2	2	2	1
23.06.79	6.3	1	1	X	1
07.07.79	5.8	'2'	2	X	X
04-08-79	6.1	1	1	1	1
18-08-79	6.1	2	2	X	2
28.10.79	6.0	2	2	2	2
02.12.79	6.0	1	1	X	1
23.12.79	6.2	1	1	X	1
25.04.80	5.5	'1'	X	1	X
12.06.80	5.6	2	X	2	2
29.06.80	5.7	1	1	X	1
14.09.80	6.2	1	X	1	1
12.10.80	5.9	2	2	2	2
28.08.81	5.8	2	2	2	X
14.12.80	5.9	?	2	1	1
27.12.80	5.9	2	2	2	2
29.03.81	5.6	2	2	2	X
22.04.81	5.9	1	1	1	1
27.05.81	5.4	'2'	X	2	X
13.09.81	6.0	1	1	1	1
18.10.81	6.0	1	1	1	1

CONTINUED

TABLE 8

(Continued)

<u>Date</u>	<u>m<sub>b</sub></u>	<u>Class*</u>	<u>EKA</u>	<u>GBA</u>	<u>WRA</u>
29.11.81	5.6	1	1	1	X
27.12.81	6.2	1	X	1	1
25.04.82	6.1	1	X	1	1
04.07.82	6.1	'1'	X	1	X
31.08.82	5.4	?	1	2	X
05.12.82	6.1	1	1	X	1
26.12.82	5.7	2	2	2	2

Summary

<u>m<sub>b</sub></u>	<u>Class 1</u>	<u>Class 2</u>
≤ 5.3	1	4
5.4-5.5	1	6
5.6-5.7	2	7
5.8-5.9	6	9
6.0-6.1	11	4
≥ 6.2	3	0
Total	24	30

\* '1' and '2' indicate classification by only one waveform

The waveform differences correlate almost perfectly with location within the test site. All Shagan River events were relocated by Joint Epicentre Determination (Douglas *et al.*, 1974). Travel times from the ISC data tapes were used and the locations were done with respect to the known (Shore, 1982) location of the 15 January 1965 cratering event. (For details see Marshall *et al.*, 1984).

The new locations are plotted in Figure 8, along with the identification as Class 1 and 2 events. Note that with only one exception the two classes separate on either side of a line striking roughly 45° west of north through the centre of the test site. Also, two of the three ambiguous events lie close to the boundary.

The most likely explanation for the waveform differences between the northeast and southwest Shagan events is that they are in different source media. There remains some possibility that path differences are responsible, but the similar effects seen at three well-separated azimuths argue against this. Also, as will be shown in Section VI, the corner frequency of the northeast Shagan event seems to be systematically lower, which suggests a higher strength source coupling medium. The argument that the northeast events are in a stronger material is further strengthened by the fact that the Class 2 waveforms at GBA and EKA are more similar to waveforms of Degelen events (Appendix A) than to the Class 1 Shagan events. However, the picture is clouded somewhat by the fact that at WRA the Degelen events write waveforms of a third class.

In summary, the waveform and spectral data suggest that the Shagan River test site is best viewed as two distinctly different sites. The evidence suggests that the events in the southwest are in a less competent or weaker material.

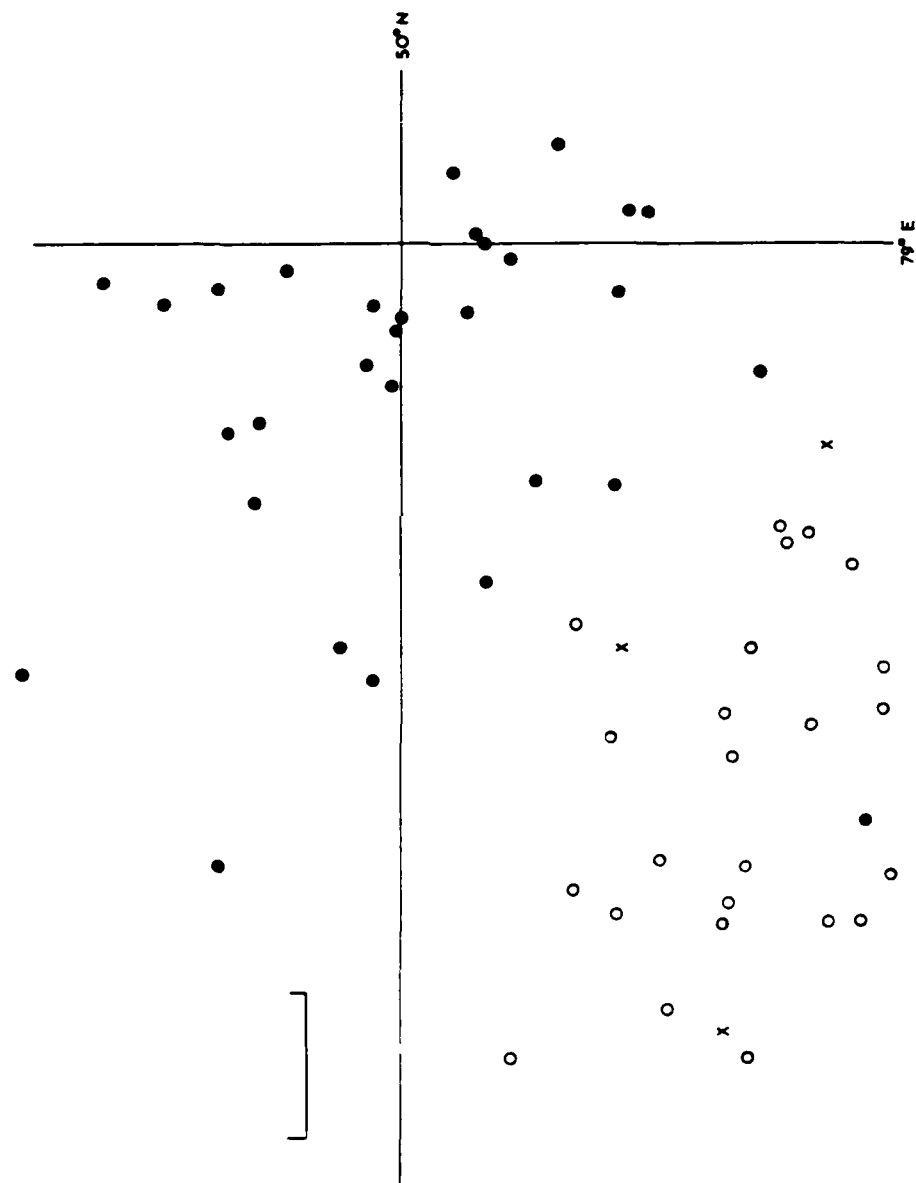


Figure 8 The locations of Shagan River explosions are plotted with symbols representing event classification according to waveform (Table 8). The open and solid circles represent Class 1 and Class 2 events respectively, while an X represents an event of ambiguous classification.

#### IV SIGNAL SPECTRUM AND $t^*$ ESTIMATION FROM ARRAY DATA

##### 4.1 Introduction

A commonly encountered problem in seismology is the need to estimate the Fourier spectrum of a signal in the presence of interfering noise. Most studies are concerned with single station recordings and employ straightforward windowing and smoothing operations to obtain the final spectral estimate. For example, Der and his colleagues (eg Der and McElfresh, 1976; Der *et al* 1982 a, b) have estimated the spectra of a large number of P wave signals from explosions and earthquakes. In their analysis the signal is Parzen windowed and the energy spectral density is then computed and smoothed. A noise power spectrum is computed the same way and subtracted from the signal energy density, and the final spectral estimate is computed from this difference. Other investigators often use even more direct procedures. For example, Sipkin and Jordan (1979) simply Fourier transform selected windows, then heavily smooth the result to obtain their multiple SCS spectral estimates.

When array data are available, much more can be done to extricate the signal from the noise, and there is a substantial literature devoted to this. The most direct method is beamforming by simple delay and sum operations. Far more elaborate techniques have been developed such as prediction-error filtering (Claerbout, 1964) and maximum-likelihood estimation (eg Capon *et al* 1968), but these methods, for all their complexity, seem to offer only a modest improvement on the results from the simple delay-and-sum beamforming.

Beamforming will improve the signal/noise by  $\sqrt{N}$ , with N the number of seismometers, if the noise is random and the signal is correlated and arrives at the expected time. Thus, the spectrum of the beam-formed array output will have much better signal/noise than any single sensor spectrum over the frequency band where these conditions are met. Spectra from the array beams have been used, for example, by Bock and Clements (1974) who processed WRA recordings of deep Fiji-Tonga earthquakes. However, they note that the spectrum of the beam-formed signal has less high frequency than the average of the spectra from the single channels. This is

consistent with the expectation that the signal coherence across the array will decrease as frequency increases. Thus, beam-forming applies a signal-dependent low-pass filter to the data.

Taking this past experience into account, a spectral estimation method was designed to exploit the advantages of arrays, while using single channel spectral estimation methods similar to those employed by Der and his colleagues. We will describe this method and give some examples of its use. We then briefly describe how these spectra are used to estimate the attenuation parameter  $t^*$ .

#### 4.2 Signal Spectrum Estimation

For each channel a narrow signal window (length  $T_S$ ) is selected and the data are 10% cosine tapered and Fourier transformed. The signal window selection is based on the beam-sum trace and this window is then used for the individual channels after shifting by the delay used in computing the beam. The energy spectral density is computed by squaring the transform and this is then converted to the units of power by normalizing by the length of the time window. Thus, if  $A_0 e^{i\phi_0}$  is the Fourier spectrum of the selected window, the apparent power is

$$A_o^2 = A_s^2 + A_n^2 + 2 A_s A_n \cos(\phi_s - \phi_n), \quad (1)$$

where subscripts s and n indicate the actual signal and the interfering noise, respectively.

A noise window of length  $T_n$  is selected prior to the signal and its power spectrum ( $\hat{A}_n^2$ ) computed in an analogous way; that is, by squaring the Fourier spectral amplitude and dividing by  $T_n$ . An estimate of the signal power ( $\hat{A}_s^2$ ) is then computed by subtracting the noise power estimate from the power in the signal window. That is,

$$\hat{A}_s^2 = A_o^2 - \hat{A}_n^2, \quad (2)$$

The final estimate of the signal amplitude spectrum  $|F(\omega)|$  is the mean of the  $\hat{A}_s^2$  from the N elements of the array. That is,

$$|F(\omega)| = \left[ \frac{T_s}{N} \sum \hat{A}_s^2 \right]^{1/2} \quad (3)$$

But, combining (1) and (2), we see that

$$\sum_{s=1}^N \hat{A}_s^2 = \sum_{s=1}^N A_s^2 + \sum_{n=1}^N \left[ A_n^2 - \hat{A}_n^2 \right] + 2 \sum_{s=1}^N A_s A_n \cos(\phi_s - \phi_n). \quad (4)$$

If the noise is random and stationary, the second term will vanish as  $N$  increases. The last term must also decrease rapidly with increasing  $N$  if the noise is uncorrelated with the signal. Thus, as  $N$  increases the signal power estimate,  $\hat{A}_s^2$  will approach the actual signal power  $A_s^2$  and  $|F(\omega)|$  will be a good estimate of the actual signal spectrum.

As an example, consider a high signal/noise GBA recording of a large Shagan River explosion. The data are plotted in Figure 9. Note that in this case there are twelve usable channels. The Fourier spectra of the signal and noise windows selected are plotted for a typical channel in Figure 10. Note that this and all subsequent spectra have been multiplied by  $f^2$  for  $f > 1$  Hz for reasons discussed later in Section 4.3. On each spectral plot we also show the original seismogram together with the signal and noise windows (including the 10% cosine taper). The signal window is very short, including an undistorted 1.0 seconds plus the tapered 0.3 seconds on each end for a total of 2.4 seconds. The ultimate objective is to estimate the attenuation that influences amplitude measures like  $m_b$ , so it is important to isolate the first arriving P wave. However, it turns out that the gross properties of the spectrum (including its rate of decay) are insensitive to the choice of window length in most cases. In analysing random and stationary processes one might prefer longer windows to suppress the effects of sidelobes of the windowing filter, but this idea is really not applicable to the short duration transient signals of principle interest.

The noise window is 3.8 seconds for this example, and windows of about this length are being used for all our analyses. Hypothetically, one might assume that a larger noise window would have the advantage of providing a somewhat more accurate estimate of the actual noise preceding the signal, while the advantages of a noise window of exactly the length of the signal window would be that the side-lobe contribution would be the same for the actual and estimated noise spectra. As a practical matter, the noise window length seems to make very little difference.

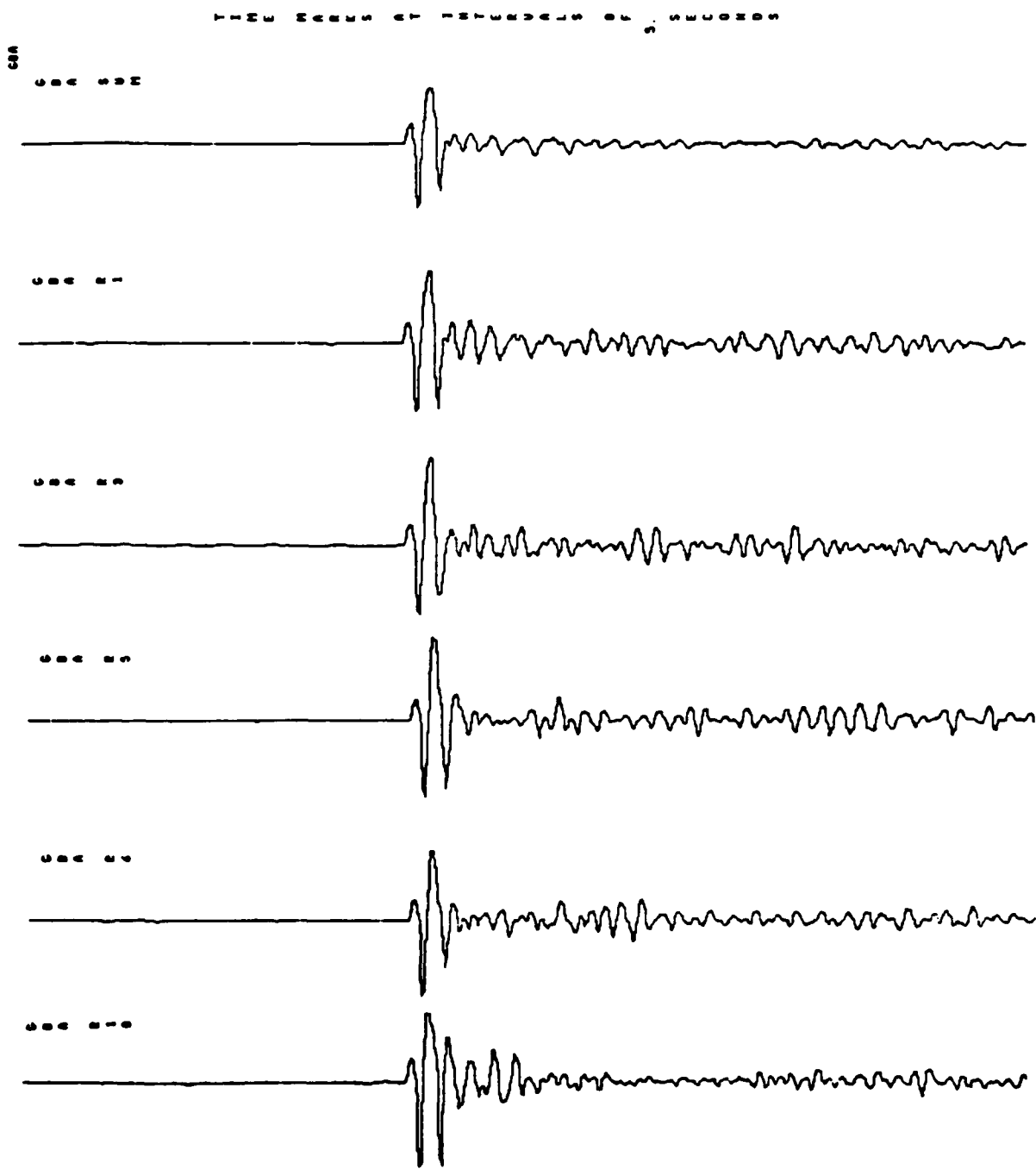


Figure 9 The GBA array sum and useful individual channel recordings are shown for the 27 December 1981 Shagan River explosion.

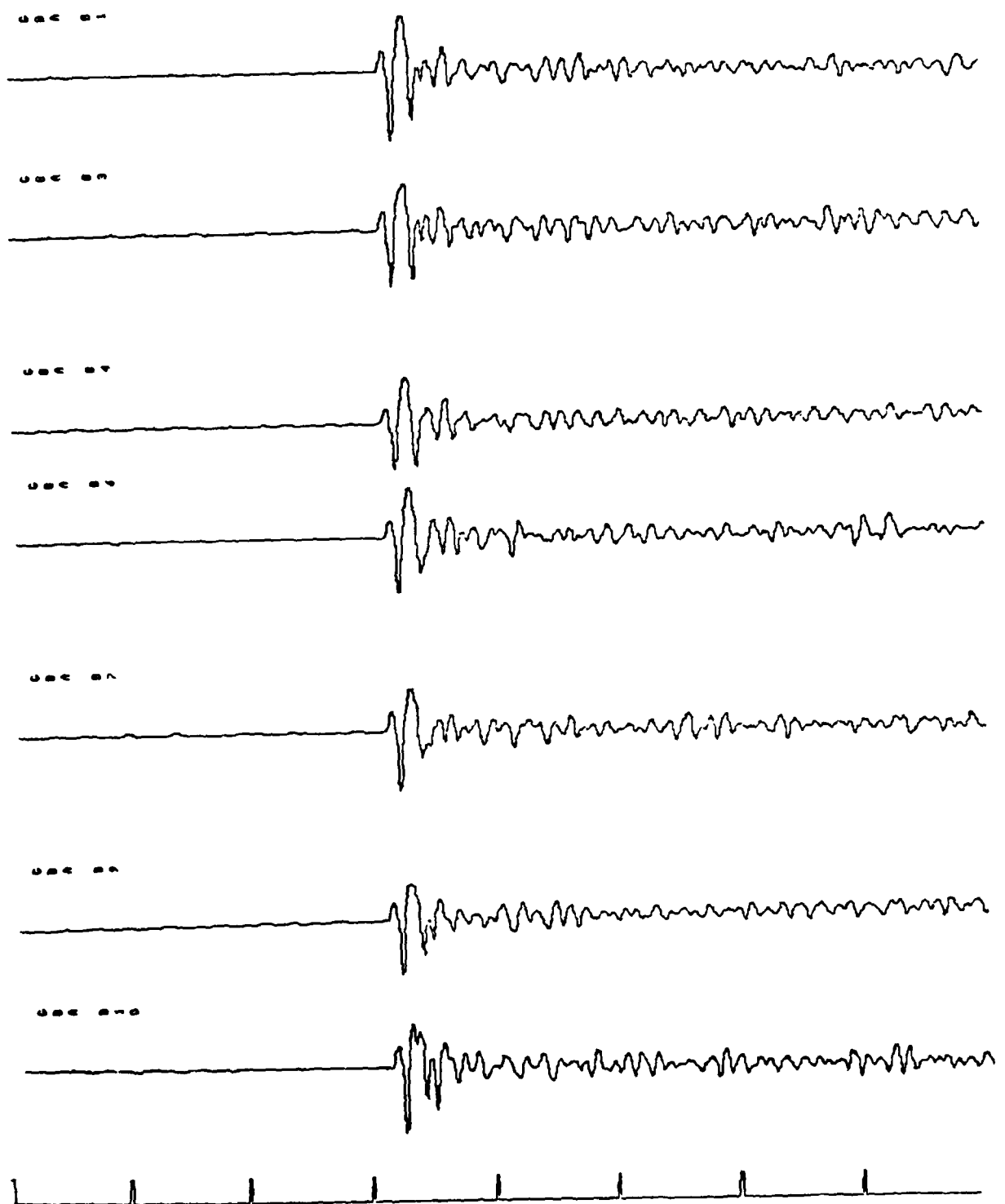


Figure 9 (continued)

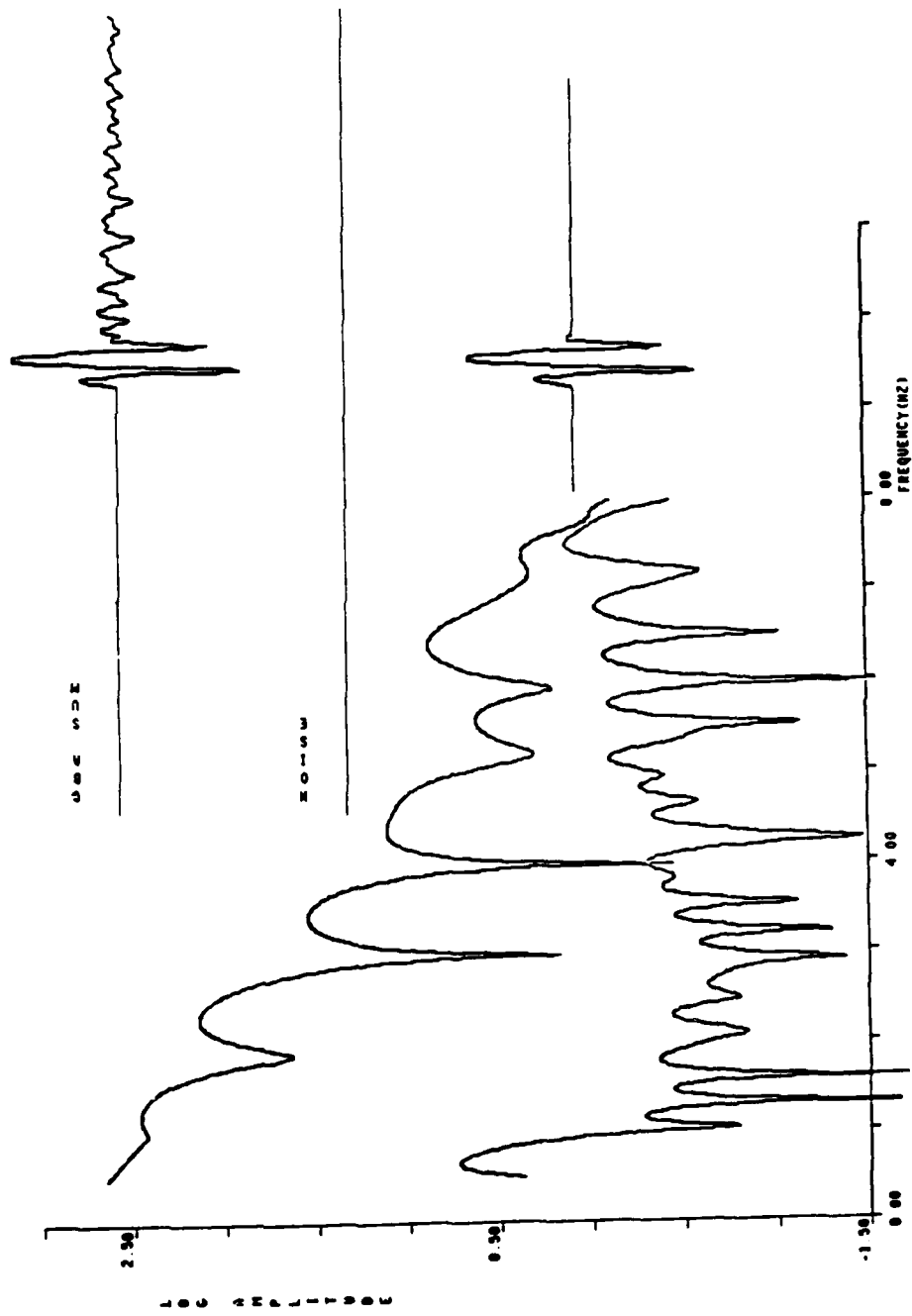


Figure 10 The Fourier spectra of the signal and noise windows are plotted for the array sum and channel  $R'$ . In all plots with this format each spectrum has been multiplied by  $f^2$  for  $f > 1$  Hz. The original (Figure 9) and windowed time series are shown on each spectral plot.

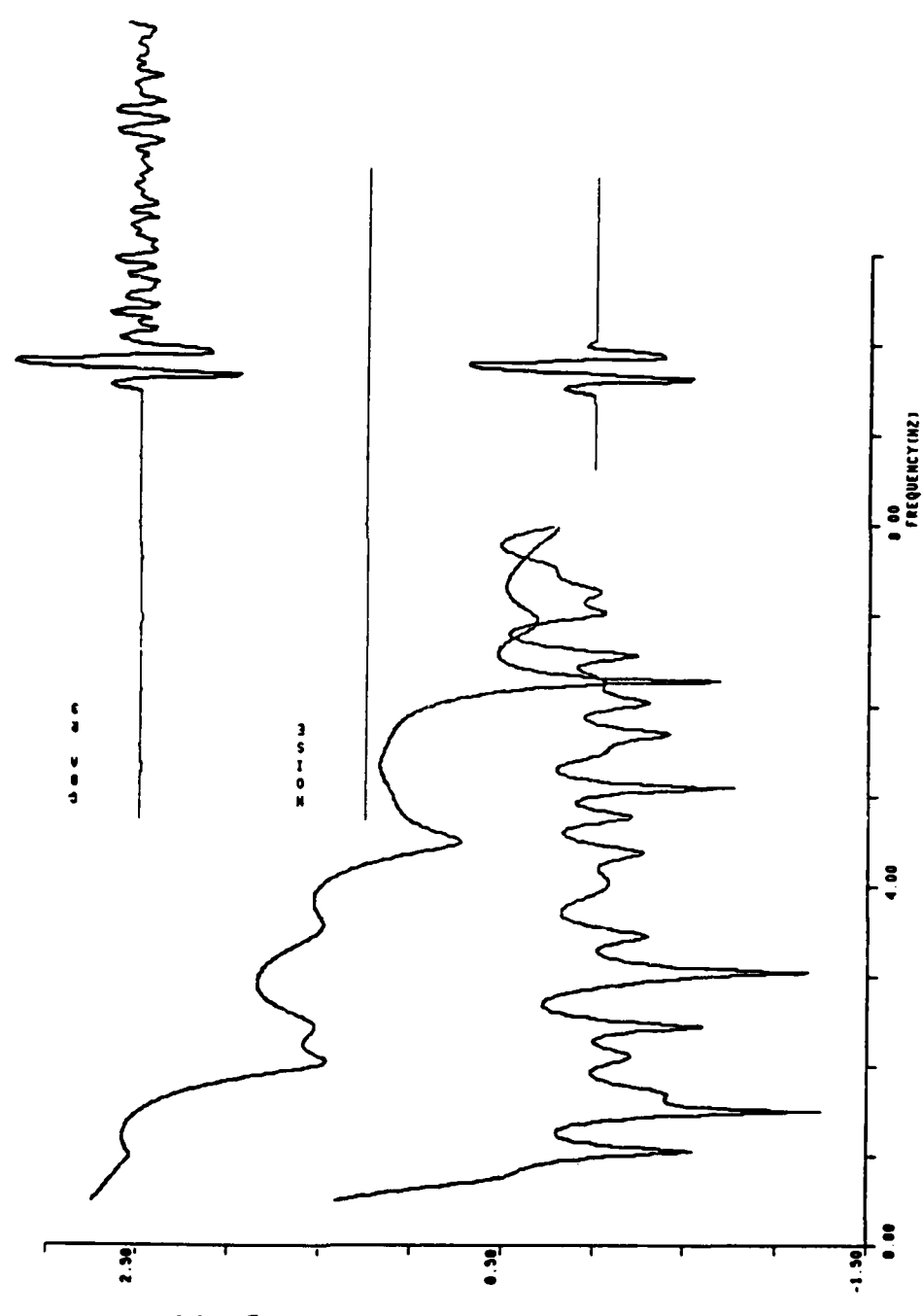


Figure 10 (continued)

The spectra exemplified in Figure 10 are processed as described above, and the final spectrum ( $|F(\omega)|$  in equation 3) is shown in Figure 11. Plotted with  $|F(\omega)|$  is the average noise spectrum estimate derived from the sum of the  $\hat{A}_n^2$ . This is important to help define the frequency band where the signal spectrum is essentially uncontaminated by noise. Also, we require

$$\sum_{n=0}^{N-1} A_n^2 > \sum_{n=0}^{N-1} \hat{A}_n^2$$

to compute  $|F(\omega)|$ .

In Figure 12 we show the  $|F(\omega)|$  and average noise spectra compared to the Fourier spectra of the signal and noise on the beam sum trace. This confirms the expectation that time domain beam summing filters out part of the high frequency energy in the signal. Similar comparisons are shown for other events in Appendix B. From these we see that using the beam sum spectrum will lead to underestimation of the high frequency energy in the signal. We also note that the noise is reduced by a factor very close to  $\sqrt{N}$  by the beam summing. As a final demonstration of the consistency of the  $|F(\omega)|$ , in Figure 13 it is superimposed on the raw Fourier spectra of each of the twelve channels. We see that  $|F(\omega)|$  is basically a smooth average of these spectra for this high signal/noise event.

The YKA recordings of SALMON (Figure 4) provide a good example of a low signal/noise event. The Fourier spectra of the sum and a typical single channel are shown in Figure 14. In Figure 15 the  $|F(\omega)|$  and average noise are plotted. When (5) is not satisfied,  $|F(\omega)|$  is undefined and a horizontal line is plotted, as can be seen at high frequencies in the plot. In Figure 16 the  $|F(\omega)|$  and average noise are compared to the Fourier spectra from the beam sum. Again, the time domain beam summing reduces the apparent high frequency content of the signal. The comparison of  $|F(\omega)|$  with the individual channel spectra is shown in Figure 17.

This spectral estimation technique is being routinely applied to, the data base described in Section II. The resulting spectra are a powerful resource for studying the combined effect of Q, the source spectrum and pp on the seismograms from large explosions.

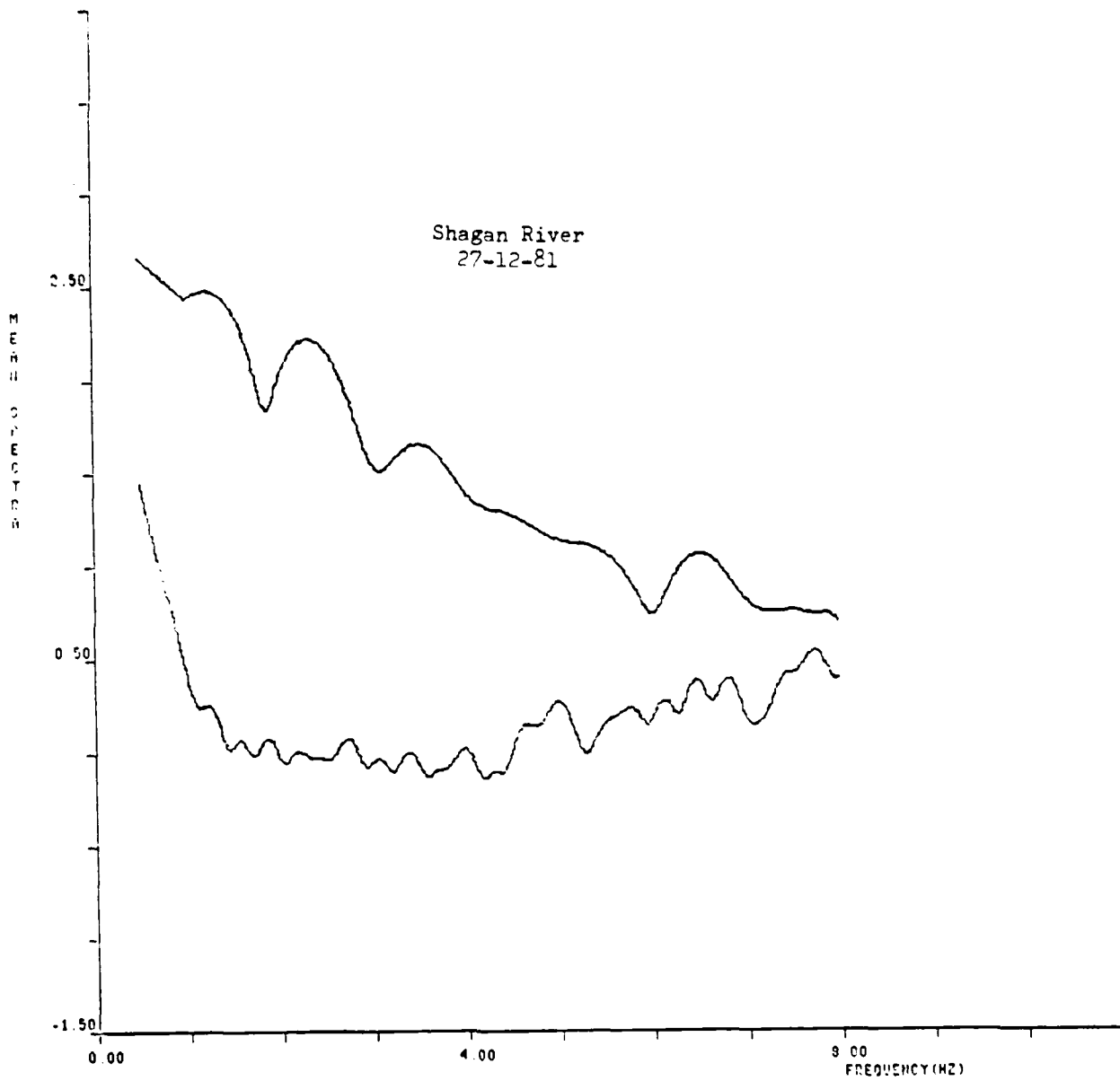


Figure 11 The  $|F(\omega)|$  computed according to Equation (3) is plotted for the GBA data of Figure 9. Also shown is the spectrum derived from the average noise power over the twelve channels processed.

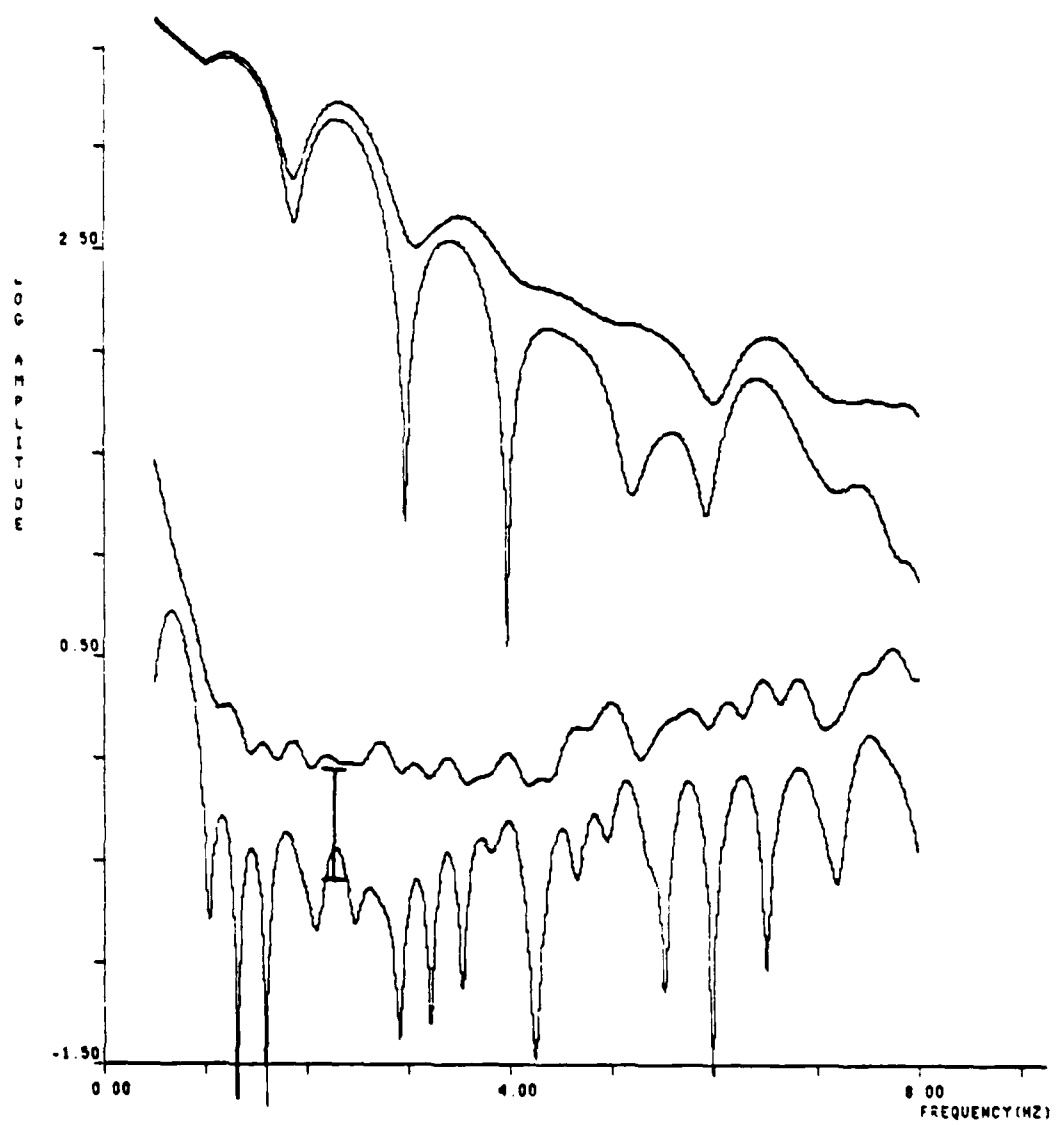


Figure 12 The  $|F(\omega)|$  and average noise spectra from Figure 11 are compared to the Fourier spectra computed from the time domain beam sum (Figure 10). The noise spectra have been shifted by 1.0 log units for clarity of presentation. A bar shows an amplitude shift by  $\sqrt{N}$  (in this case  $N = 12$ ).

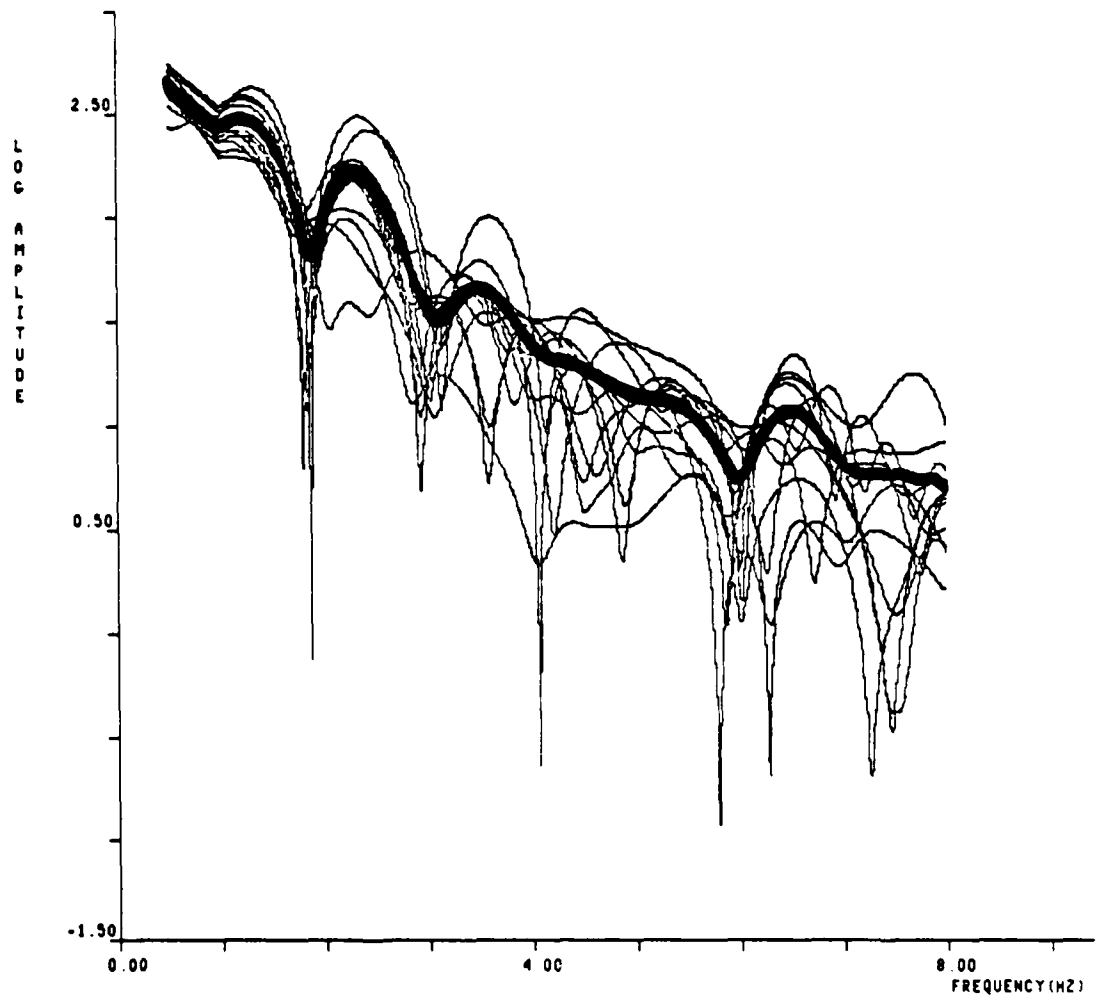


Figure 13 The  $|F(\omega)|$  is superimposed on the Fourier transform amplitudes for the signal windows from the GBA individual channels for the 27 December 1981 Shagan River explosion.

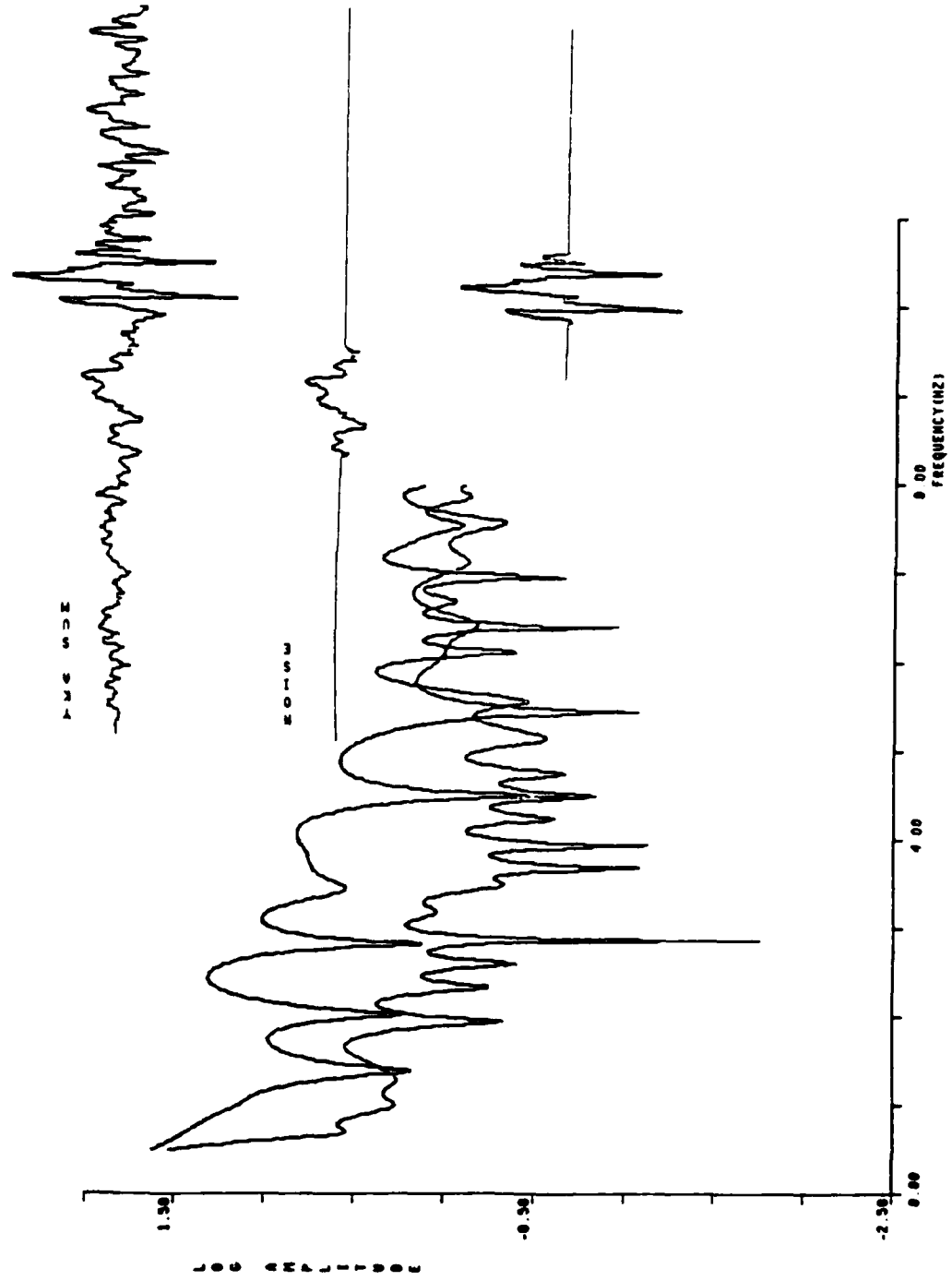


Figure 14 The Fourier spectra of the signal and noise windows are plotted for the array sum and channel R6. The data are YKA recordings of SALMON (Figure 4).

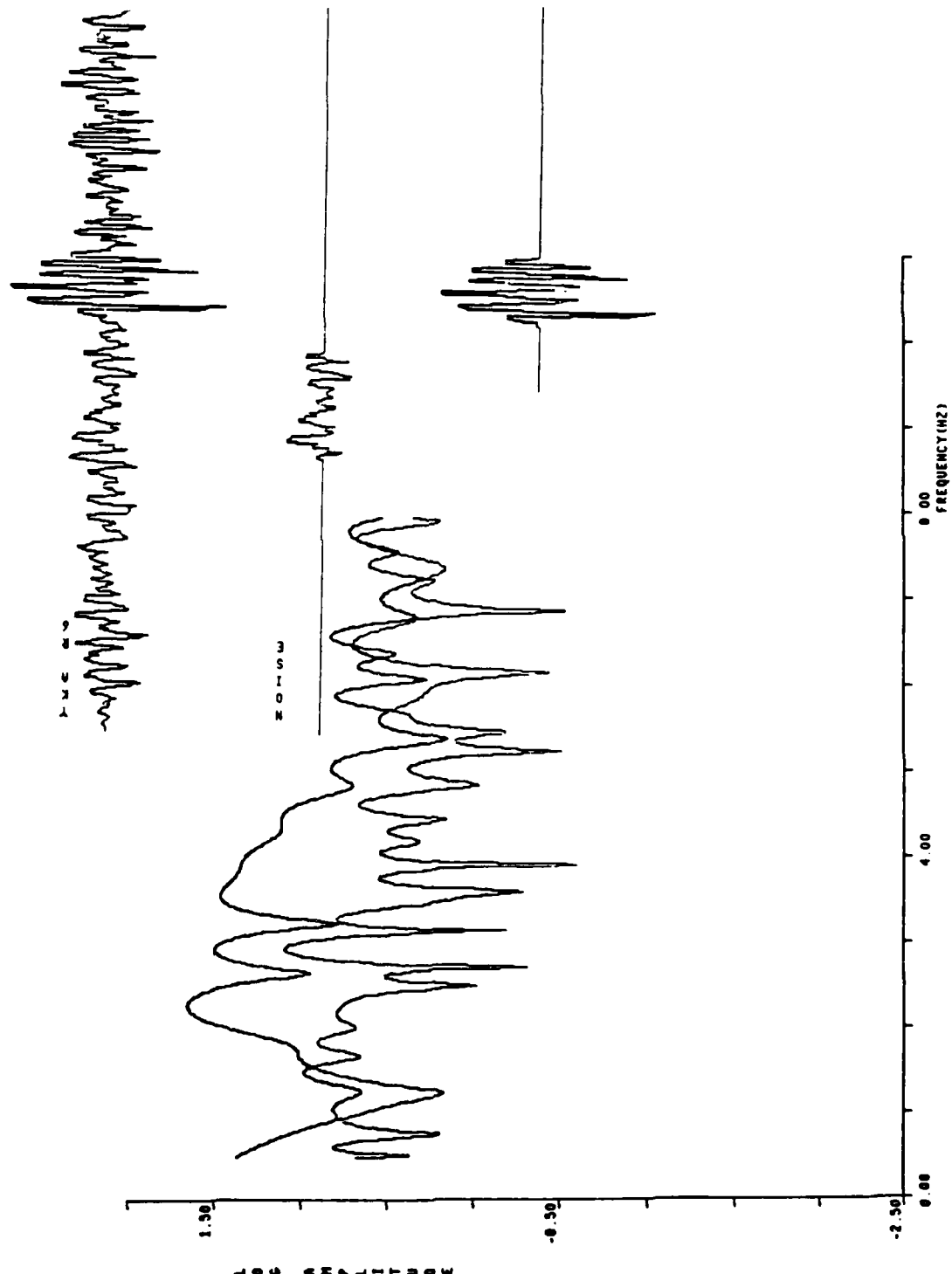


Figure 14 (continued)

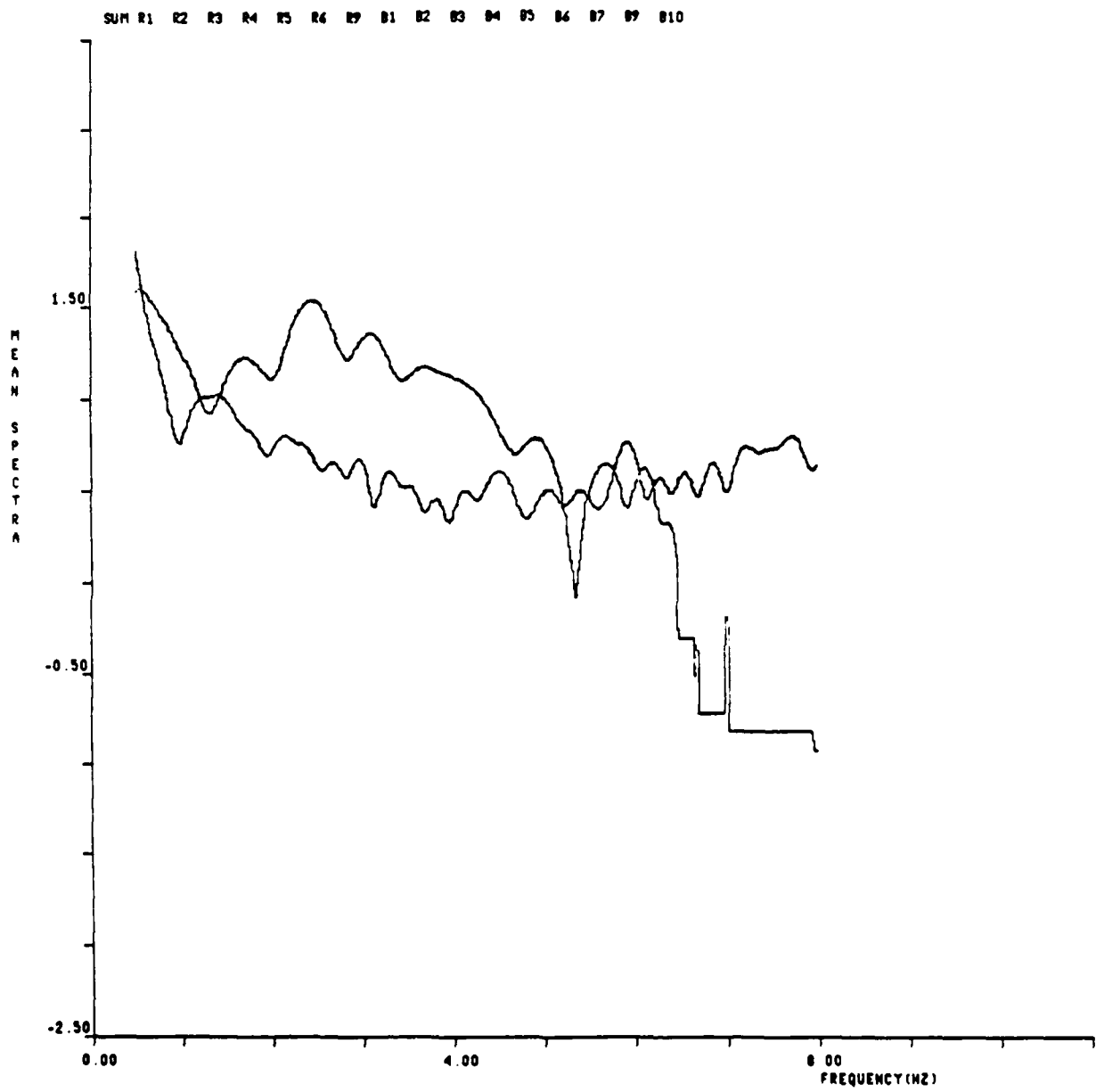


Figure 15 The  $F(\omega)$  and average noise spectra are plotted for the YKA recordings of SALMON. Sixteen channels were processed.

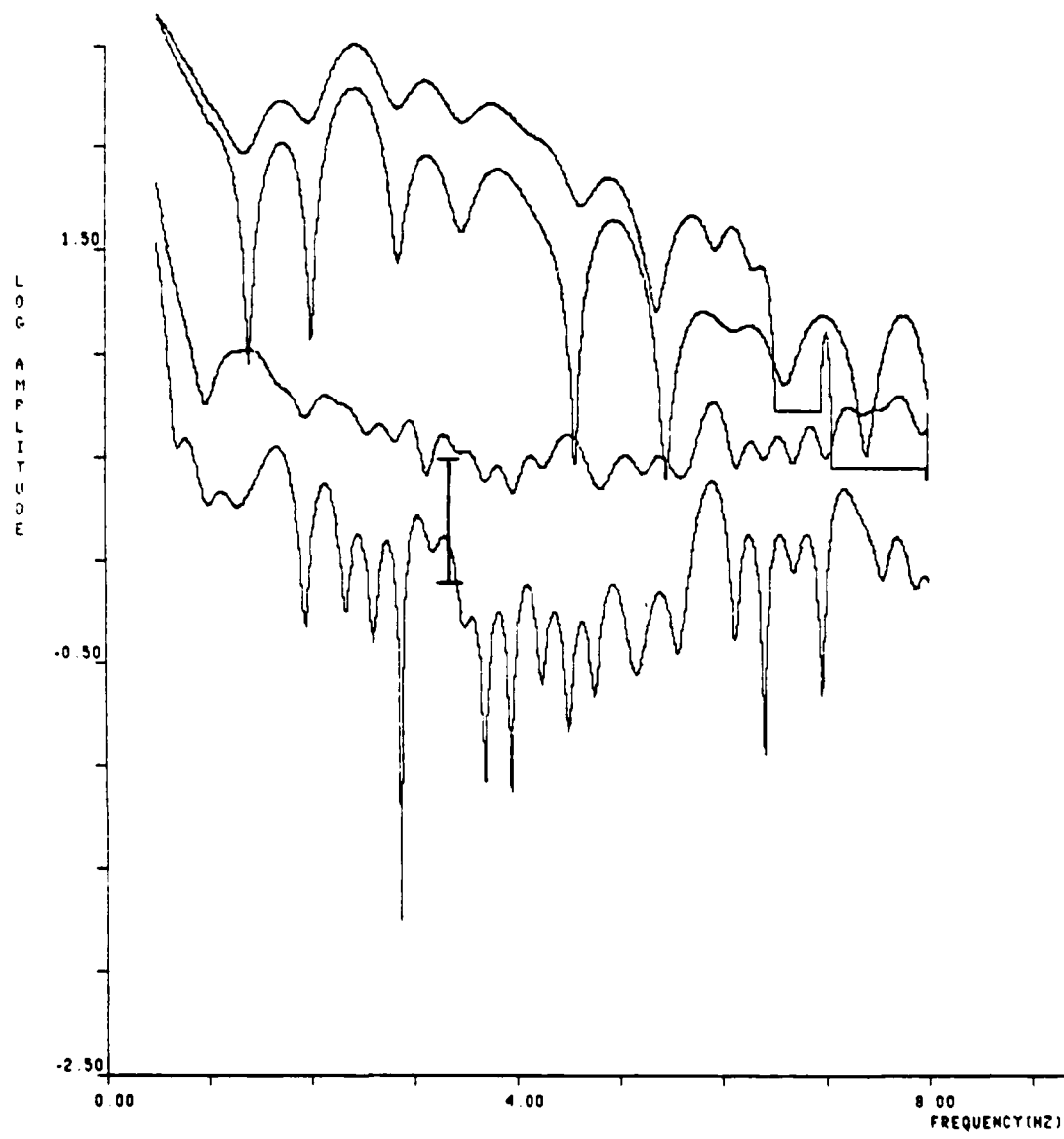


Figure 16 The  $|F(\omega)|$  and average noise spectra from Figure 15 are compared to the Fourier spectra computed from the time domain beam sum. The noise spectra have been shifted by 1.0 log units and a bar shows an amplitude shift by  $\sqrt{16}$ .

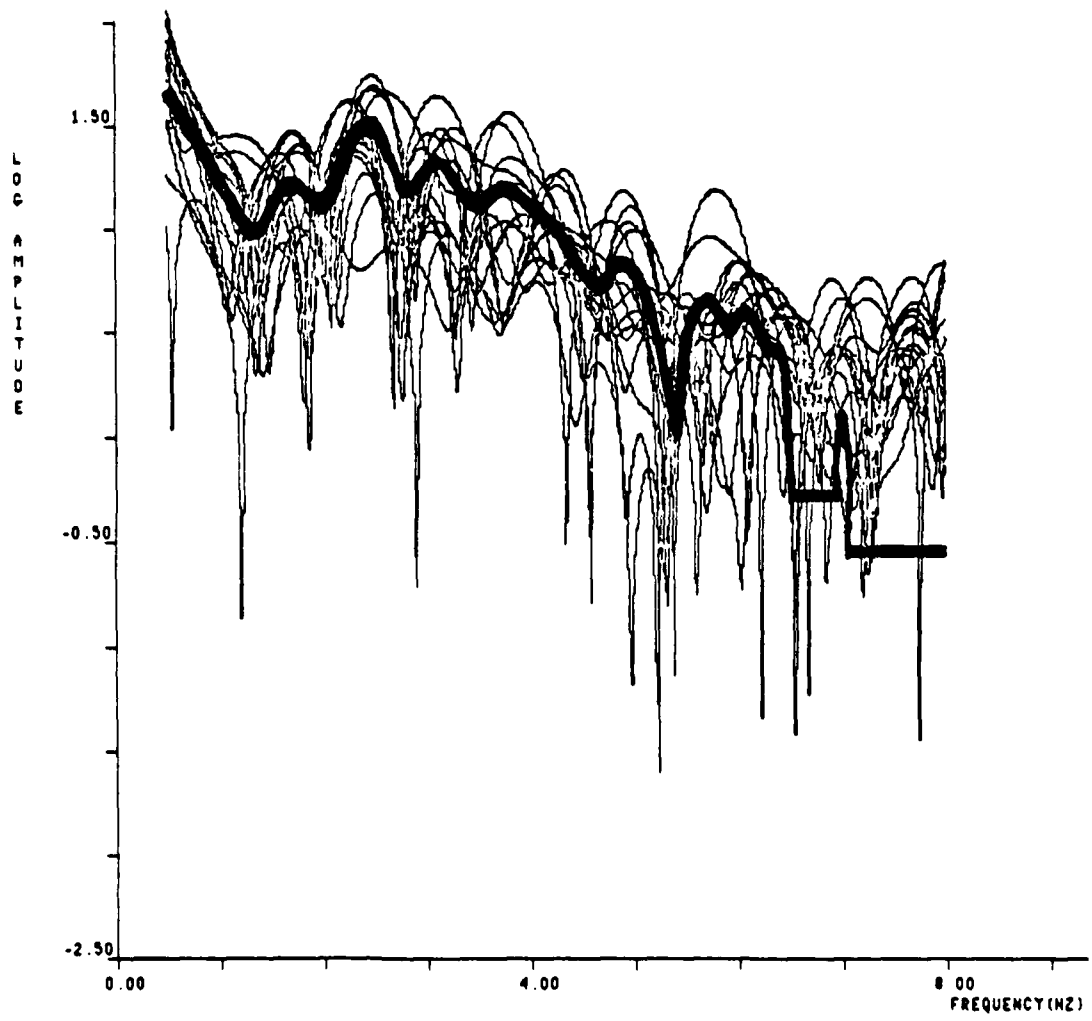


Figure 17 The  $|F(\omega)|$  for SALMON at YKA is superimposed on the Fourier transform amplitudes from the individual channel spectra.

## 4.3

 $t^*$  Estimation from Signal Spectra

The observed signal amplitude spectrum  $|F(\omega)|$  is assumed to be a product of the source spectrum,  $S(\omega)$ , the seismometer response,  $I(\omega)$ , a transfer function intended to represent the elastic properties of the

travel path,  $T(\omega)$  and a transfer function  $G(\omega)$  representing the attenuation that occurs along the path. That is,

$$F(\omega) = S(\omega) I(\omega) T(\omega) G(\omega). \quad (5)$$

The instrument response is known and  $T(\omega)$  is assumed to vary about a frequency independent constant value which includes geometric spreading and crustal amplification. The  $S(\omega)$  includes all the P waves leaving the immediate source region within a second or two (since very short time windows are used) of the explosion detonation. That is, the direct P, pP and any other surface reflections that may be present, any propagating P waves from spall closure and associated phenomena, and any P waves from tectonic release occurring immediately after the explosion.

The attenuation operator  $G(\omega)$  is usually expressed as:

$$G(\omega) = \exp \left[ -\omega \int \frac{ds}{2 \alpha Q(\omega)} \right] = \exp (-\pi f t^*),$$

where  $\alpha$  is P wave velocity and the integral is taken along the ray path. In this formulation  $Q$  includes both anelastic attenuation and any additional attenuation due to scattering. The  $Q$  may depend on frequency, if necessary, and this poses no difficulty in computing  $t^*$ , which will then also depend on frequency (eg, Anderson and Given, 1982).

If we correct for instrument response and assume  $T(\omega)$  oscillates about a frequency-independent constant, we have

$$\log [F(\omega)] = \log [S(\omega)] - [\pi \log e] t^* f + \text{constant}. \quad (7)$$

Thus, if we know the dependence of  $S(\omega)$  on frequency over some frequency band, we can determine  $t^*(f)$ .

The most commonly used source models for explosions are characterised by an  $f^{-2}$  decay above some corner frequency (which depends on yield and source depth). The semi-empirical models of Mueller and Murphy (1971) and von Seggern and Blanchard (1972) have this form. A model with an  $f^{-3}$  decay was suggested by Helmberger and Hadley (1981) and has recently been used by Burdick *et al.* (1984) and Lay *et al.* (1984) to model an extensive set of near-field and teleseismic data from the three US Amchitka explosions (LONGSHOT, MILROW and CANNIKIN). However, Lay *et al.* (1984) point out that their conclusions are rather insensitive to the assumed asymptotic frequency behaviour of their model.

Whether  $f^{-2}$  or  $f^{-3}$  is a more accurate description of the decay of the source function beyond the corner frequency is the kind of qualitative question for which detailed finite difference explosion coupling calculations like those done by Cherry *et al.* (1975) are best suited. In Figure 18 we show the  $|S(\omega)|$  computed for explosions in three different materials. The Mueller and Murphy (1971) source in granite is also shown. We see that the finite difference source functions show a more complex behaviour that varies with material properties. Still, it is clear that the spectral decay is between  $f^{-2}$  and  $f^{-3}$  in the range of interest (frequencies between the corner and 8 Hz). Another important point is that in all cases the spectrum is decaying like  $f^{-2}$  or faster for frequencies above about 2 Hz. For yields larger than 100 kt this corner will occur at somewhat lower frequencies. If the depth is fixed, the corner scales with the cube-root of the yield, but, if the depth increases, as expected, with yield, the corner shifts more slowly. The Mueller/Murphy model predicts corner frequency scaling with yield to the 0.19 power when depth is proportional to the cube-root of yield. The finite difference calculations are generally consistent with this depth-dependence of the corner frequency (eg, Bache, 1982).

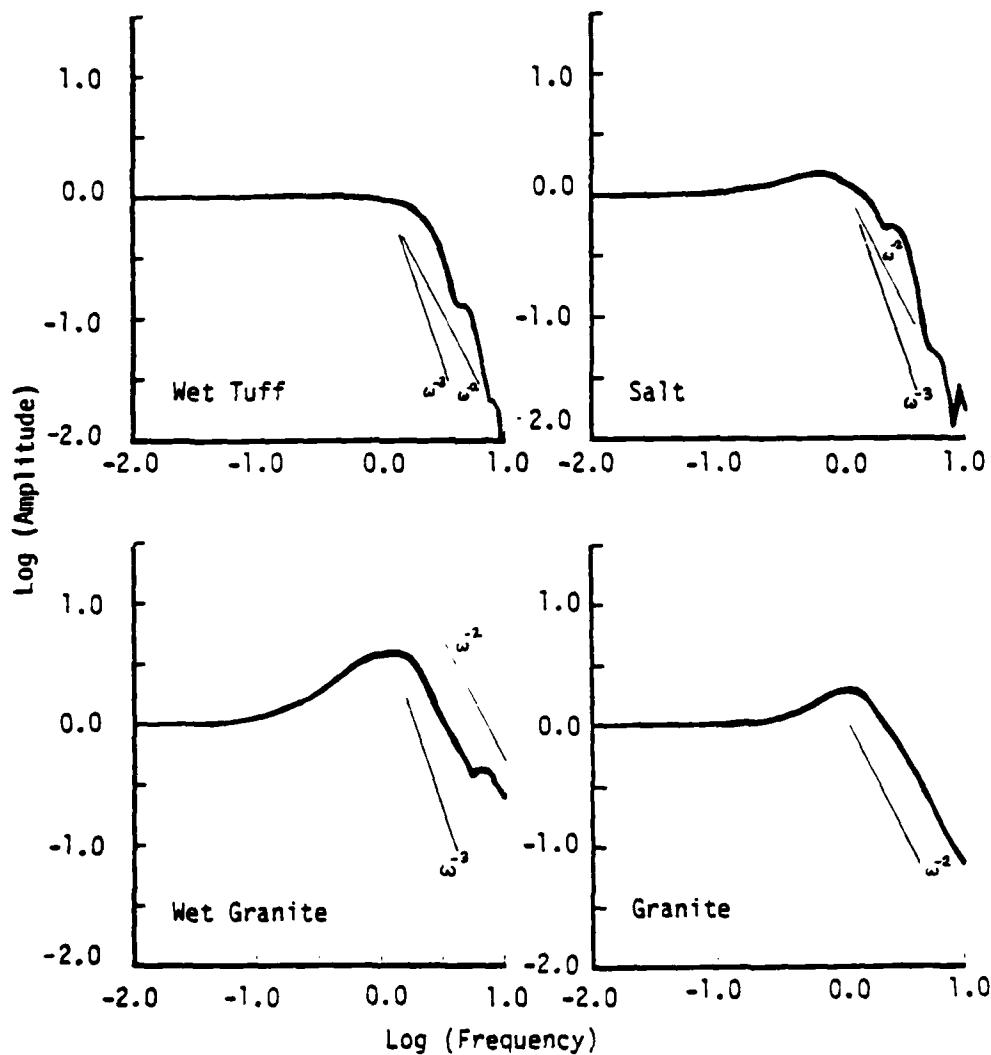


Figure 18 The amplitude of the far-field displacement spectrum (in a whole space) is shown for finite difference calculations in three different source materials and (lower right) for the Mueller and Murphy (1971) source in granite. The yield is 100 kt (adapted from Stevens and Day, 1984).

Taking all this into account, we can be fairly certain that

$$S(\omega) \approx \omega^{-n}, \quad 2 < n < 3, \quad (8)$$

for frequencies above 2 Hz or so. We should also keep in mind that the effective  $n$  could be less than 2 when the explosion is accompanied by large secondary sources (eg tectonic release) which have higher corner frequencies, and this might happen from time to time. Using (8), (7) becomes

$$\log |F(\omega)| = -n \log f - (\pi \log e) t^*(f) f + \text{constant}, \quad (9)$$

Then plotting  $\log |F(\omega)|$  versus  $f$  allows  $t^*(f)$  to be estimated for any choice of assumptions about  $S(\omega)$ , or  $n$  in this parameterization. But we have the additional constraint that  $t^*$  must be the same for all events in a small source area. Thus, we can hope to obtain good estimates for both  $t^*$  and  $S(\omega)$  from broad band spectra for large suites of events.

## V SEISMIC NOISE CHARACTERISTICS OF THE UK ARRAYS FROM 0.5 TO 8 Hz

There are various consistency checks that can be made to, gain confidence in the validity of the spectra being computed, especially at high frequencies. One is comparison with the spectrum from the beam sum (Figures 12 and 16 and Appendix B). Another is that events in the same area give remarkably consistent results, as will be seen in later sections. These features, while very encouraging, do not entirely eliminate the possibility of contamination of the results by system noise or errors in the assumed instrument amplification. However, the spectral characteristics of the seismic noise described in this section provide an independent check which indicates that these kinds of system errors are insignificant.

The noise at the UK arrays has been previously studied for many purposes, including estimation of detection thresholds (Burch, 1968), evaluation of the effectiveness of the delay-and-sum beaming procedures used for event detection (eg Burch 1968; Muirhead, 1968), and even in an unsuccessful attempt to detect gravity waves (Weichert, 1973). However, none of these earlier studies present their results in a form convenient for comparison with often referenced noise spectra published by Fix (1972), Peterson (1980) and Herrin (1982). The purpose here is to make that comparison, but more important to address the difficult question of the extent of contamination of the spectral estimates by system noise.

The noise estimates are a by-product of the spectral calculations described in Section 4.1. Recall that the power spectrum is computed for a 3.8 second window of noise just before the P wave on each element of the array. The mean of these provides the noise estimate for that event. Except for the small shift due to moveout of the P wave across the array (the maximum aperture varies from 10 to 26 km for the four arrays), all these estimates are taken at the same time. However, since the noise is incoherent across the array (eg, Figures 12 and 16), this estimate is essentially equivalent to taking N separate 3.8 second samples from an element with "average" properties for the array location.

For each event studied, a noise estimate is computed. Averaging many such estimates, an overall average noise power for the station is computed. No attempt was made to collect an unbiased temporal sample; the selection is controlled by the time explosions occur. For GBA (India) and EKA (Scotland) the noise estimates to be shown are associated with Soviet explosions in eastern Kazakhstan, and thus are mainly taken between 0300 and 0500 GMT. The YKA (Canada) estimates are associated with French Mururoa explosions, and are mainly taken between 1600 and 2000 GMT. In terms of local time, this is 0830-1030 for GBA, 0300-0500 for EKA and 0900-1300 at YKA.

Typical noise estimates are shown in Figure 19. The instrumentation is basically identical at these sites, except that some of the GBA data were recorded digitally. The question to be addressed is, what properties of these spectra represent the characteristics of true earth noise at these sites? The GBA and EKA estimates are averages from 14 randomly selected "event" samples. The YKA estimate is from 10 events, but here some selection has been made to avoid days of unusually high noise. These spectra can be shifted up or down by 5-10 dBs, depending on the sample selection, but the general spectral shape seems to be consistently maintained. This is nicely demonstrated by closer examination of the GBA data. Some were originally recorded on analog tape, while some are from after March 1979, when digital recording equipment was installed. Noise estimates from 14 event samples of each type are compared in Figure 20. Also shown are the envelopes enclosing each sample set.

In Figure 20 the average noise from the digital recordings is about 6 dBs less below 1 Hz, and the separation increases to 8-10 dBs at higher frequencies. The low frequency difference is due to the remarkable coincidence that 12 of the 14 digitally recorded events were on days of quiet or average noise, while 10 of the analog recorded events were on days of above average noise. Comparing different samples of the digital noise data shows that increasing the ambient noise tends to raise the spectrum rather uniformly across the entire frequency band. Thus, the high frequency portion of the analog power spectrum probably includes 2-4 dBs due to noise in the analog system.

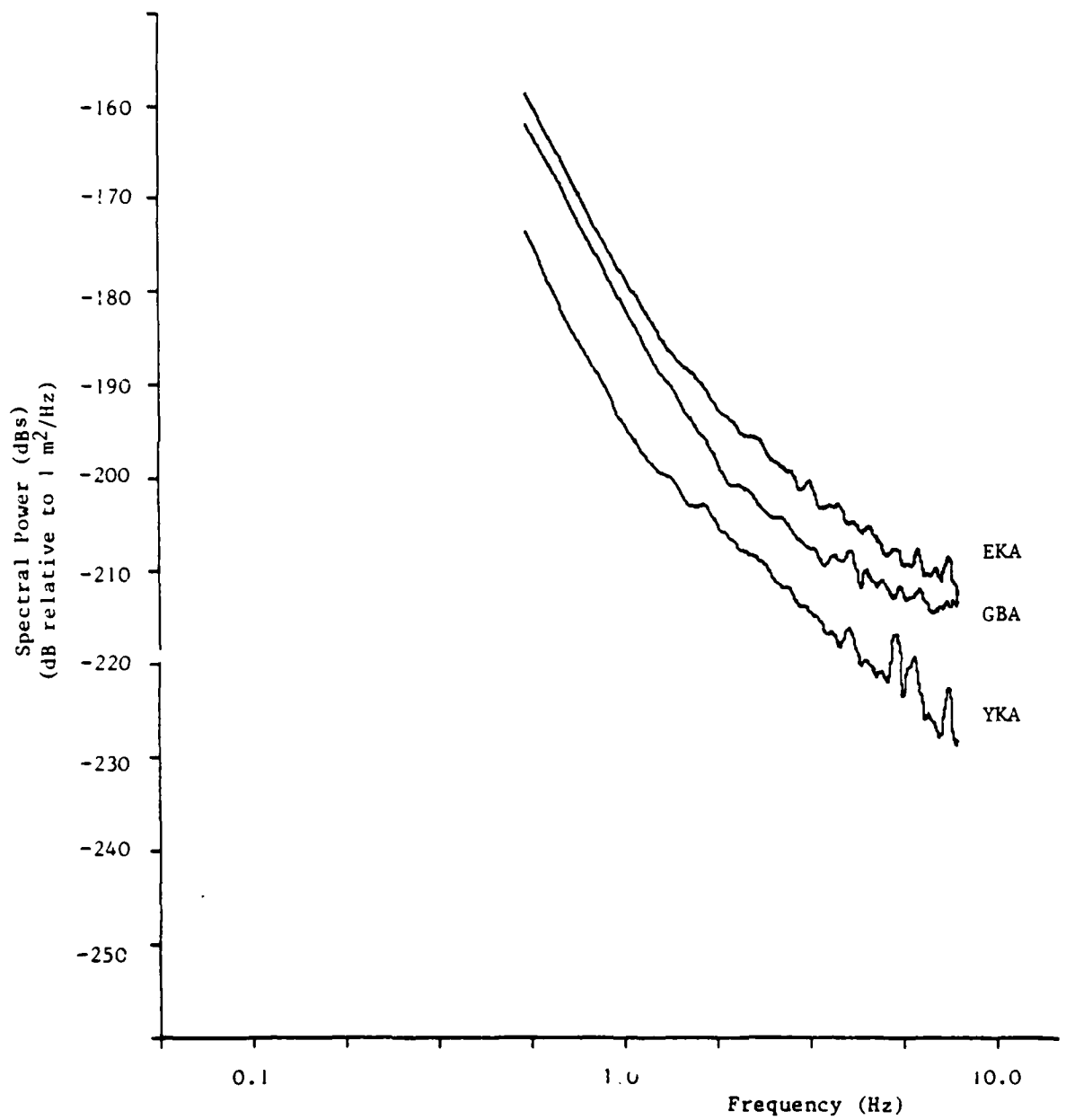


Figure 19 Typical noise power spectra for the UK arrays.

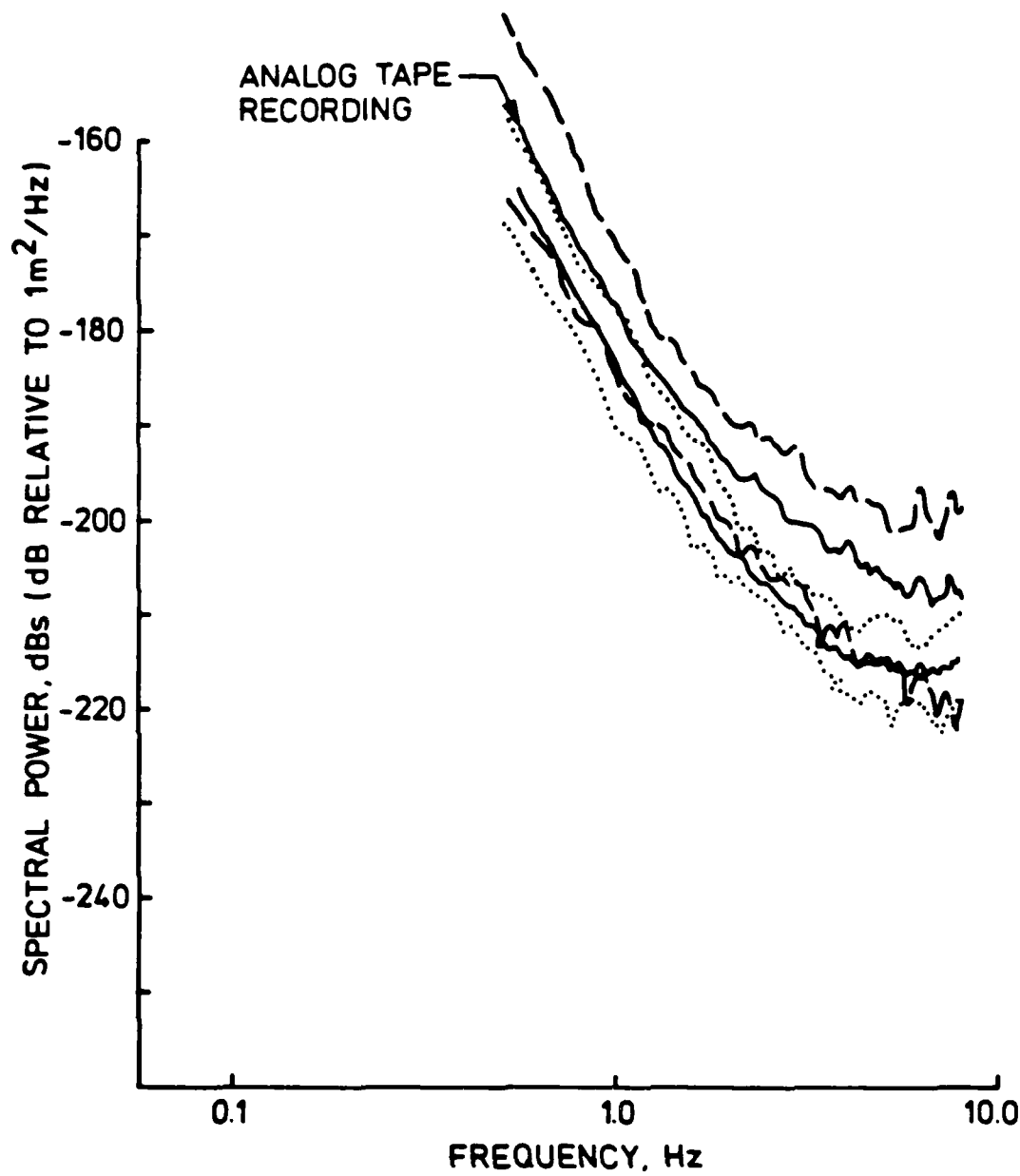


Figure 20

The average noise power spectra are compared for events originally recorded on analog tape and events recorded digitally. There are fourteen event estimates in each set and the envelope enclosing them is also shown.

A prominent feature of the GBA noise data is the flattening that occurs (at about -215 dBs in the digital sample) above 4 Hz. Herrin (1982) notes that flattening occurs at about this level for some of the quieter SRO sites, but attributes it to self-noise in the SRO instrumentation. Is self-noise also the reason for the flattening at GBA? Note in Figure 19 that the nearly identical analog system at EKA shows a tendency to flatten (at about -209 dB above 6 Hz for this sample), while the noise from the also identical YKA system decreases steadily, reaching -227 dB at 8 Hz. This strongly suggests that self noise is not a dominant factor shaping the GBA digital noise spectrum.

An experiment suggested by H Bungum (NORSAR, personal communication) was carried out as a further check on the validity of the measured noise spectra. In this experiment three 90 second noise samples were recorded digitally on a moderately quiet day at one EKA sensor. The system operated normally for the first and third samples, but the gain was increased by a factor of 21 for the middle one. Nine 3.8 second windows were taken at ten second intervals from each sample and the average noise computed as before. The result is shown in Figure 21. The three spectra are essentially the same, proving that discretization error is not important. In Figure 22 the mean of these three spectra is compared to the average (analog recorded) EKA noise from Figure 19. The spectrum from Figure 19 is lower by 2-3 dBs up to about 4 Hz. The slight trend toward flattening that then occurs is probably due to noise in the analog system. In fact, the analog system noise of 2-4 dBs estimated for GBA from the spectra in Figure 20 is the right size to explain the spectral differences in Figure 22.

In Figure 23 the analog recorded YKA spectrum from Figure 19 and the digitally recorded GBA and EKA spectra from Figures 20 and 22 are compared to the noise spectrum for the very quiet Lajitas, Texas site (Herrin, 1982). Also shown is the NORSAR noise model (Bungum, 1983) based on measurements made with a gain amplified version of the NORSAR instrumentation. The important feature of the NORSAR noise is that it has a constant slope (50 dBs per decade) from 2-3 Hz to well above 10 Hz. The Lajitas, EKA and YKA data also follow a straight line, though with a smaller slope.

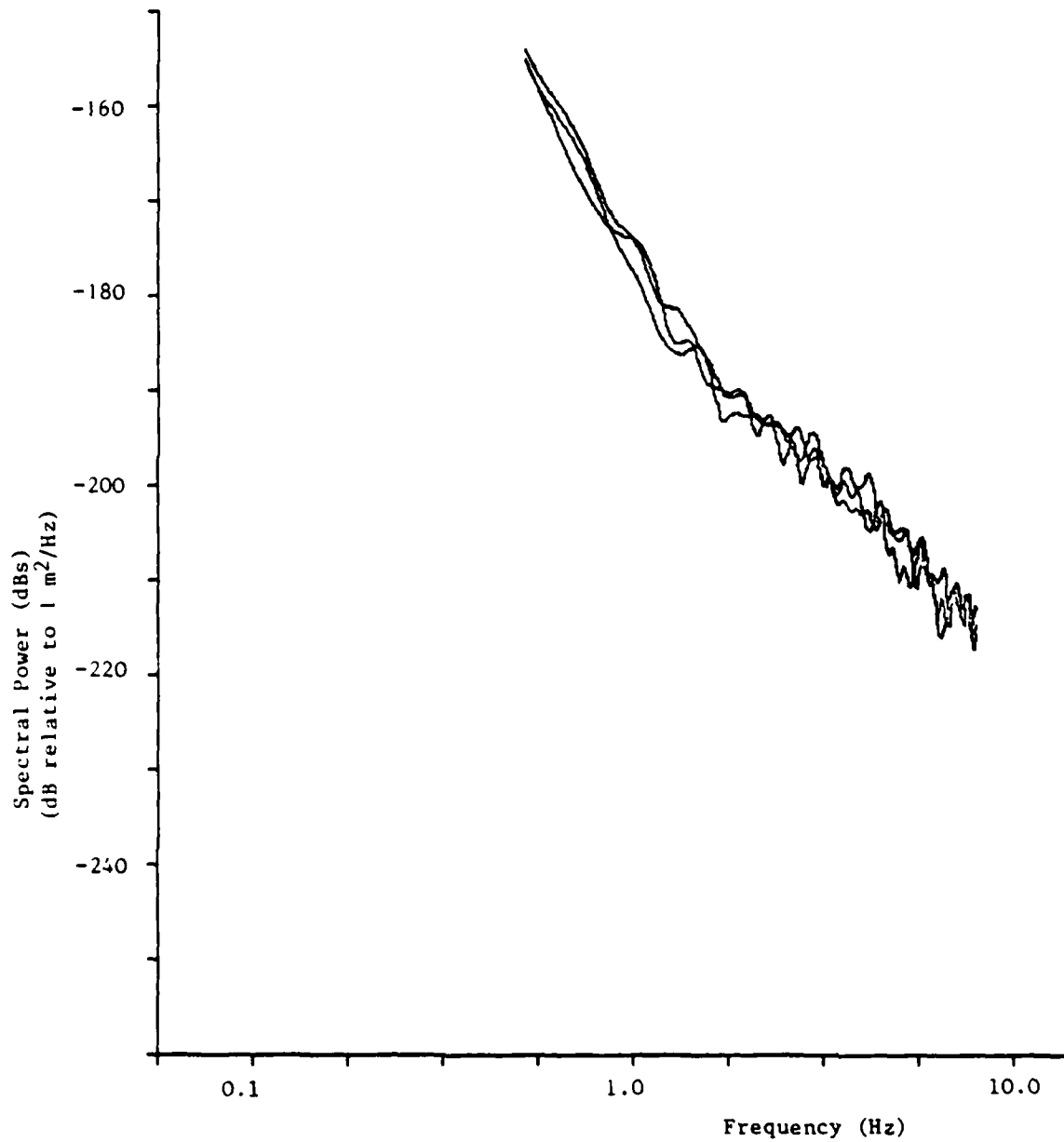


Figure 21

The noise power spectra are compared for three samples of the EKA noise, two with normal gain recording and one with the gain increased by a factor of twenty-one.

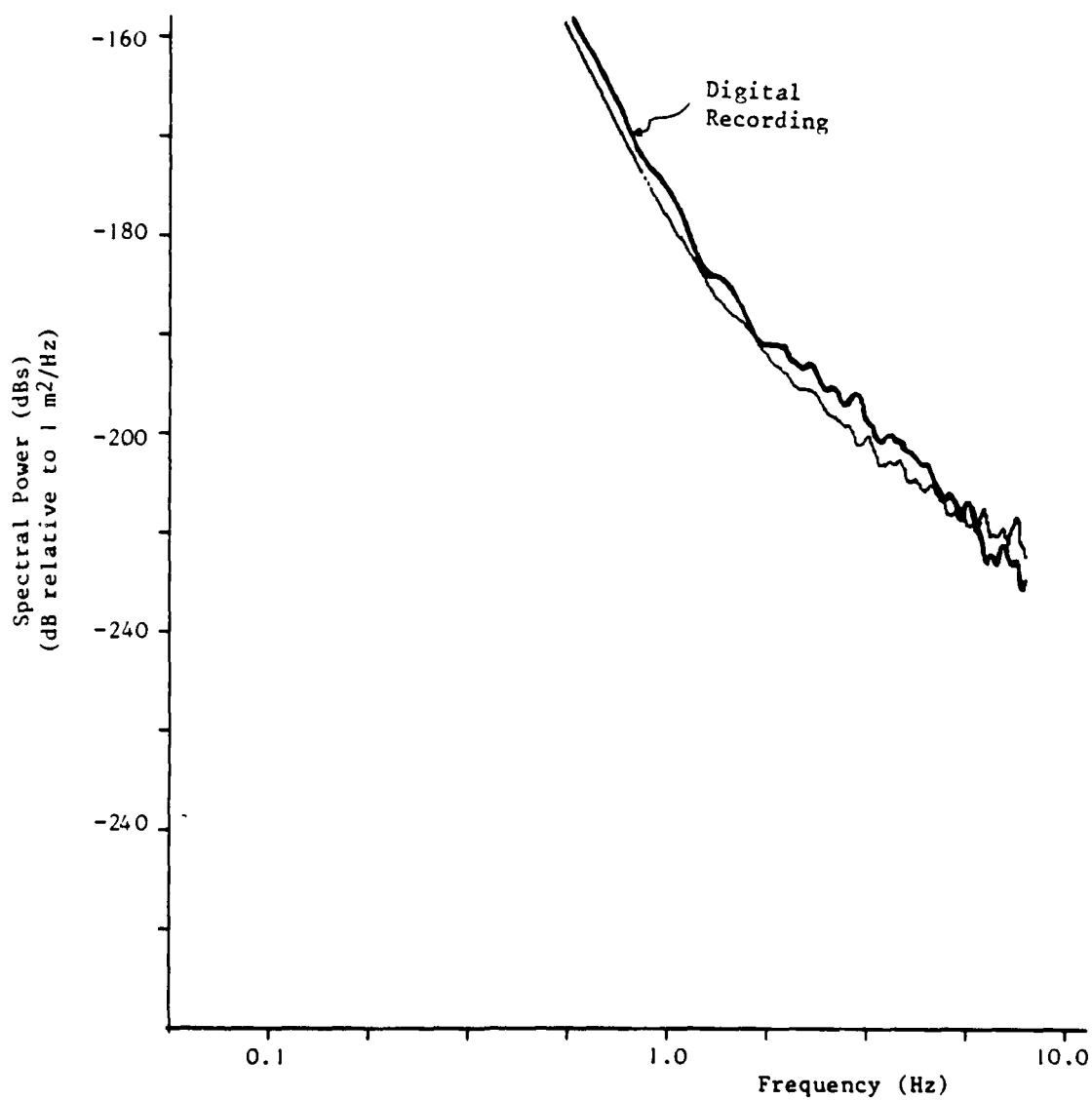


Figure 22

The average of the digitally recorded noise power spectra from Figure 3 is compared to the estimated noise from analog recordings shown in Figure 1.

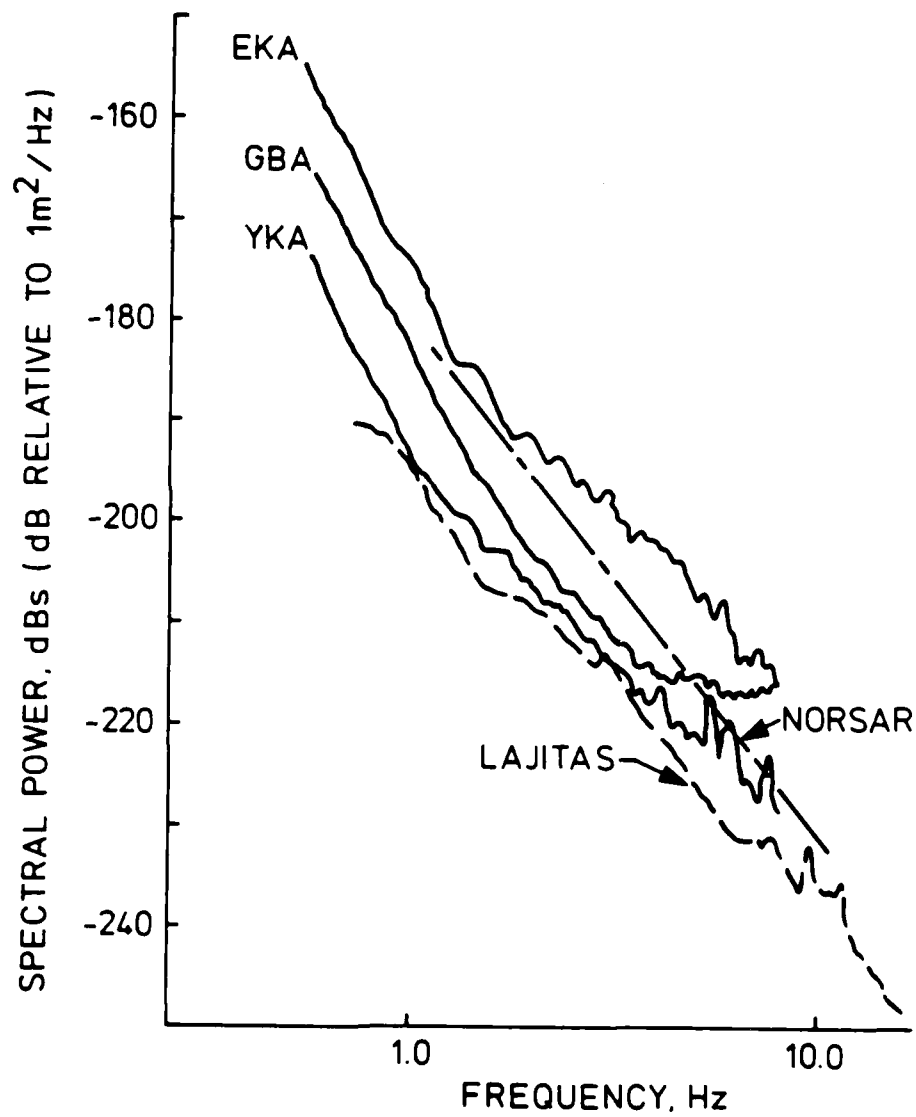


Figure 23      Noise power estimates from the UK array stations are compared to the noise power at Lajitas, Texas and the NORSAR noise model.

The GBA spectrum in Figure 23 is different from the others in that it approaches a constant value above 4 Hz. But actual earth noise can behave like this, as was shown in some experiments recently done by R Burch (Blacknest) and J Durham (Sandia). In these experiments several US and UK seismometers were operated simultaneously on the same pad at the Albuquerque seismometer test facility. The recorded data were processed to separate the correlated (presumably true earth noise) and uncorrelated (presumably system noise) portions of the signal. The earth noise was found to be about 20 dBs larger than the system noise below 10 Hz. Different seismometers gave almost precisely (agreement to within a dBs or so) the same earth noise spectrum. This proves that the system response is known very well, eliminating another possible source of error in the spectral estimates. A typical noise spectrum is compared to the GBA noise in Figure 24. Except for the spectral lines due to cultural sources of noise in Albuquerque, the two spectra are quite similar, yet we know that the Albuquerque data represent true ground motion.

Noise spectra that follow a constant slope (like the NORSAR, YKA and EKA noise) are seen at Albuquerque when quiet times are selected and the data are from a borehole instrument (J Durham, personal communication). It has long been known (eg, the Geotechnical Corporation, 1967) that differences of exactly this kind (constant slope falloff versus spectral flattening) are seen between surface and borehole instruments at some sites, and Albuquerque is apparently one of them. It is likely that GBA is another.

These results indicate that the UK array spectra shown in Figure 23 represent the true earth noise at those sites. Large ( $>\pm 10$  dBs) temporal variations of the noise occur, but the primary effect is to shift the entire spectrum; the spectral shape is relatively constant. At two of the sites the spectrum decays with a constant slope which is less than the slope characterizing the NORSAR noise. At GBA the spectrum flattens above 4 Hz, but this appears to be a characteristic of the true earth noise, rather than a system noise limitation.

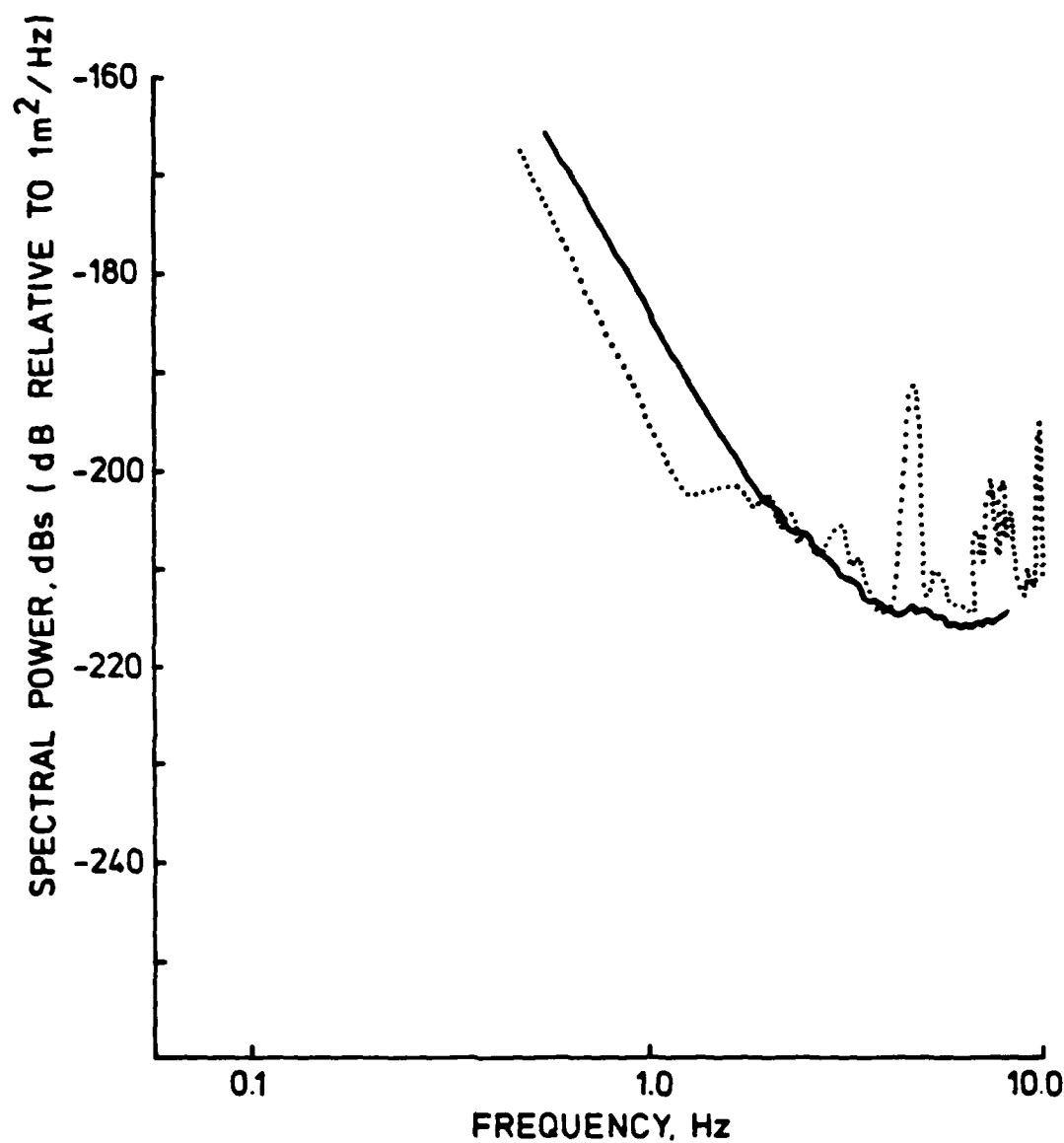


Figure 24 The noise power estimated from GBA digital recordings is compared to that measured at the Sandia Albuquerque seismometer test facility.

Recall that the signal spectra (eg Figure 11) are based on the difference between the signal energy density and noise power (equation 2). Thus the effect of additive system noise, like that seen by comparing the analog and digital noise estimates at EKA and GBA, will be properly removed. More serious would be some multiplicative error (eg erroneous instrument amplification) but all indications are that no such error is occurring. Thus, this study of the noise greatly enhances confidence in the reliability of the P spectra estimates.

In the analysis in this section we have not, to this point, considered the data from WRA. This station poses a special problem because the digitizing system installed in June 1977 appears to scatter small random spikes through the data. These are often impossible to detect in the time series because they are so small. Their effect on the spectrum is essentially to add a constant with amplitude proportional to the size of the spike. This amplitude is small compared to the spectral amplitude for frequencies below 3 Hz or so which dominate the time signal, but can be as large or larger than the actual spectral amplitude at high frequencies. Thus, the presence of spikes is often revealed by an otherwise inexplicable flattening of the high frequency spectrum at an unusually large amplitude. In many cases the fault is obvious, but there are ambiguous cases as well. In analyzing the data the procedure was generally to discard the channel if there was any doubt. The success of this quality control effort can be judged by subsequent results which show WRA spectra to be consistent with those from the more reliable stations. The noise data provide further cause for confidence and are plotted in Figure 25 where they are compared to the Figure 23 noise estimates from the other three UK array stations. We see that the WRA noise essentially parallels the GBA noise and could therefore be correct for all the same reasons. However, since the data review was done with the objective of deleting channels for which the signal was contaminated, this noise estimate includes the effect of at least a few spurious spikes. But the effect is apparently not very large since the noise remains within reasonable limits.

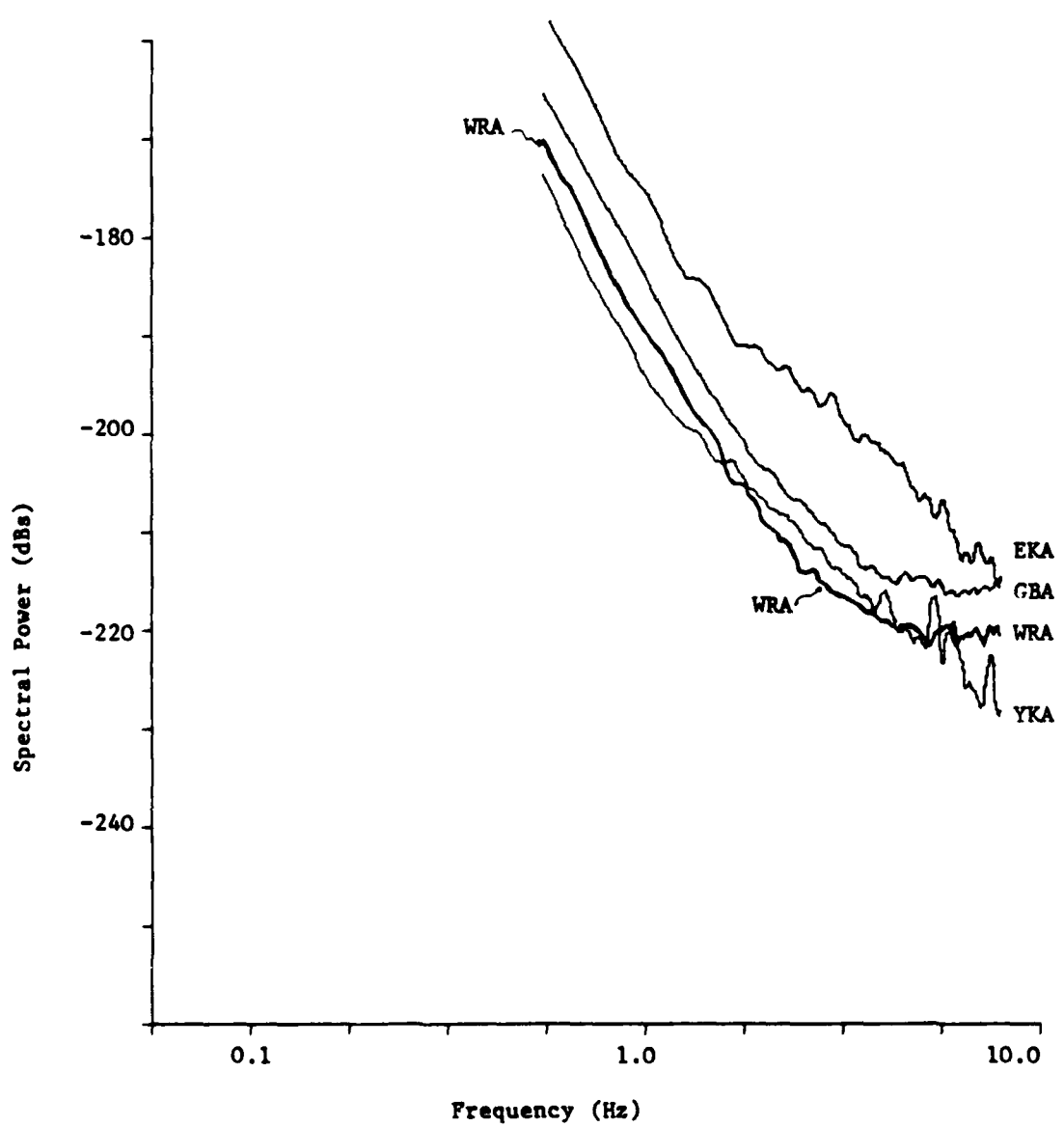


Figure 25 Noise estimates are compared for the four UK array stations

## VI AN ATTENUATION MODEL FOR E KAZAKH TO THE UK ARRAY STATIONS

### 6.1 Introduction

Using the techniques described in Section IV, spectra have been computed for Shagan River and Degelen Test Site explosions recorded at the four UK array stations. In this section we describe the results of these calculations and derive from them a model for the attenuation on these paths. All spectra calculated for E Kazakh events are collected in Appendix C. In this section we show key examples that illustrate our conclusions about the path attenuation.

The best and most complete data are those from GBA and EKA, and the GBA data will be described in some detail to explain how the results are derived. At YKA the signals from most E Kazakh explosions are clipped (Table 4), so only a relatively small data suite is available. As was described in the previous section, the data from WRA are often contaminated by small random spikes, and while every effort was made to delete channels where this occurs, the confidence in WRA spectra is necessarily less than in the spectra from the other stations. Still, the data from all four stations are remarkably consistent and lead to the same conclusions about  $Q$ . We can then account for the effect of  $Q$  and draw some interesting conclusions about the nature of the source function.

### 6.2 Spectra for GBA

The E Kazakh explosion data were divided into three groups: southwest Shagan River, northeast Shagan River and Degelen Mountain. The justification for the bisection of Shagan River was described in Section III. The  $|P(\omega)|$  was computed for each event as in Figures 11 and 15. A cutoff frequency was selected for each spectrum by noting where the  $|P(\omega)|$  drops below the level of the average noise. For example, for the large SW Shagan event in Figure 18 the cutoff frequency would be 8 Hz, while for SALMON at YKA (Figure 15) a value of 5.1 Hz was chosen. In view of (4), this is believed to be a conservative criterion that should avoid any biasing noise contamination of the spectra.

In Figure 26 the  $|F(\omega)|$  for thirteen SW Shagan River events are plotted. The best way to analyse such data is to begin with the simplest assumptions and let the results suggest the need for more complex models. Thus, we assume an  $\omega^{-2}$  source model above 1 Hz and a frequency-independent Q model. A least-squares linear fit was computed for each spectrum and is shown in the figure along with the  $t^*$  (computed from equation 9 with  $n = 2$ ) associated with that line.

We expect spectra like those in Figure 26 to vary due to differing source geology, depth of burial and contribution of prompt secondary source radiation from tectonic stress release. For example, where the true source function falls off more rapidly than  $\omega^{-2}$ , the spectrum will decrease more rapidly, biasing toward a lower  $t^*$ . If the source corner frequency were to move to 1 Hz and above, we would have a region where  $n < 2$  and the plotted spectrum would flatten or even curl downwards toward low frequency. Indeed, it appears that this corner frequency effect can be seen by comparing the smallest and largest  $m_b$  event spectra.

Many of the effects that cause variations among the event spectra are probably poorly correlated from event-to-event, so a clearer picture of the spectral shaping effect of the "average source" and attenuation can be obtained by stacking the individual event spectra. The stacking is done by multiplying the event spectra by  $\exp(\pi f \hat{t}^*)$ , where  $\hat{t}^*$  is the mean  $t^*$  for this suite of events, then normalising so each (corrected) spectrum has the same mean. The stacked spectrum is then the average of these multiplied by  $\exp(-\pi f \hat{t}^*)$ . The stacking is only done over the frequency band where there are at least three event spectra.

The stacked spectrum for SW Shagan to GBA is shown in Figure 27 plotted from 1-8 Hz and from 2.5 to 8 Hz. Above 2.5 Hz the spectrum is remarkably smooth and close to a straight line. The simplest interpretation is that for these frequencies the average source is proportional to  $\omega^{-2}$  and  $t^*$  is independent of frequency. Different models are possible, but require a neat cancelling of effects. Below 2.5 Hz the spectrum increases and it will be shown that this is due to frequency dependence of Q.

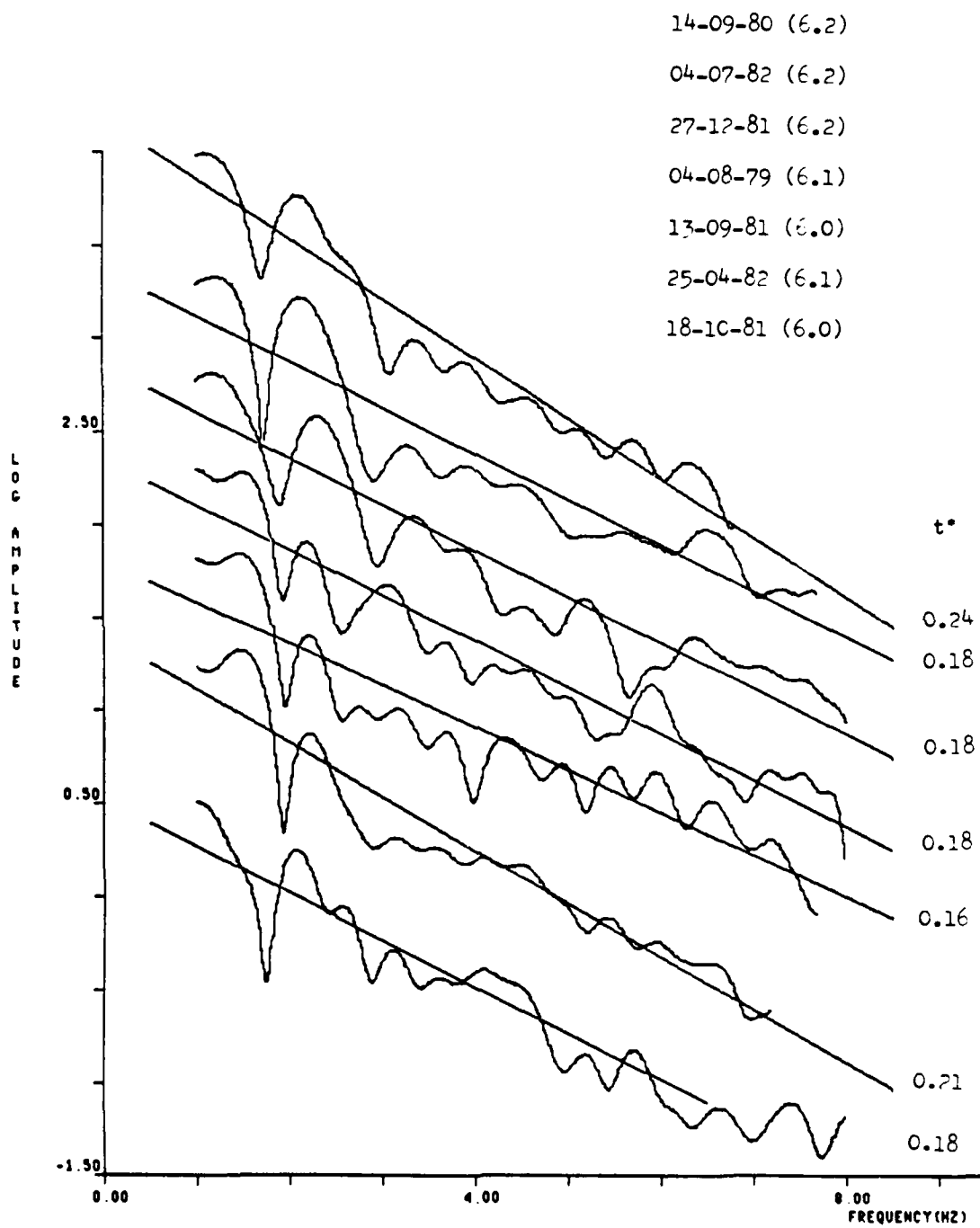


**Figure 26** The  $|F(\omega)|$  are plotted for twelve southwest Shagan River events. The events and their ISC  $m_b$  are listed in order at the top of the figure. Each spectrum has been multiplied by  $f^2$ . A least squares fit to each line is shown and the value of  $t^*$  consistent with that line is given. The amplitude scale is arbitrary since the spectra have been shifted for convenient display.

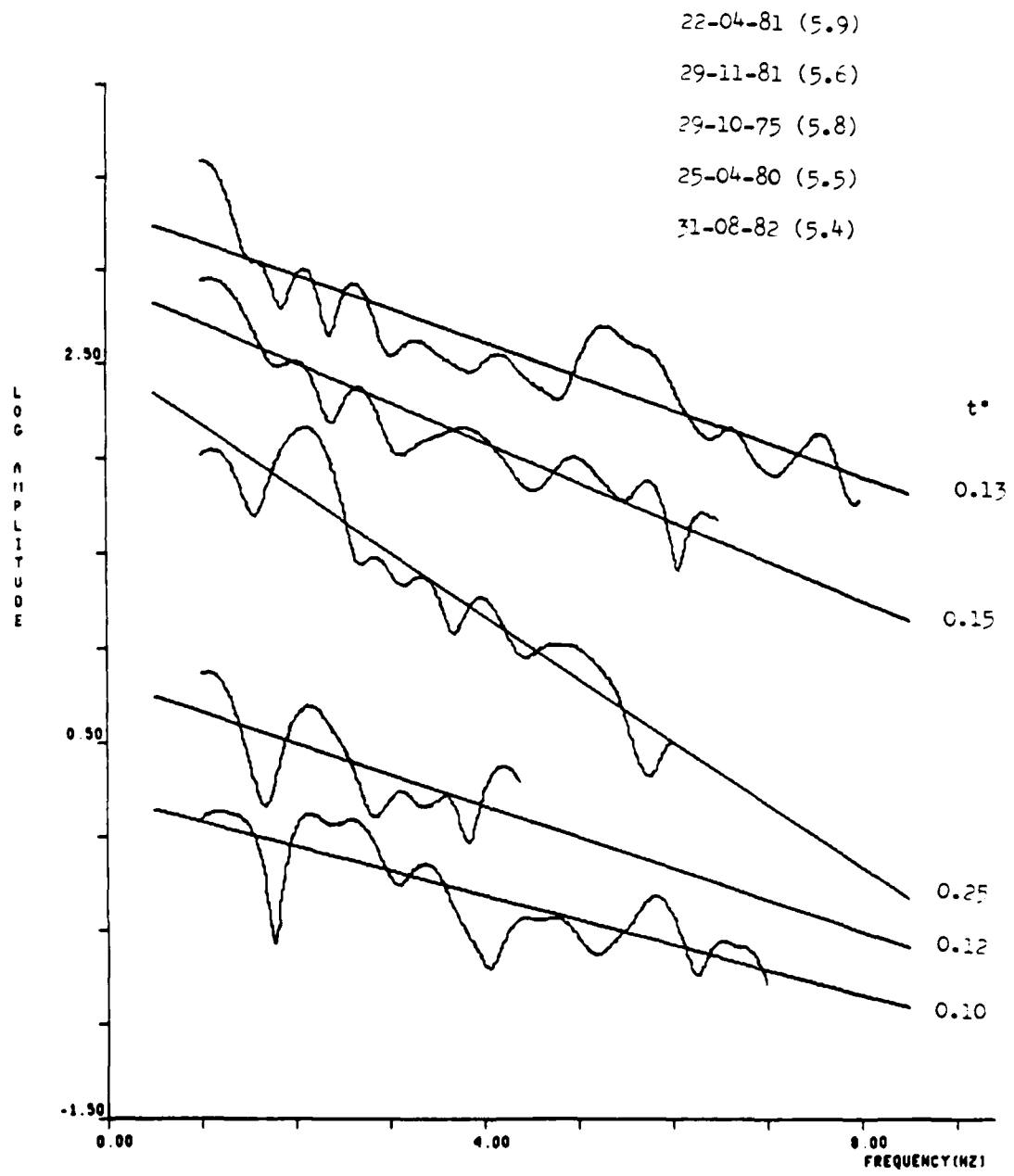


Figure 26 (continued)

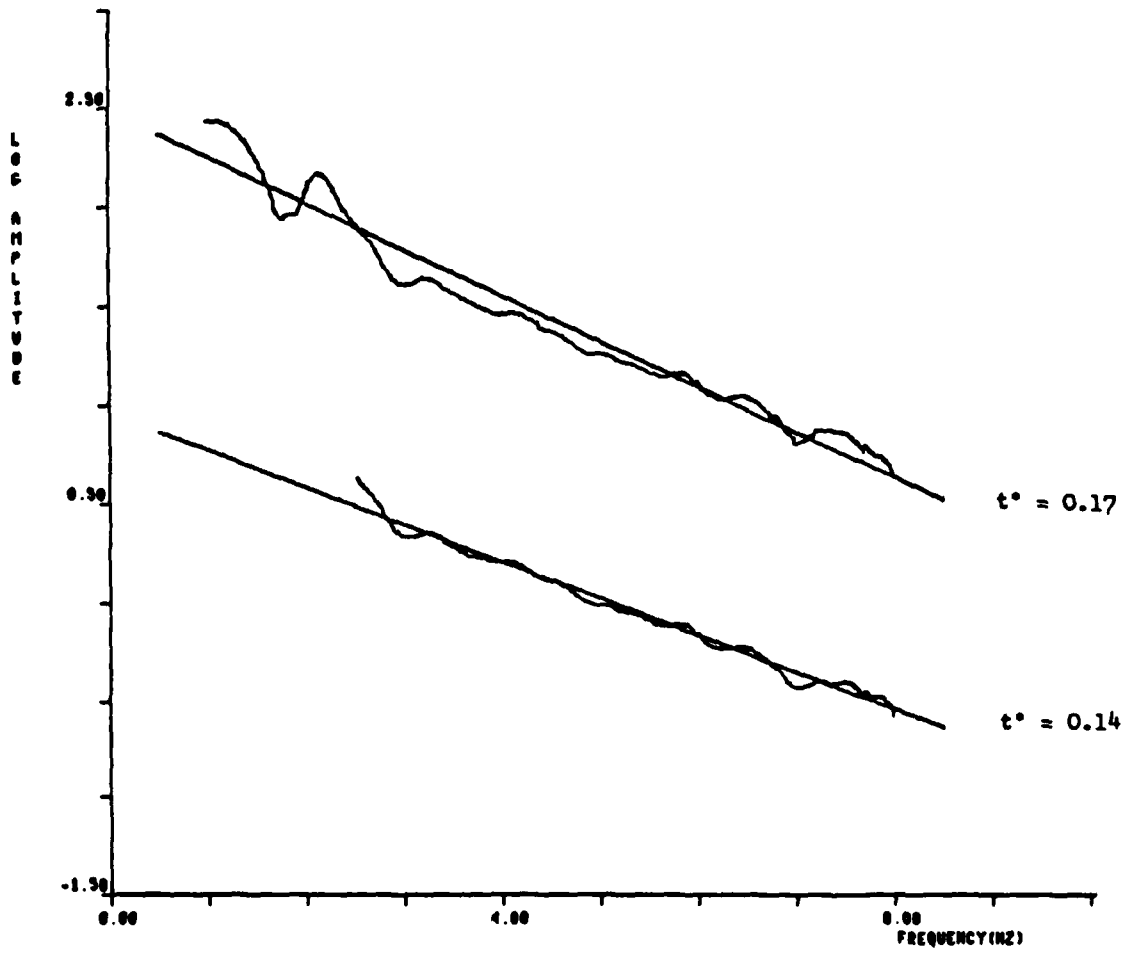


Figure 27 The stacked spectrum derived from the event spectra in Figure 3 is plotted over the 1.0-8.0 and 2.5-8.0 Hz bands. A least squares linear fit and the  $t^*$  derived from the slope of that line are shown.

## 6.3

Attenuation from E Kazakh to the UK Array Stations

In Figure 28 stacked spectra are plotted for all four UK arrays. Except for YKA, where the data are sparse because the clipping threshold is about  $m_b$  5.5, the E Kazakh events are divided into three populations. The individual event spectra included in each stacked spectrum are plotted in Appendix C.

The three populations of events are characterised by differences that are consistent from station-to-station, and are best explained by attributing them to systematic differences in the source corner frequency. That is, it appears that the assumption of an  $f^{-2}$  source is reasonable above 1 Hz for the SW Shagan events, but that the corner frequency is almost certainly greater than 1 Hz for the Degelen events, with the NE Shagan events intermediate between the two. The SALMON spectrum is included as an extreme example of a high corner frequency event (the yield is about 5 kt). Certainly we expect the Degelen events to have higher corner frequencies due to differences in yield. The differences between the mean  $m_b$  for the SW Shagan and Degelen populations is 0.64 at GBA, 0.54 at WRA and 0.43 at EKA. In the simplest interpretation, assuming yield proportional to  $m_b$  and corner frequency to cube-root of yield, this translates to a corner frequency shift of 40-60% (evidence of a yield related corner frequency shift is also seen in the event spectra in Figure 26). But there must also be some source material property contribution to the corner frequency shift. This is seen in several ways. First, for YKA the Degelen population actually has a larger average  $m_b$  than the Shagan population, yet a perceptible difference still remains. More interesting, the difference between NE and SW Shagan River events is best explained by the latter having a lower corner frequency, since the difference persists even when the event populations have the same mean  $m_b$  (Figure 29).

Above 2.5 Hz all the spectra for E Kazakh events are fit very well by a frequency-independent  $t^*$  of 0.14 seconds. This is seen in Figure 28 and is confirmed by computing the best (least squares) fitting lines to these spectra. The small differences that do occur are well within the range expected for minor deviations of the average source from the assumed  $f^{-2}$  behaviour. Of course, the average source could have a steeper falloff, and this would lead to a lower  $t^*$  estimate. It is also interesting to note that there appear to be no significant differences in the attenuation for  $f > 2.5$  Hz for these four travel paths.

PRECEDING PAGE BLANK-NOT FILMED

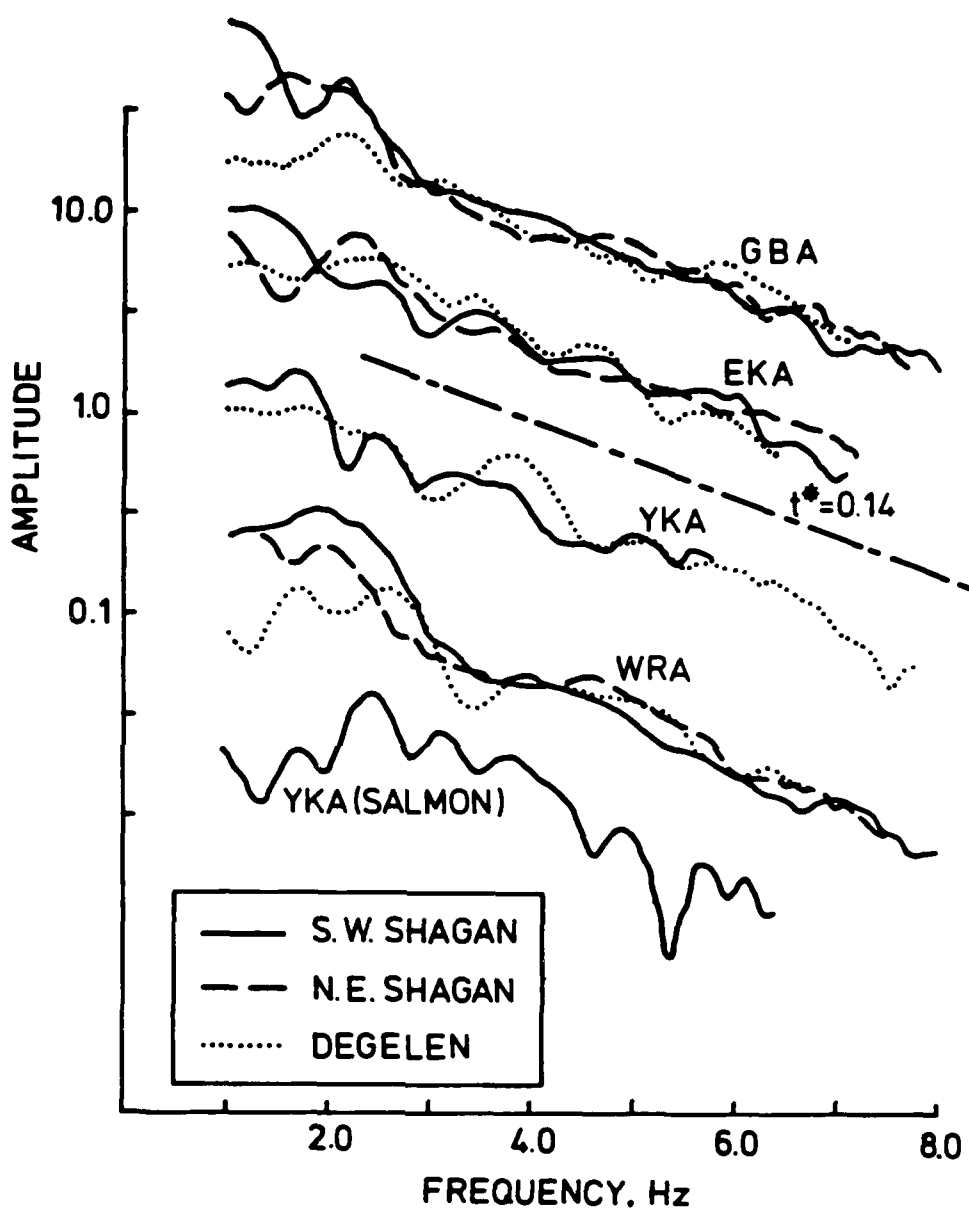


**Figure 28** The stacked spectra are shown for E Kazakh explosions recorded at the UK arrays. The total number of event spectra included are 36 at GBA, 38 at EKA, 16 at YKA and 28 at WRA. The events are divided into three populations, except at YKA where unclipped data were available for only five Shagan River events. At each station the stacked spectra were superimposed so that the least squares linear fit in the 2.5-8.0 Hz band passes through the same value at 5 Hz. Also shown is the spectrum for SALMON at YKA and a line with slope corresponding to  $t^* = 0.14$ .

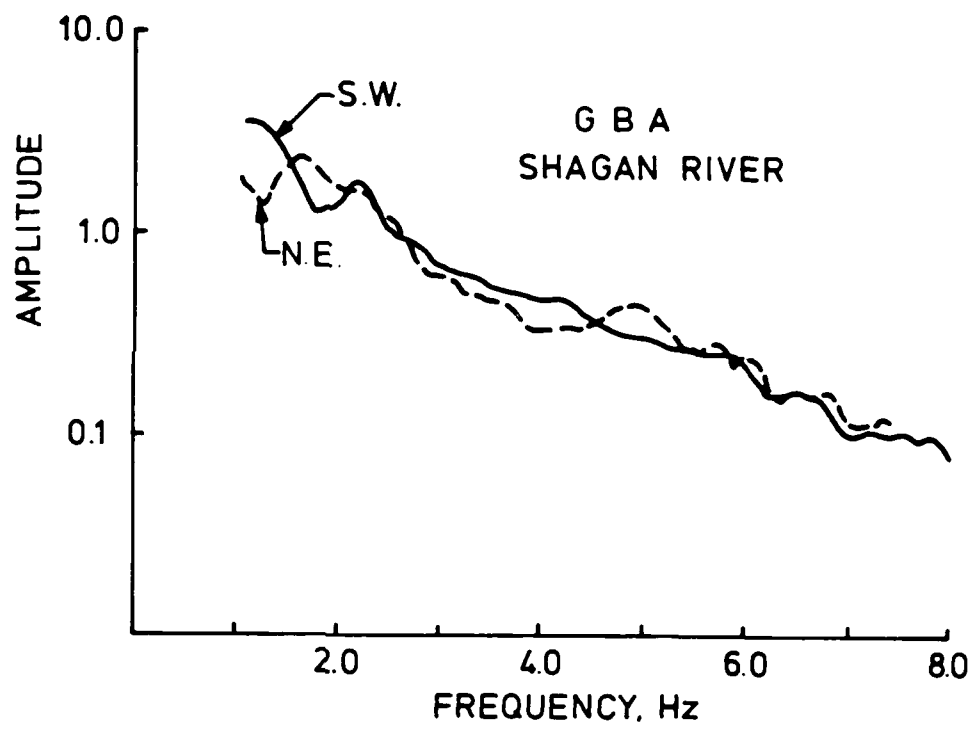


Figure 29 Stacked spectra are compared for eight event populations of NE and SW Shagan events chosen so the mean  $m_b$  is nearly the same. The events are listed in Table 9.

Table 9  
Events Included in Stacked Spectra in Figure 29

SW SHAGAN		NE SHAGAN	
Date	$m_b^*$	Date	$m_b^*$
04-08-79	6.18	14-12-80	5.98
13-09-81	6.10	12-10-80	5.91
18-10-81	6.07	23-11-76	5.91
22-04-81	5.98	28-08-76	5.90
29-11-81	5.73	27-12-80	5.86
29-10-75	5.69	26-12-82	5.7†
25-04-80	5.48	04-11-78	5.61
31-08-82	5.4†	27-12-74	5.60
Mean	5.83	5.81	
Standard Deviation	0.30	0.15	

\* From Marshall et al (1984) unless marked otherwise

† From PDE

Over the whole band the spectra are best modelled with an absorption band Q (Lui *et al* 1976; Minster, 1978; Lundquist and Cormier, 1980) that includes two bands, one to fit the decreasing  $t^*$  between 1 and 2.5 Hz, and a second that keeps the apparent  $t^*$  nearly constant from 2.5 to 8.0 Hz. To minimize contamination by source effects at the low frequency end, we fit only the lowest corner frequency events, which are large  $m_b$  explosions at SW Shagan River. We also need some constraint at long periods. Most long period  $t^*$  estimates are near 1 second (eg Anderson and Given, 1982), but are based on global or broad regional averages, so smaller values are likely for paths like these. Values like 0.5 or 0.6 seconds seem reasonable, but this remains a subject for investigation.

In Figure 30 a double absorption band model is fit to the best estimate for the GBA spectrum. Three models are shown to illustrate the trade-offs among the controlling parameters. The best is Model 2, which has a long period  $t^*$  of 0.6 seconds and a  $\tau_M$  of 0.05 seconds. Models 1 and 3 indicate the sensitivity to  $t_o^*$  and  $\tau_M$ . Other models fitting as well as model 2 must have  $t_o^* < 0.6$  and  $\tau_M < 0.05$  or  $t_o^* > 0.6$  and  $\tau_M > 0.05$ . If we impose the reasonable constraint that  $0.5 < t_o^* < 1.0$ , then an estimate for the bounds is  $0.04 < \tau_M < 0.08$ . The second (lower  $t^*$ ) absorption band is relatively well constrained to have an almost frequency-independent Q that gives a  $t^*$  of about 0.1 seconds, so the spectrum has a nearly constant slope over the 2.5 to 8.0 Hz band.

Similar double absorption band models can be fit to WRA and EKA spectra for large  $m_b$  events in the SW Shagan River Area, and several examples are shown in Figure 31. The three 5-event populations are listed in Table 10. Note that there are no events in common between GBA and EKA and only two in common for GBA-WRA and EKA-WRA. The WRA spectrum is unusual in the way it decreases below 2 Hz. This may be a pP effect that is especially strong for this particular set of events. Assuming this to be the case, there appears to be no significant difference in the attenuation along the paths to GBA and WRA. Comparison of stacked spectra for sets of common events (Figure 32) also indicates no difference. On the other hand, for EKA (Figure 33) the effects of frequency-dependent Q appear to be less than for GBA over the frequency band plotted, suggesting a larger  $\tau_M$ . If  $t_o^*$  is fixed at 0.6 sec, the best  $\tau_M$  is about 0.1 sec. The large event data are not available for a similar analysis of the path to YKA, but comparing spectra for common Degelen events (Figure 34), it can be seen that the

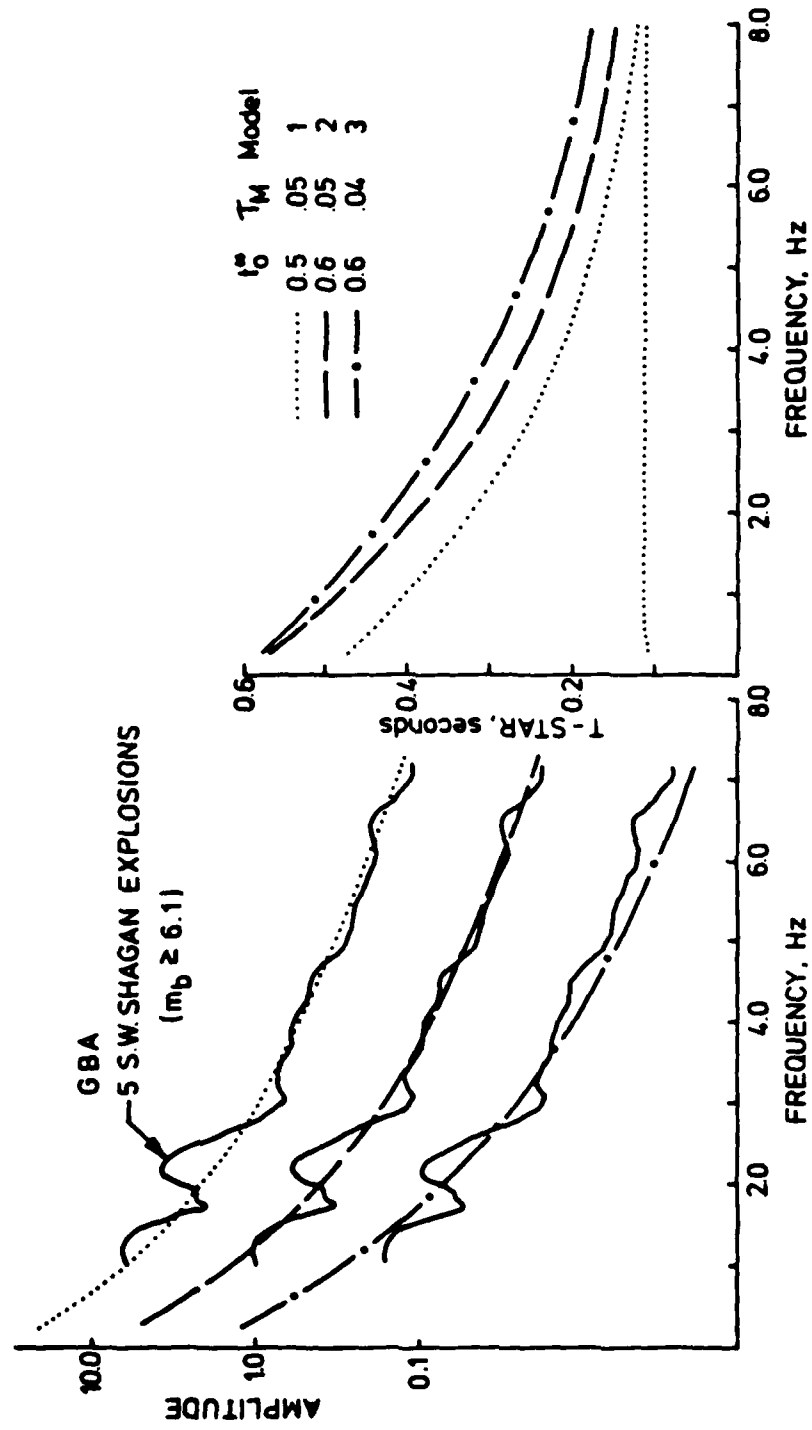


Figure 30 The GBA stacked spectrum for large S.W. Shagan explosions is fit with several double absorption band Q models. The models are shown at the right with the key parameters listed. The  $t^*$  is the  $t^*$  in the flat part of the upper band and  $t^*$  is the short period half amplitude point. All three models have a second absorption band with  $t^*$  essentially constant at 0.11 seconds over the range plotted.

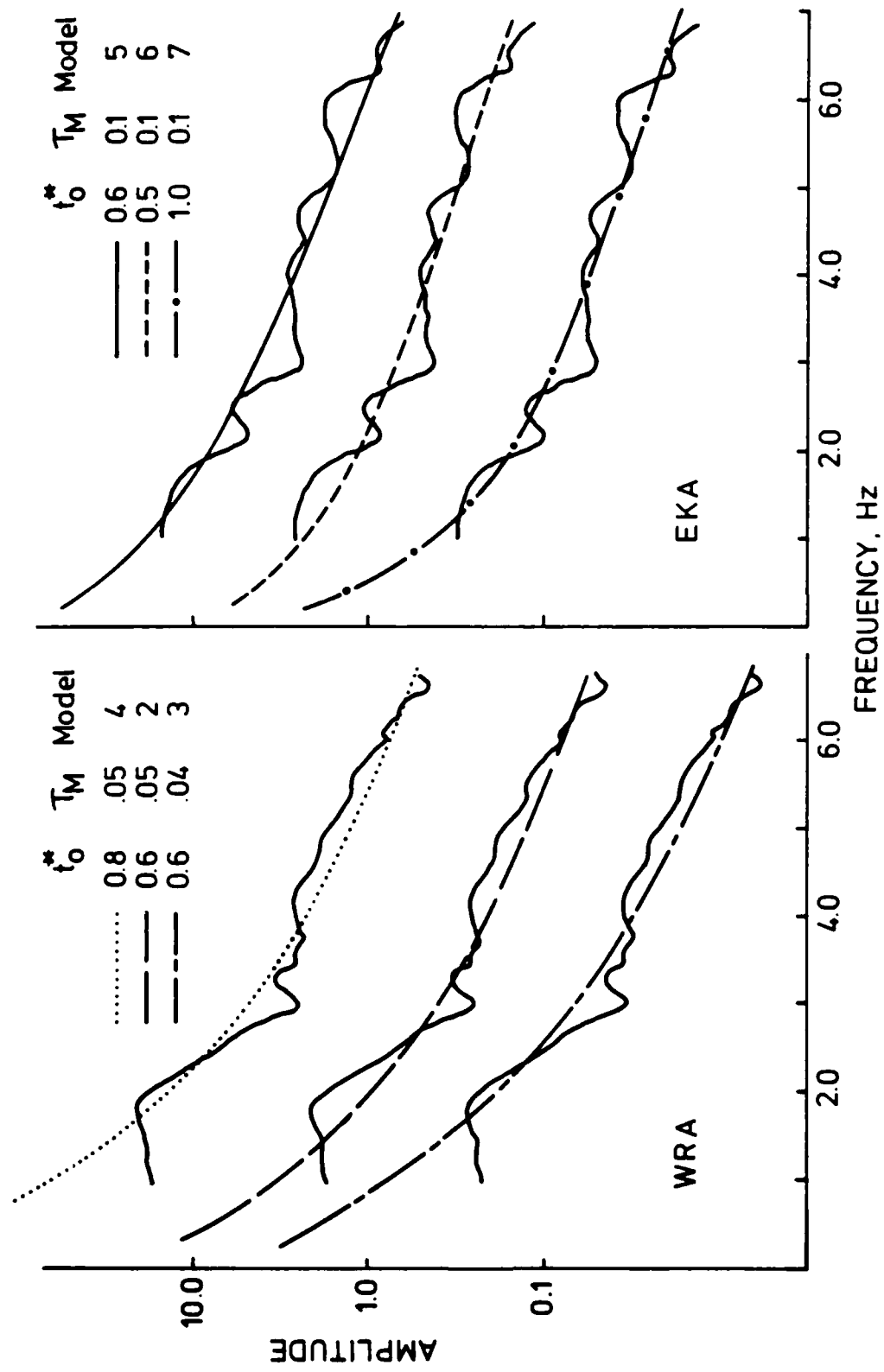


Figure 31 WRA and EKA stacked spectra for five large ( $m_b > 6.0$ ) S.W. Shagan explosions are fit with double absorption band Q models. The models are similar to those in Figure 6 and the key parameters are listed. The second (lower  $t^*$ ) absorption band is the same as in Figure 6 except Model 5 for which this band has a somewhat larger (0.14 sec) constant  $t^*$  level.

Table 10

Large SW Shagan River Events Used to  
Determine an Attenuation Model

GBA		EKA		WRA	
Date	$m_b^*$	Date	$m_b^*$	Date	$m_b^*$
27-12-81	6.28	23-06-79	6.23	04-08-79	6.18
14-09-80	6.25	04-08-79	6.18	13-09-81	6.10
25-04-82	6.10	18-10-81	6.07	05-12-82	6.1†
05-12-82	6.1†	15-09-78	6.01	18-10-81	6.07

\* From Marshall et al (1984) unless marked otherwise  
† From PDE

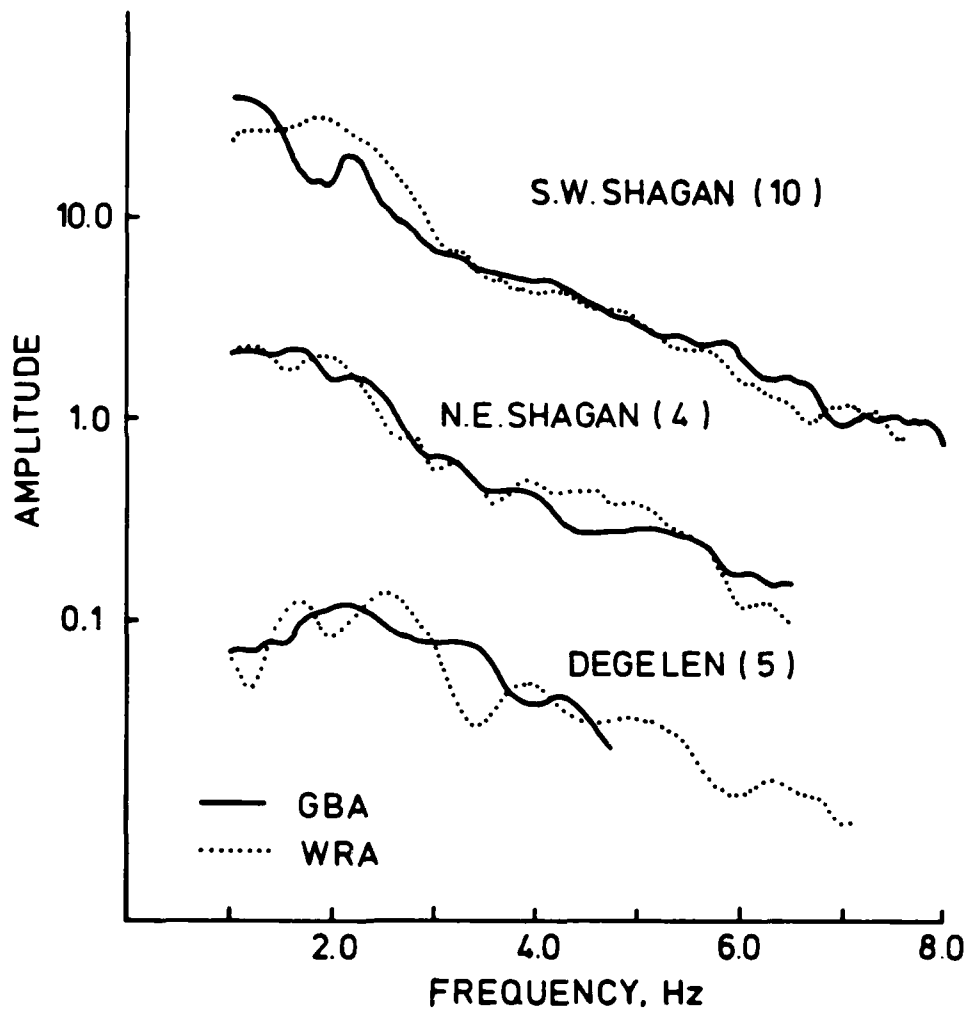


Figure 32 Stacked spectra are compared for event sets common to GBA and WRA. The number of events included in each stacked spectrum is indicated in parentheses.

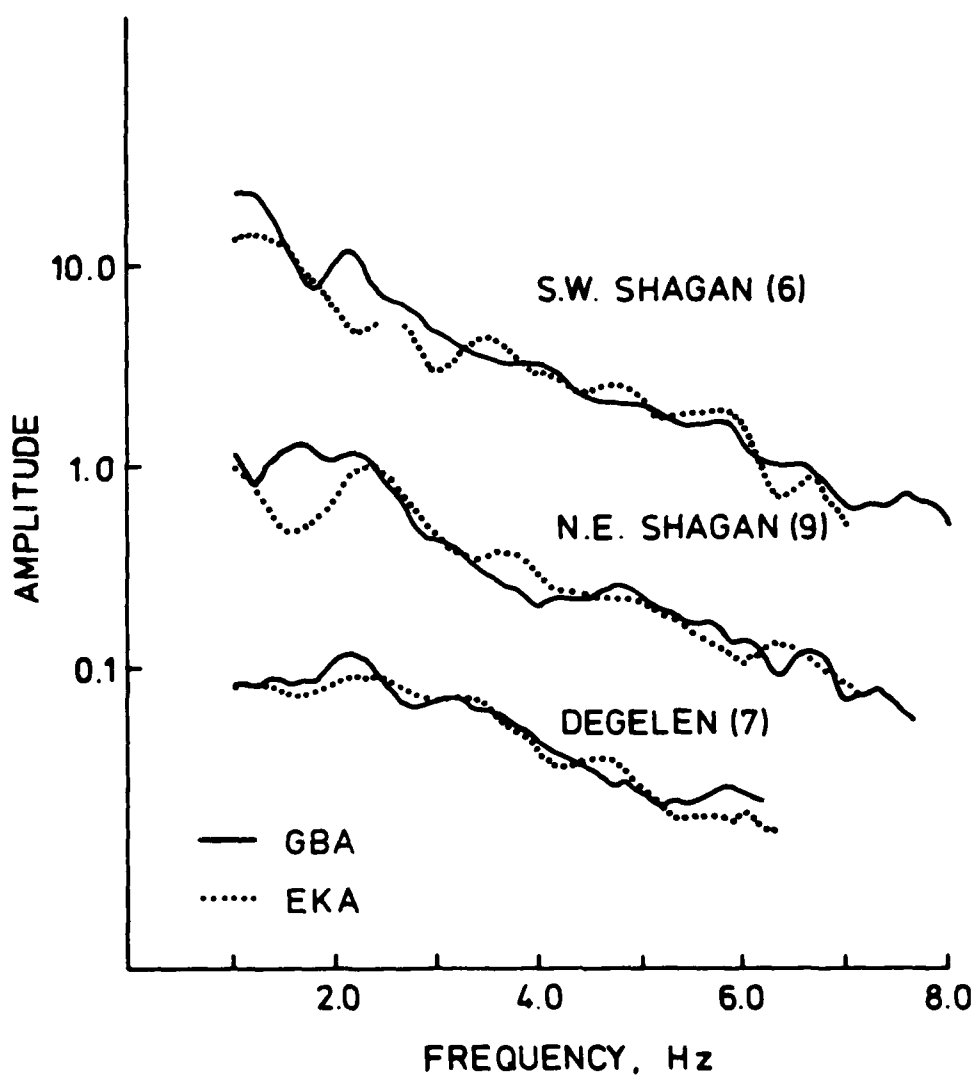


Figure 33 Stacked spectra are compared for event sets common to EKA and GBA.

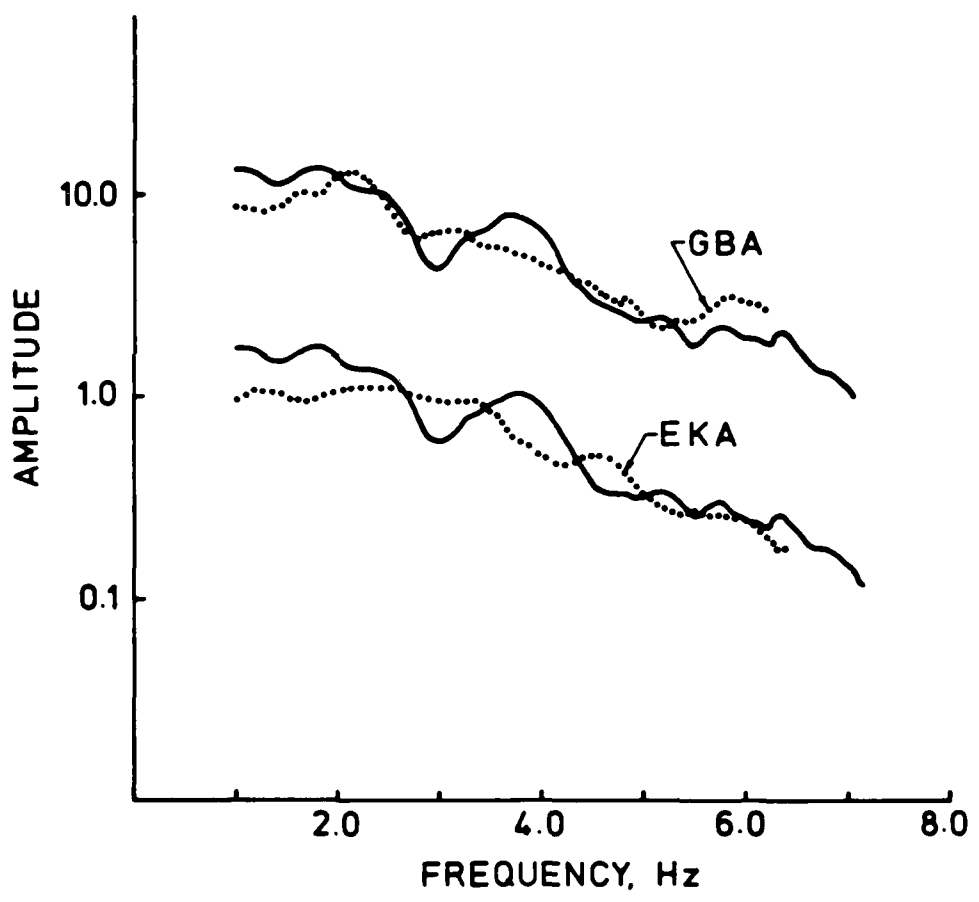


Figure 34 Stacked spectra for YKA are compared to spectra for the same Degelen events at GBA and EKA. There are seven events in each set.

attenuation on the YKA path is at least as strong as on the GBA and WRA paths, and there is some indication that the frequency dependence is greater at low frequencies. This suggests  $\tau_M$  slightly less or  $t_o^*$  slightly more than for the GBA and WRA paths, but the differences are small.

The interpretation of the two absorption bands is that one represents mainly intrinsic attenuation, and the other is mainly due to scattering (thus it is not really an "absorption band"). Richards and Menke (1983) point out that scattering due to many weak inhomogeneities has the effect of a frequency-independent Q, just like the lower  $t^*$  part of the model. Since some scattering will always occur, there must be a minimum level for the total  $t^*$ , and perhaps the  $t^*$  of 0.1 seconds for the lower band is near that minimum. Where scattering is the predominant mechanism, we expect the coda to contain relatively more high frequency energy than the initial pulse. Comparison of our short time window spectra with spectra computed for windows including some of the P coda (Figure 35) shows that this is indeed the case. Thus, the lower  $t^*$  must be due almost entirely to scattering. The mechanism for the attenuation represented by the larger  $t^*$  absorption band remains a subject for speculation, but the effect seems to be intrinsic absorption. Our conclusion that  $\tau_M$  is 0.05 to 0.1 seconds for this band is consistent with earlier work to define the frequency dependence of  $t^*$  near 1 Hz. For example, Der *et al* (1982) suggest  $\tau_M = 0.08$  sec for shield-to-shield paths.

Excellent recordings of PcP are obtained at GBA for large E Kazakh explosions, and these can be used to further define the Q model. The results are shown in Figure 36. Differences in the attenuation for P and PcP are difficult to resolve, but if there is a difference, it is toward somewhat greater attenuation of PcP. This means slightly lower  $\tau_M$  or greater  $t_o^*$ . A model between those in the figure (eg  $t_o^* = 0.7$ ,  $\tau_M = .05$ ) provides a good fit.

In summary, our preferred  $t^*$  is given by Model 2 (Figure 30) for GBA and WRA, slightly lower  $t^*$  for EKA and slightly higher  $t^*$  for YKA, while the GBA PcP seems to be somewhat more attenuated than any of the P waves. These five ray paths are spaced to sample the mantle quite evenly, as seen in Figure 37.

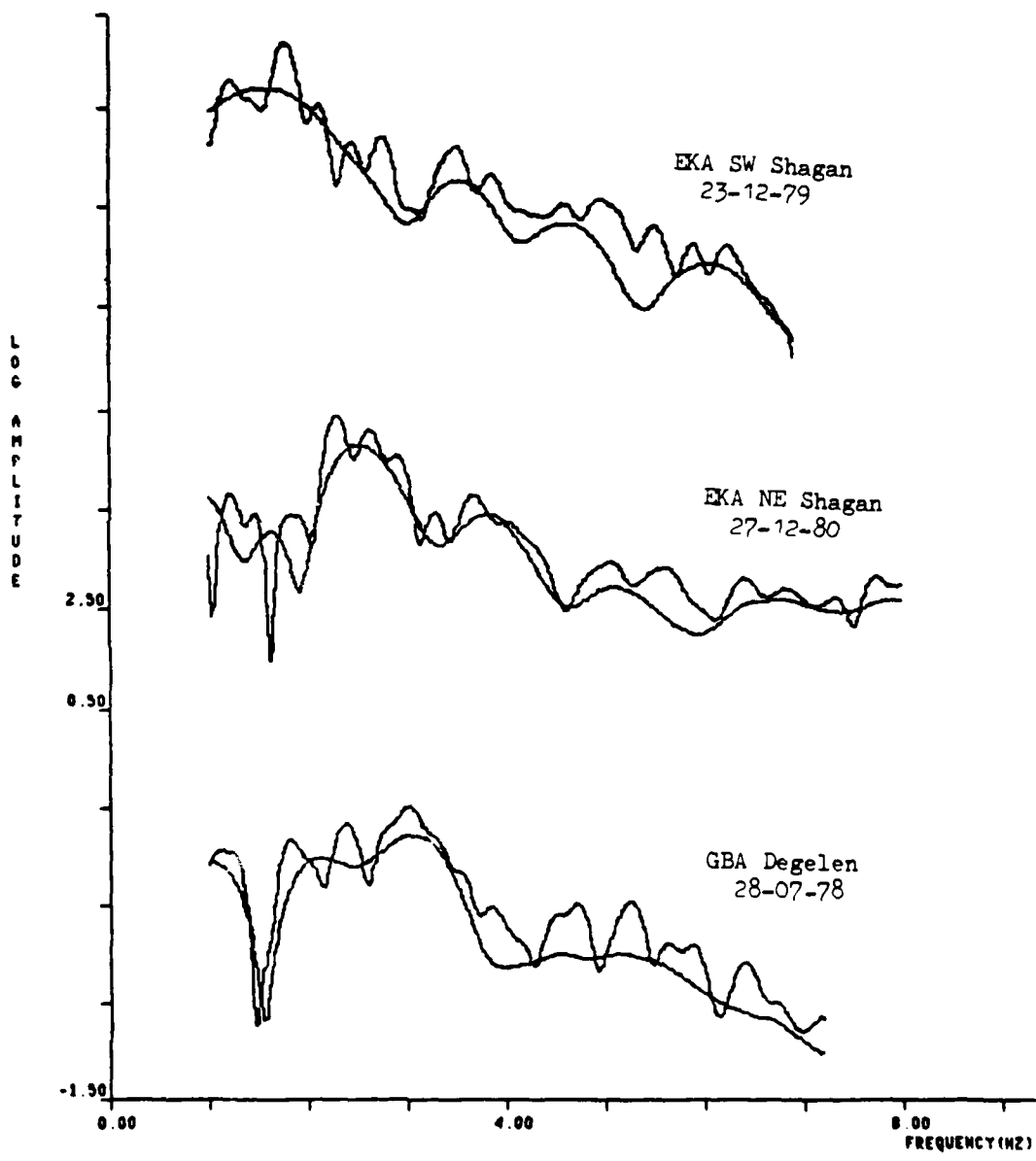


Figure 35 Several comparisons are made between event spectra computed for different time windows. In each case the window length is 5 seconds for the less smooth of the two. The short window length is 2.4 seconds for the middle comparison and 2.2 seconds for the others.

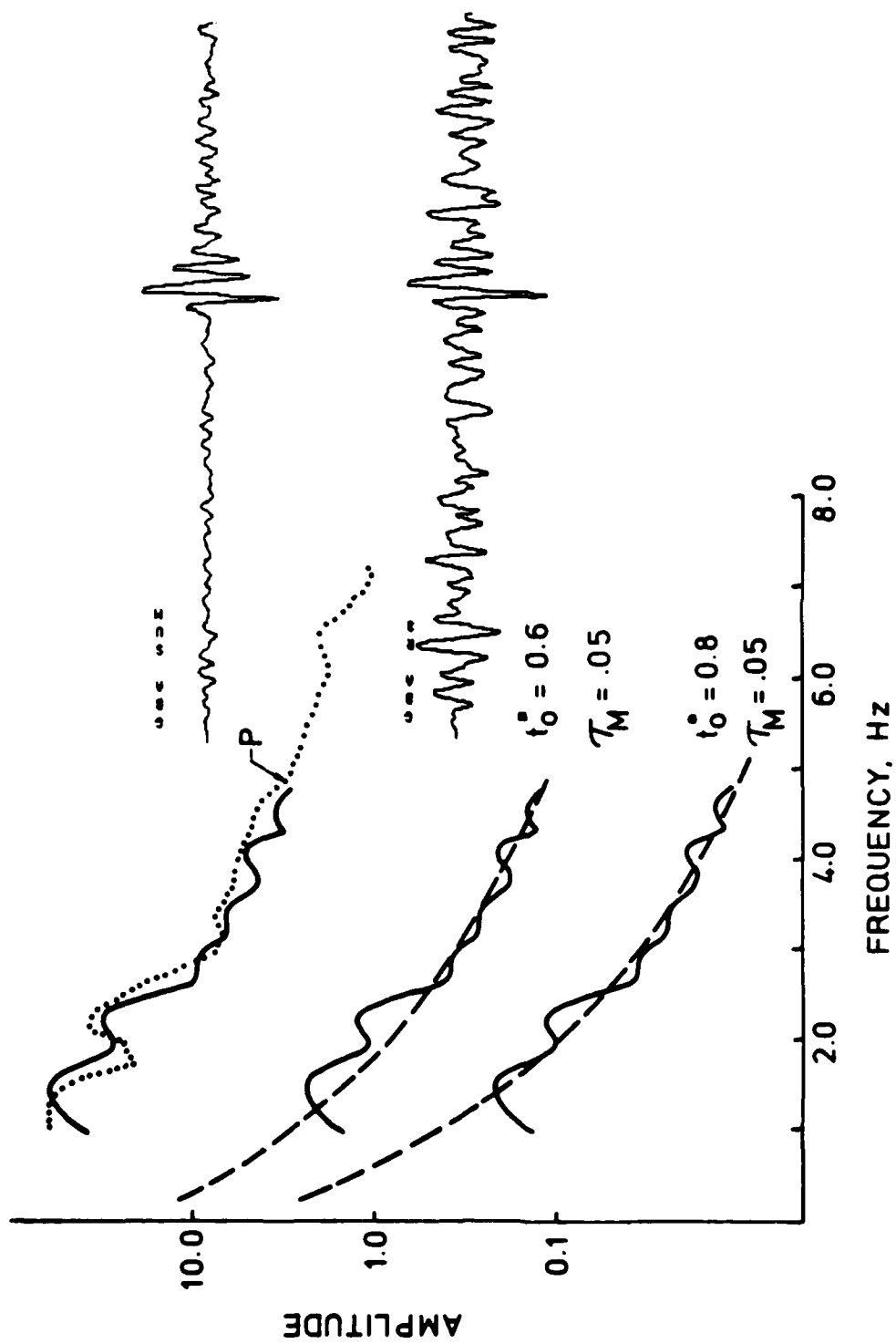
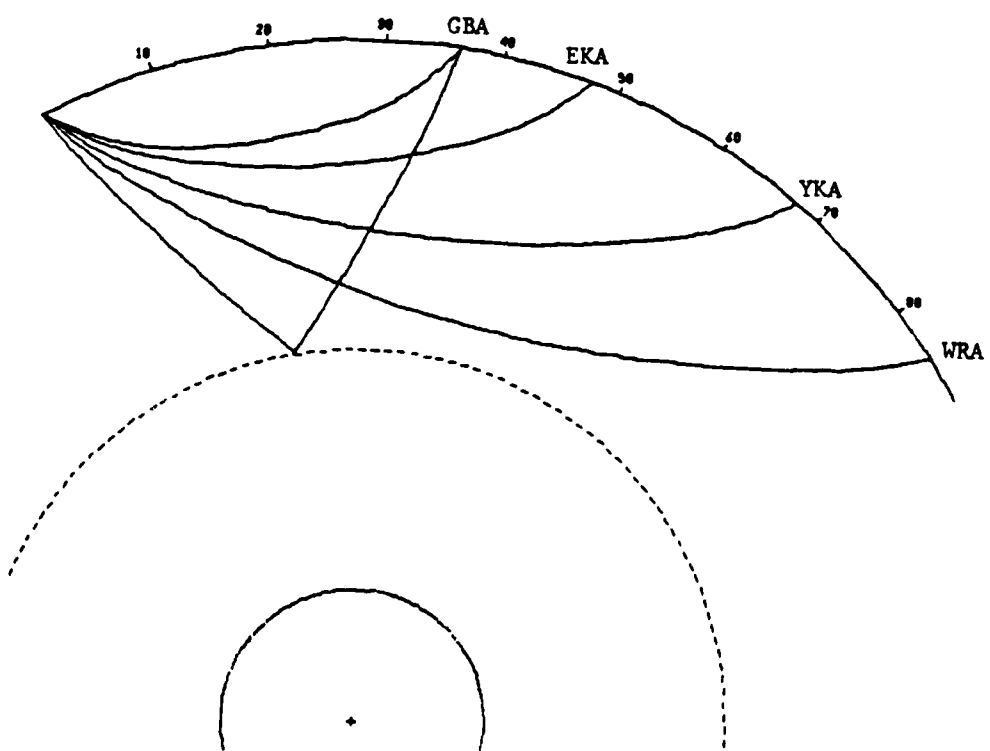


Figure 36 The stacked spectra for GBA recordings of Pcp for 5 large S.W. Shagan River events is compared to the P spectrum (Figure 6) for the same events and is fit with two double absorption band Q models. At the right is shown a typical single channel and beam sum Pcp recording.



**Figure 37** The ray paths for the UK array stations are plotted for a Jeffreys-Bullen earth model. The plot is drawn to scale and the depth to the outer core is 2890 km. The source-station azimuths (measured clockwise) are  $6^\circ$  for YKA,  $129^\circ$  for WRA,  $182^\circ$  for GBA and  $309^\circ$  for EKA.

The depth of penetration of the ray and the preferred  $t^*$  values are as follows:

	Depth (km)	1 Hz	2.5 Hz	5.0 Hz
GBA	870	0.60	0.45	0.33
EKA	1160	0.50	0.33	0.25
YKA	1790	0.60	0.49	0.34
WRA	2540	0.60	0.45	0.33
GBA Pcp	2890	0.70	0.50	0.35

These values cannot be fit by a smooth azimuthally symmetric model; differences between stations must be due to azimuthal effects. But to see the kind of Q model implied by these  $t^*$ , we can assume that Model 2 also represents the EKA and YKA paths. This would be entirely appropriate if the differences are caused by the receiver half of the path, and the Q model would then represent Central Asia.

The Q model from the inversion is plotted in Figure 38 for 1 and 5 Hz and is compared to the Q at 1 Hz from the Anderson and Given (1982) model which is based on worldwide average data over the entire band from normal mode periods to 1 Hz. Our Q model at 1 Hz is essentially the same as this model. The only significant difference is near the core-mantle boundary, but this depends entirely on our Pcp  $t^*$  which is not very well constrained. In fact, if the Pcp  $t^*$  is said to be almost the same as the P  $t^*$ , which is possible (Figure 36), there will be no low Q near the boundary. Also shown in the figure is the model resulting from assuming  $t^* = 0.14$  sec for the four P waves and 0.19 sec for GBA Pcp. This  $t^*$  is a good fit to the data above 2.5 Hz (Figures 29 and 36) if a frequency-independent Q is assumed. This shows that large errors in Q result if frequency dependence is present, but not included in the model.

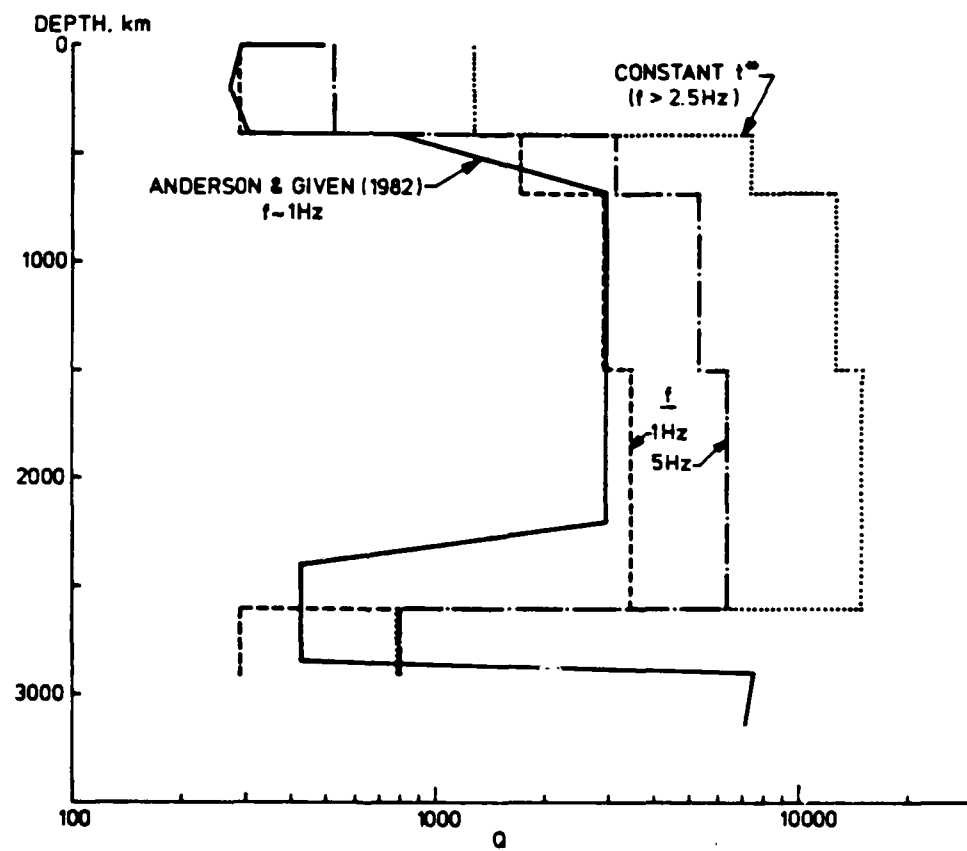


Figure 38 A Q model for central Asia derived from UK array observations of E Kazakh explosions is plotted for 1 and 5 Hz. Also shown is a Q model derived by assuming a frequency-independent  $t^*$  and using the value the best fits the spectral falloff for  $f > 2.5$  Hz.

Synthetic Seismograms

It is one thing to show that the spectra of E Kazakh explosions are consistent with a Q model like that in Figure 38. It is quite another to fit this into a complete model for P-wave signals from explosions, for this requires consideration of the phase spectrum of the Q and source, as well as proper representation of the pP phase. Computing synthetic seismograms with currently available models, we can see that some important issues remain unsolved.

In Figure 39 typical single sensor GBA recordings of two large SW Shagan River explosions are compared to several synthetic seismograms. The synthetic seismograms were computed with a program based on Douglas *et al* (1972) and include reasonable models for the crystal structure at the source and receiver and the Carpenter (1966) geometric spreading factor. The Mueller and Murphy (1971) source model was used and the yield was fixed at 150 kt. The first synthetic seismogram is for a frequency independent  $t^*$  of 0.2 seconds and the source depth (corresponding to a P-pP lag time of 0.44 sec) was chosen so the period  $T_c$  (twice the first trough to second peak time) would be about the same as observed. At first glance, the waveform comparison may not seem too bad, but there are some important discrepancies. In particular, the onset is too abrupt, the first peak is too large and the  $T_b$  period (twice the first trough to first peak time) is about 0.2 seconds too small. Further, looking back at Figure 26, we see a robust spectral hole at frequencies no larger than 2.0 Hz for the  $m_b > 6.0$  events, suggesting P-pP lag times of 0.5 - 0.6 sec for these events. But the most significant discrepancy is in the  $m_b$ , for the amplitude of the synthetic seismogram is nearly an order of magnitude too large. This discrepancy, in itself, is a strong indication that there must be rapid shift to greater attenuation in the 1 - 2 Hz band which controls the amplitude.

Our preferred model for attenuation along the GBA E Kazakh path is Model 2 in Figure 30, and the other two synthetics were computed with it (the Doornbos, 1983, formulation was used for the computations). The first has  $T_b$  and  $T_c$  periods very near those observed and an  $m_b$  that is also in reasonable agreement. However, the P-pP lag time is too short to be consistent with the major spectral hole, and the final synthetic was computed with a P-pP lag time consistent with the spectral evidence. These synthetics clearly represent a step in the right direction, and the major discrepancies are what we should expect. The most obvious is the

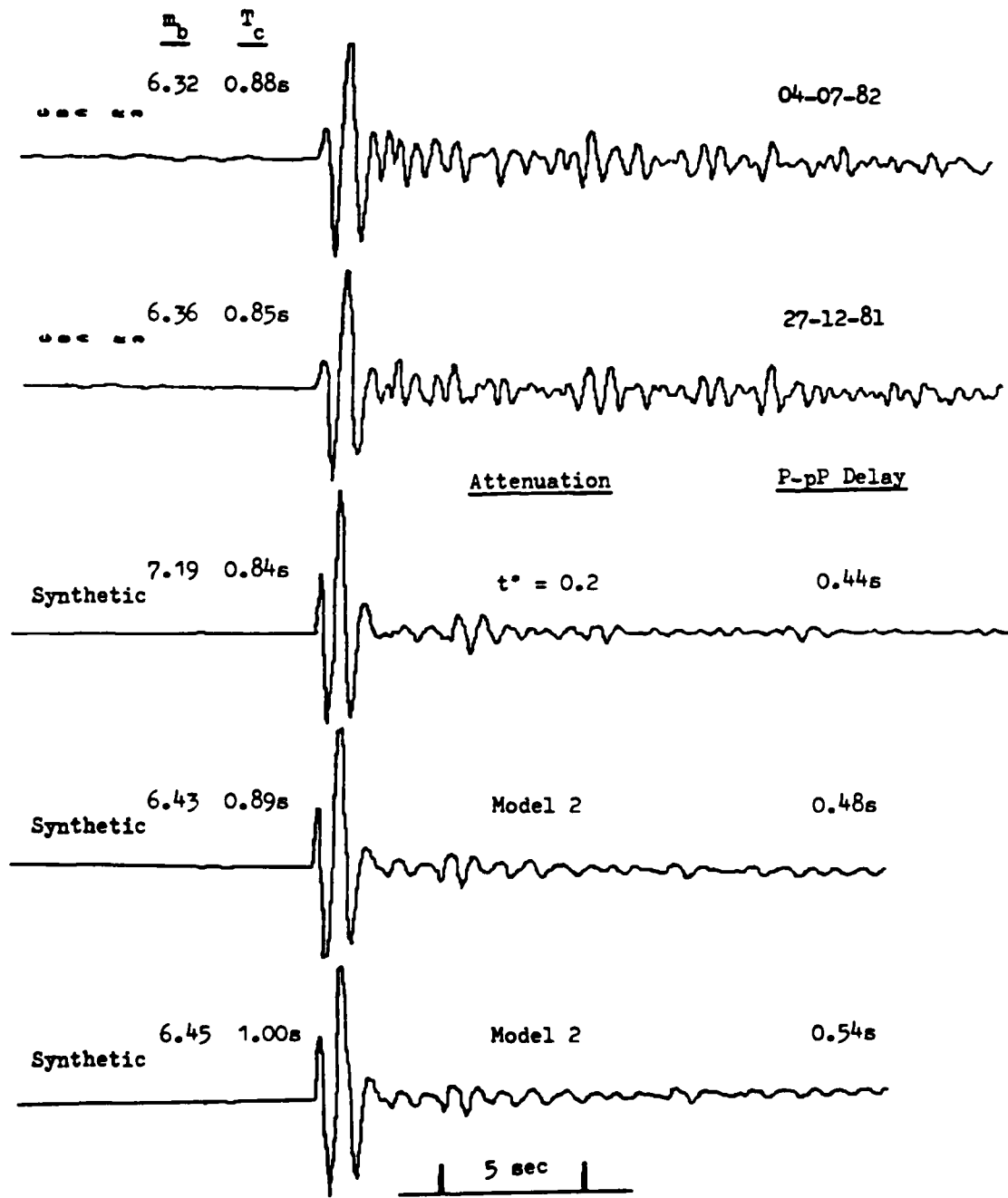


Figure 39 Single sensor recordings of two typical SW Shagan River explosions are compared to several synthetic seismograms. For the observations the  $m_b$  is for this element; the PDE  $m_b$  are 6.1 (04-07-82) and 6.2. The  $T_c$  is twice the first trough to second peak and is used to calculate the  $m_b$ . The key parameters for the synthetics are the attenuation model and P-pP delay time, and these are indicated.

shape and relative amplitude of the first peak, which is sensitive to the high frequency portion of the Q model. But we have concluded that scattering is the dominant attenuation mechanism at high frequencies, and expect an absorption band model derived from the amplitude spectrum to underpredict the dispersion and pulse-broadening associated with scattering (Richards and Menke, 1983). Thus, a correct representation of the phase spectrum for a Q due to scattering will clearly change the appearance of the first peak toward that seen in the observed seismograms.

The second major problem with the synthetics is that elastic theory is used to compute pP, and there is ample evidence from previous work (eg Bache, 1982) and from these data to conclude that this cannot be correct. Synthetic and observed amplitude spectra are compared in Figure 40. The first trough in the observed spectra can reasonably be assumed to be due to P-pP interference, but there is no more than a hint of higher frequency peaks. This is about what one should expect for a pP reflection coefficient that is smaller than the elastic and strongly dependent on frequency. The next generation of synthetic seismograms must include such a coefficient along with the proper phase spectrum for a Q due to scattering, and is expected to closely resemble the observations in all important respects. These improvements may change the  $m_b$  of the synthetics by several tenths, so we must be cautious about interpreting the attenuation effect on  $m_b$  until they are included.

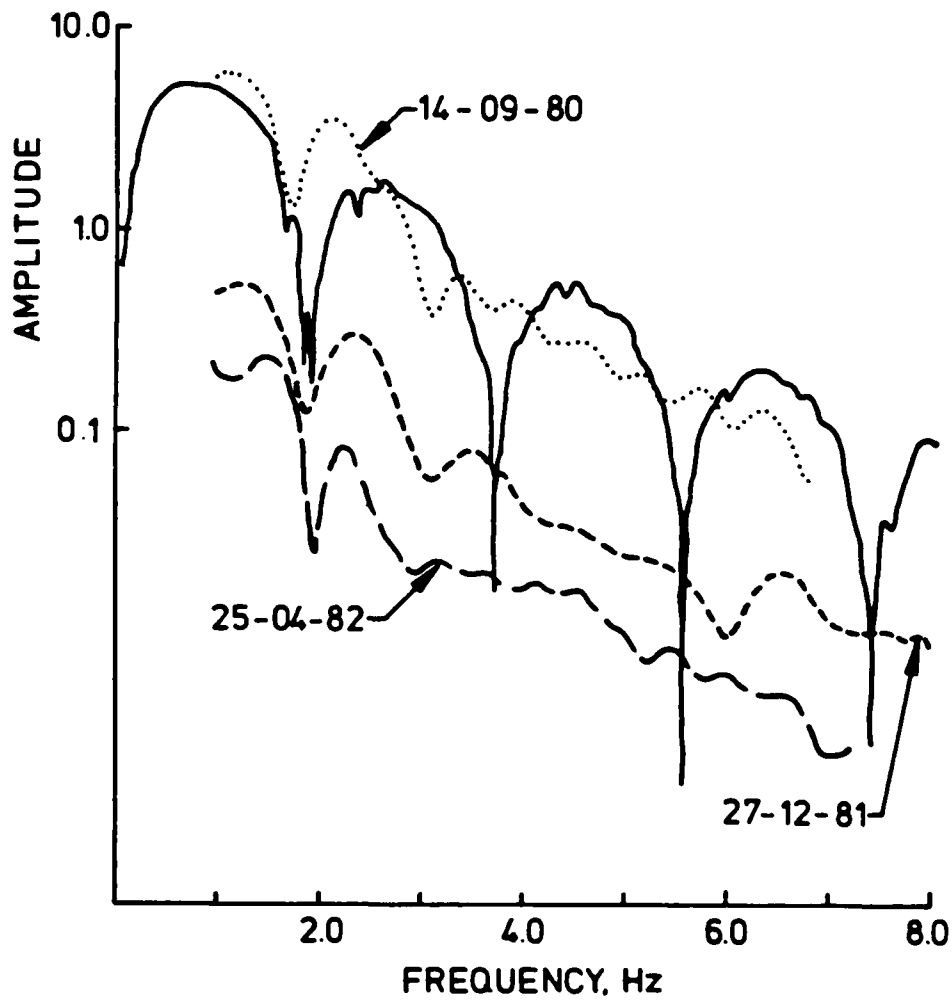


Figure 40 The amplitude spectrum of the synthetic seismogram computed with attenuation Model 2 and a P-pP delay of 0.54 seconds is compared to the GBA spectra for three typical SW Shagan events.

## VII SPECTRA FOR SALMON AND THE AMCHITKA AND FRENCH SAHARA EVENTS

### 7.1 Introduction

In Section VI we showed that our techniques lead to a greatly improved understanding of the separate effects of source and attenuation on explosion P waves. As was pointed out in Section II, the data are available to apply these techniques to study events in other test areas, including French Mururoa, the Nevada Test Site and Novaya Zemlya. These are areas where the events are numerous enough so that we can hope to separate source and attenuation effects. We will be trying to do so and will describe the results in a future report.

There are other test sites and isolated events for which the data are sparse, but quite important. We have computed spectra for several of these and describe the results in this section.

### 7.2 SALMON and the Amchitka events

The one available spectrum (YKA) for the SALMON event ( $\sim 5$  kt in a Mississippi salt dome;  $m_b \sim 4.5$ ) was plotted in Figure 29 as an example of an event for which the corner frequency must be over 1 Hz. This means that we cannot infer much about  $t^*$  below 3 - 4 Hz without correcting for the source, with all the uncertainty that entails. However, comparison with YKA spectra from the smallest E Kazakh events is enlightening (Figure 41). At high frequencies ( $> 3$  Hz) there is not much difference, though it appears that the SALMON spectrum falls off slightly more rapidly. The low frequency behaviour is consistent with the expectation that SALMON has a higher corner frequency.

The available spectra for the Amchitka events are plotted in Figure 42. Array spectra are only available for LONGSHOT. At EKA this suggests strong frequency-dependence of attenuation, but the effect is not seen in the single element spectra for the other events. For the other two events we have only one single element spectrum and can only draw conclusions from the most robust features. It does appear that the CANNIKIN spectrum decays faster, but for this huge event ( $\approx 5000$  kt), we should be so far beyond the corner frequency that the source decay may be more rapid. At YKA and EKA the attenuation above 2 Hz seems little different than for SALMON (or the E Kazakh events). The similarity to the E Kazakh paths is also seen in comparing long and short window spectra; the results

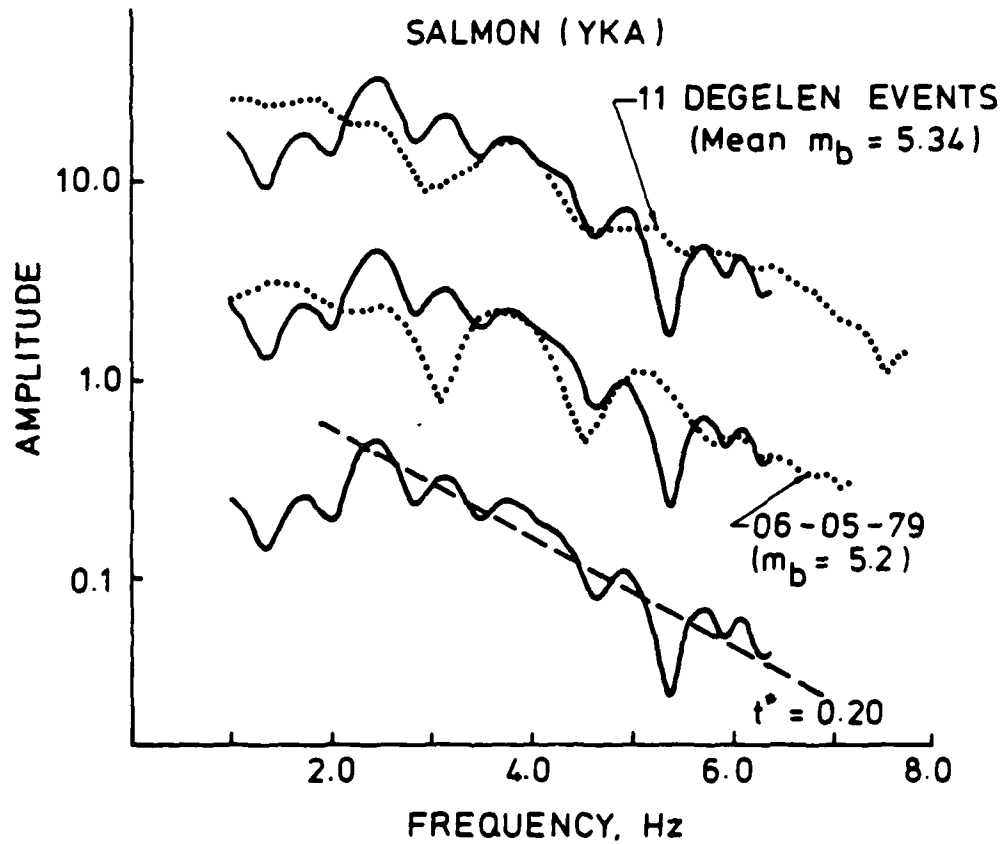


Figure 41 The YKA SALMON spectrum is compared to the YKA stacked Degelen spectrum from Figure 5 and the spectrum for one of the smallest Degelen events. At the bottom it is shown with a line corresponding to a frequency-independent  $t^*$  of 0.2 seconds.

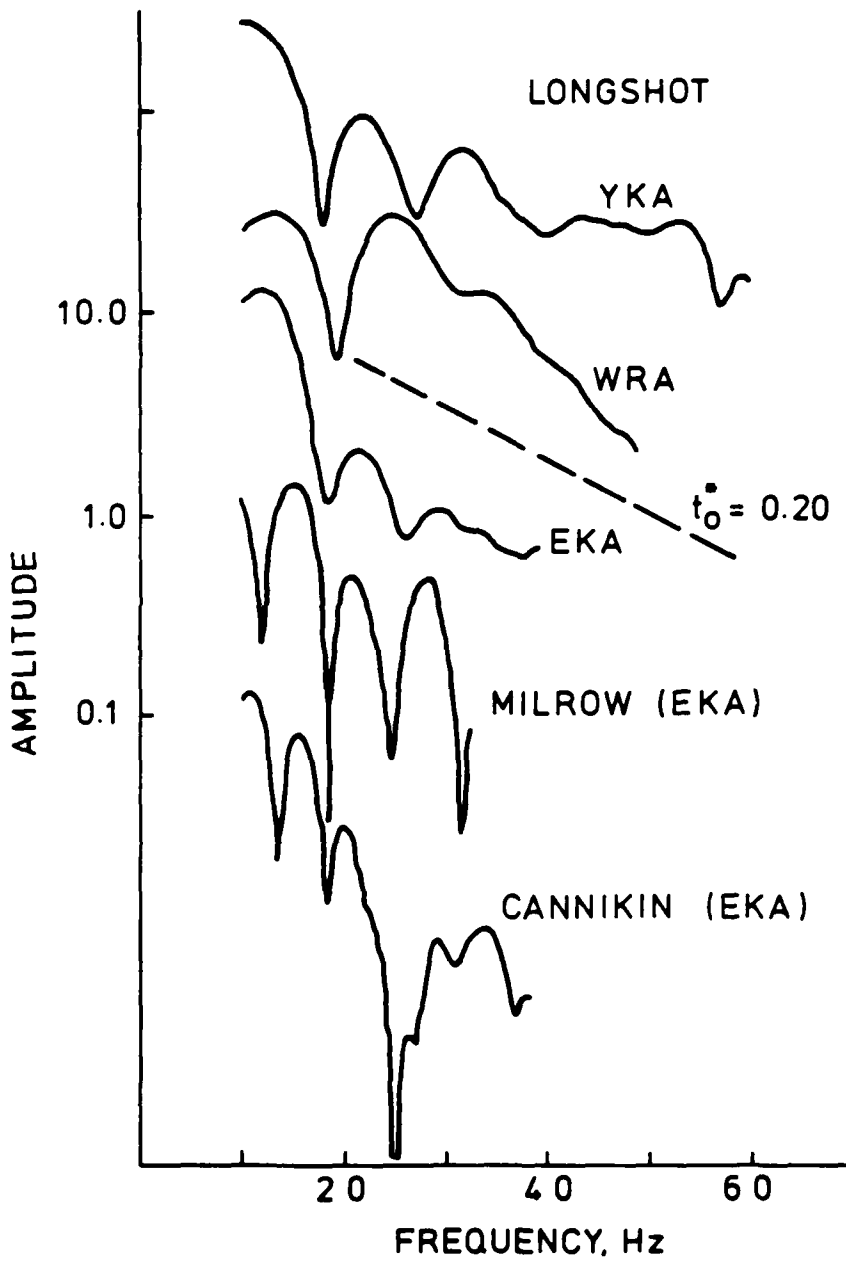


Figure 42 The available spectra are plotted for the Amchitka events. For MILROW and CANNIKIN these are not array spectra, but are computed from a single low-gain channel.

for LONGSHOT at YKA and EKA look much like Figure 8. At WRA the spectral decay is greater and long and short window spectra plot together over the whole band; thus, there seems to be more intrinsic attenuation on this path.

Developing a more quantitative model for the Q for  $f < 2$  Hz, the band of importance for  $m_b$ , will require correction for the source. Analysis of the spectral nulls in Figure 42 shows some of the difficulties that must be faced in doing so. The first null is at frequencies corresponding to a P-pP lag time of 0.55 sec for LONGSHOT and 0.85 sec for MILROW, values consistent with previous work (eg King *et al* 1974). The first CANNIKIN null corresponds to 0.75 sec, much too early to be pP. But there are actually several nulls at regular intervals and these appear to be multiples of 0.9 Hz for LONGSHOT, 0.6 Hz for MILROW and 0.6 Hz for CANNIKIN. These suggest lag times (1.1 sec and 1.6 sec) that cannot be right for pP. Thus, it appears that a phase later than pP (spall slapdown?) is an important contributor to the spectrum for these events and interpretation is that much more difficult.

### 7.3 French Sahara Events

The well-determined spectra for French tests in the Sahara are plotted in Figure 43. The best data are from EKA and they show a consistent pattern, assuming that SAPHIR ( $\sim 120$  kt) is the largest corner frequency event. The preferred model for E Kazakh-GBA fits these data rather well, so one can only argue that attenuation on the French Sahara-EKA path is greater than from E Kazakh by assuming that the SAPHIR spectrum is contaminated by some source effect (eg the corner frequency may be greater than for the SW Shagan events). However, an indication that the attenuation is different than on the E Kazakh-GBA path is that short time window SAPHIR spectra have more high frequency energy than long time window spectra. Thus, the attenuation has apparently not reached the level where scattering predominates.

There is strong evidence that there is greater attenuation on the French Sahara-YKA path, though it is troublesome to note the large differences in the low frequency character of the spectra for the same event at these two stations. Again, as for SALMON and the Amchitka events, a quantitative estimate for the attenuation will require a confident correction for the source.

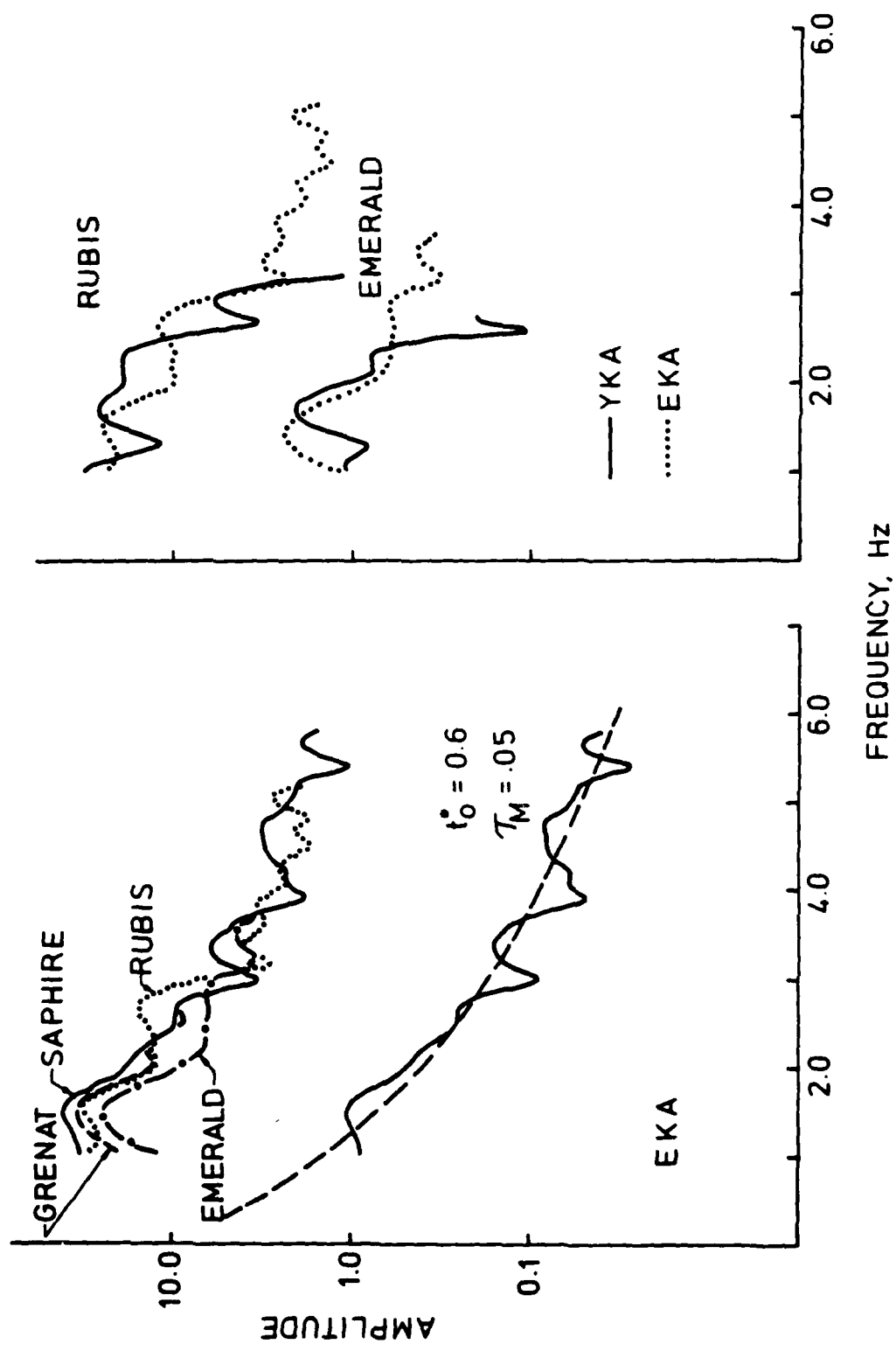


Figure 47. The spectra for French Sahara explosions are plotted and the EKA SAPHIR spectrum is fit with Model 2 from Figure 6.

## VIII AKNOWLEDGEMENTS

This work was done while the author was a Visiting Research Fellow at Blacknest, United Kingdom Ministry of Defense. It could not have been done without the great care and effort expended by the Blacknest staff, especially John Young and Peter Marshall, to collect and organize the data. Penny Warburton, Catherine Pooley and Hilary Trodd also made major contributions to the data collection and quality control effort.

As a visitor who has had to cope with an unfamiliar computer system and develop and apply the several programs needed for this analysis, the author acknowledges a special debt to John Young, who made it possible. Lolitia Bache also helped with the calculations.

The interpretation of the data has benefited from discussions with Peter Marshall and Alan Douglas of the Blacknest staff. Also, Bob Blandford of DARPA originally suggested the power spectrum stack method used to compute event spectra from array data.

The work was supported by Defense Advanced Research Projects Agency under contract DNA 001-83-C-0383 which is administered by the Defense Nuclear Agency.

PRECEDING PAGE BLANK-NOT FILMED

## IX REFERENCES

Anderson, D L and J W Given (1982). "Absorption band O model for the earth", J Geophys Res, 81, 3893-3904

Bache, T C (1982). "Estimating the yield of underground nuclear explosions", Bull. Seism. Soc. AM, 72, 5131-5168.

Bock, G and J R Clements (1982). "Attenuation of short-period P, P<sub>c</sub>P, S<sub>c</sub>P and pP waves in the earth's mantle", J Geophys Res, 87, 3905-3918

Bungum, H (1983). "Seismic noise at high frequencies", NORSAR. Semi-annual Tech. Sum., 1 October 82-31 Mar 83

Burch, R F (1968) "A comparison of the short period seismic noise at the four UKAEA type arrays and an estimate of their detection capabilities", AWRE Rep. RT No. 079/68, Aldermaston.

Burdick, L J, T Wallace and T Lay (1984). "Modelling near-field and tele seismic observations from the Amchitka test site", submitted to J Geophys Res.

Capon, J, R Greenfield, R J Koller and R T LaCoss (1968). "Short-period signal processing results for the large aperture seismic array", Geophys. 33, 452-472

Carpenter, E W (1966) "A quantitative evaluation of telesismic explosion records", Proc R Soc Lond A, 290, 396-407

Chang, A C and D H von Seggern (1980). "A study of amplitude anomaly and  $m_b$  bias at LASA subarrays", J Geophys Res. 85, 4811-4828

Cherry, J T, N Rimer and W O Wray (1975). "Seismic coupling from a nuclear explosion; The dependence of the reduced displacement potential on the non-linear behaviour of near-source rock environment", SSS - R - 76 - 2742, S-Cubed, La Jolla, California

Claerbout, J F (1964). "Detection of P-waves from weak sources at great distance". Geophys. 29, 197-211

Der, Z A, T W McElfresh and A O'Donnell (1982a). "An investigation of the regional variations and frequency dependence of anelastic attenuation in the United States in the 0.5-4.0 Hz band", Geophys J, 69, 67-99

PRECEDING PAGE BLANK-NOT FILMED

Der, Z A, W D Rivers, T W McElfresh, A O'Donnell, P J Klouda and M E Marshall (1982b). "Worldwide variations in the attenuative properties of the upper mantle as determined from spectral studies of short-period body waves". Phys. Earth Planet Inter., 30, 12-25

Der, Z A and T W McElfresh (1976). "Short-period P wave attenuation along various paths in North America as determined from P wave spectra of the SALMON nuclear explosion", Bull. Seism. Soc. Am., 66, 1609-1622.

Doornbos, D J (1983) "Observable effects of the seismic absorption band in the earth". Geophys J R Astr Soc, 75, 693-711

Douglas, A (1966) "A special purpose least squares program" AWRE Report No: O-54/66, Aldermaston.

Douglas A, J A Hudson and C Blamey (1972). "A quantitative evaluation of seismic signals at teleseismic distances - III. Computed P and Rayleigh-wave seismograms", Geophys. J., 28, 385-410

Douglas A, R C Lilwall and J B Young (1974). "Computer programs for epicentre determination", AWRE Report No. O 28/74, Aldermaston.

Fix, J E (1972). "Ambient earth motion in the period range from 0.1 to 2560 s", Bull. Seism. Soc. Am., 62, 1753-1760

Helmberger D V and D M Hadley (1981). "Seismic source functions and attenuation from local and teleseismic observations of the NTS events JORUM and HANDLEY", Bull. Seism. Soc. Am., 71, 51-67

Herrin, E (1982). "The resolution of seismic instruments used in treaty verification research", Bull Seism. Soc. Am., 72, 561-567

King C Y, A M Abo-Zena (1974) "Teleseismic source parameters of the LONGSHOT, MILROW and CANNIKIN nuclear explosions". J Geophys Res., 79, 712-718

Lay T, D V Helmberger and D G Harkrider (1984). "Source models and yield-scaling relations for underground nuclear explosions at Amchitka Island", submitted to Bull. Seism. Soc. Am.

Lui H P, D L Anderson and H K Kanamori (1976) "Velocity dispersion due to anelasticity implications for seismology and mantle composition". Geophys J R Astr Soc. 47, 41-58

Lundquist G M and V F Cormier (1980) "Constraints on the absorption band model of Q", J Geophys. Res., 88, 1235-1242

Marshall P D, R C Lilwall and T C Bache (1984). "Body wave magnitudes and locations of Soviet underground explosions at the Semipalatinsk Test Site" AWRE Report (in preparation).

Minster, J B (1978) "Transient and impulse responses of a one-dimensional linearity attenuating medium - II. A parametric study". Geophys. J R Astr Soc 52, 503-524

Meuller, R A and J R Murphy (1971). "Seismic characteristics of underground nuclear detonations", Bull. Seism. Soc. Am., 65, 1675-1692

Muirhead K J (1968) "The reduction and analysis of seismic data using digital computers", PhD Thesis, University of Tasmania.

Peterson J (1980) "Preliminary observations of noise spectra at SRO and ASRO stations", US Geol Surv Open-file Rept. 80

Richards P G and W Menke (1983) "The apparent attenuation of a scattering medium" Bull Seism Soc Am, 73, 1005-1021

Shore M J (1982) "Seismic travel-time anomalies from events in the western Soviet Union", Bull Seism Soc Am, 72, 113-128

Sipkin S A and T H Jordan (1979) "Frequency dependence of  $Q_{Scs}$ ", Bull Seism Soc Am, 69, 1055-1079

Stevens, J L and S M Day (1984). "The physical basis of  $m_b:M_g$  and Variable Frequency Magnitude methods for earthquake/explosion discrimination" submitted to J Geophys Res.

The Geotechnical Corporation (1964). "Deep-hole Seismometer (Variable-reluctance type)" Final report, Project VT/1139, Tech. Report 64-108, Garland, Texas.

von Seggern D H and R R Blandford (1972). "Source time functions and spectra for underground nuclear explosions", Geophys J, 31, 83-97

Weichert D H (1973). "An attempt to detect gravitational waves with the Yellowknife seismic array", Geophys J R Astr Soc, 35 337-342

APPENDIX A

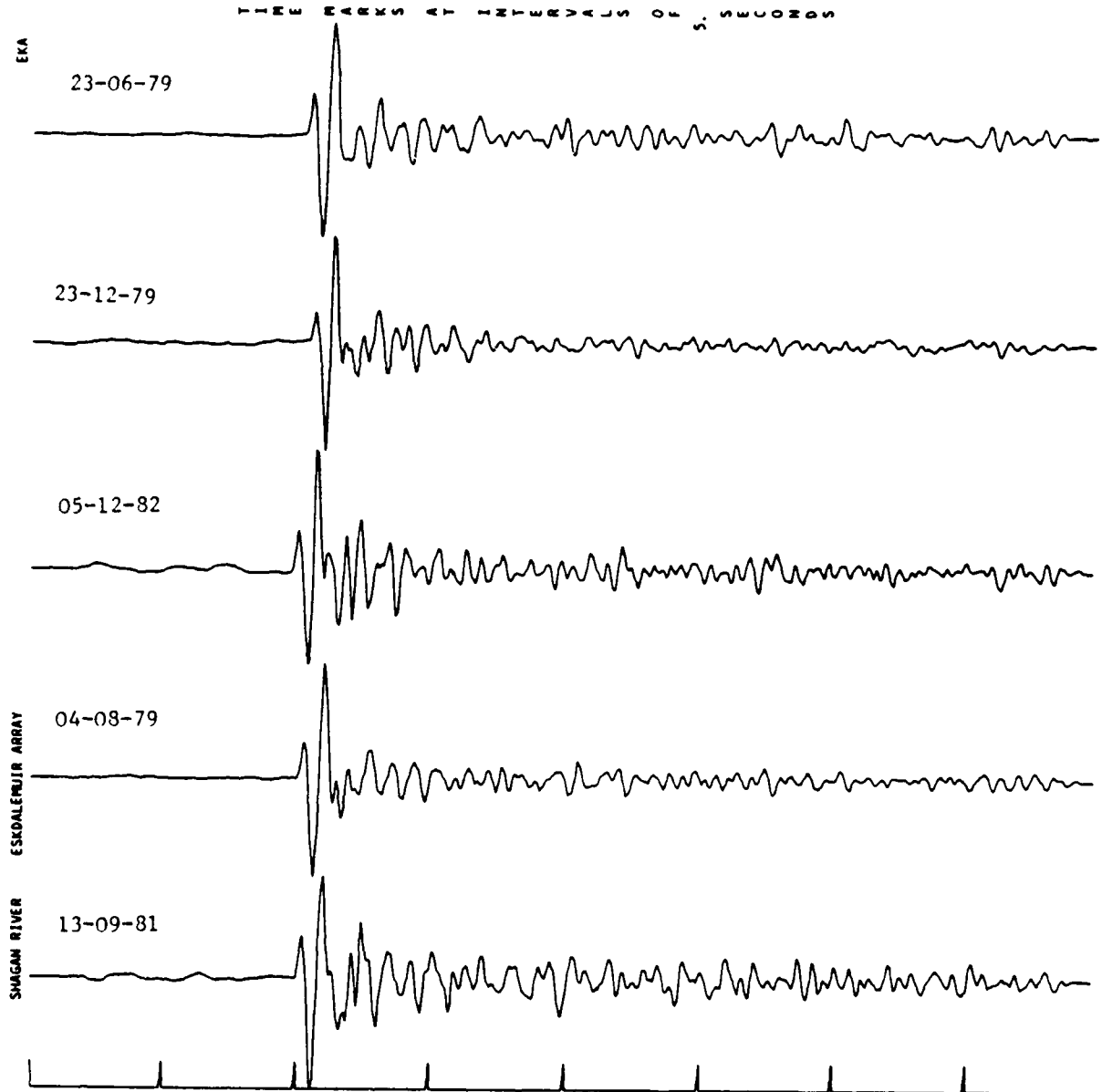
WAVEFORMS FOR SEMIPALATINSK EXPLOSIONS

In Section II, Table 4 , the large Shagan River explosions are listed with an indication of the UK array stations for which good data are available. The same information is given for a large sample of Degelen explosions in Table 3. In this Appendix are shown the waveforms corresponding to these tables. These are beam sum seismograms resulting from delay-and-sum processing of the individual channels, using the slowness derived from the ISC locations and the Jeffreys-Bullen travel time tables. During the processing, channels which have a maximum amplitude larger than 90% of the clipping level are discarded. All data were examined and channels with obvious faults (spikes, dropouts and excessive system noise) were also discarded.

The beam sum displayed here was computed from essentially the same channels used to compute the spectra discussed in Sections IV and VI for EKA, GBA and YKA. Occasionally there are faults (small spikes) that only become apparent when the high frequency spectra are examined, but fewer than 5% of the data were discarded for this reason. However, the small spike problem is much more severe at WRA, and 30-50% of the channels used to compute the WRA beam sum seismograms displayed here were discarded in computing the final spectra.

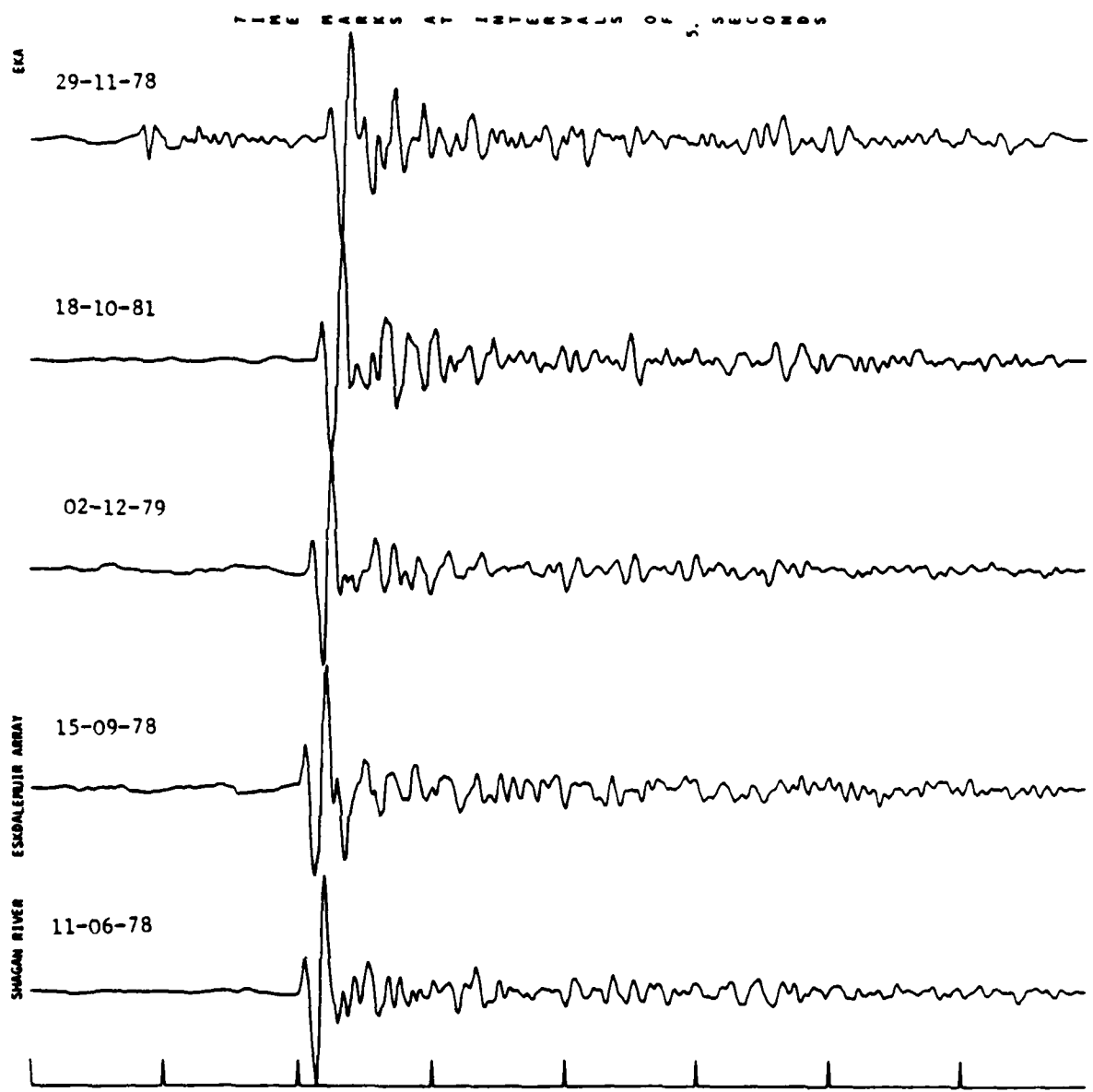
The seismograms are divided into three classes: SW Shagan River, NE Shagan River and Degelen. The reasons for the bisection of the Shagan River site are given in Section III.

PRECEDING PAGE BLANK-NOT FILMED

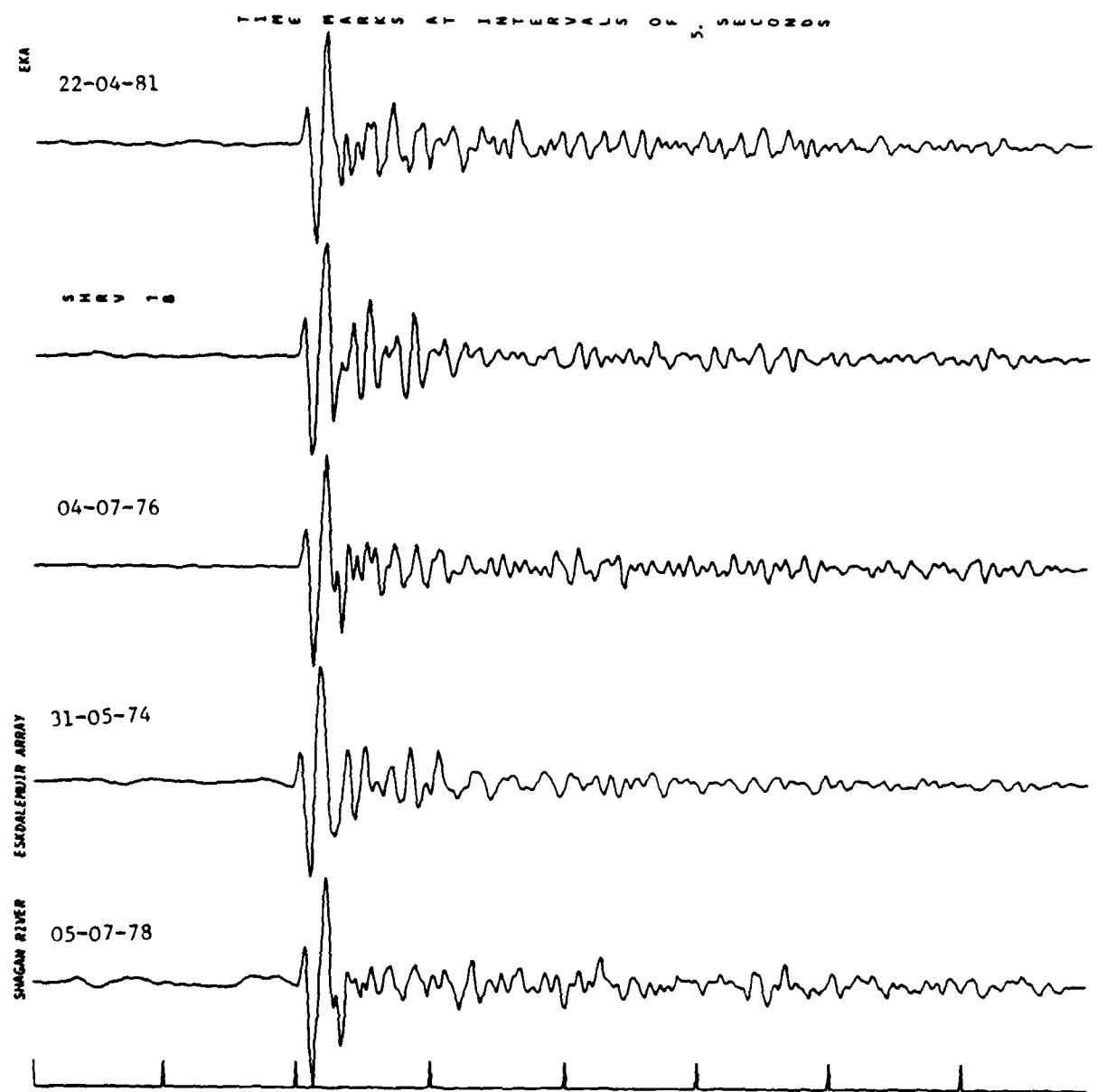


PRECEDING PAGE BLANK-NOT FILMED

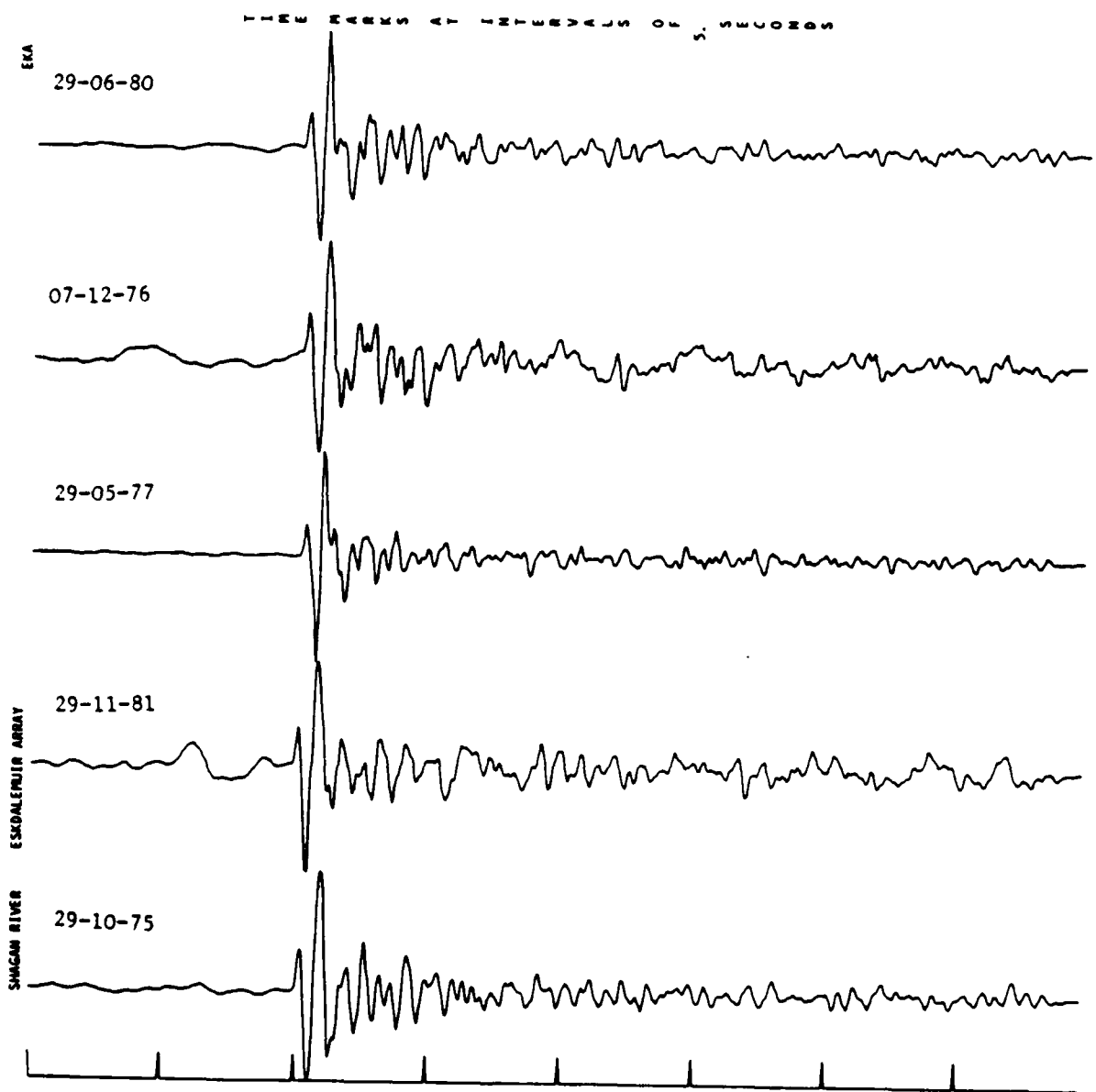
EKA Southwest Shagan River



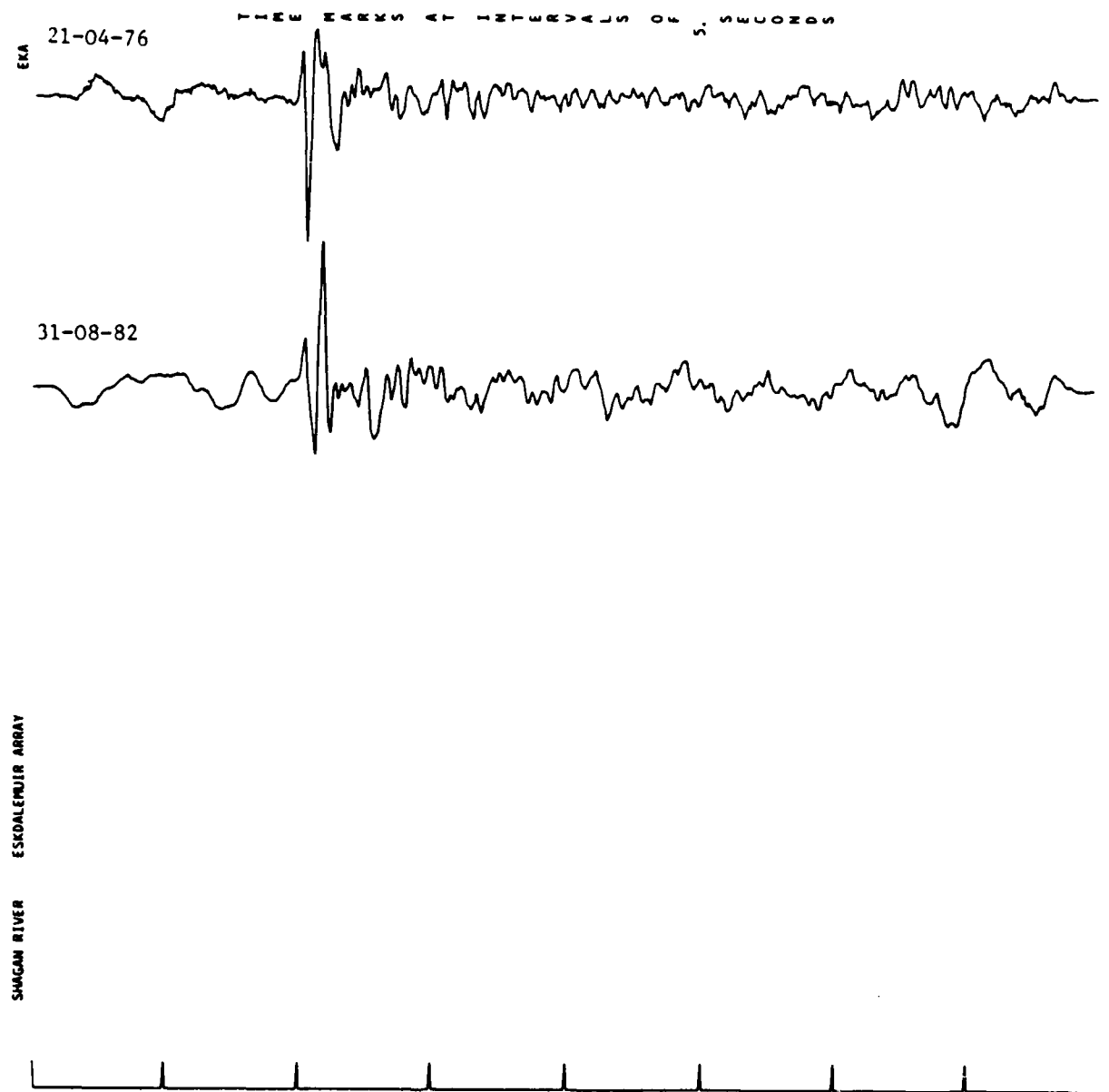
EKA Southwest Shagan River



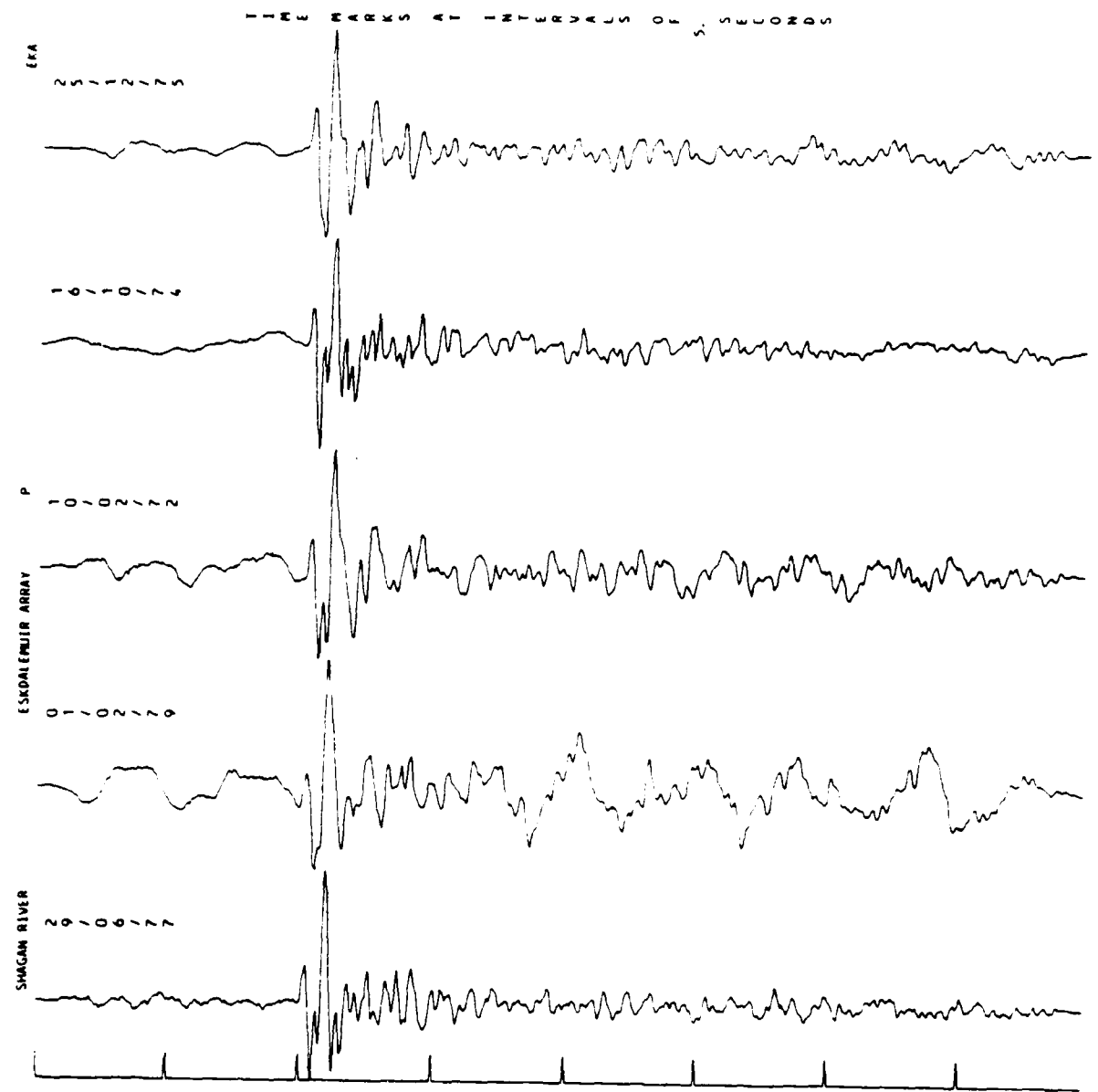
EKA Southwest Shagan River



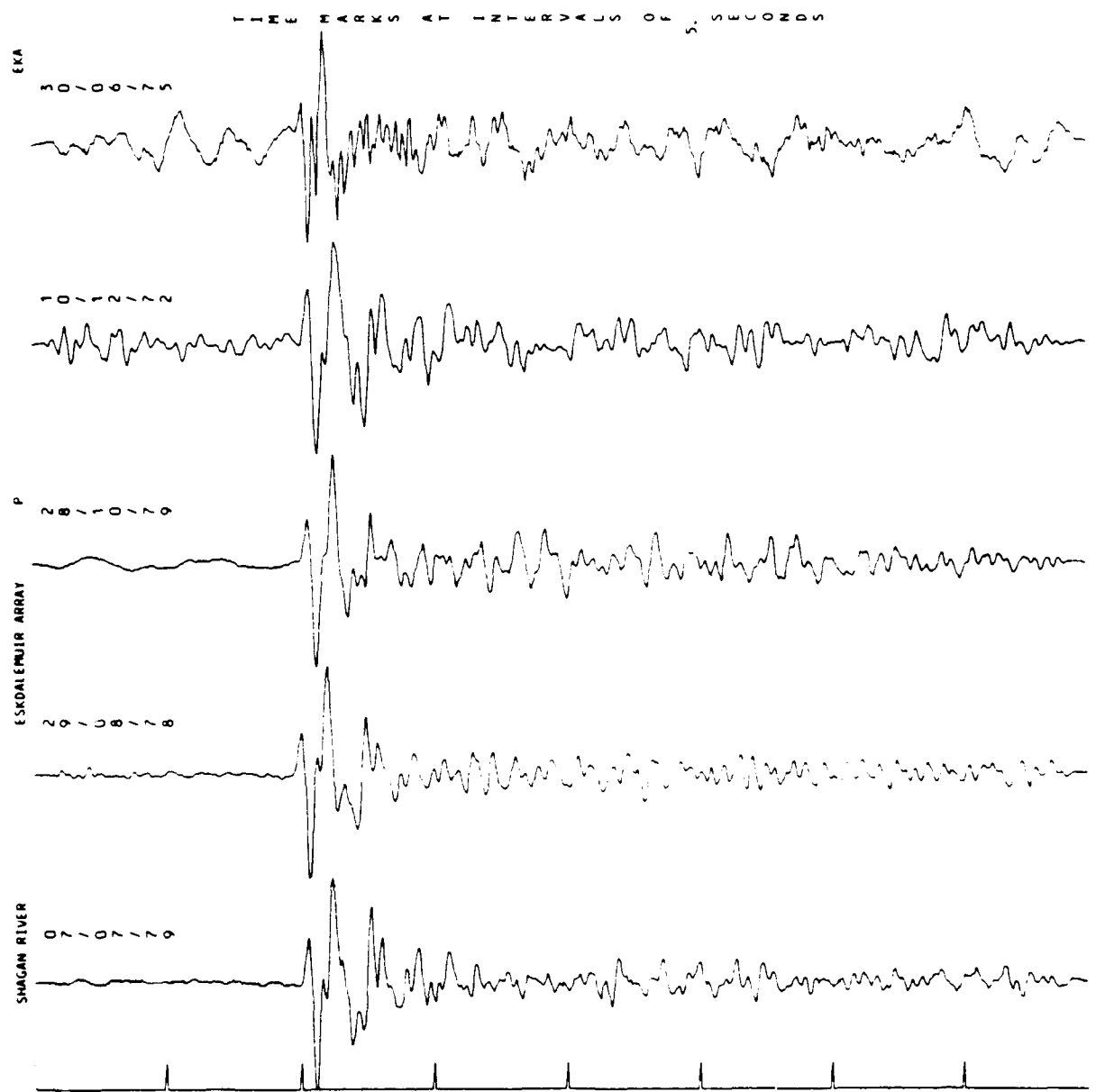
EKA Southwest Shagan River



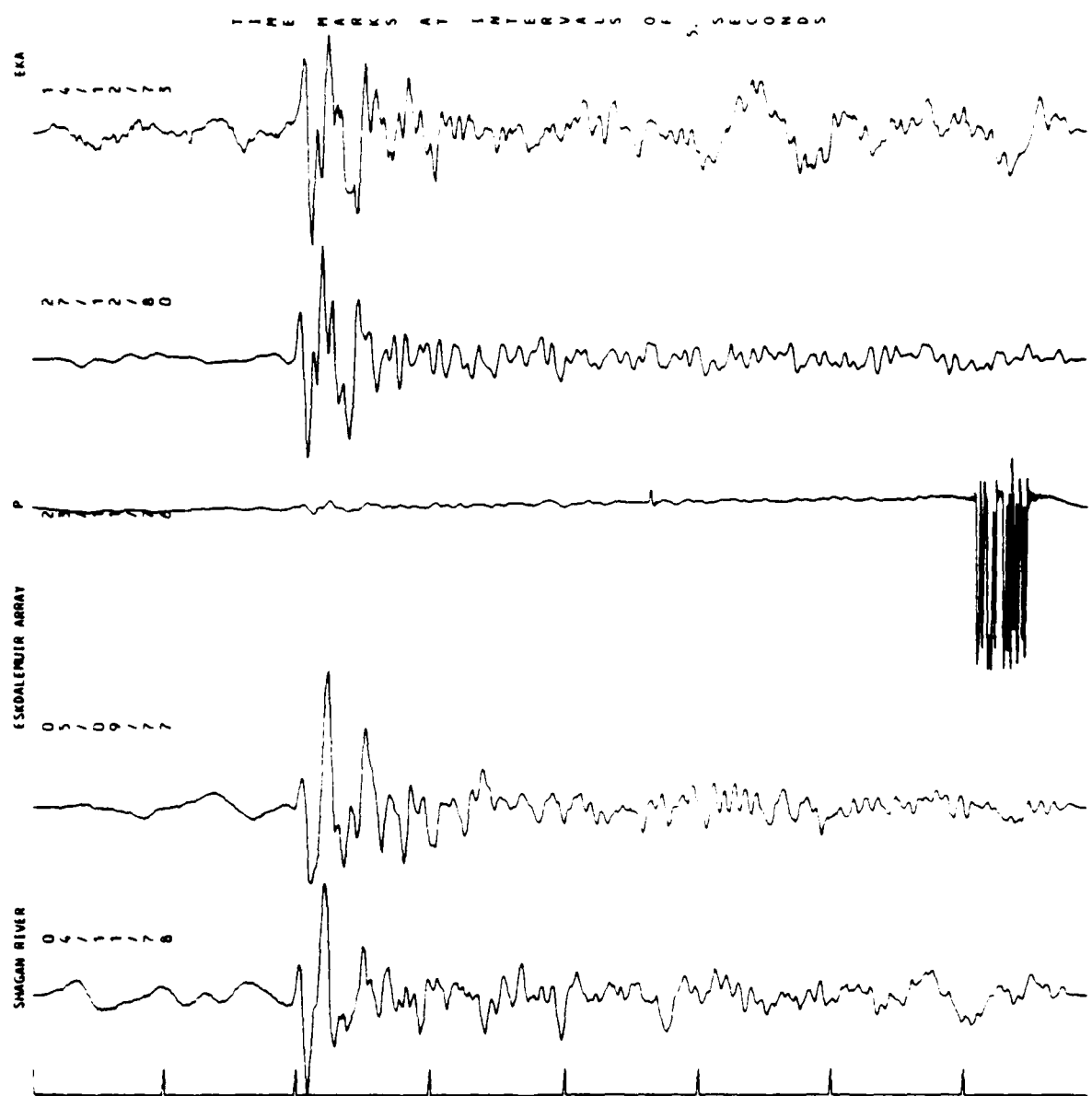
EKA Southwest Shagan River



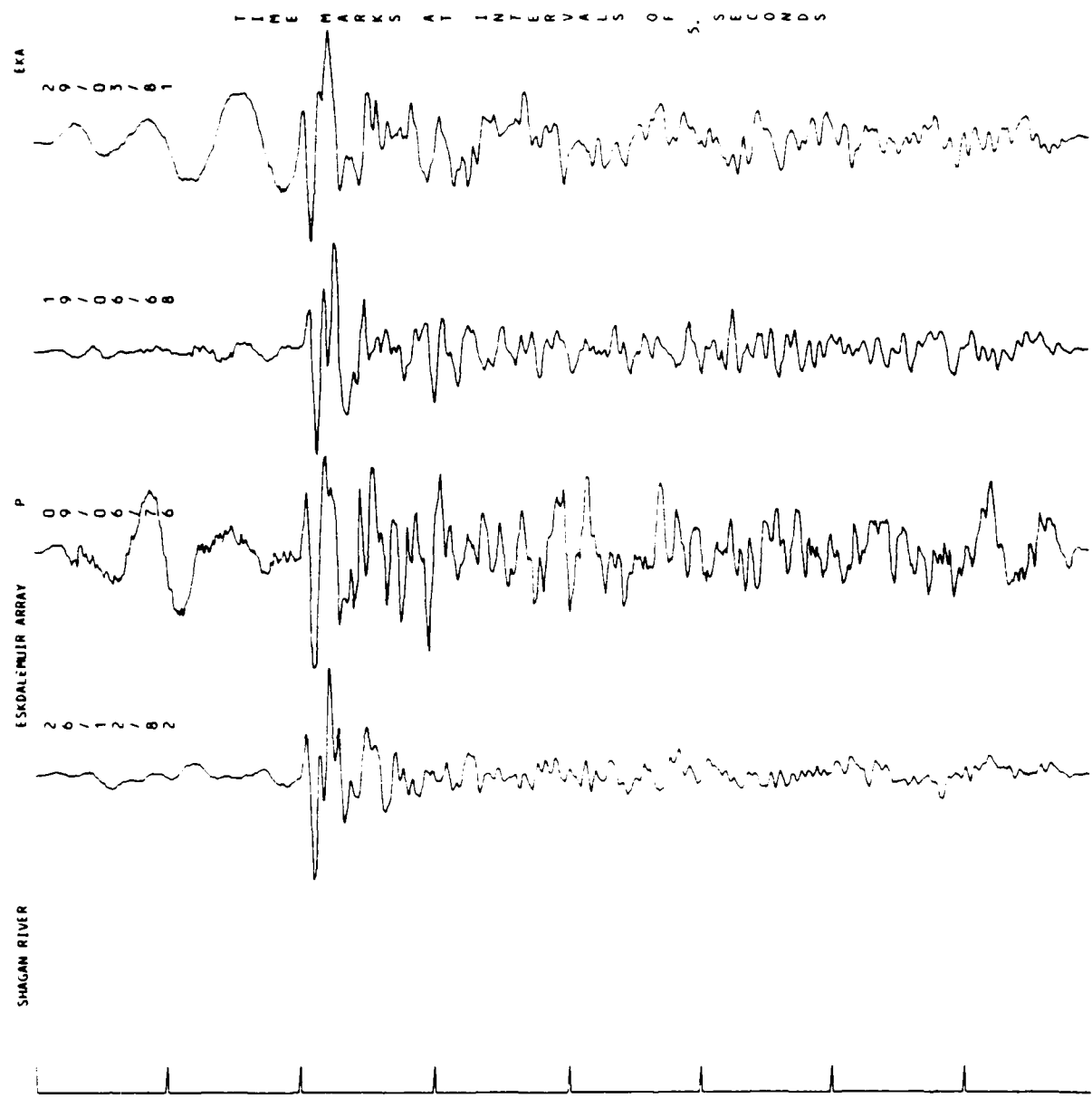
EKA Northeast Shagan River



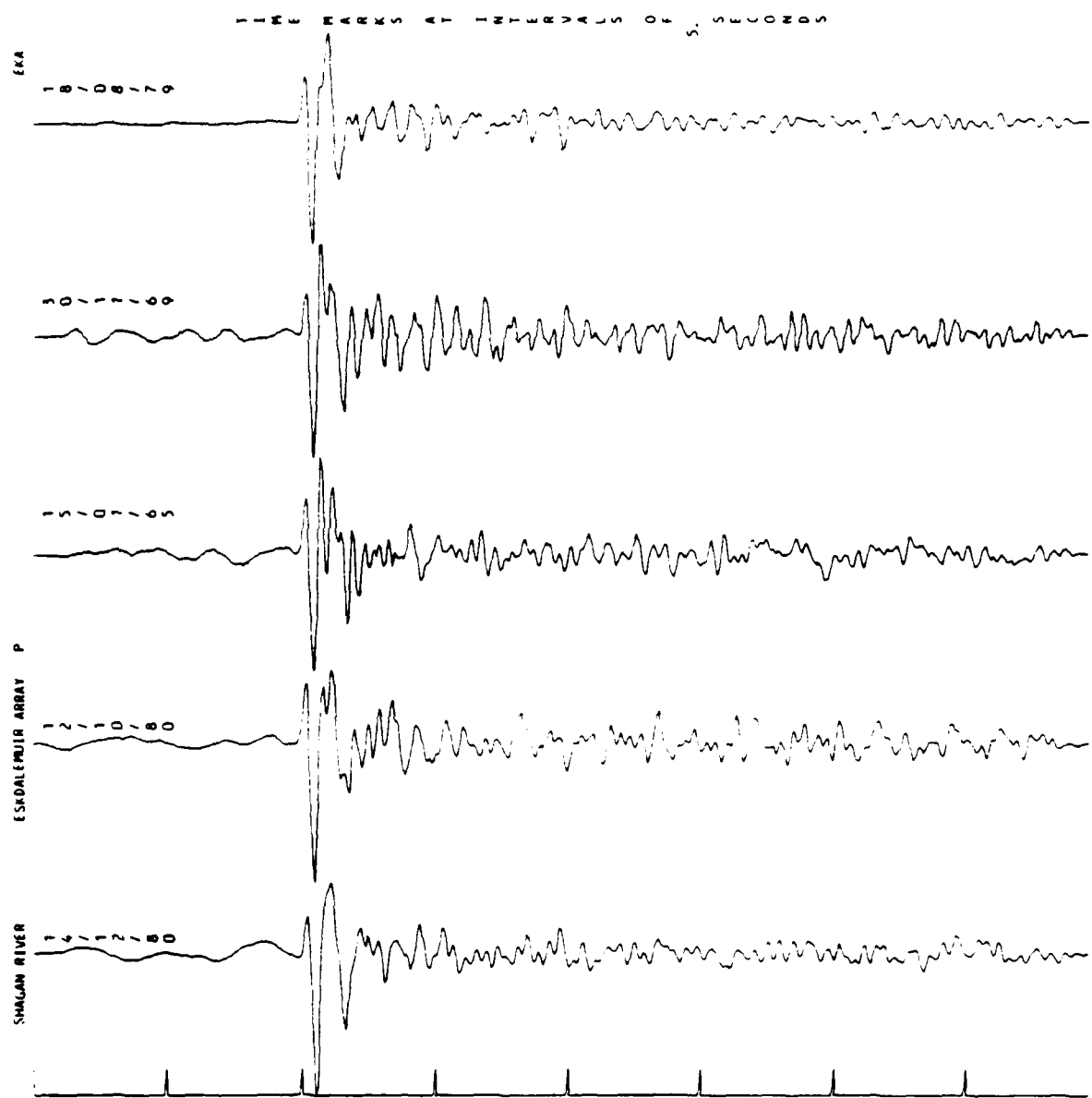
EKA Northeast Shagan River



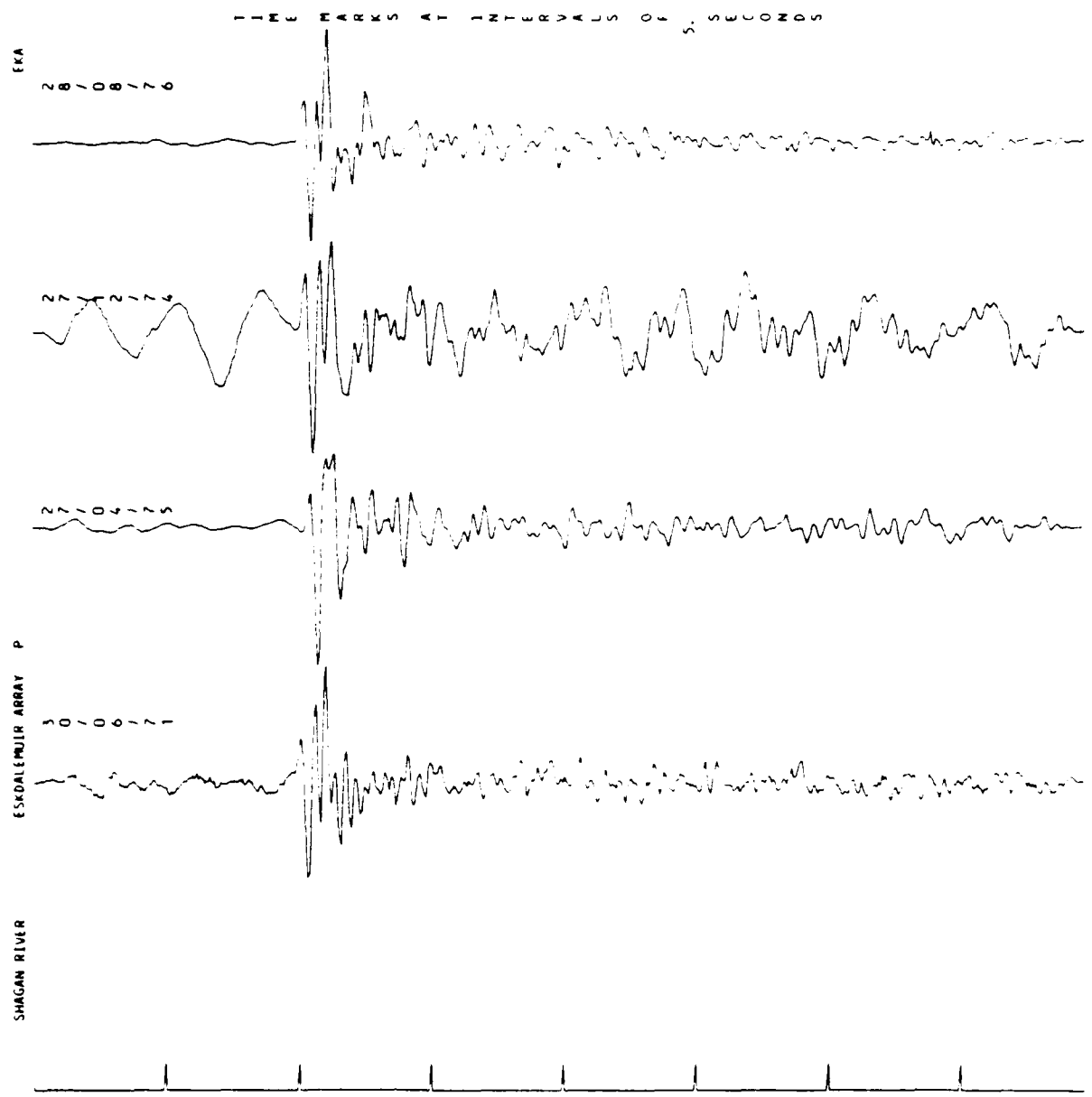
EKA Northeast Shagan River

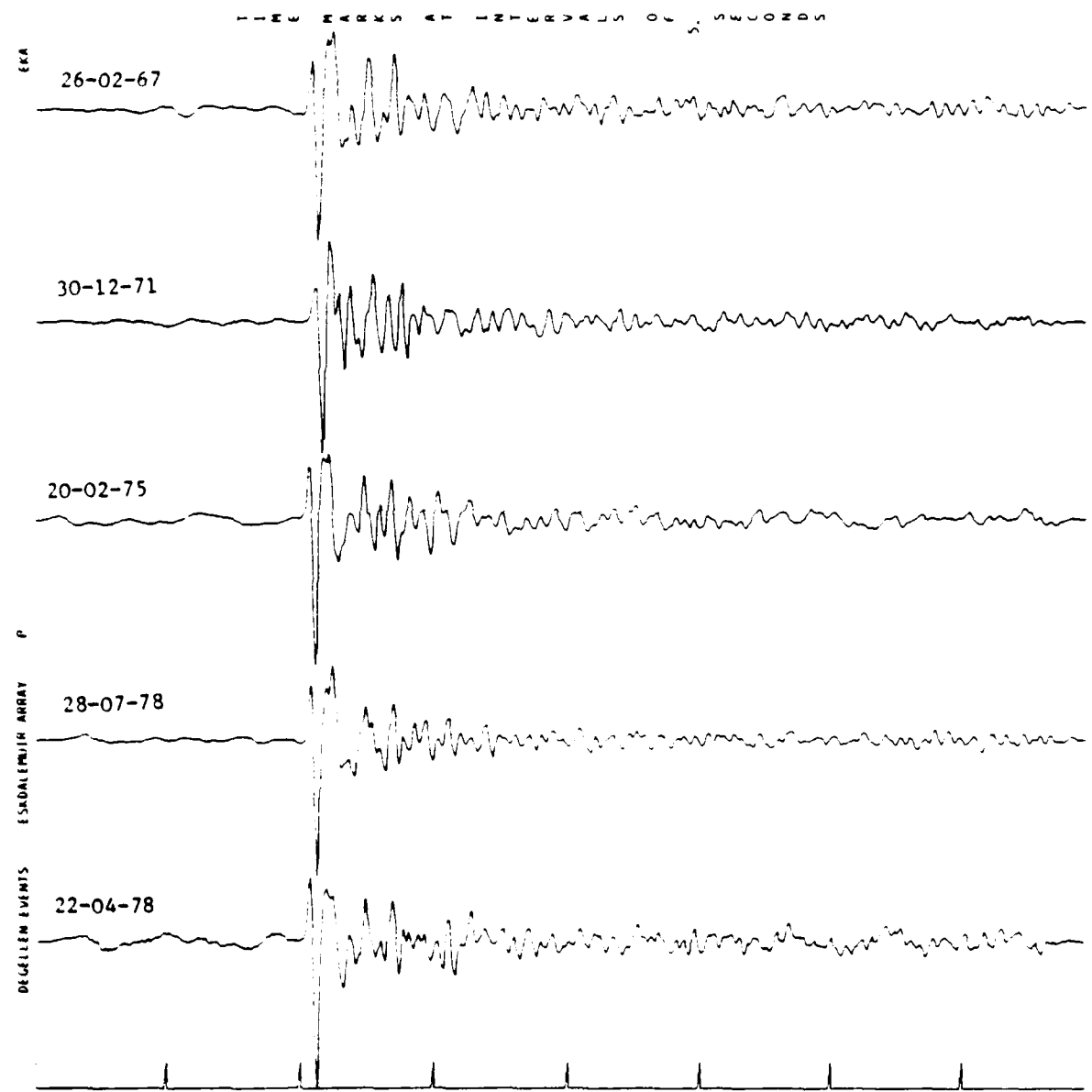


EKA Northeast Shagan River

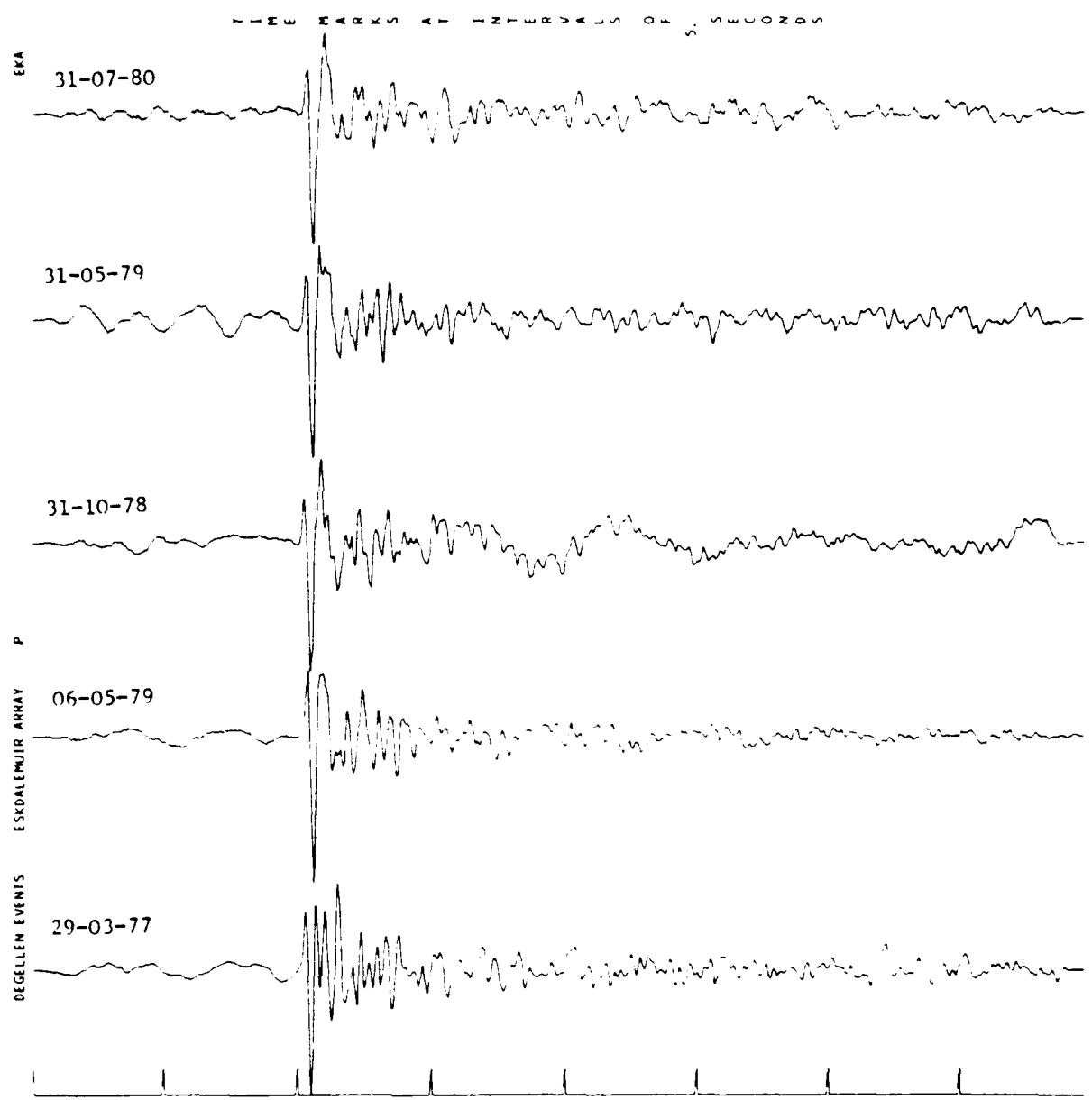


EKA Northeast Shagan River

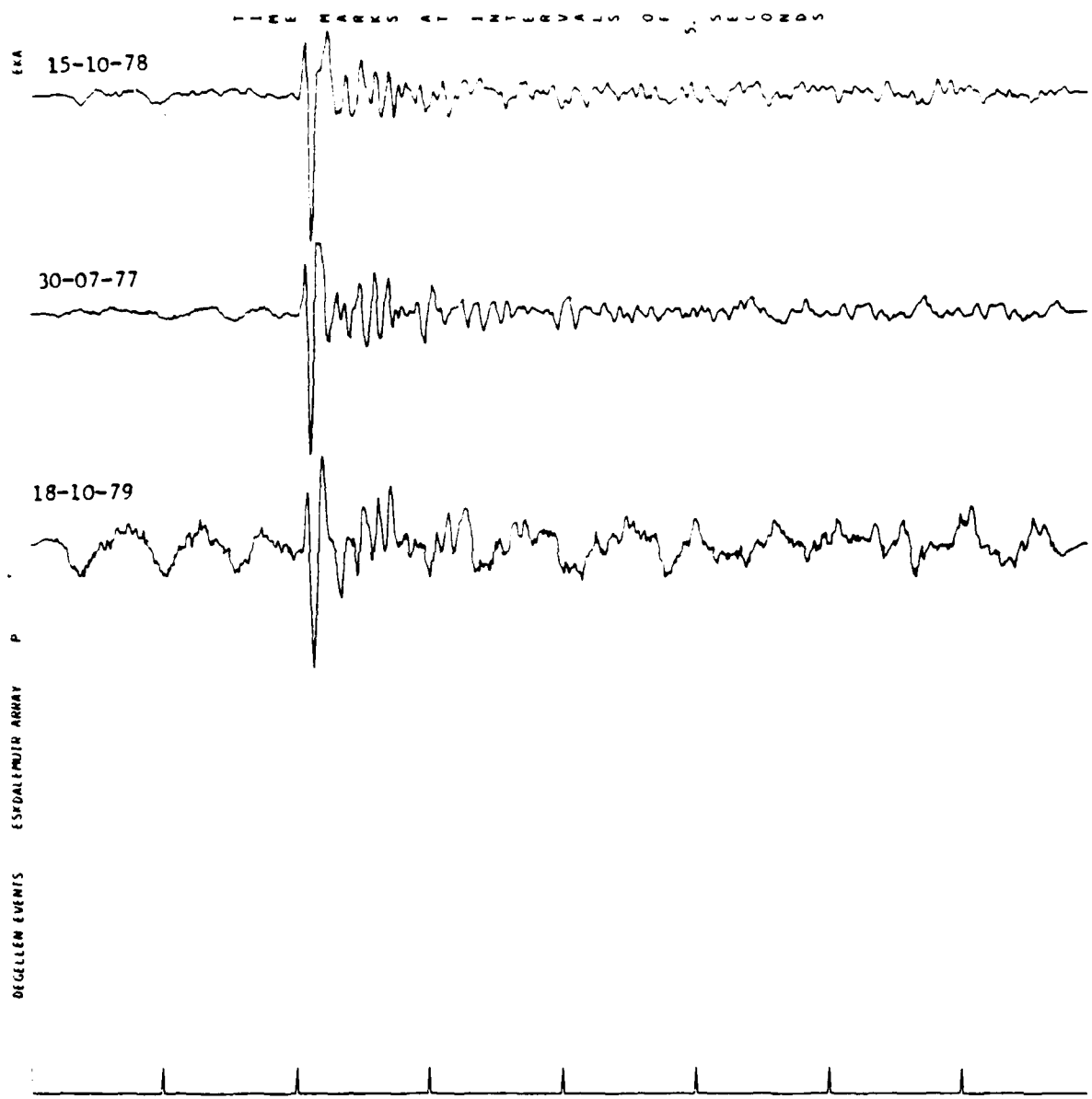




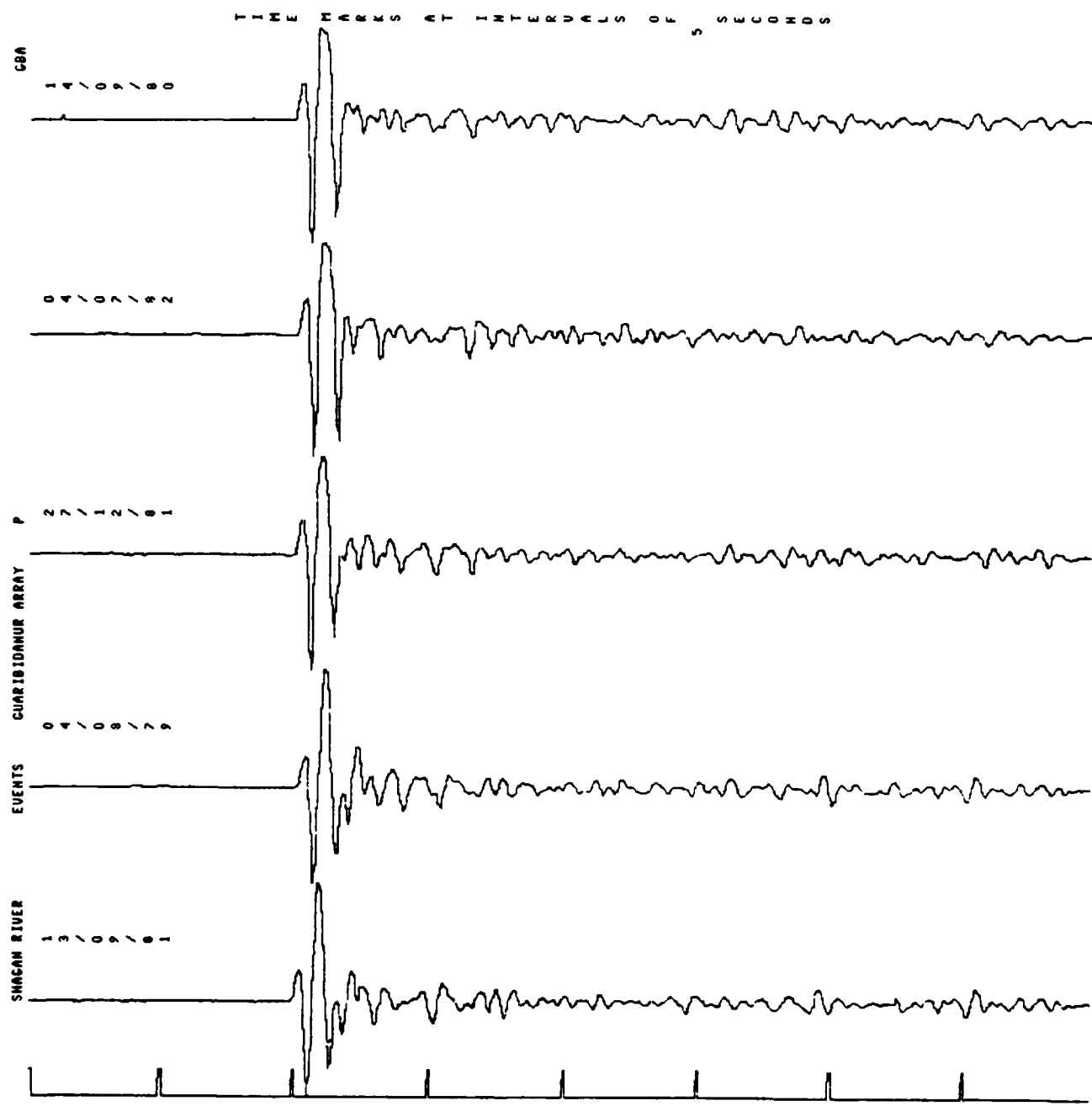
EKA Degelen



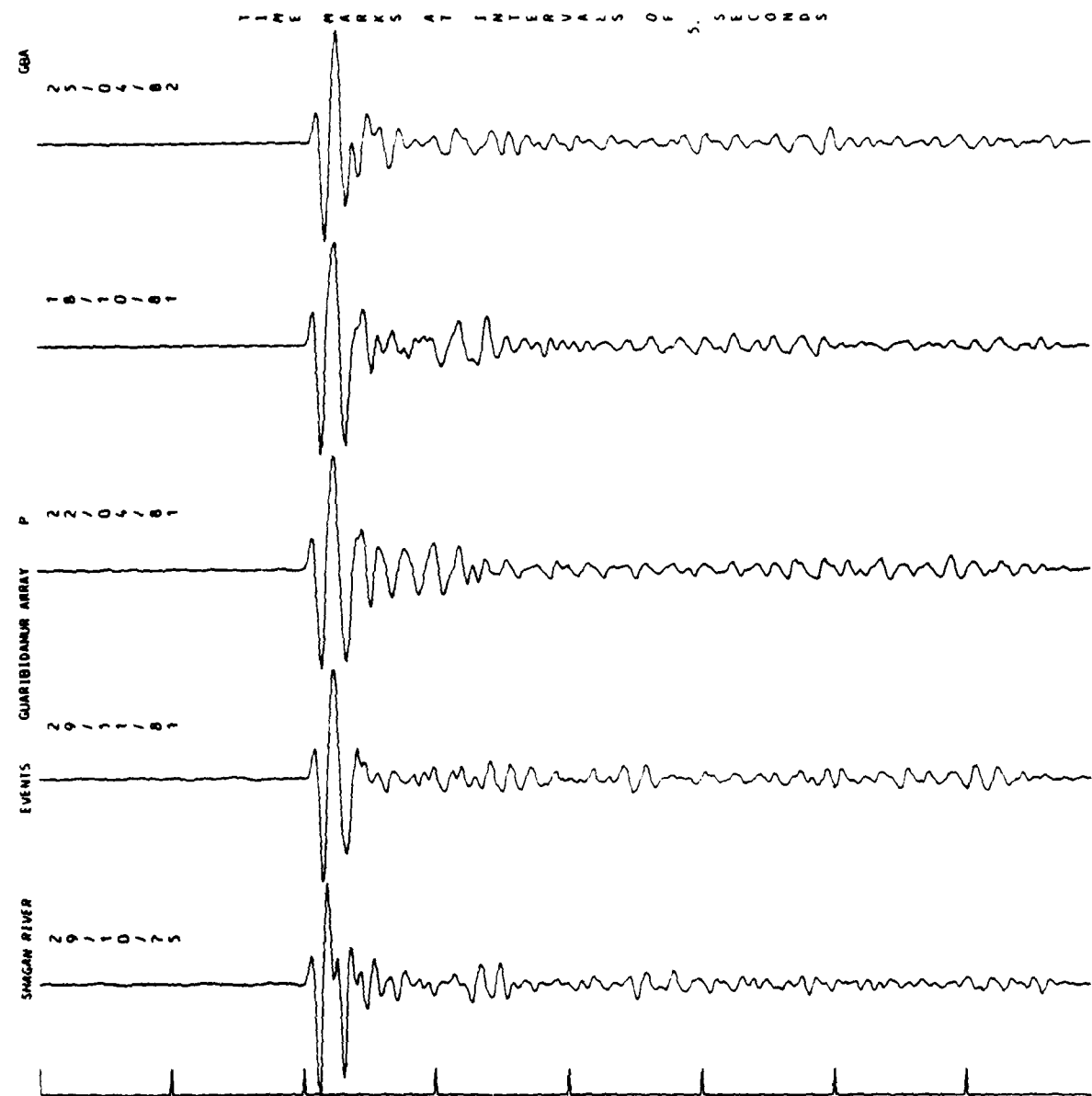
EKA Degelen



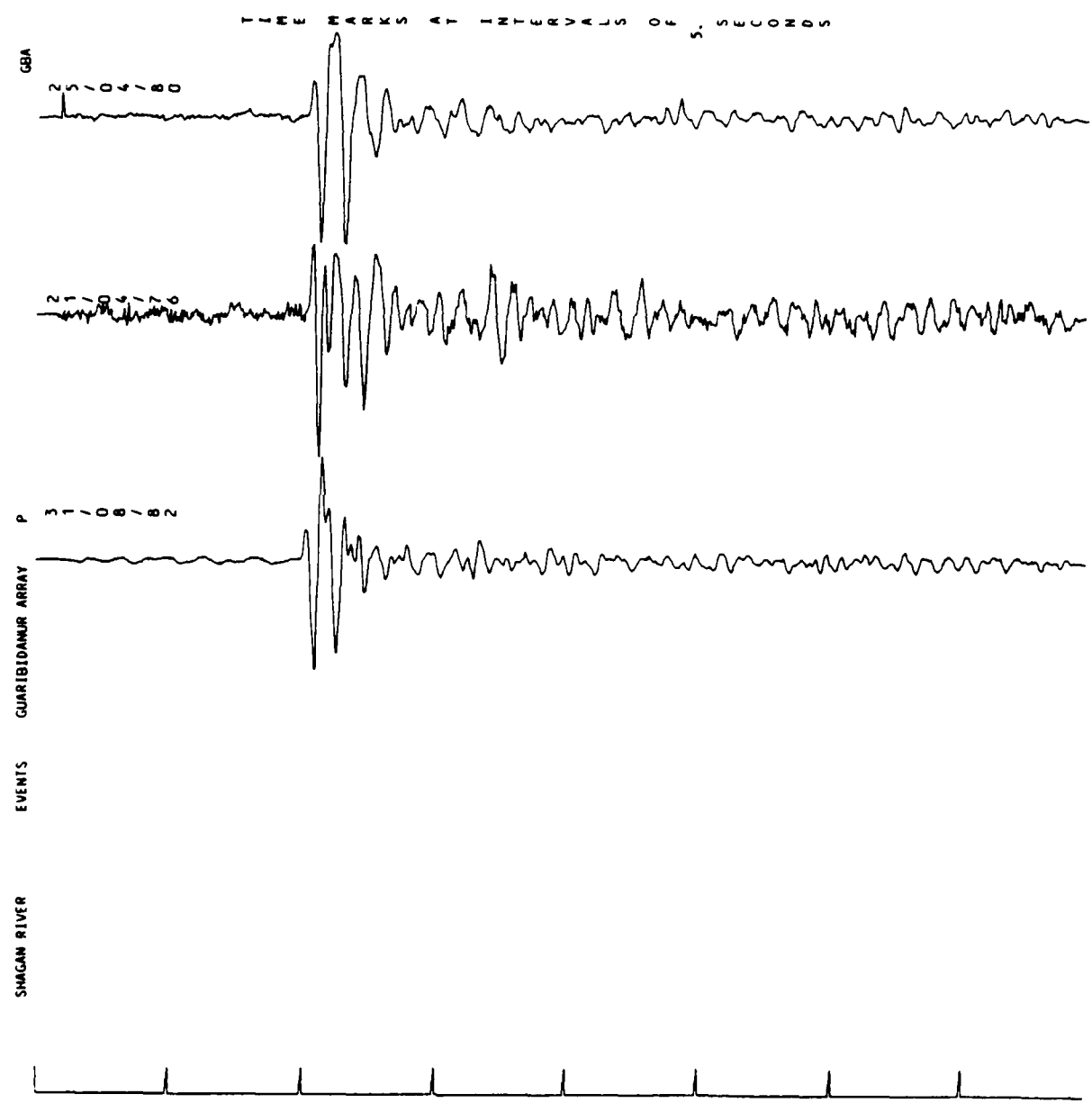
EKA Degelen



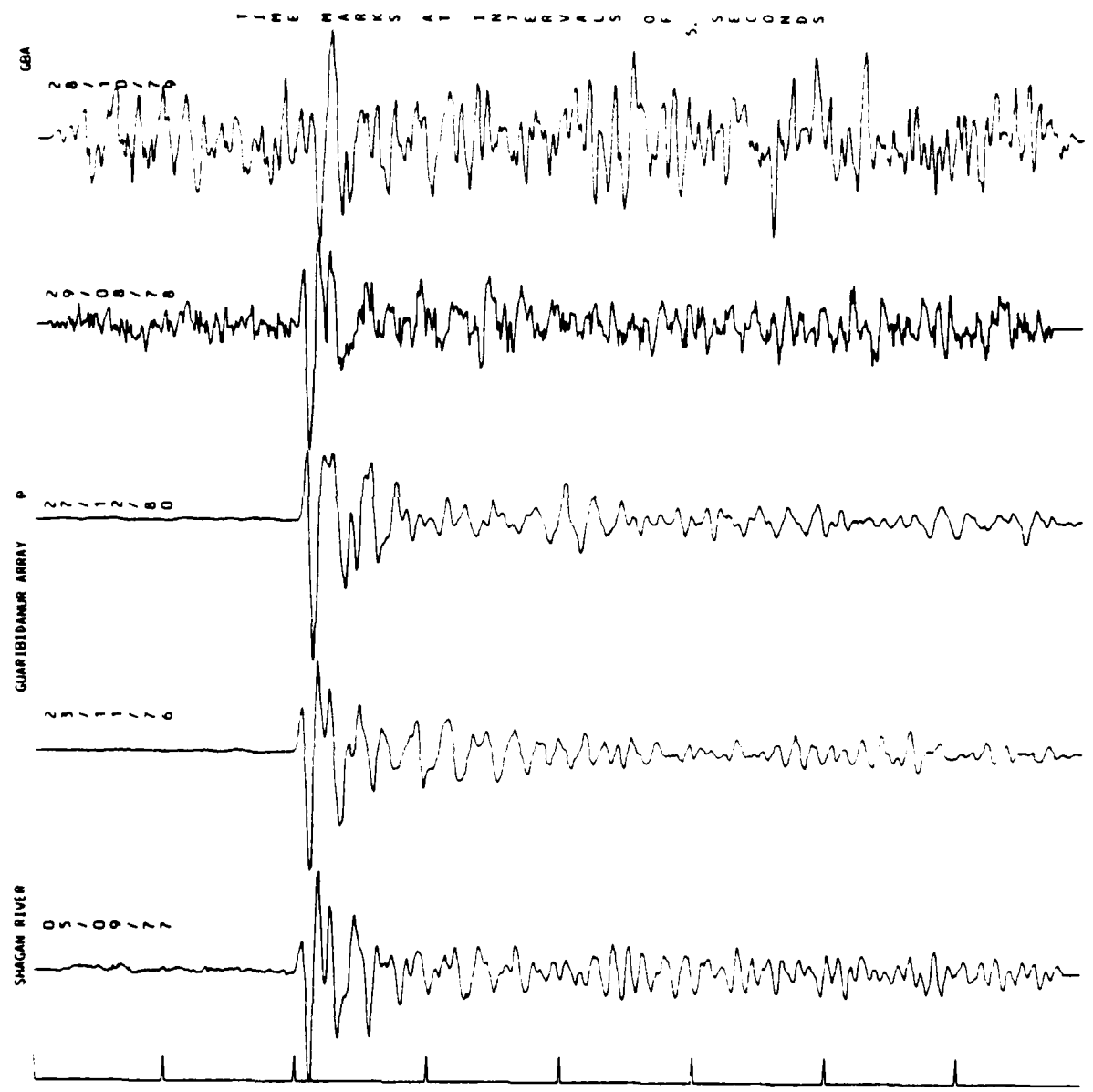
GBA Southwest Shagan River



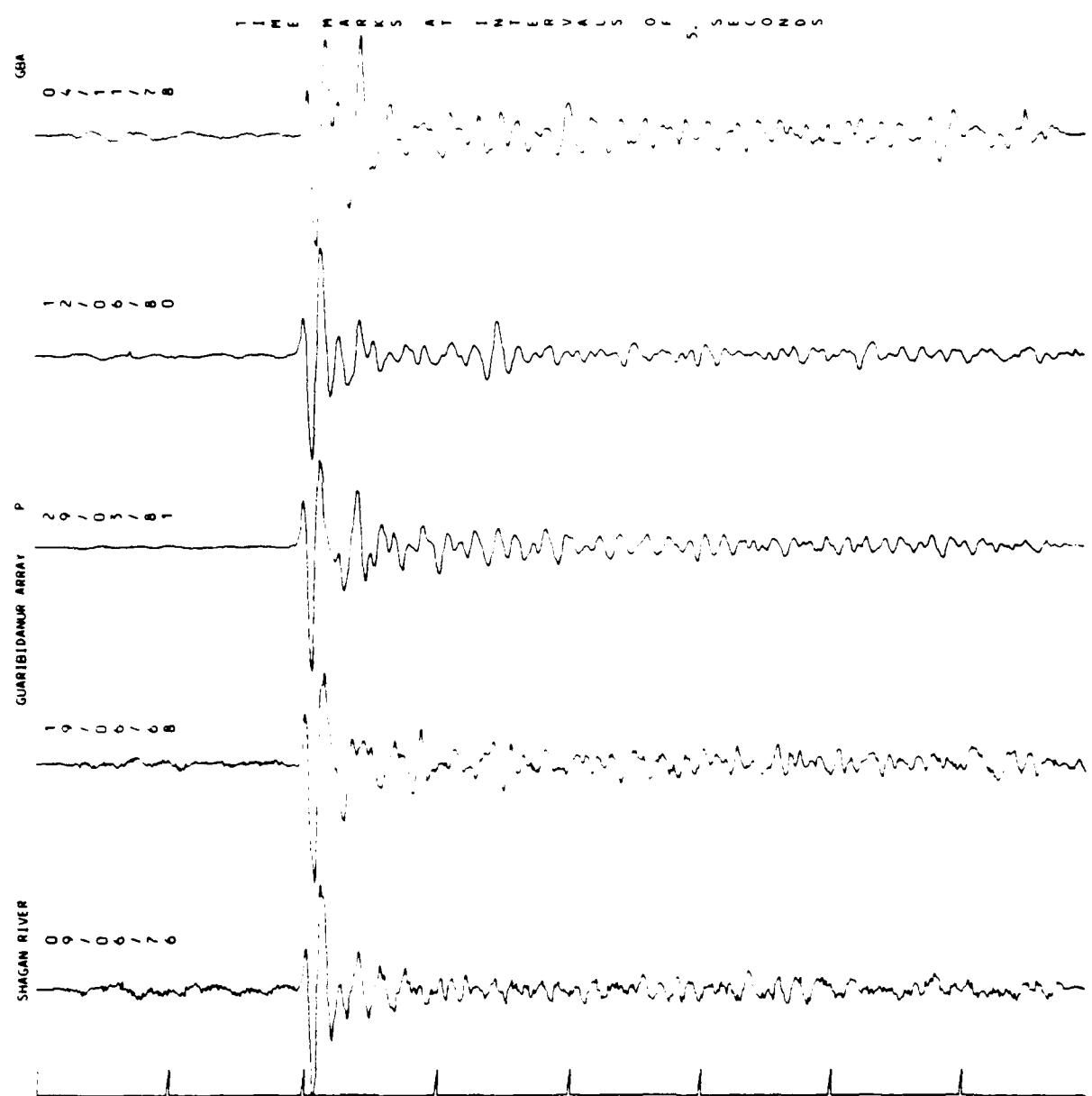
GBA Southwest Shagan River



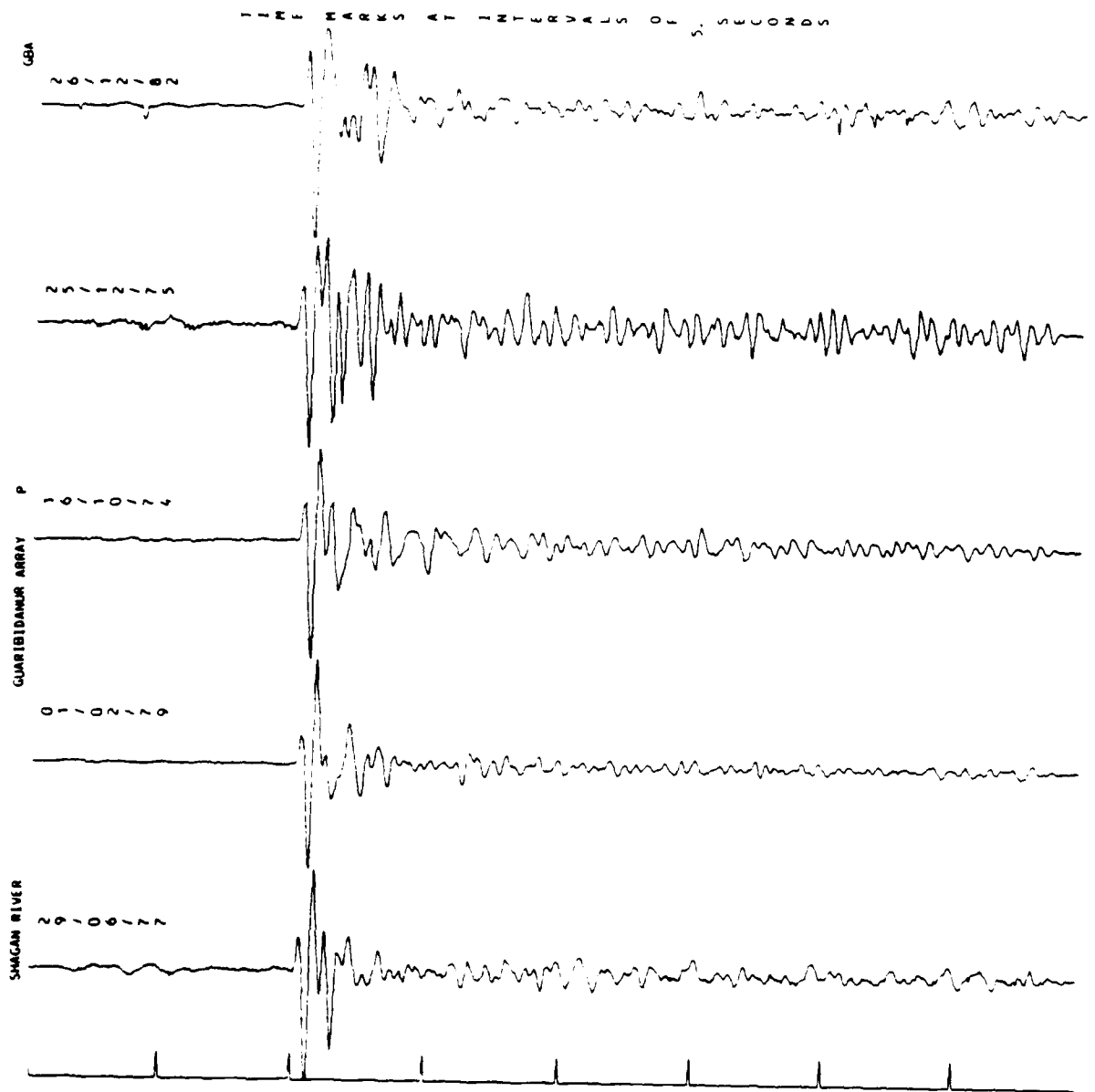
GBA Southwest Shagan River



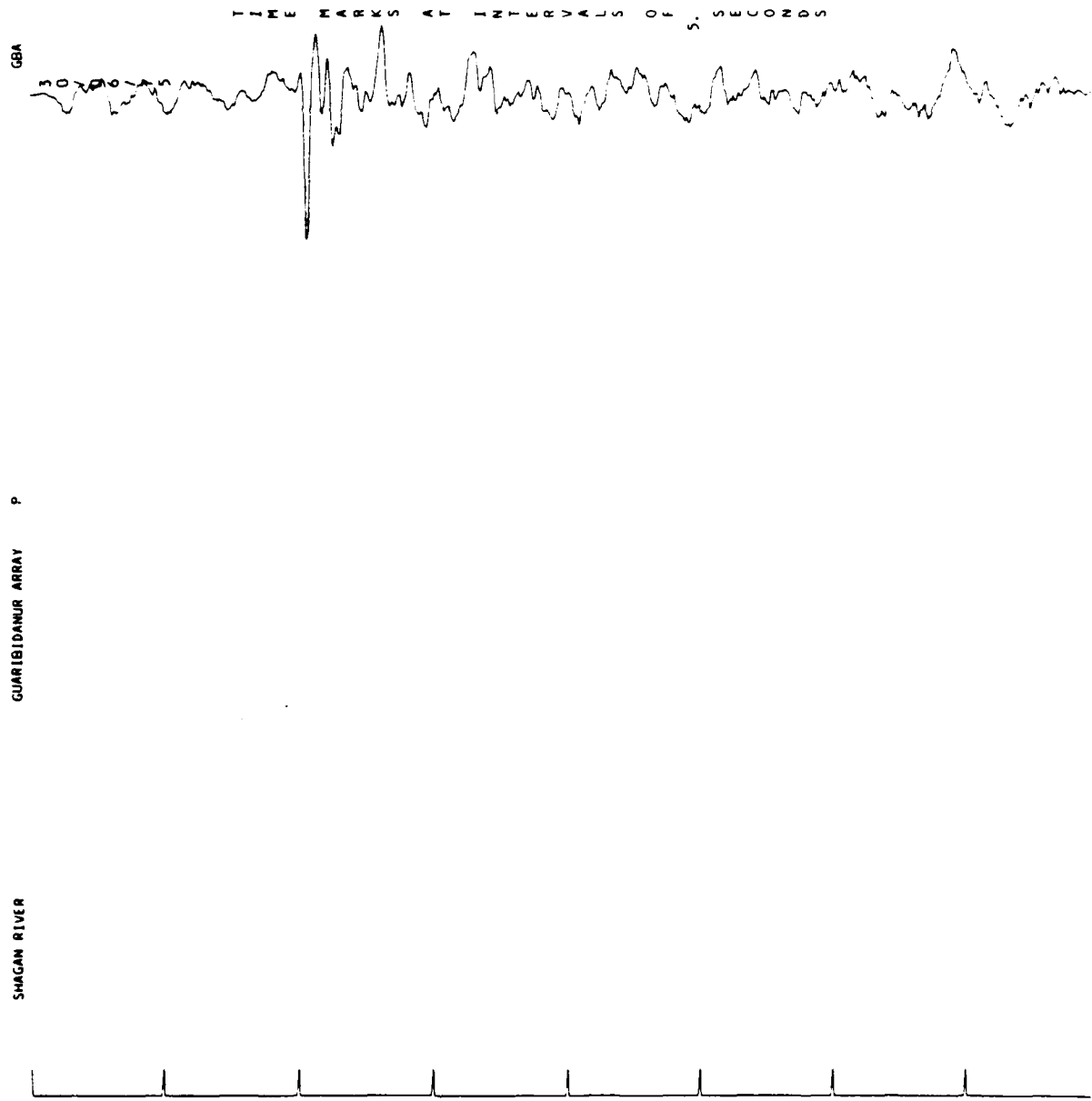
GBA Northeast Shagan River



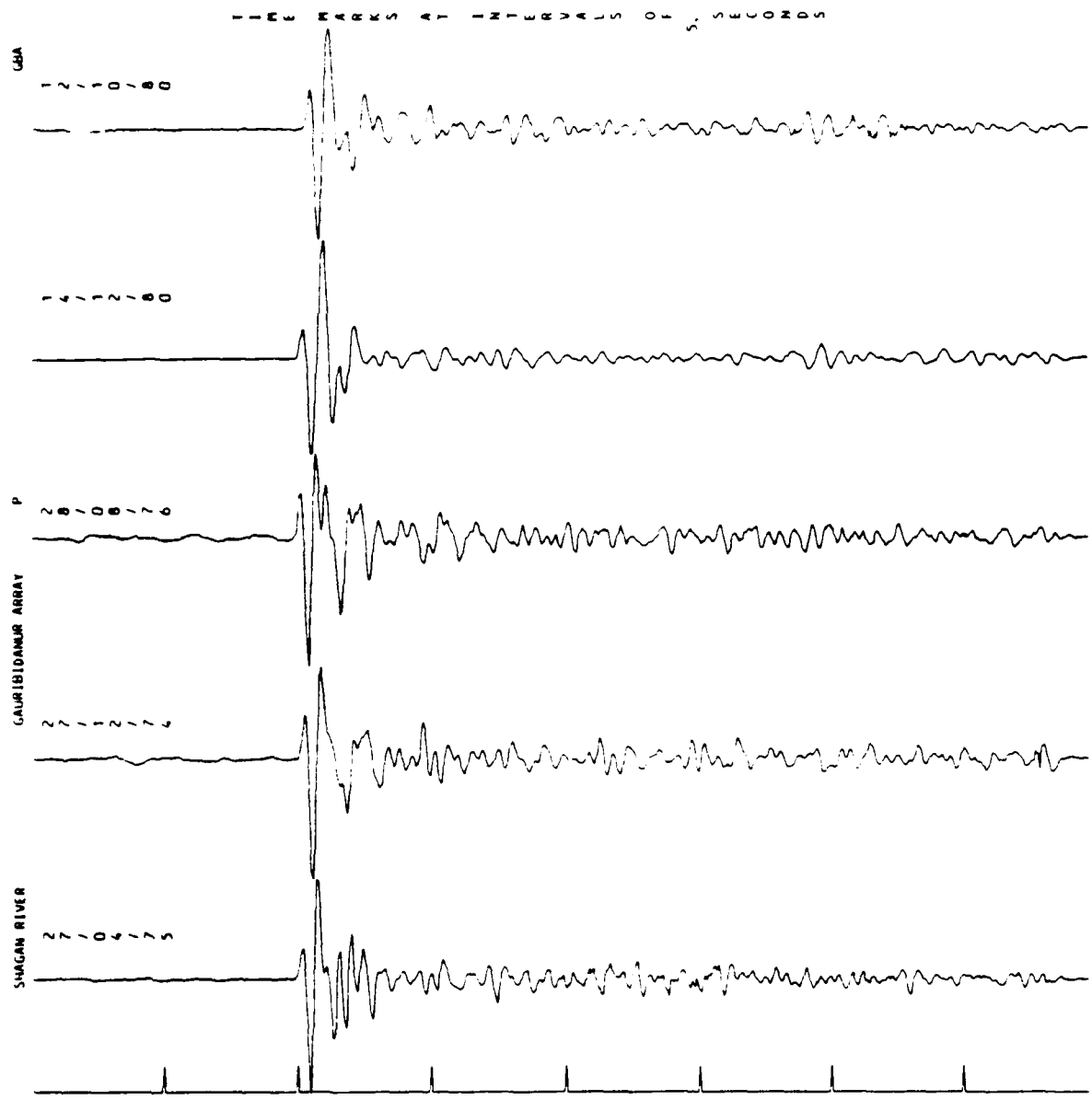
GBA Northeast Shagan River



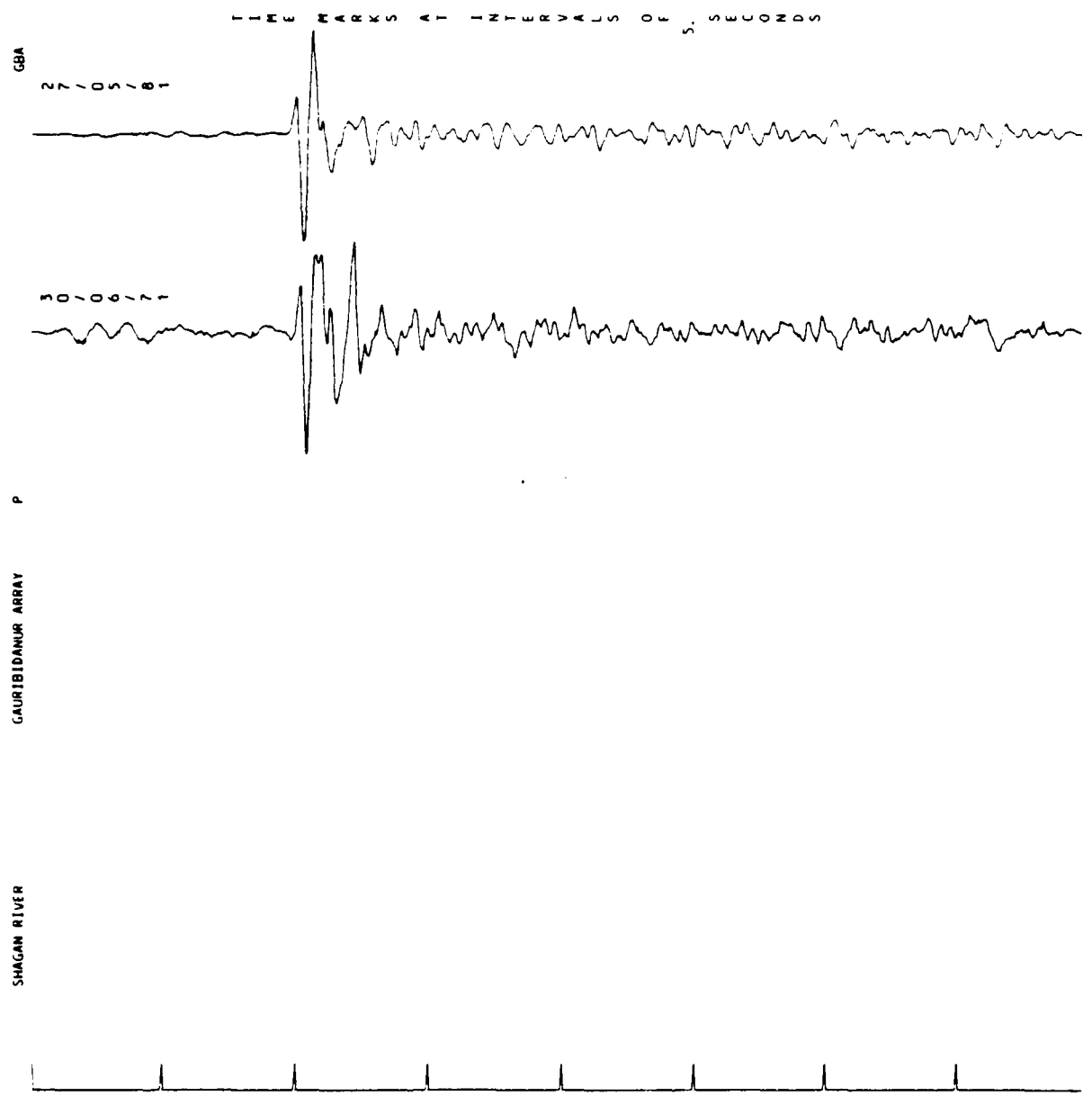
CBA Northeast Shagan River

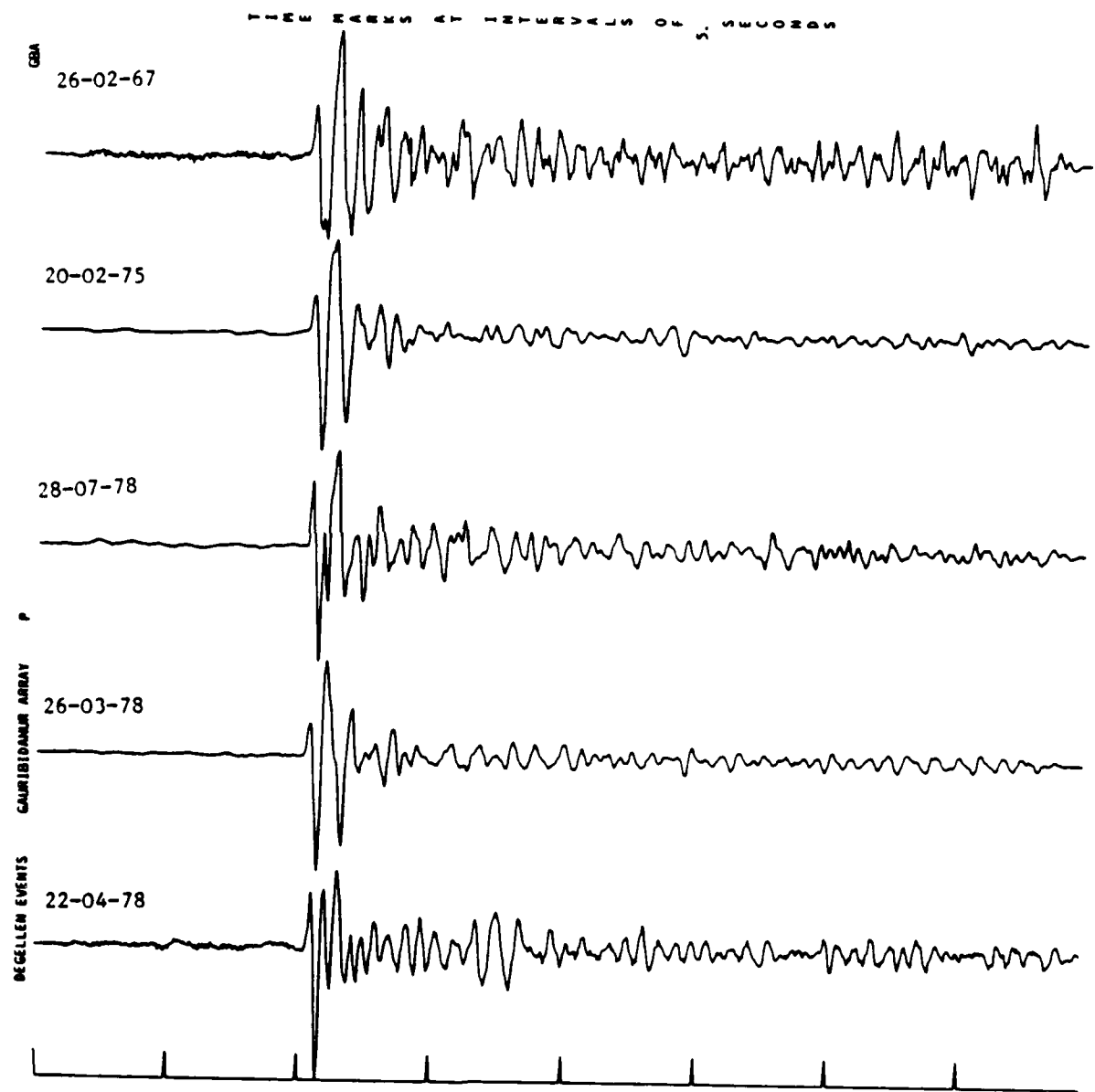


GBA Northeast Shagan River

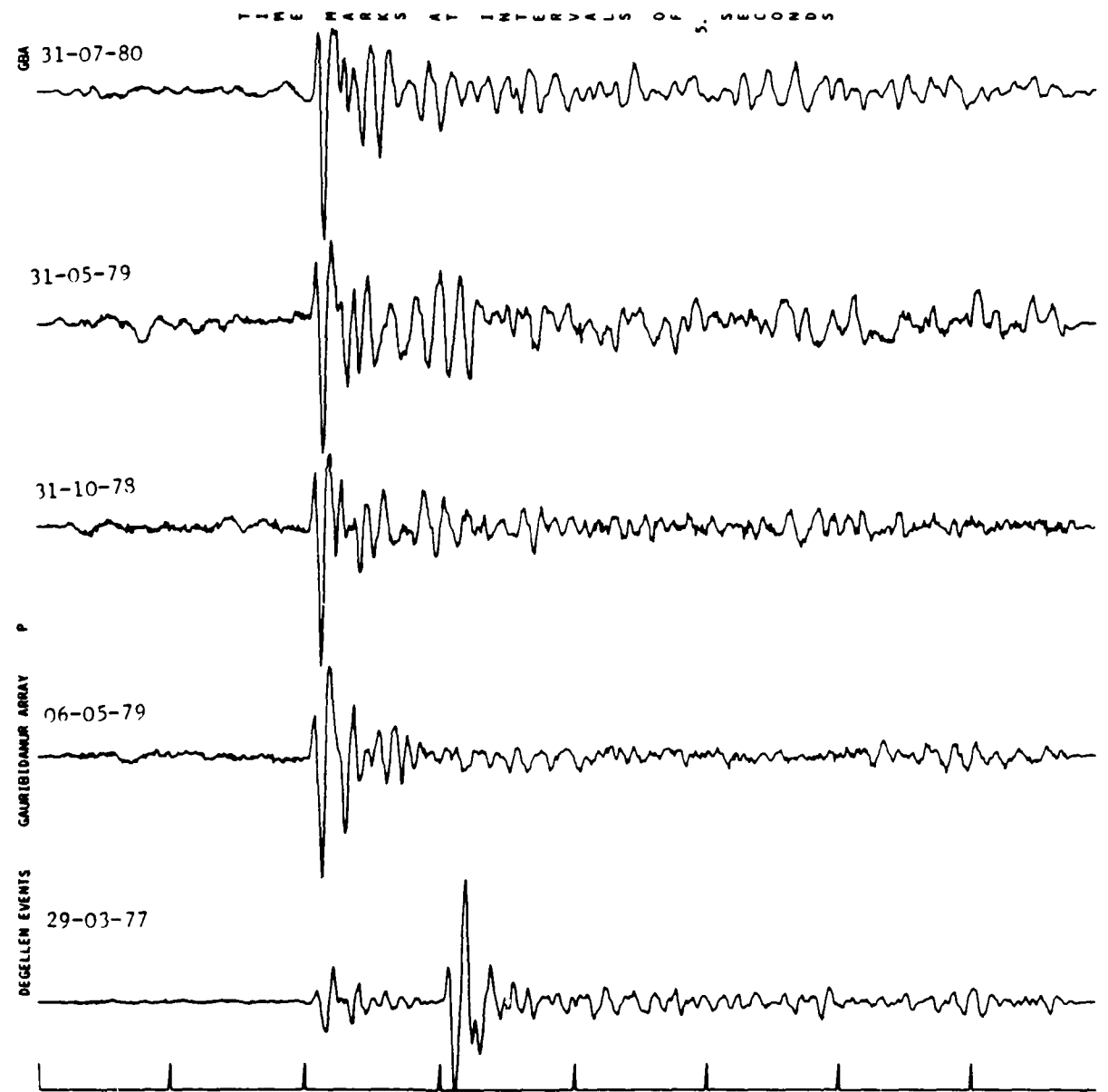


GBA Northeast Shagan River

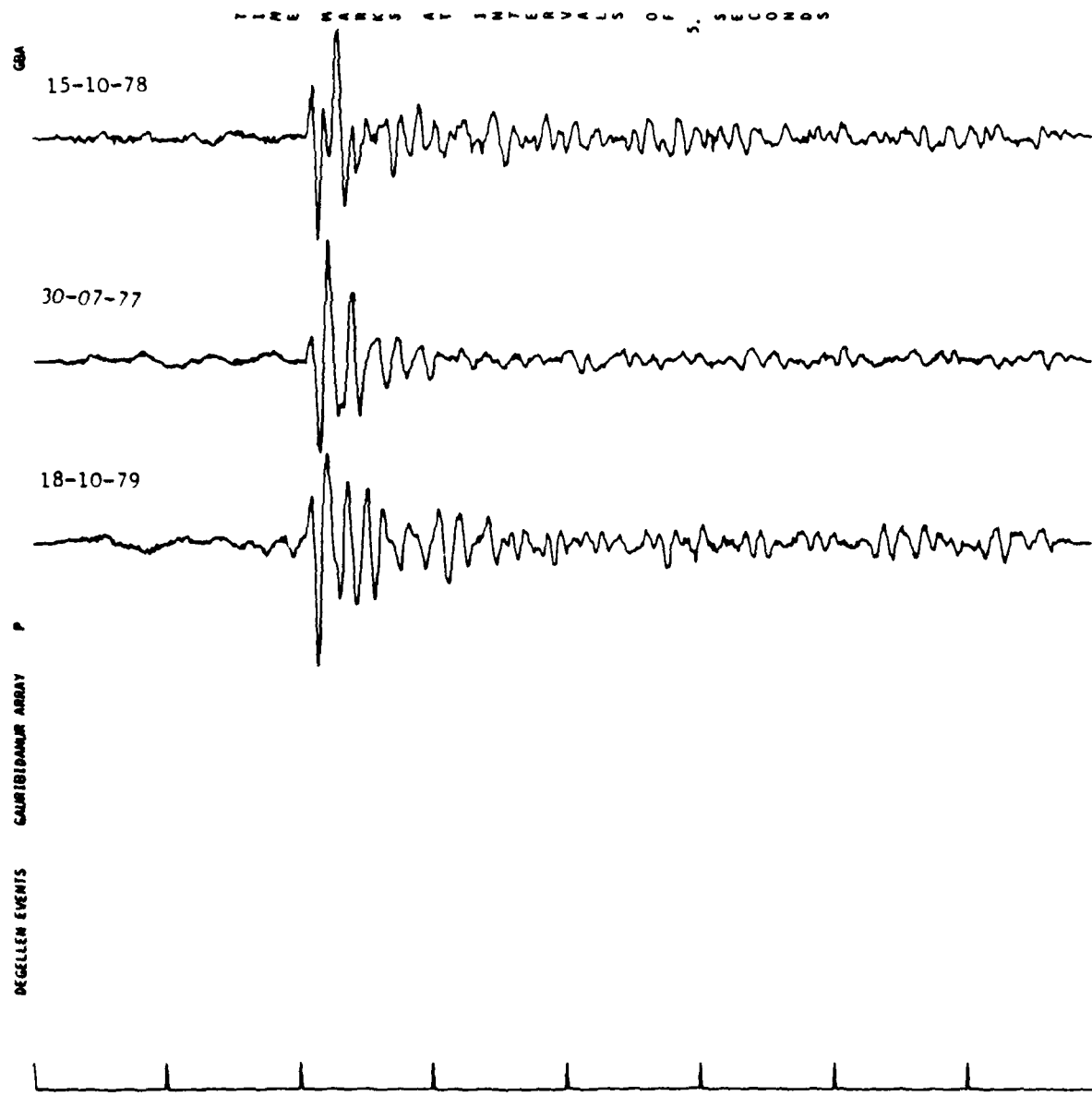




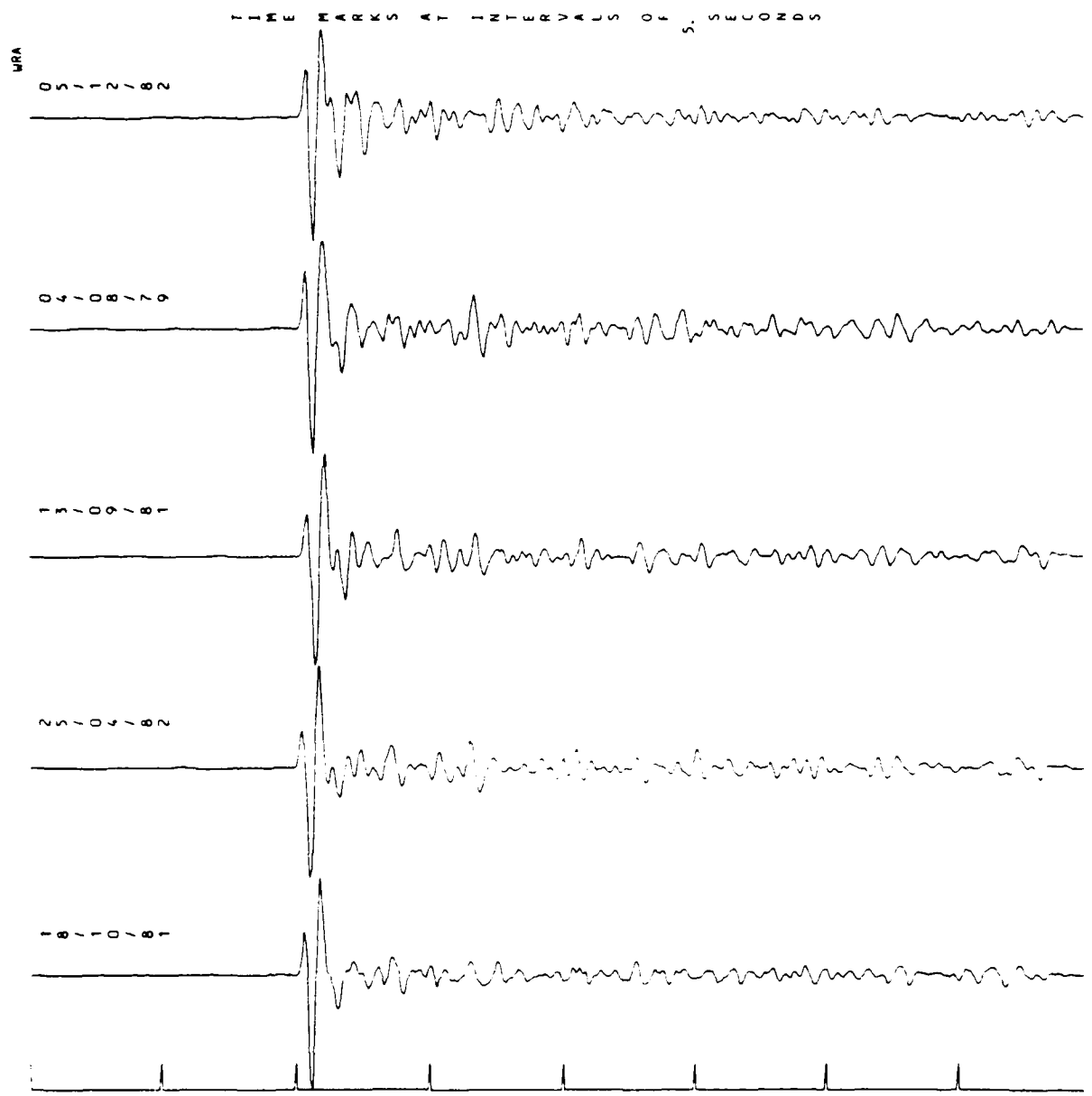
GBA Degelen



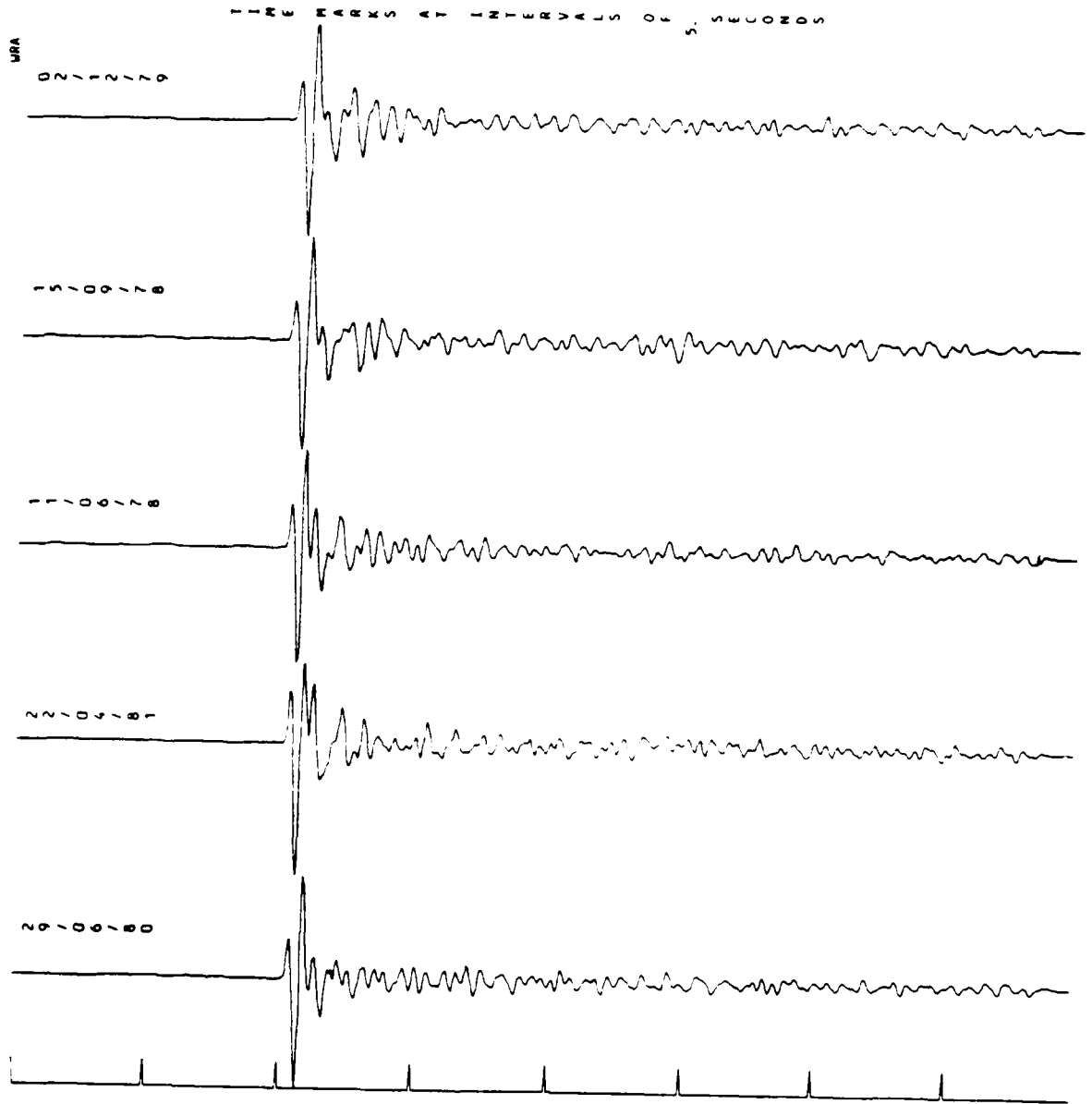
GBA Degelen



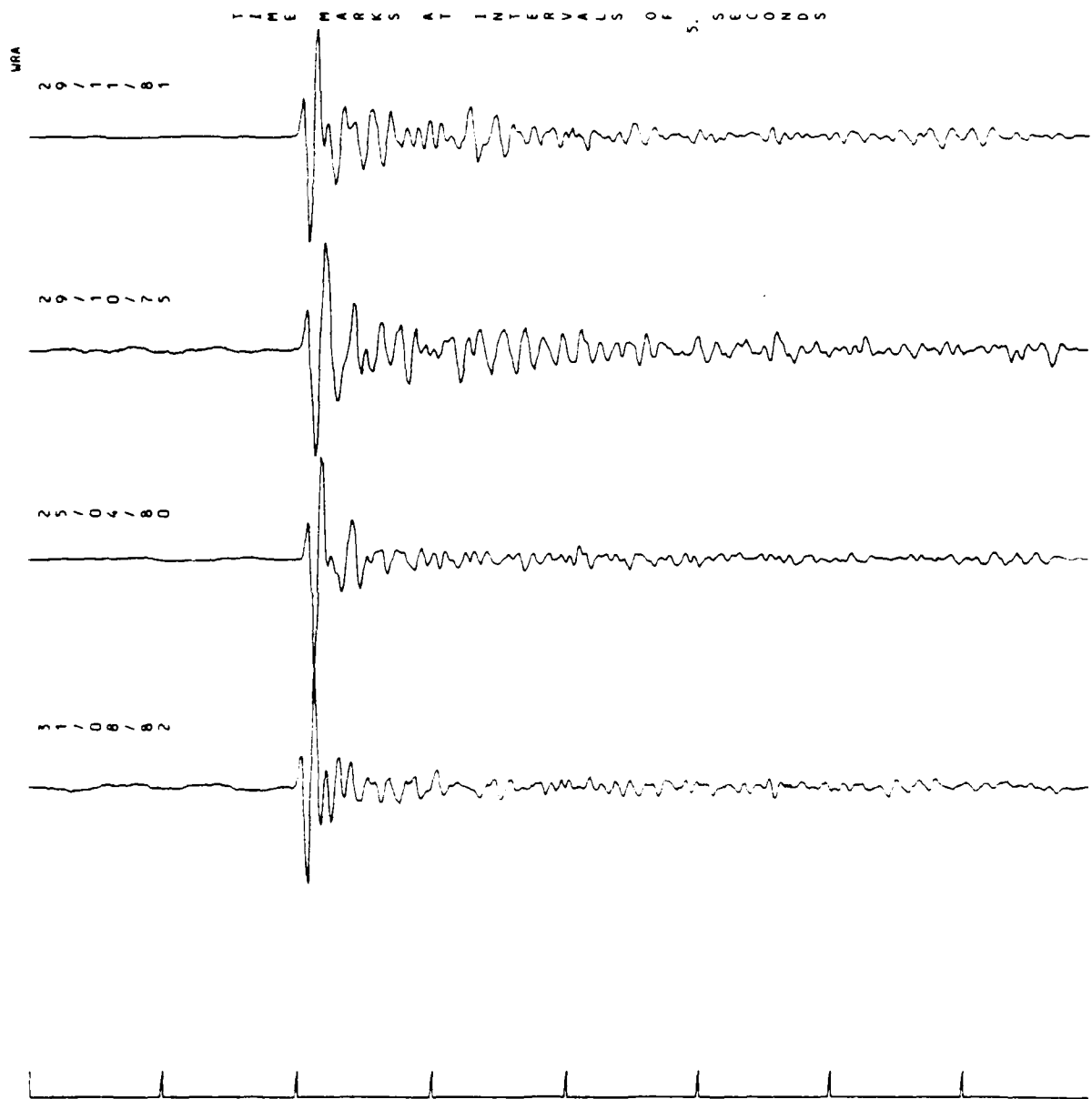
CBA Degelen



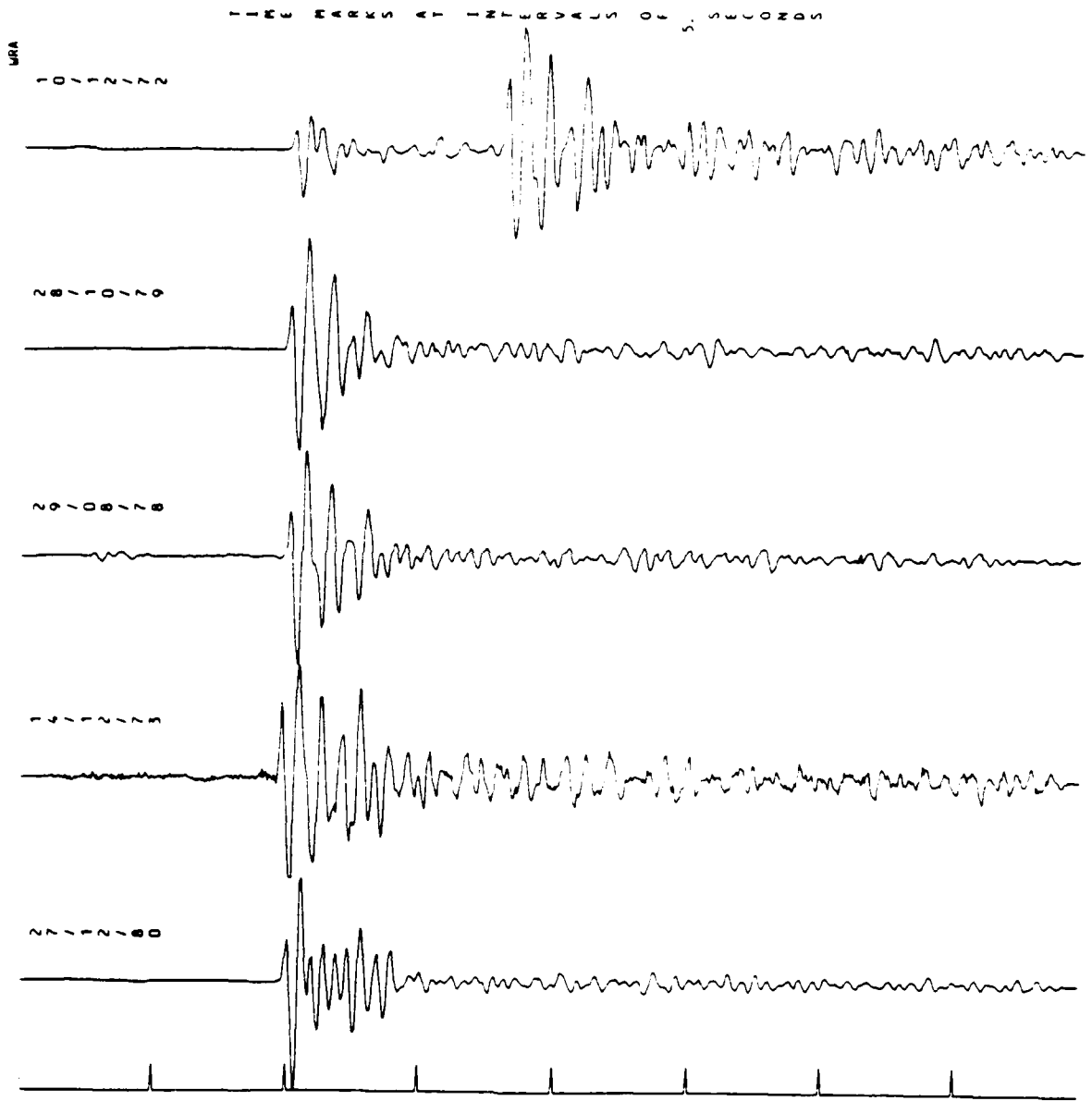
WRA Southwest Shagan River



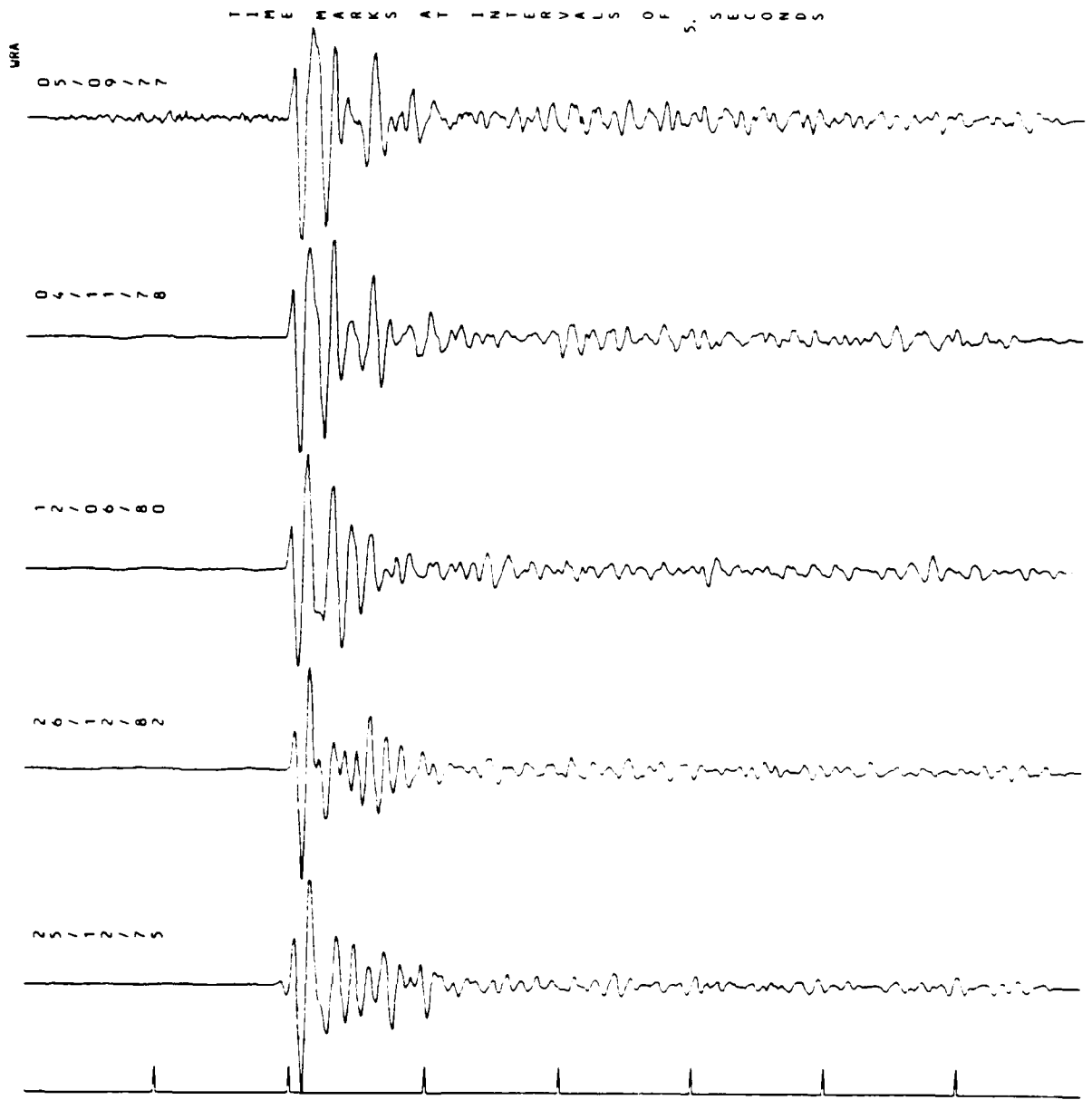
WRA Southwest Shagan River



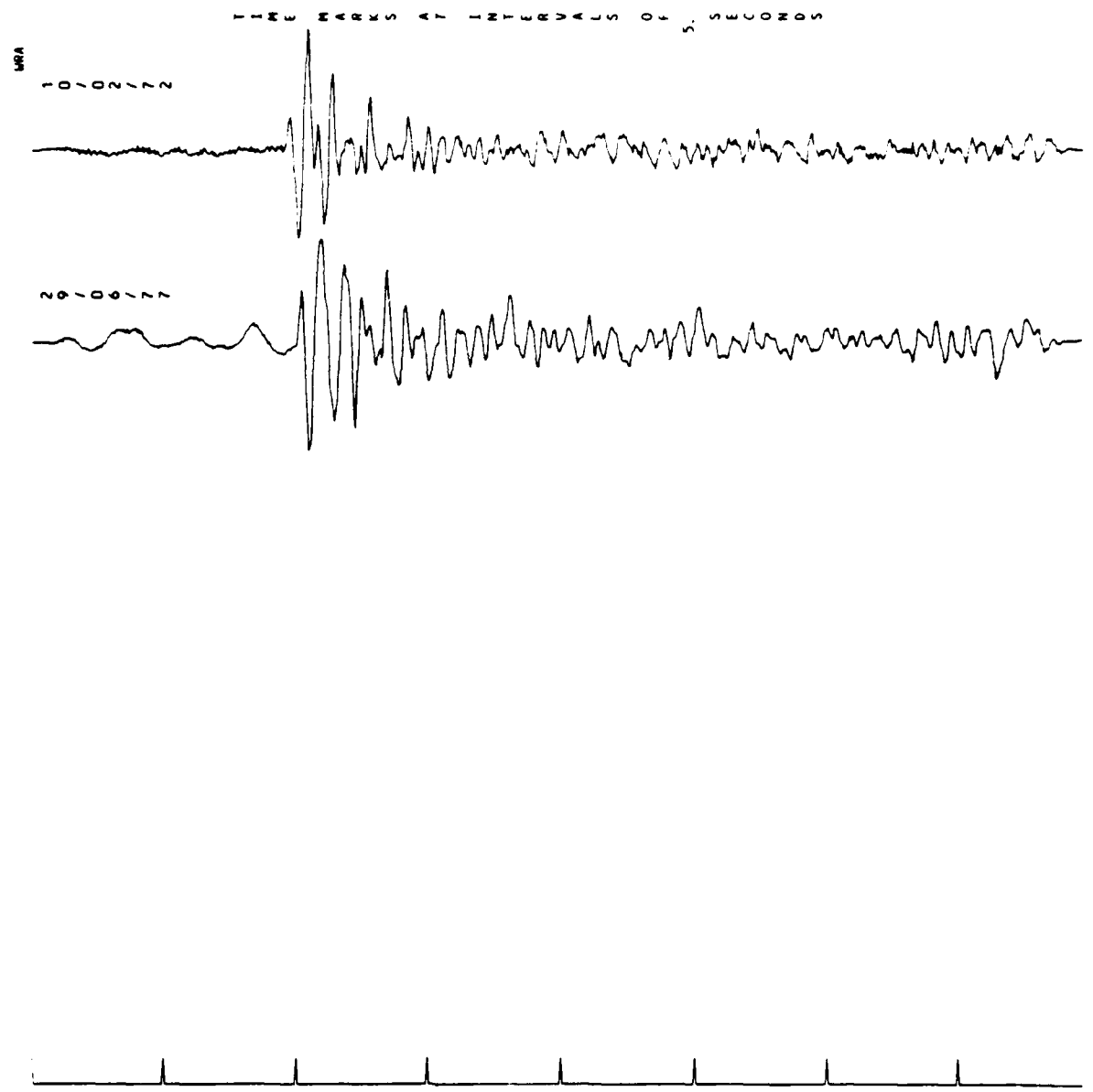
WRA Southwest Shagan River



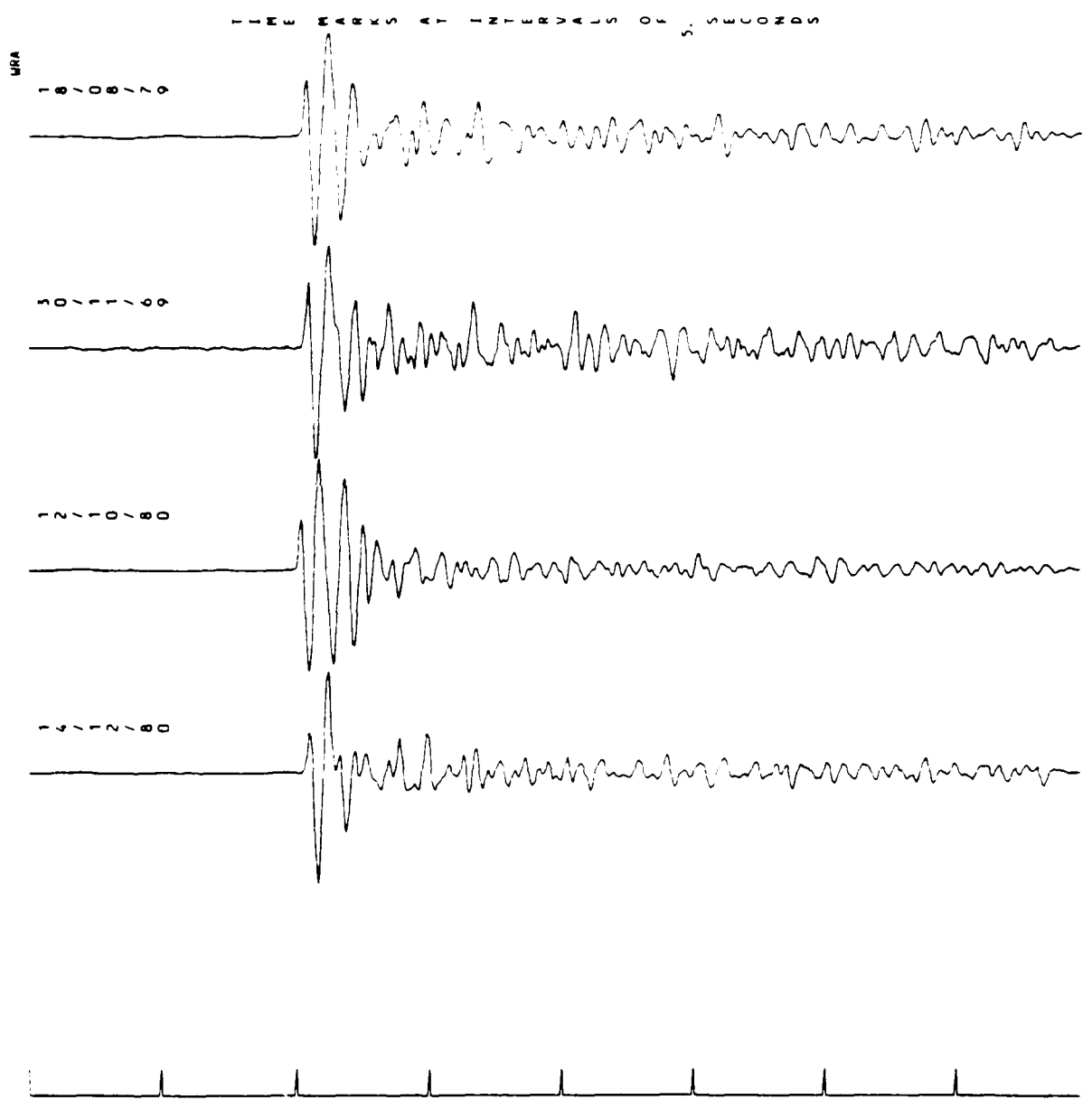
WRA Northeast Shagan River



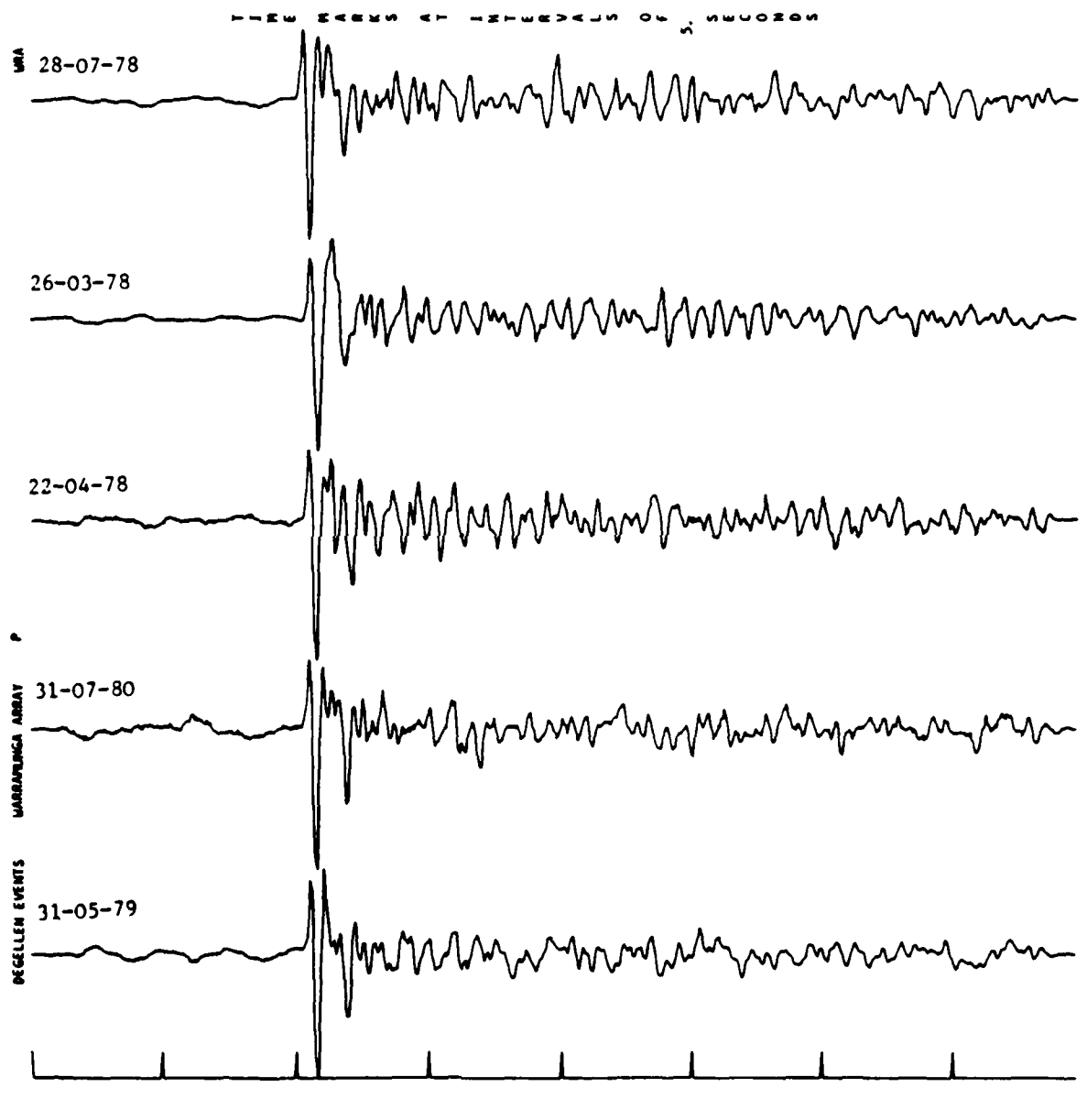
WRA Northeast Shagan River



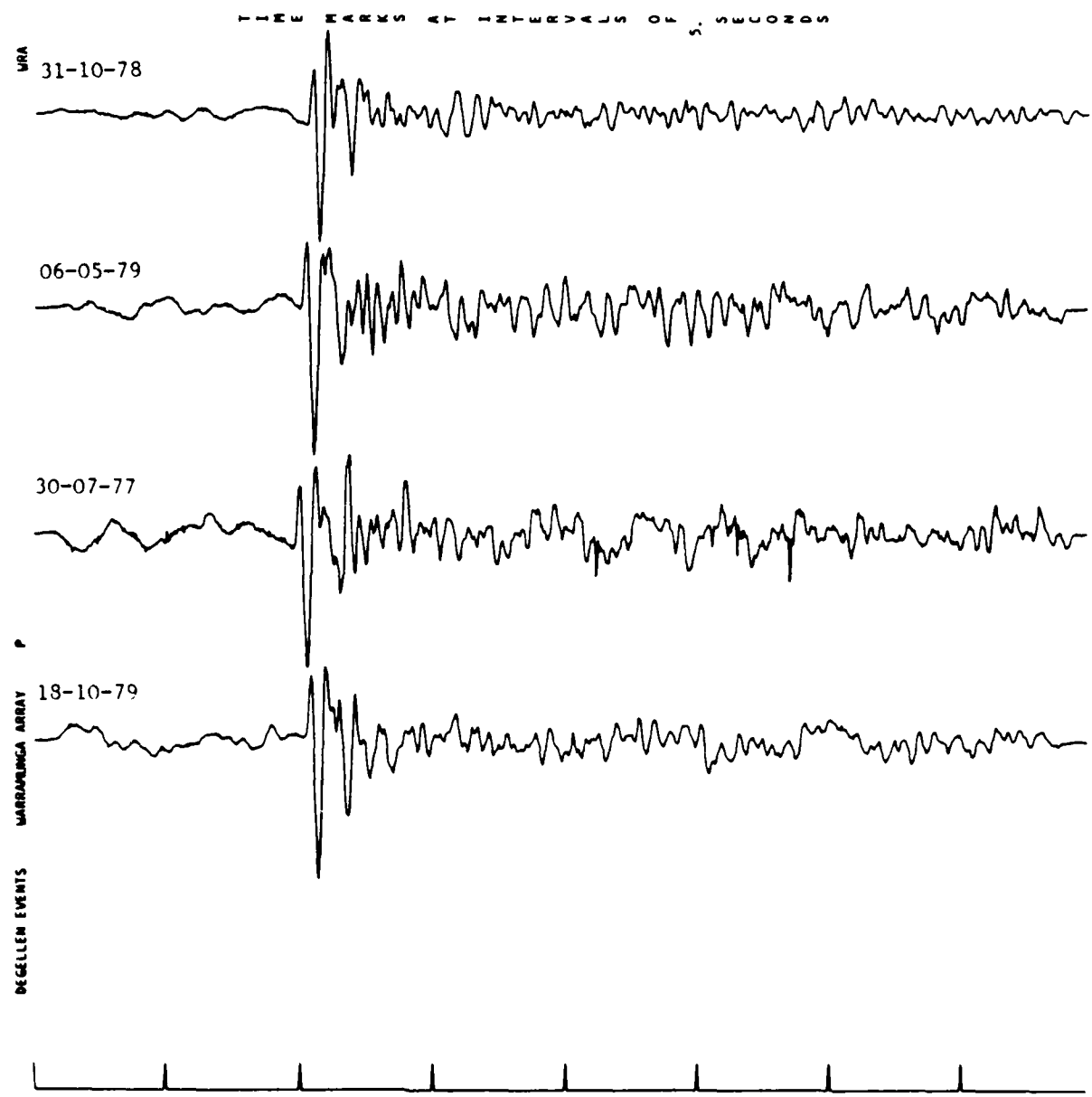
WRA Northeast Shagan River



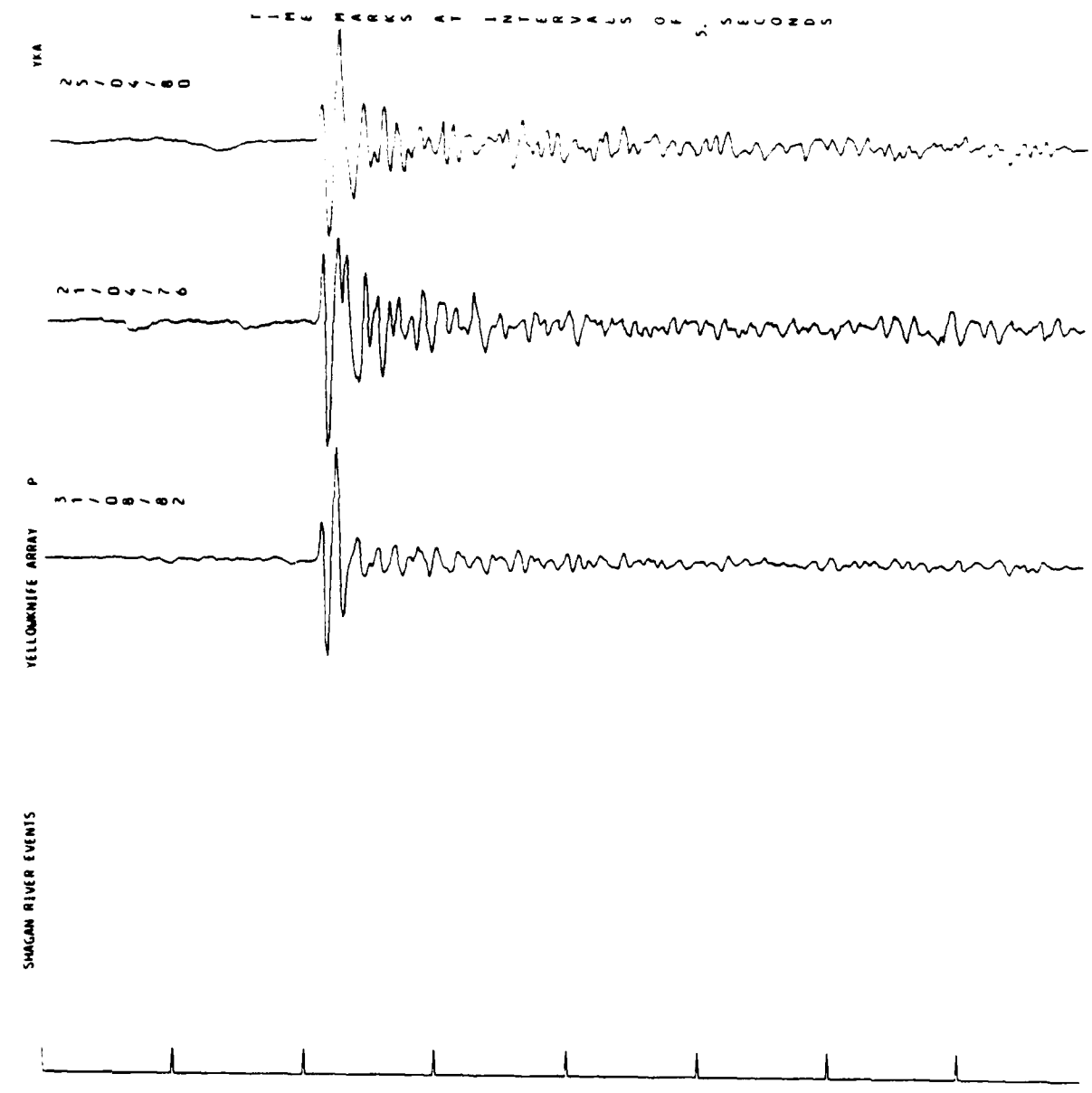
WRA Northeast Shagan River



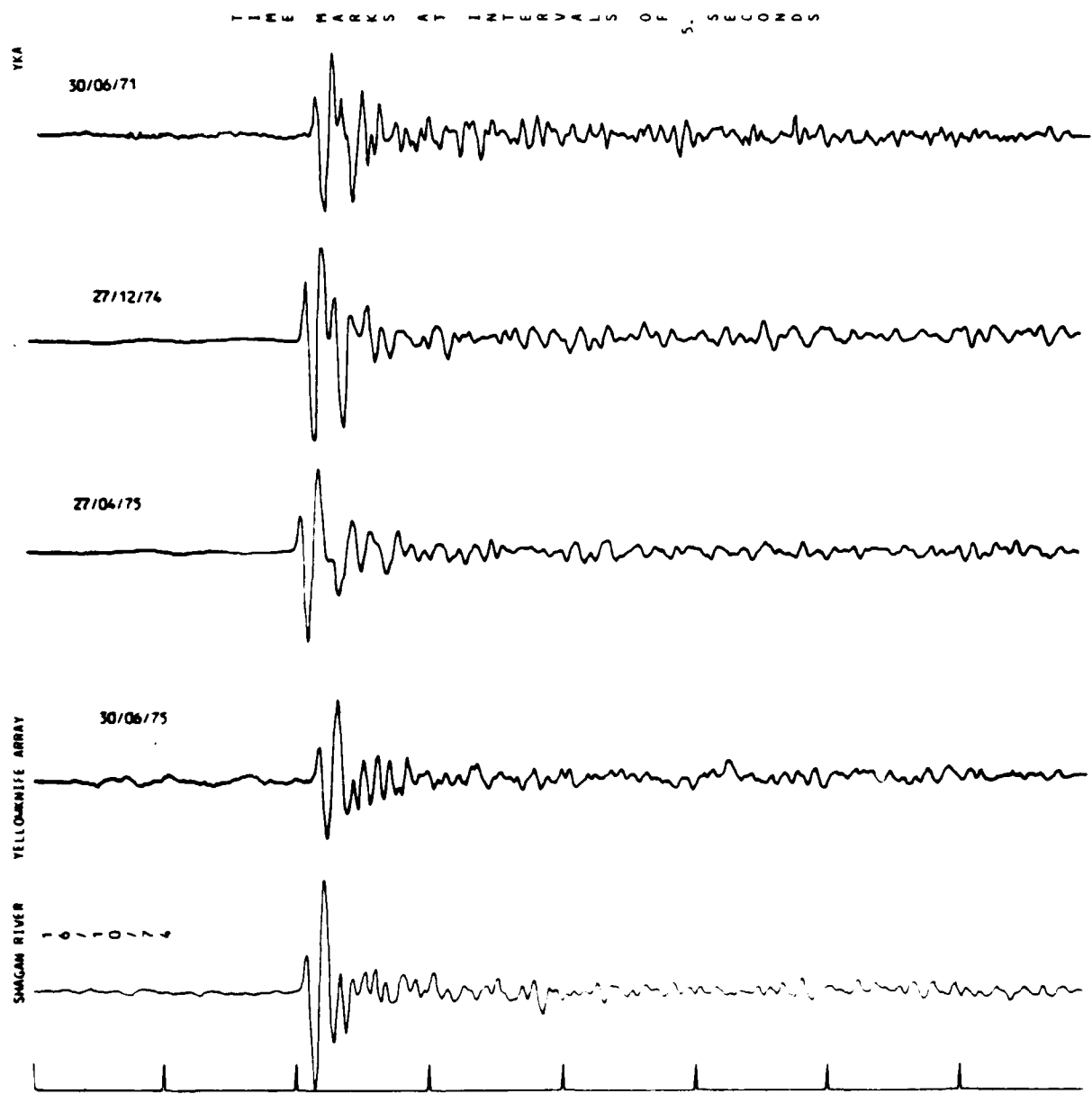
WRA Degelen



WRA Degelen

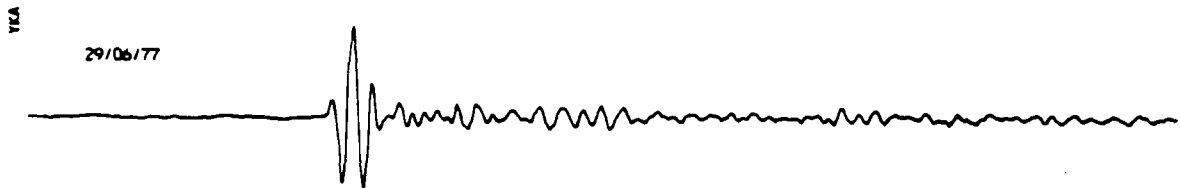


**YKA Shagan River**



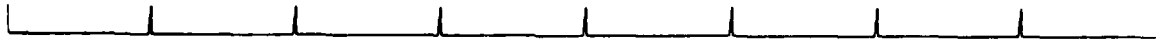
YKA Shagan River

NEW MARKS AT 12500 FEET OF S. MULDOON

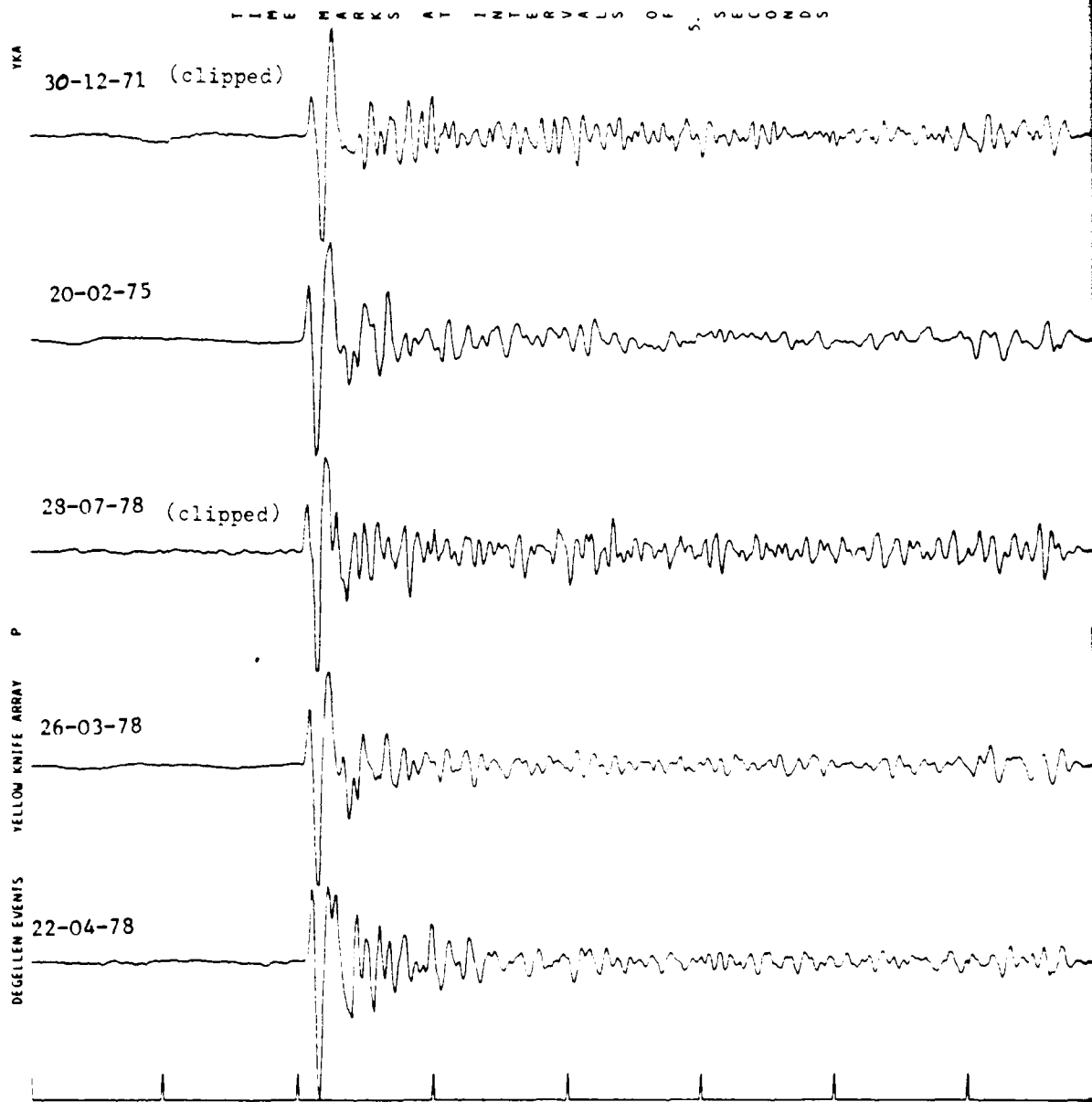


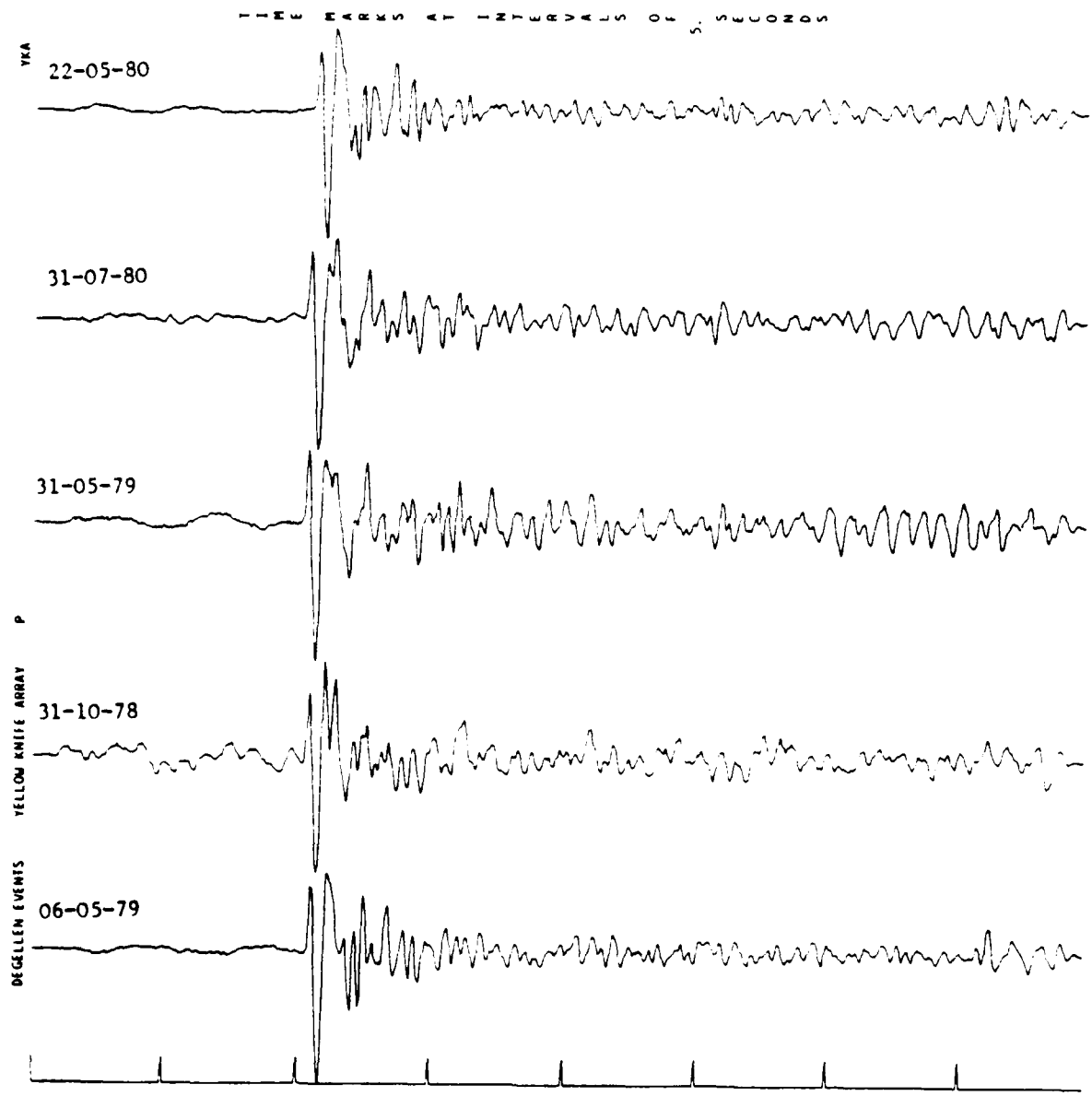
YELLOWKNIFE ARRAY

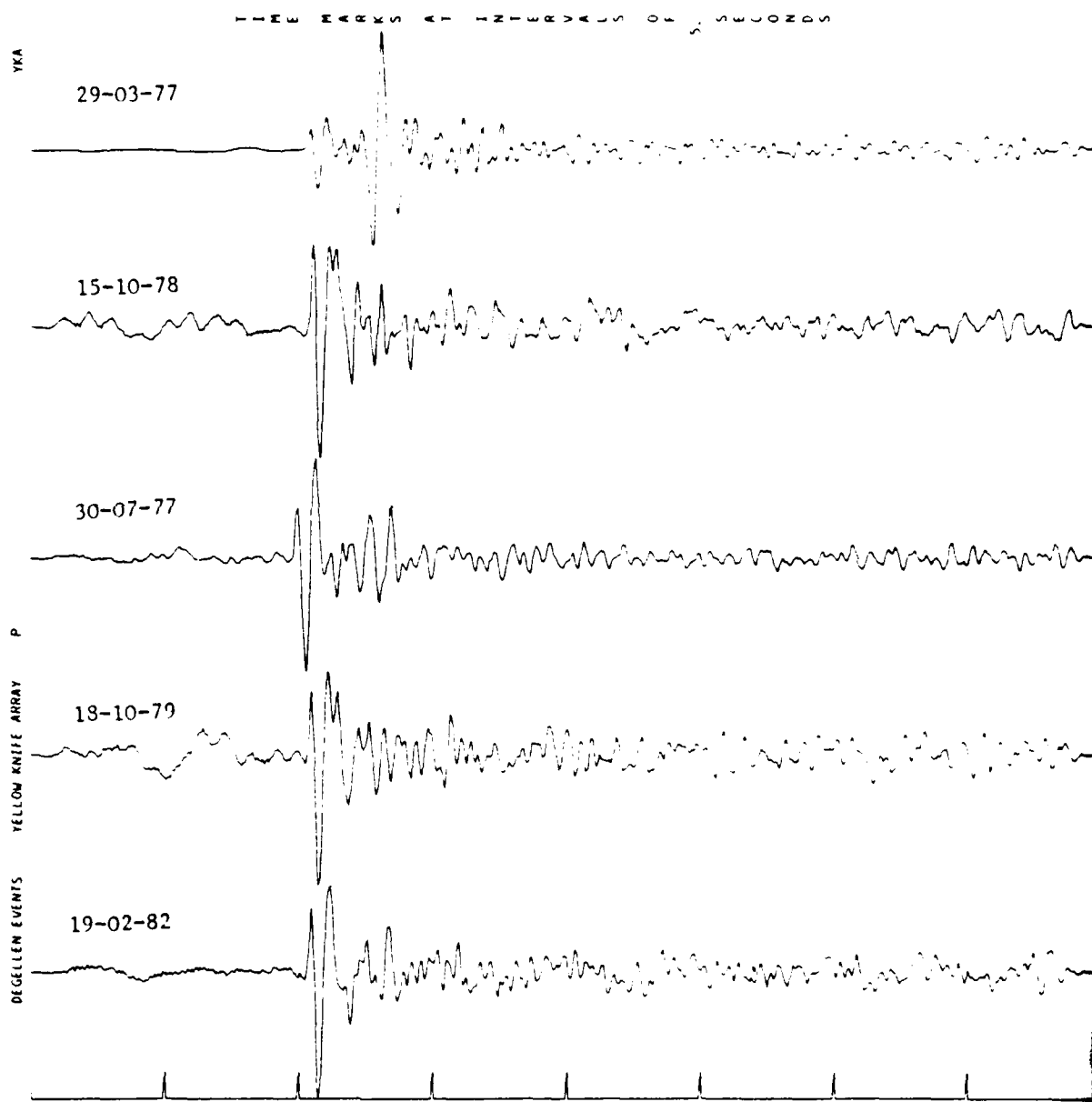
SHAGAN RIVER



YKA Shagan River







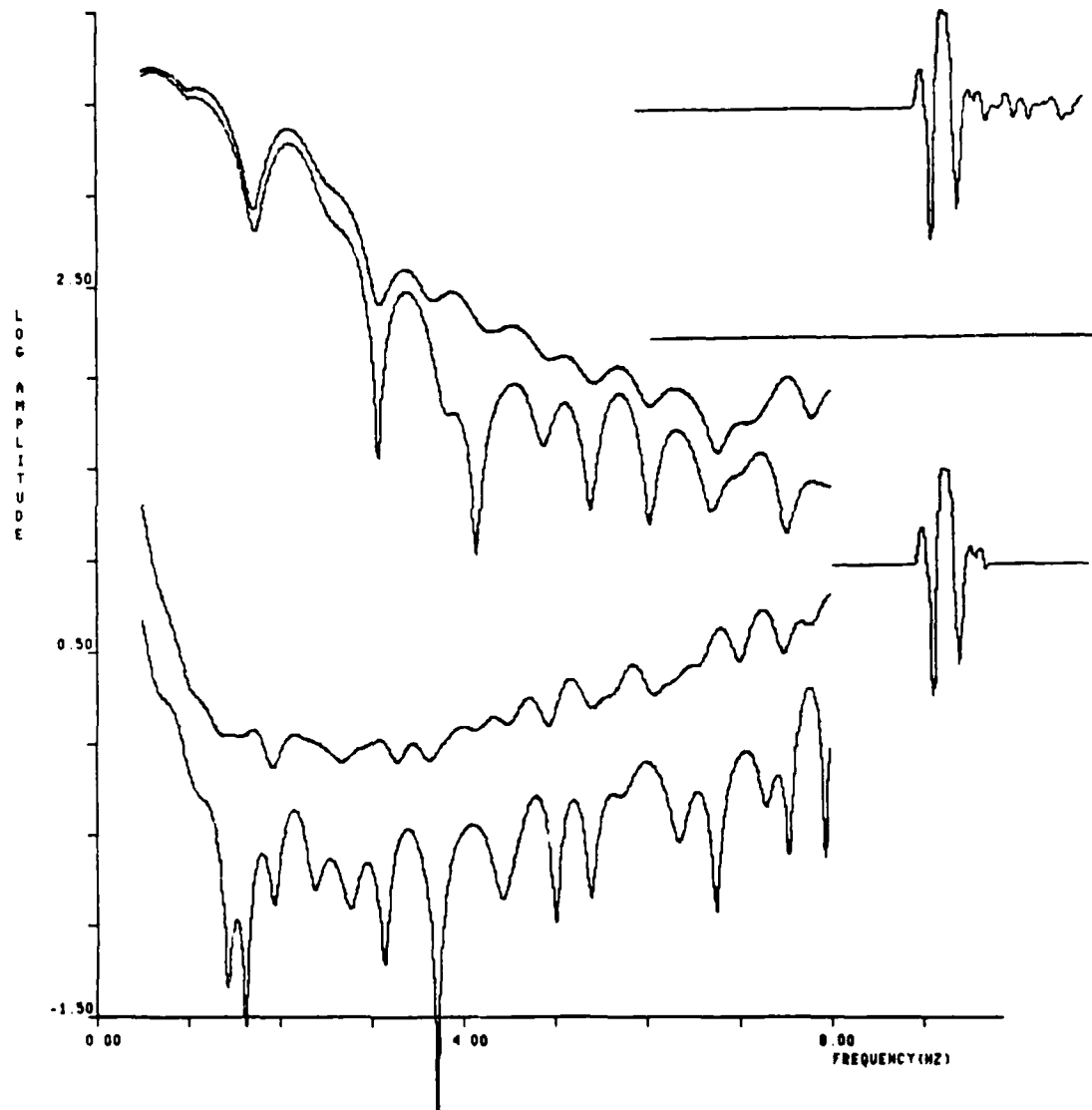
APPENDIX B  
GBA SPECTRUM CALCULATIONS

The procedure for calculating spectra is described in Section IV. In Figures 12 and 16 some important features of the calculation are demonstrated by comparing the final event spectrum calculated by the method of Section IV with the Fourier spectrum computed from the seismogram obtained by delay-and-sum beam forming. In this Appendix ten more comparisons of this kind are made for GBA recordings of Shagan River events.

Each plot shows the signal and noise spectra computed the two ways. All spectra have been multiplied by  $f^2$  for  $f > 1$  Hz. The noise spectra have been shifted down by 1.0 log units. In each case the smoother spectrum that is larger at high frequencies is computed by the method of Section IV. For some of the lower signal/noise events this spectrum has flat places that occur when the spectrum is undefined (see Section IV). The average noise from the individual sensors is larger than the noise on the beam sum channel by about  $\sqrt{N}$ , with N the number of channels processed.

In the upper right of each plot is the beam sum seismogram and the signal and noise windows selected. The individual channel processing is done with these same windows.

PRECEDING PAGE BLANK-NOT FILMED

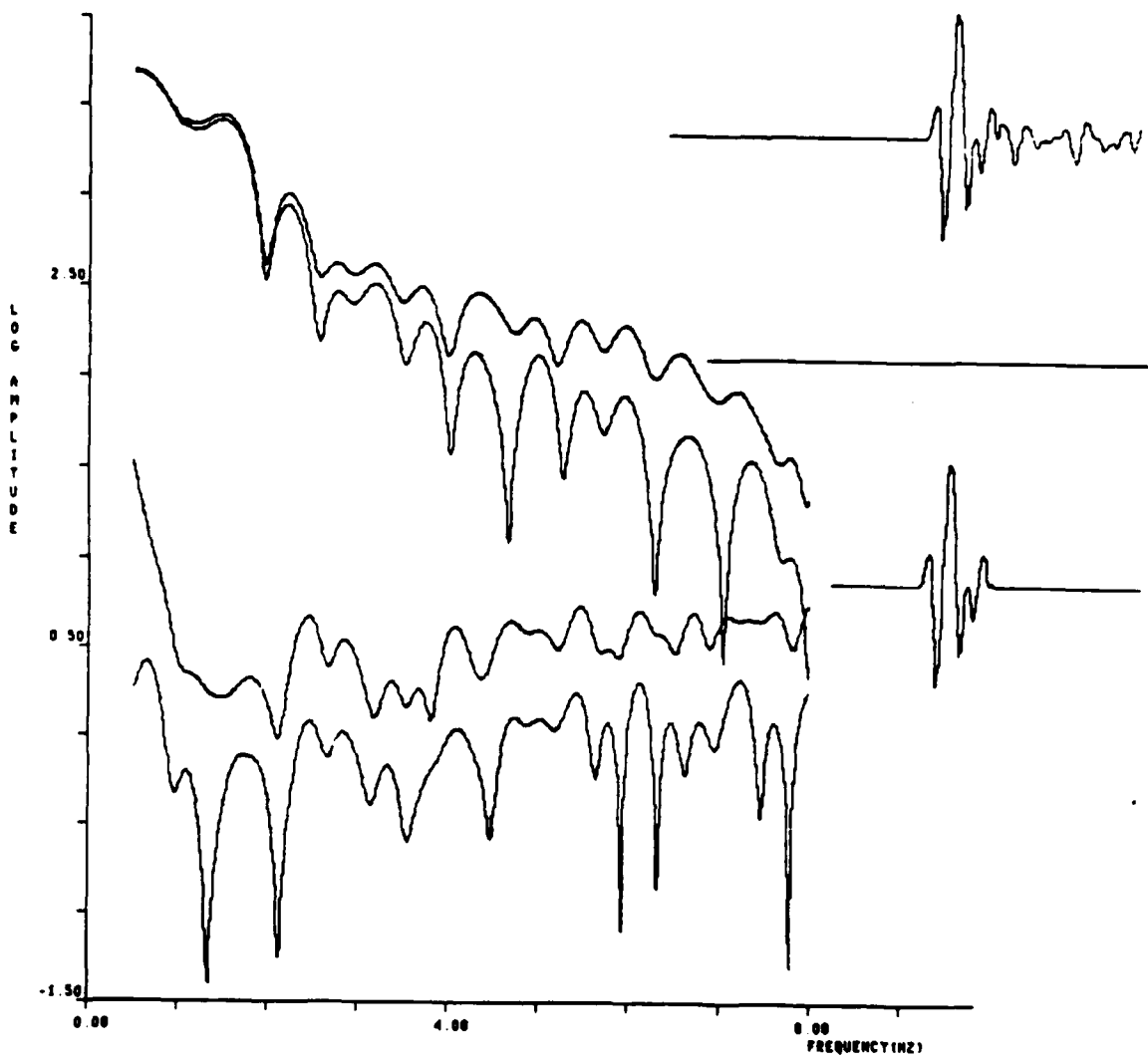


Southwest Shagan

14-09-80

$m_b = 6.2$

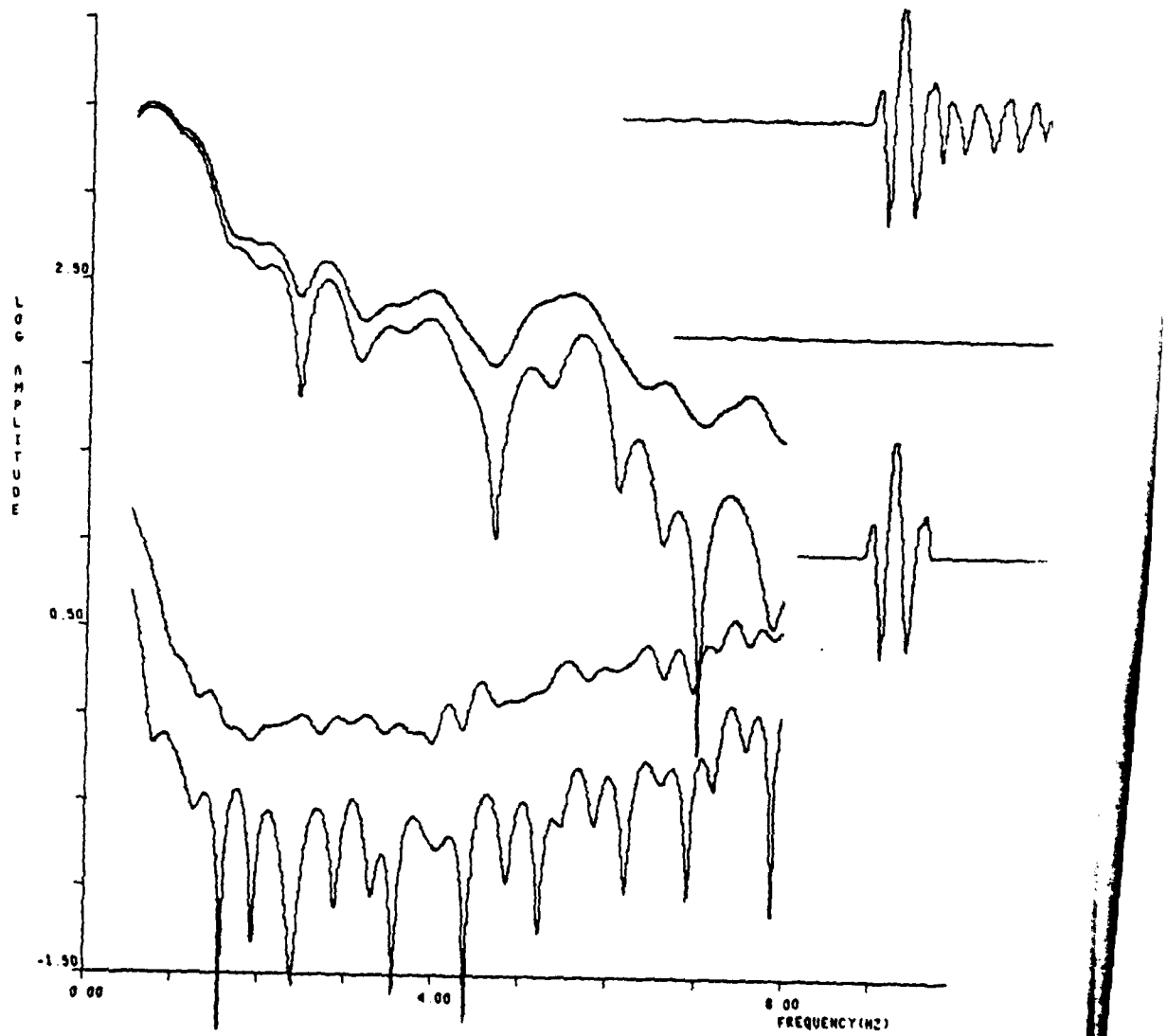
PRECEDING PAGE BLANK-NOT FILMED



Southwest Shagan

13-09-81

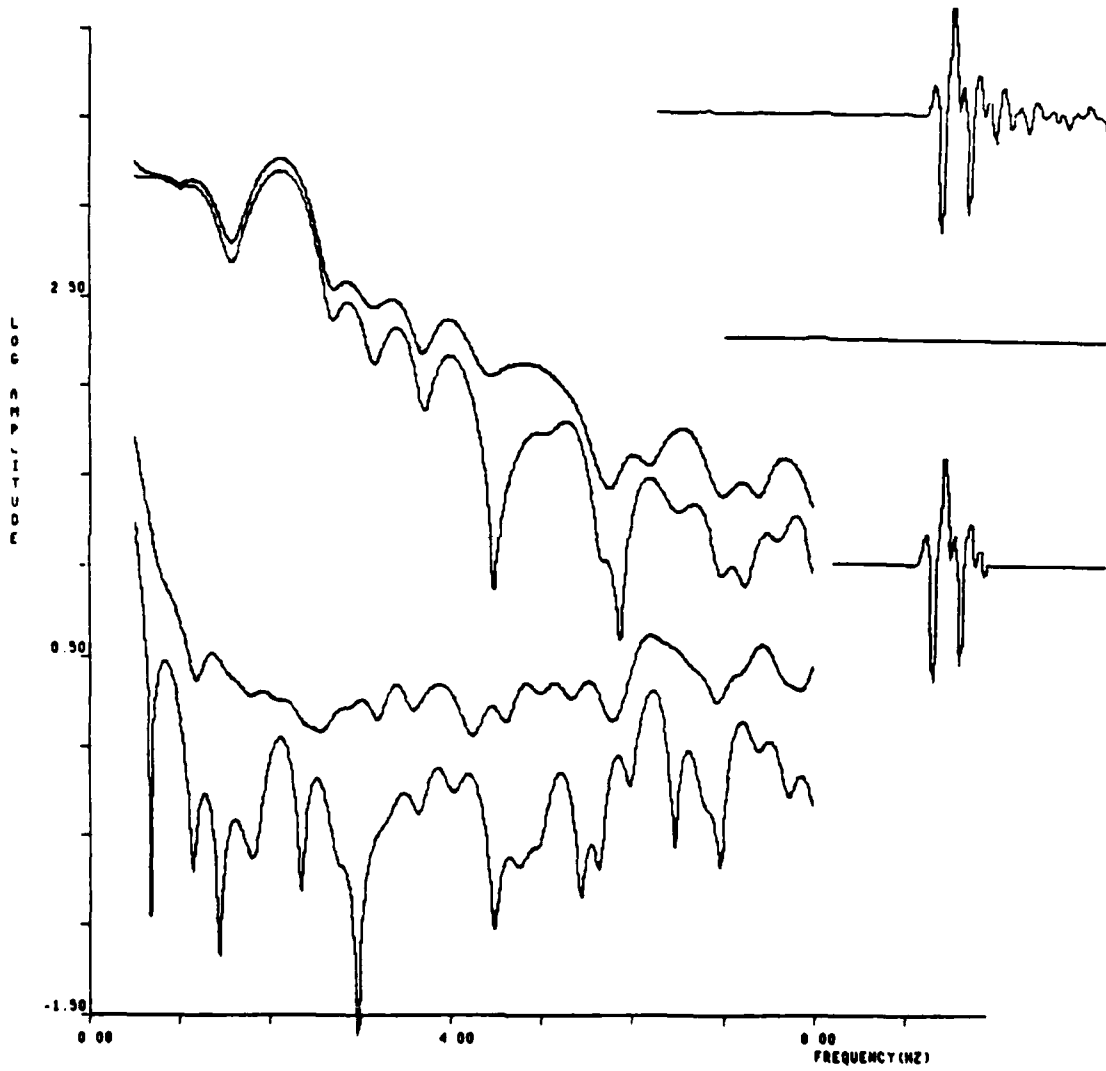
$m_b = 6.0$



Southwest Shagan

22-04-81

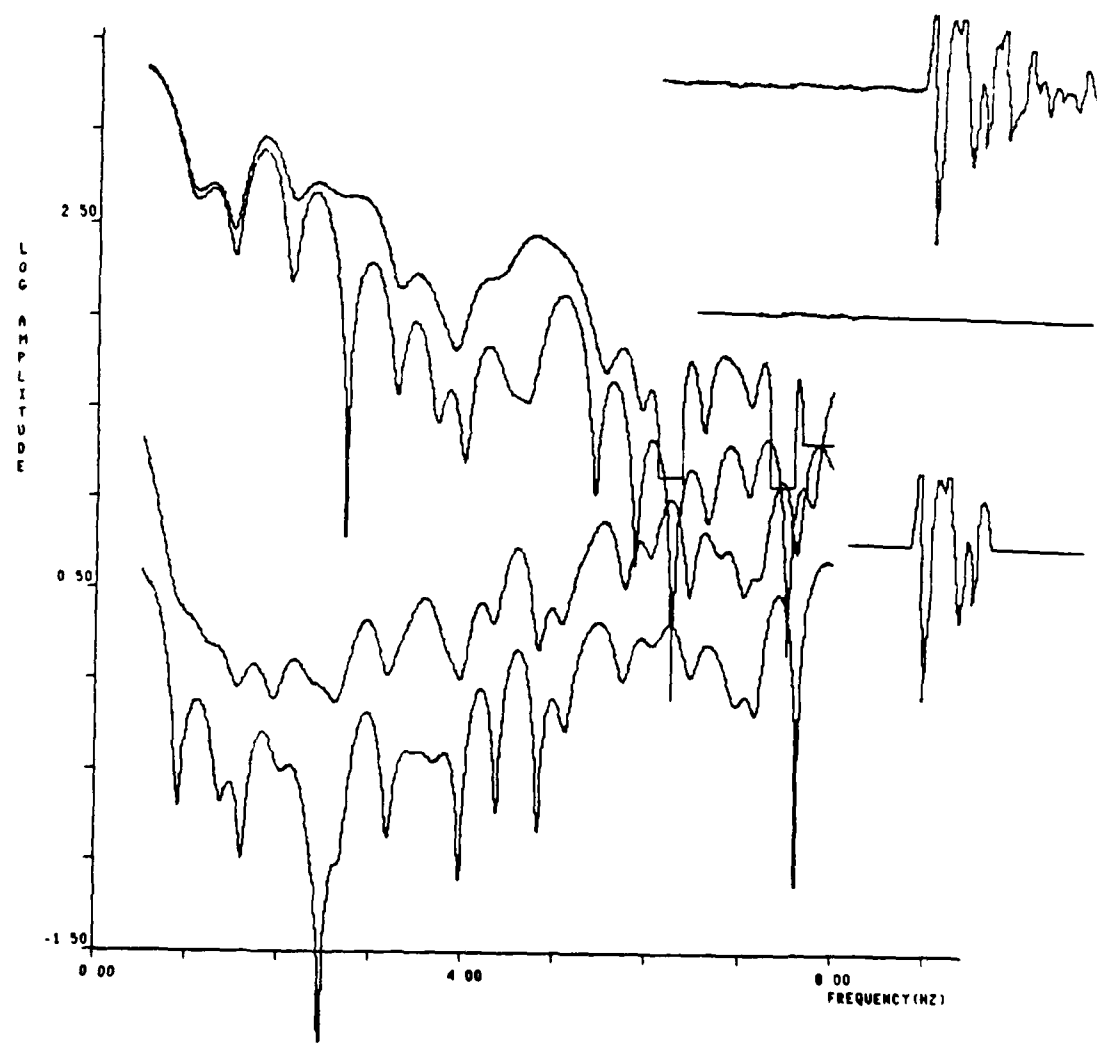
$m_b = 5.9$



Southwest Shagan

29-10-75

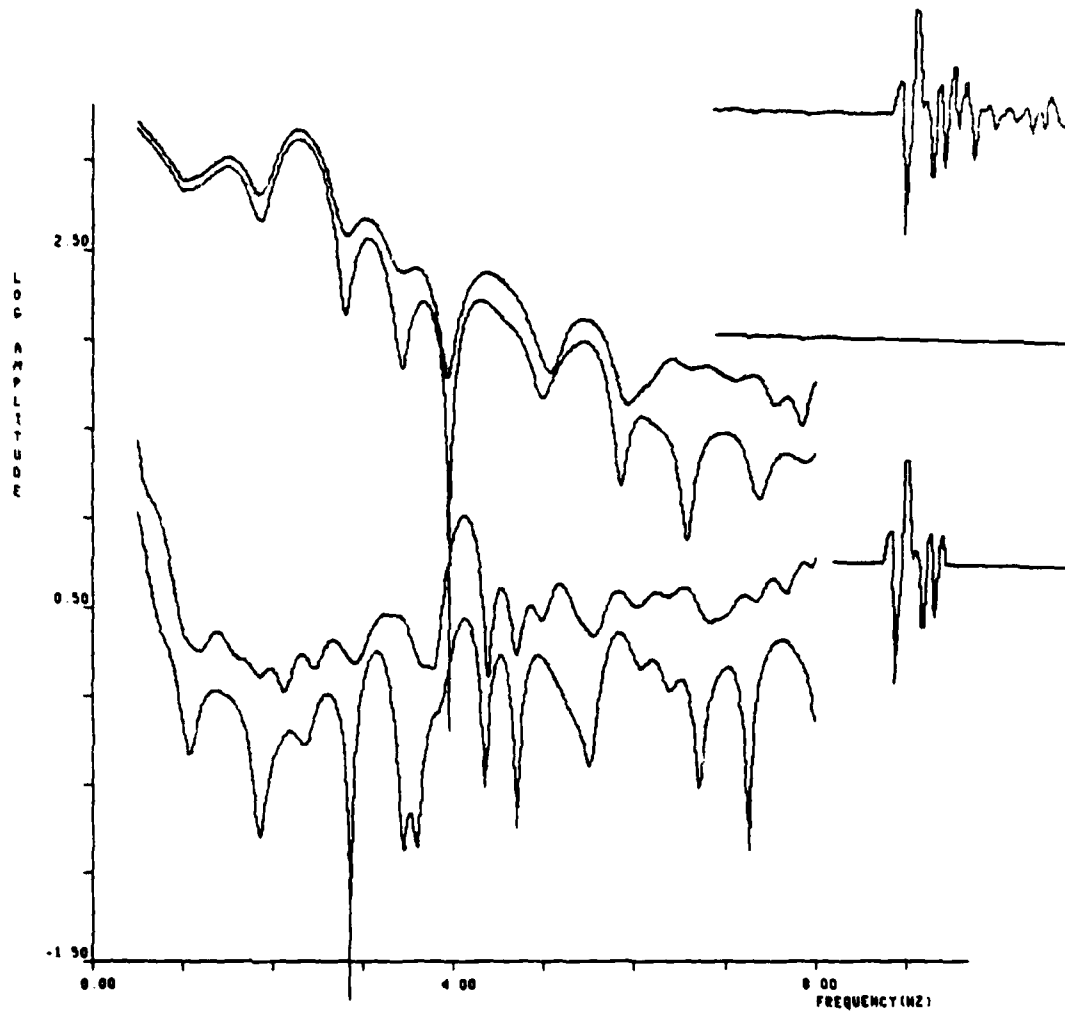
$m_b = 5.8$



Northeast Shagan

27-12-80

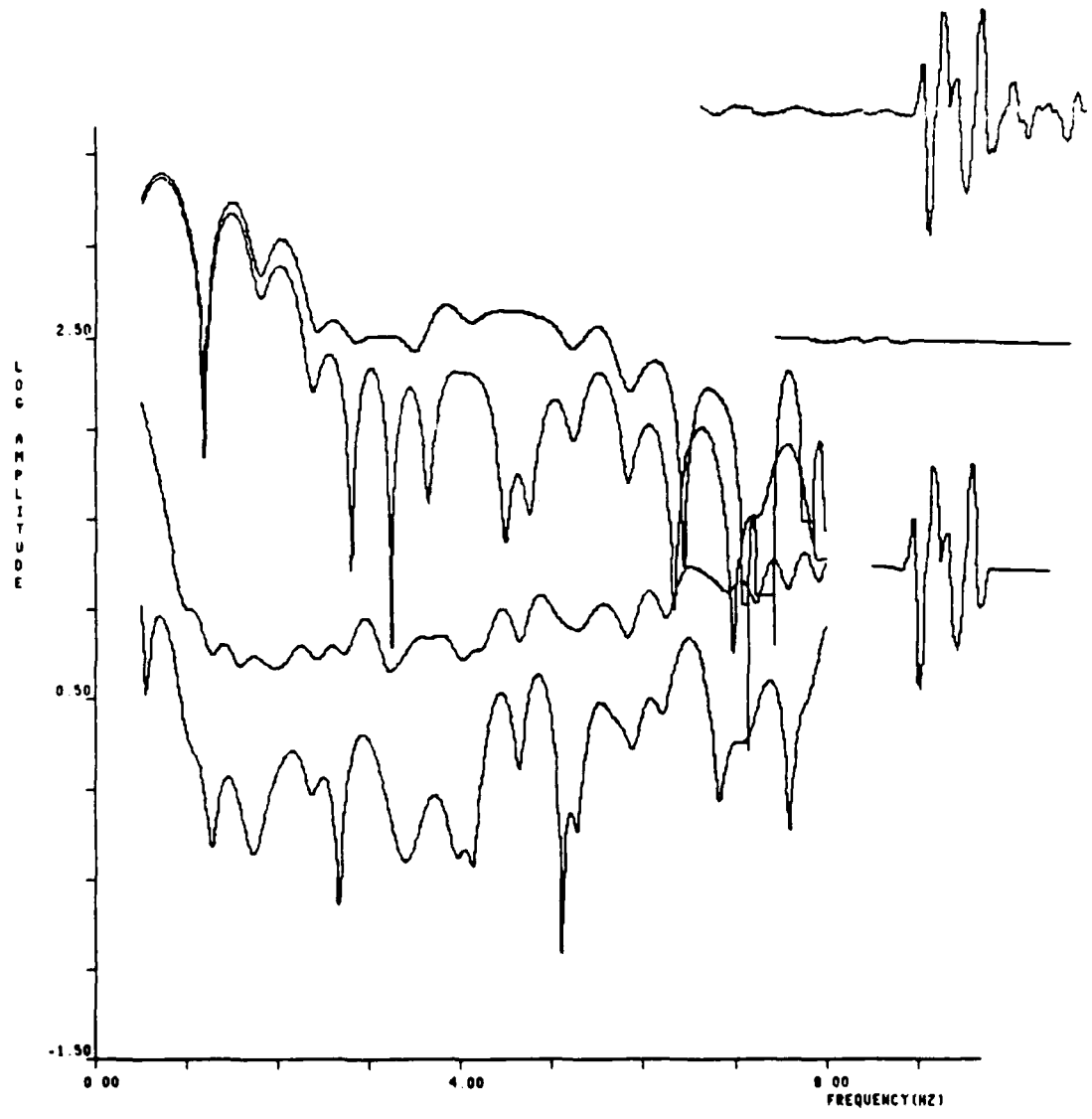
$m_b = 5.9$



Northeast Shagan

27-07-75

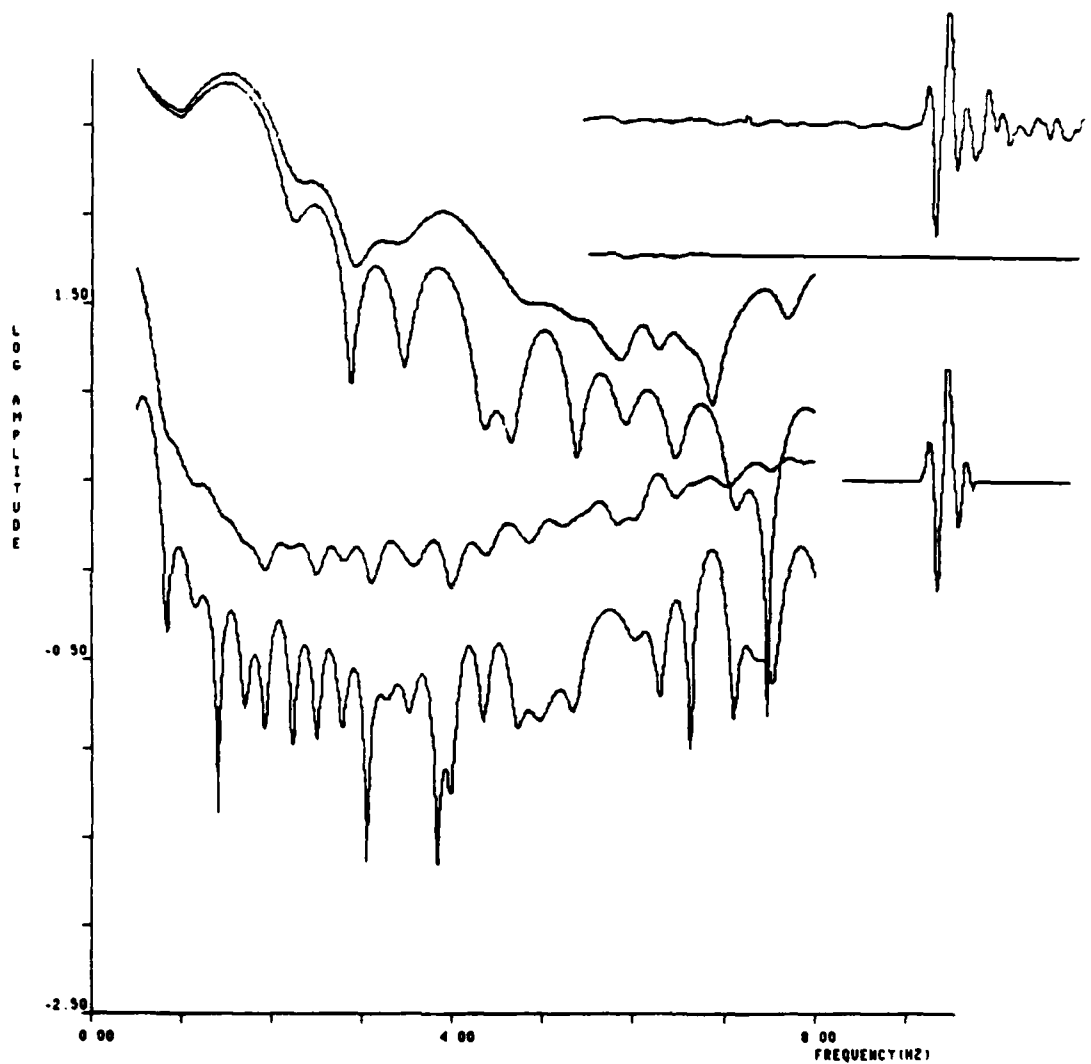
$m_b = 5.6$



Northeast Shagan

04-11-78

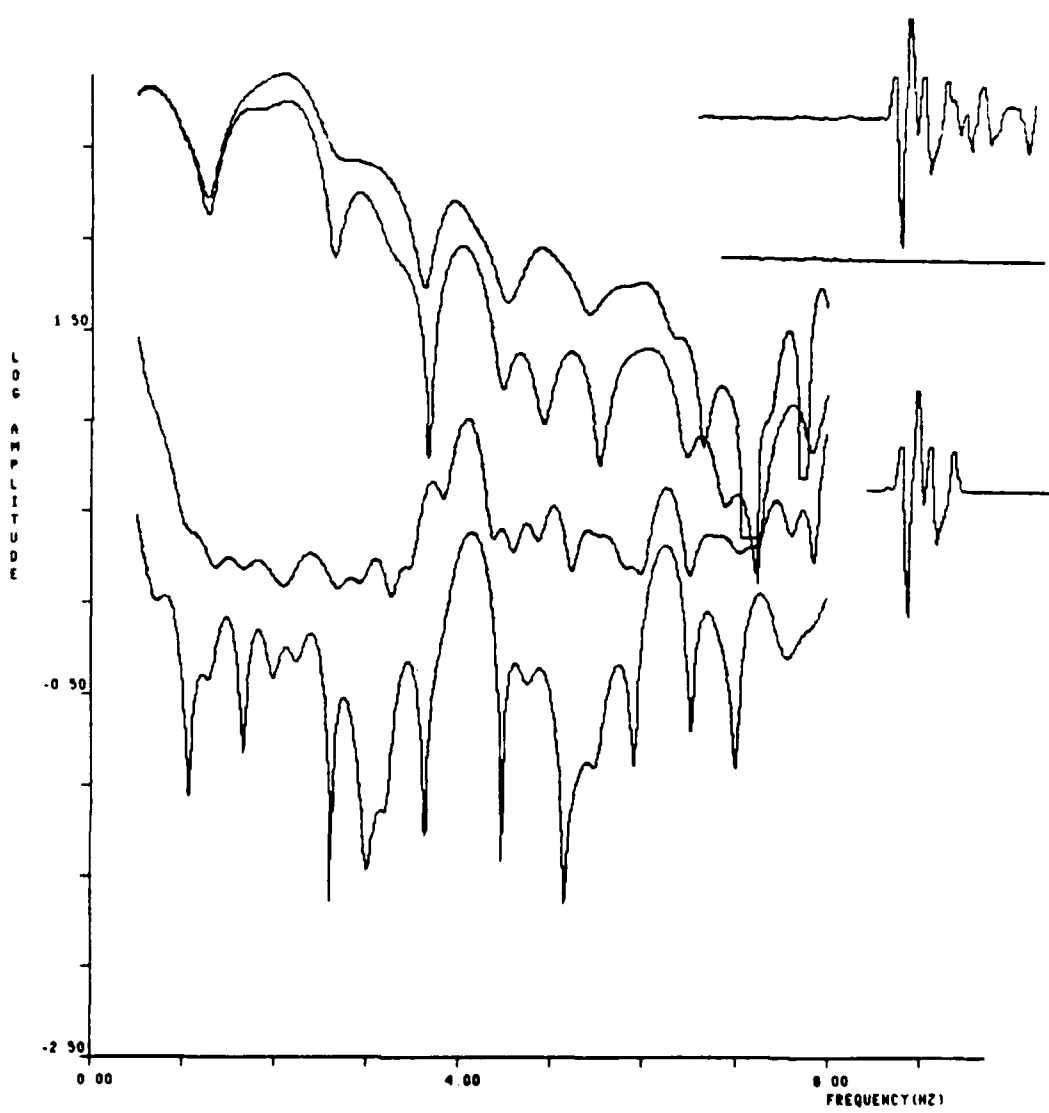
$m_b = 5.6$



Northeast Shagan

12-06-80

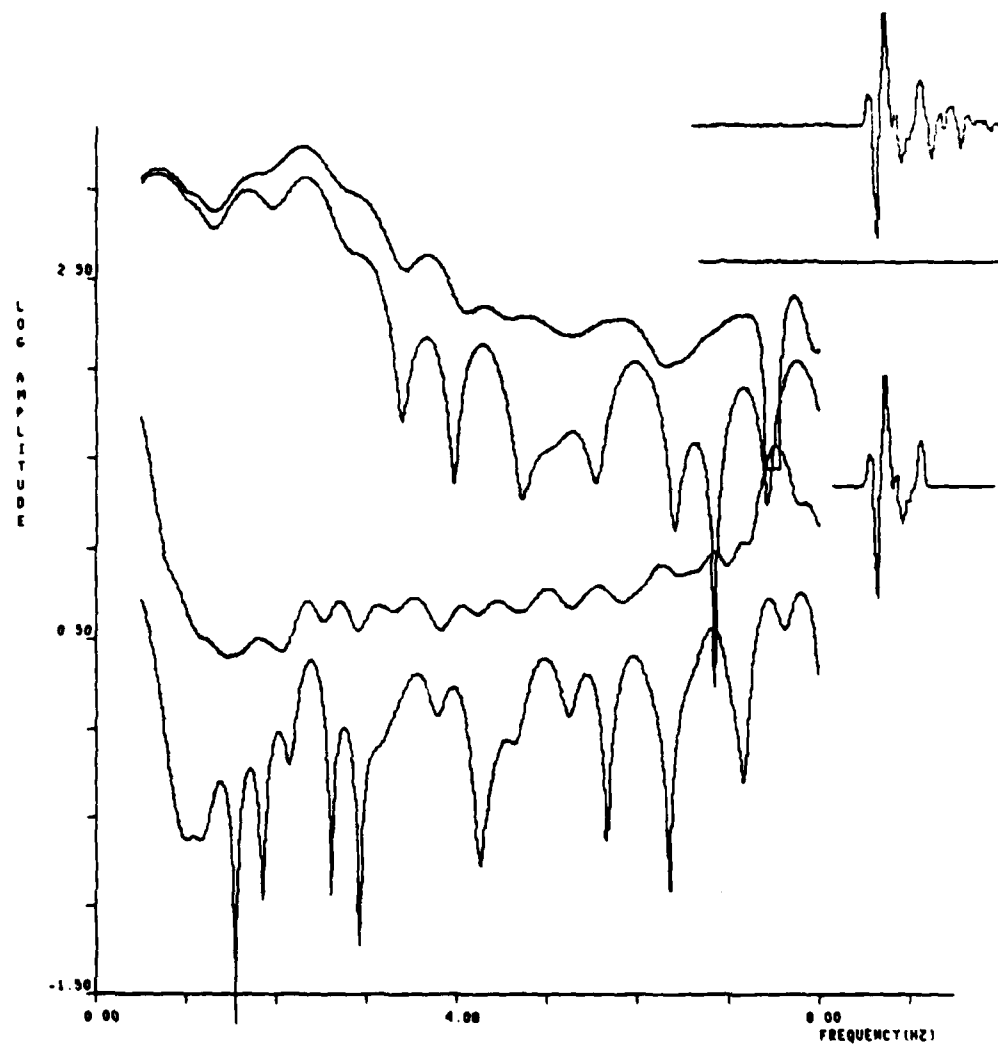
$m_b = 5.6$



Northeast Shagan

16-10-74

$m_b = 5.5$



Northeast Shagan

01-02-79

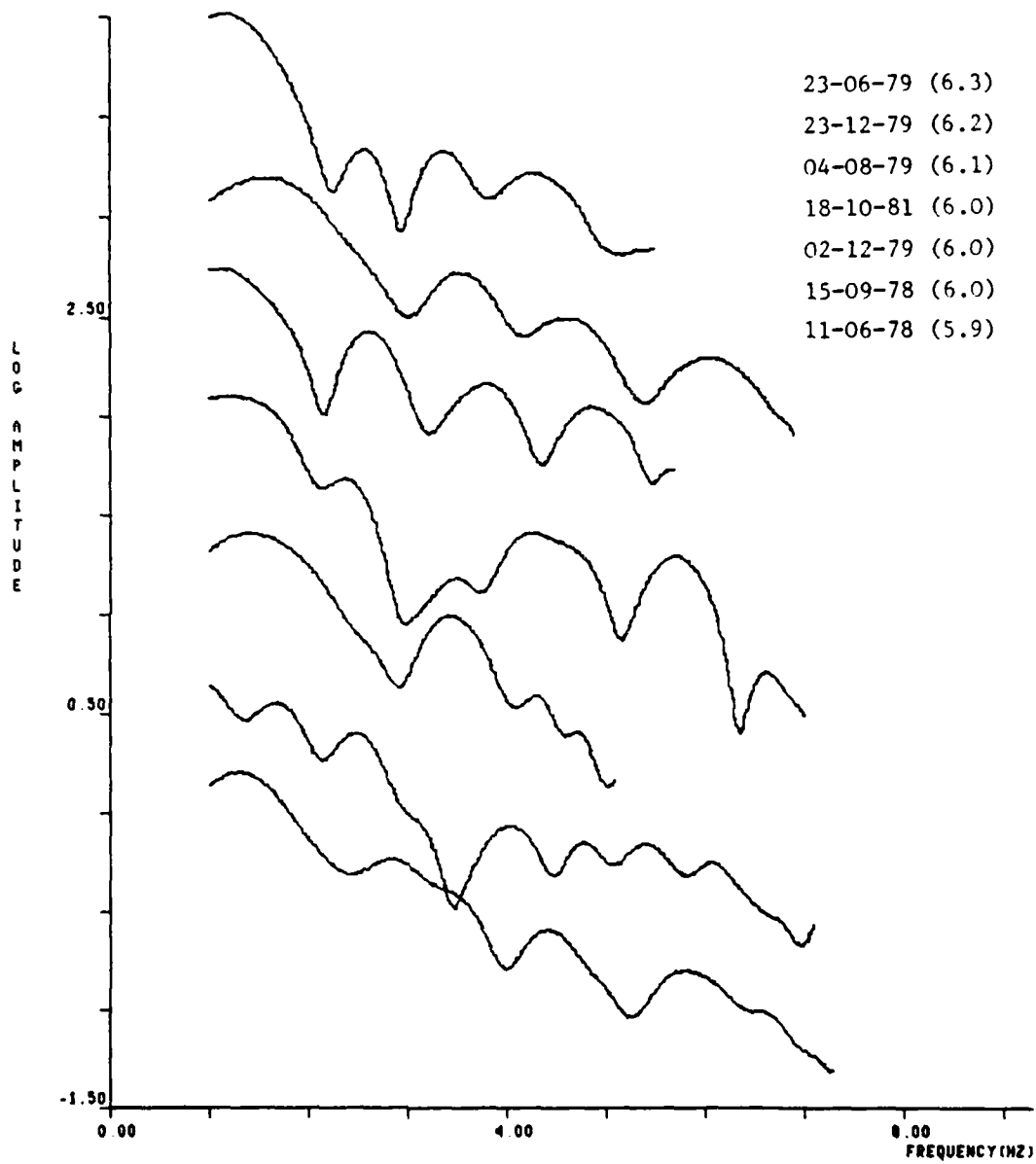
$m_b = 5.4$

APPENDIX C

SPECTRA FOR EAST KAZAKH EXPLOSIONS

The spectra used in the analysis discussed in Section VI are all plotted in this Appendix. They are computed with the methods described in Section IV. In making the plots a different cutoff frequency was selected for each spectrum. This is the frequency at which the signal spectrum drops below the level of the average noise (Section 6.2).

The events are divided into three groups (SW Shagan, NE Shagan, Degelen) for each station but YKA where all Shagan event spectra are plotted together. The amplitude scale is entirely arbitrary and was chosen to separate the spectra on the plot. Each set of spectra is plotted twice and the events are identified with their ISC or PDE (post-1980) magnitudes. The second plot includes the least squares fit to each spectrum. If Q were frequency-independent, the slope of this line would be directly proportional to  $t^*$ , and this value of  $t^*$  is indicated. These lines are not thought to provide a very good indication of the actual  $t^*$ , as described in Section VI, but are useful when comparing spectra from different events.



PRECEDING PAGE BLANK-NOT FILMED

Figure A.1 EKA Recordings of Southwest Shagan River Explosions

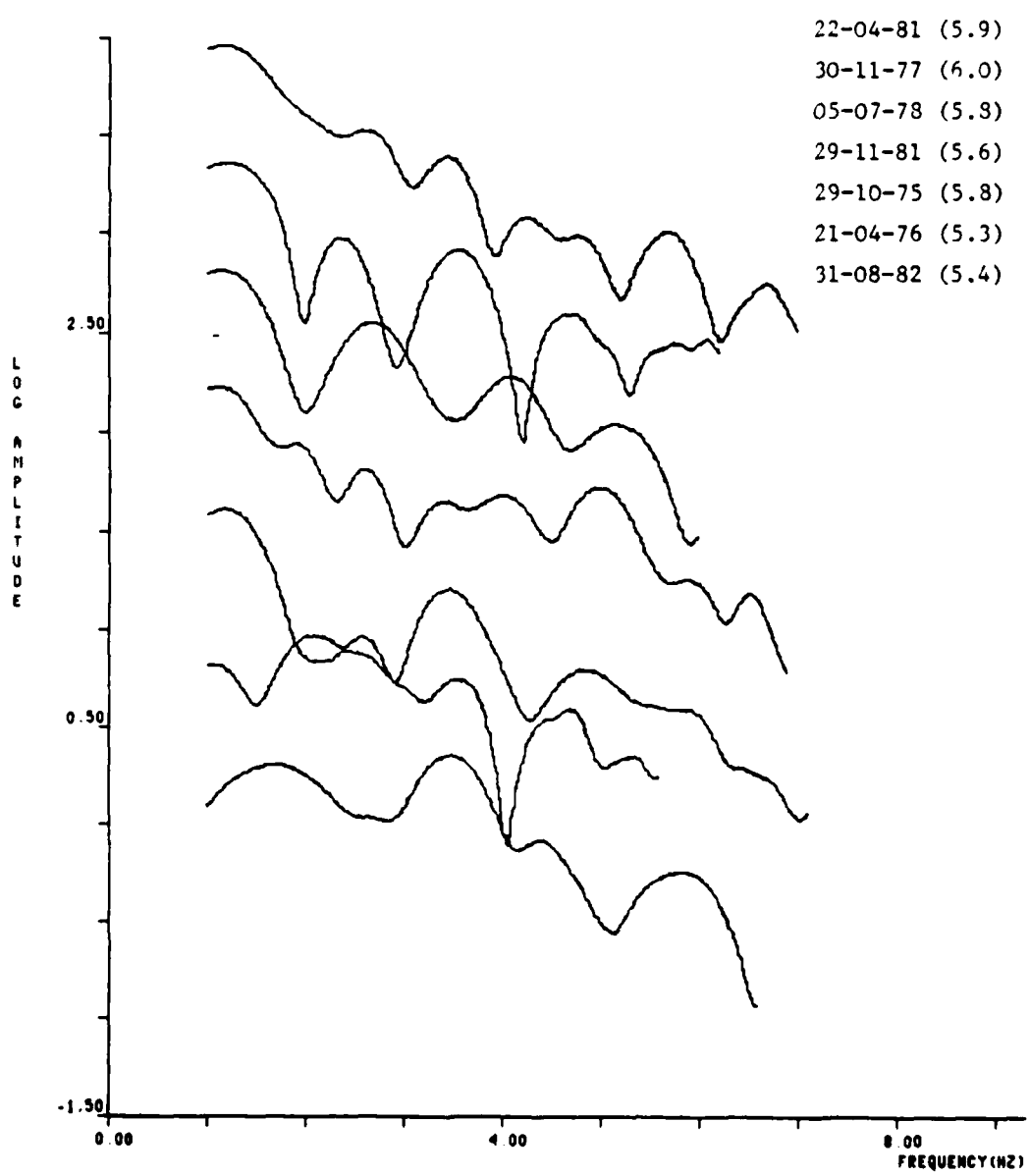


Figure A.1 (continued)

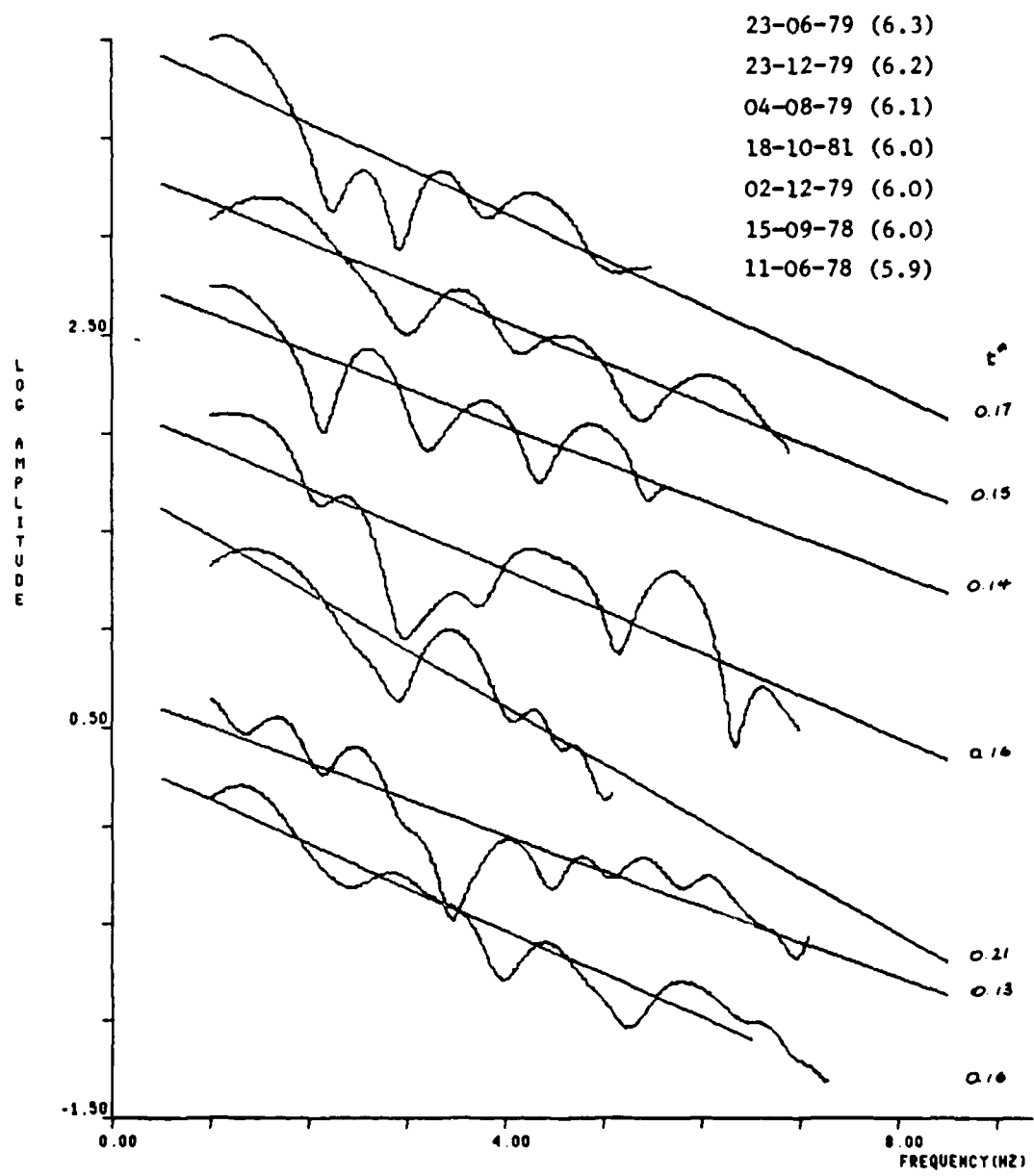


Figure A.1 (continued)

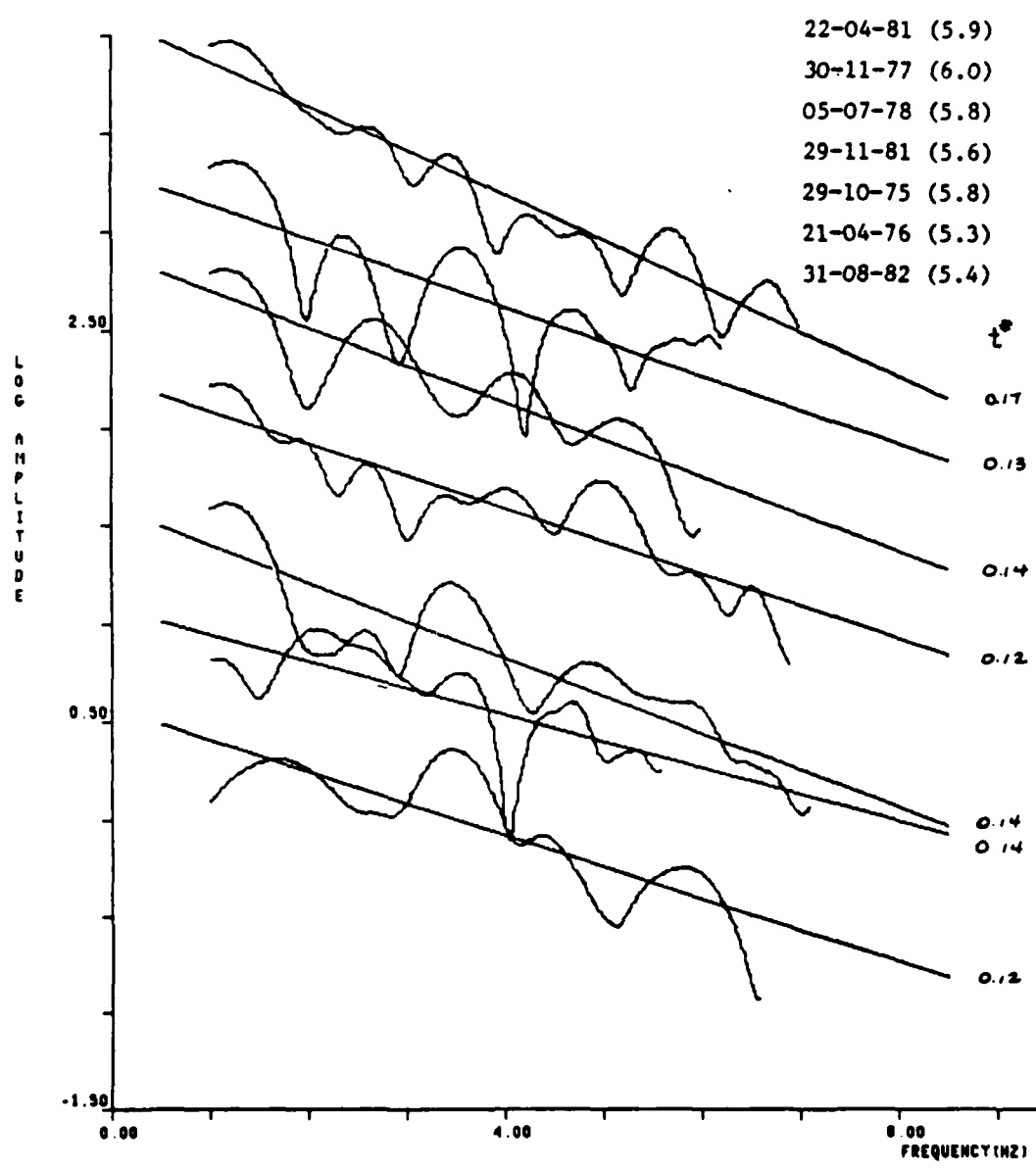


Figure A.1 (continued)

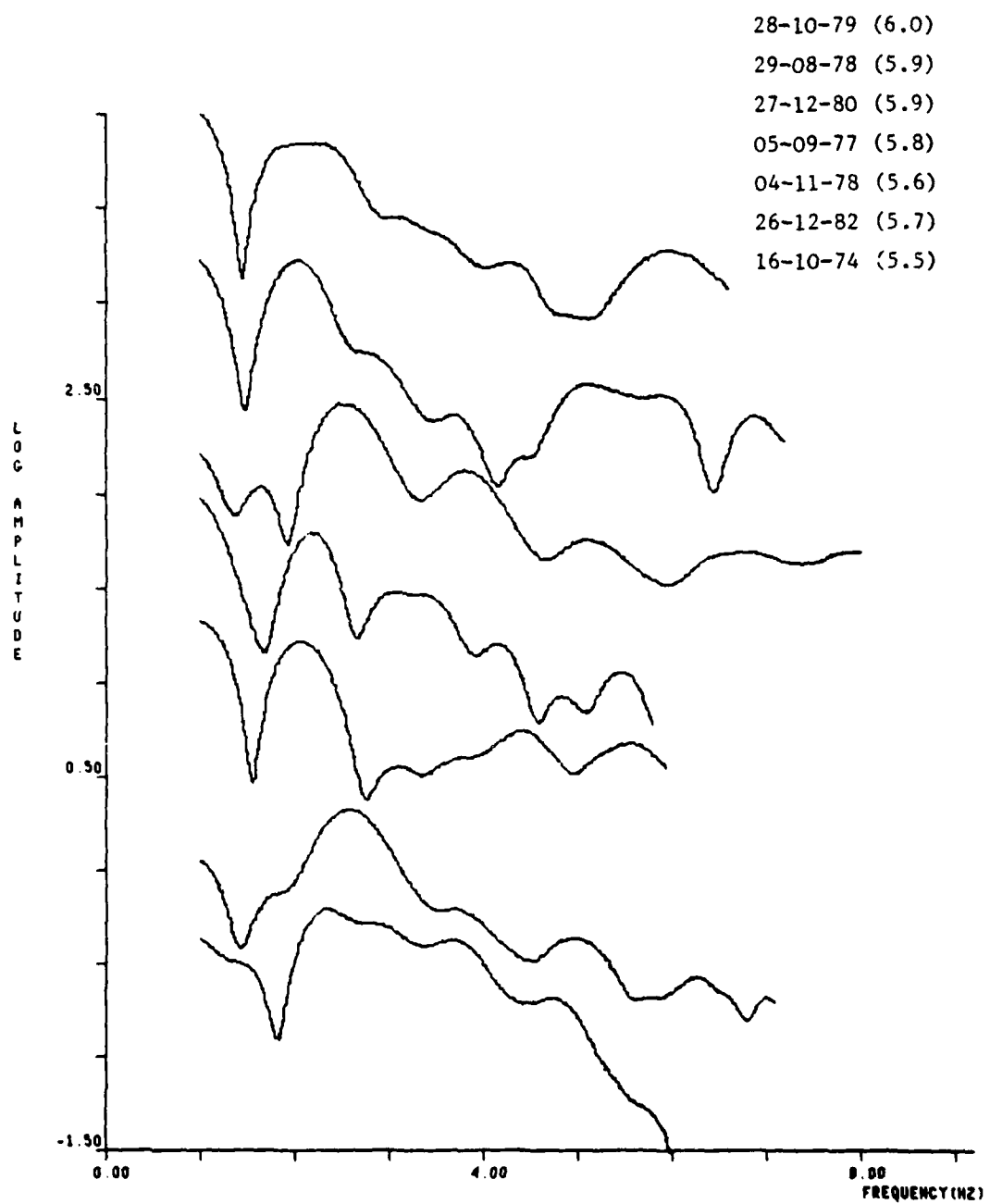


Figure A.2 EKA Recordings of Northeast Shagan River Explosions

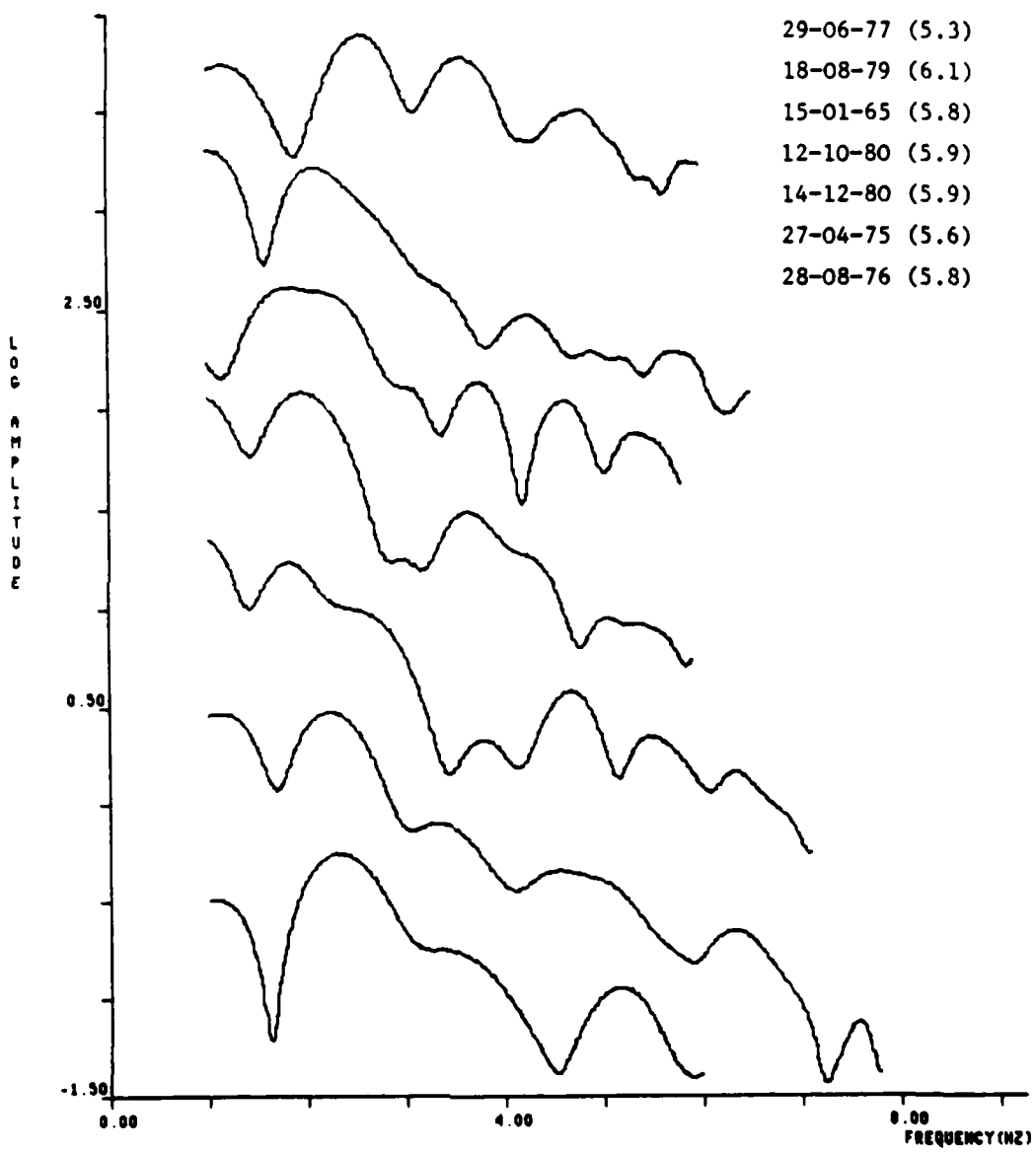


Figure A.2 (continued)

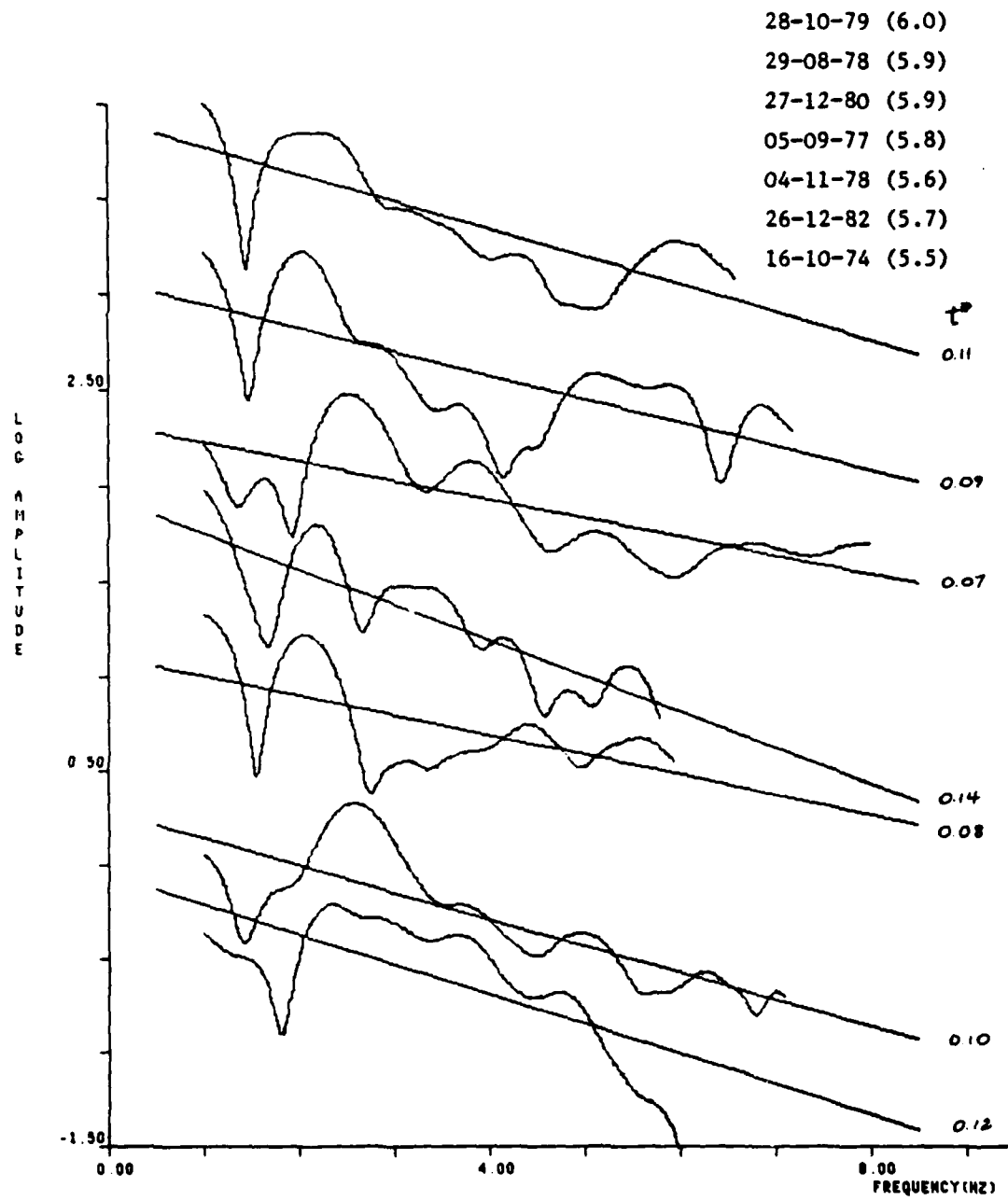


Figure A.2 (continued)

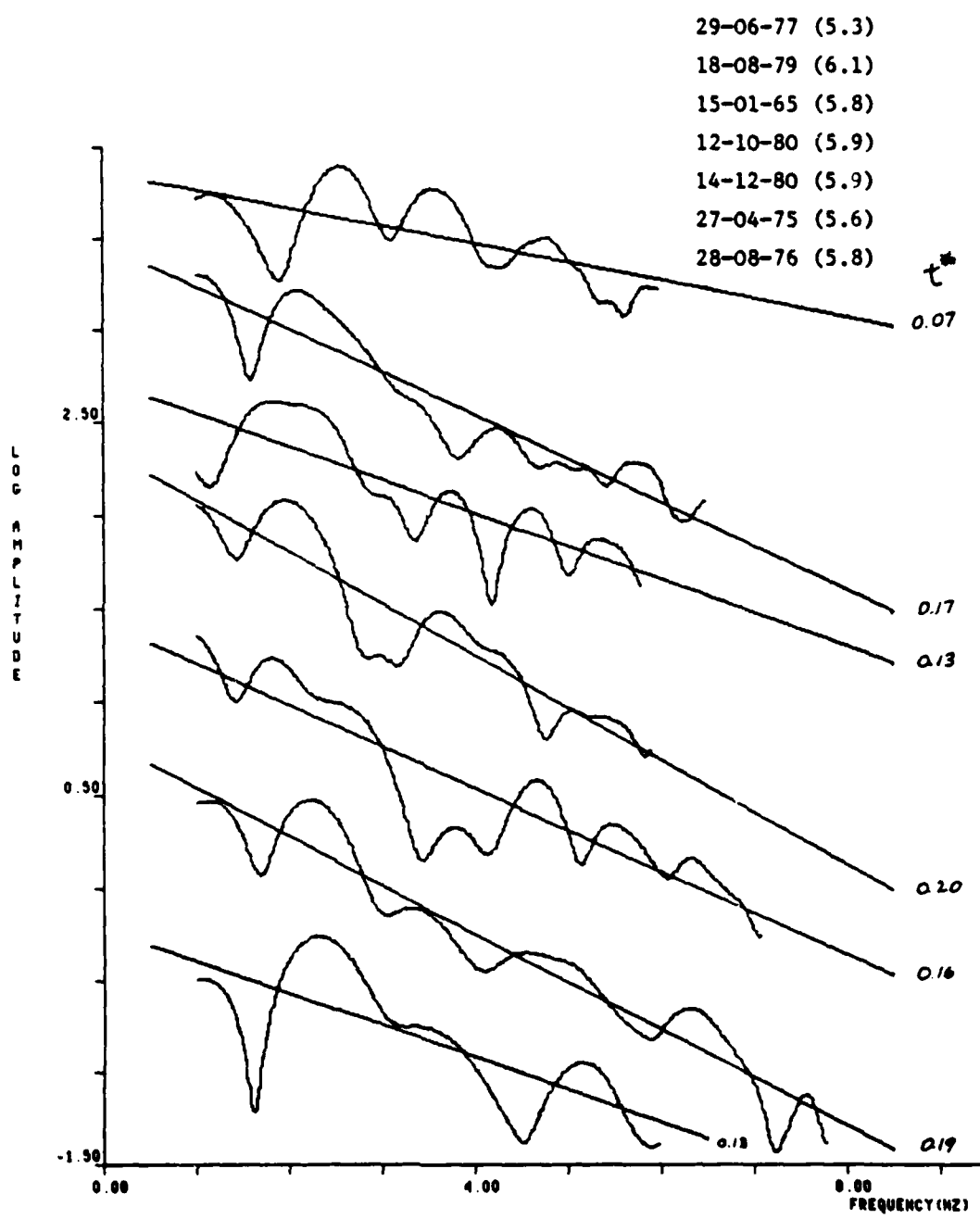


Figure A.2 (continued)

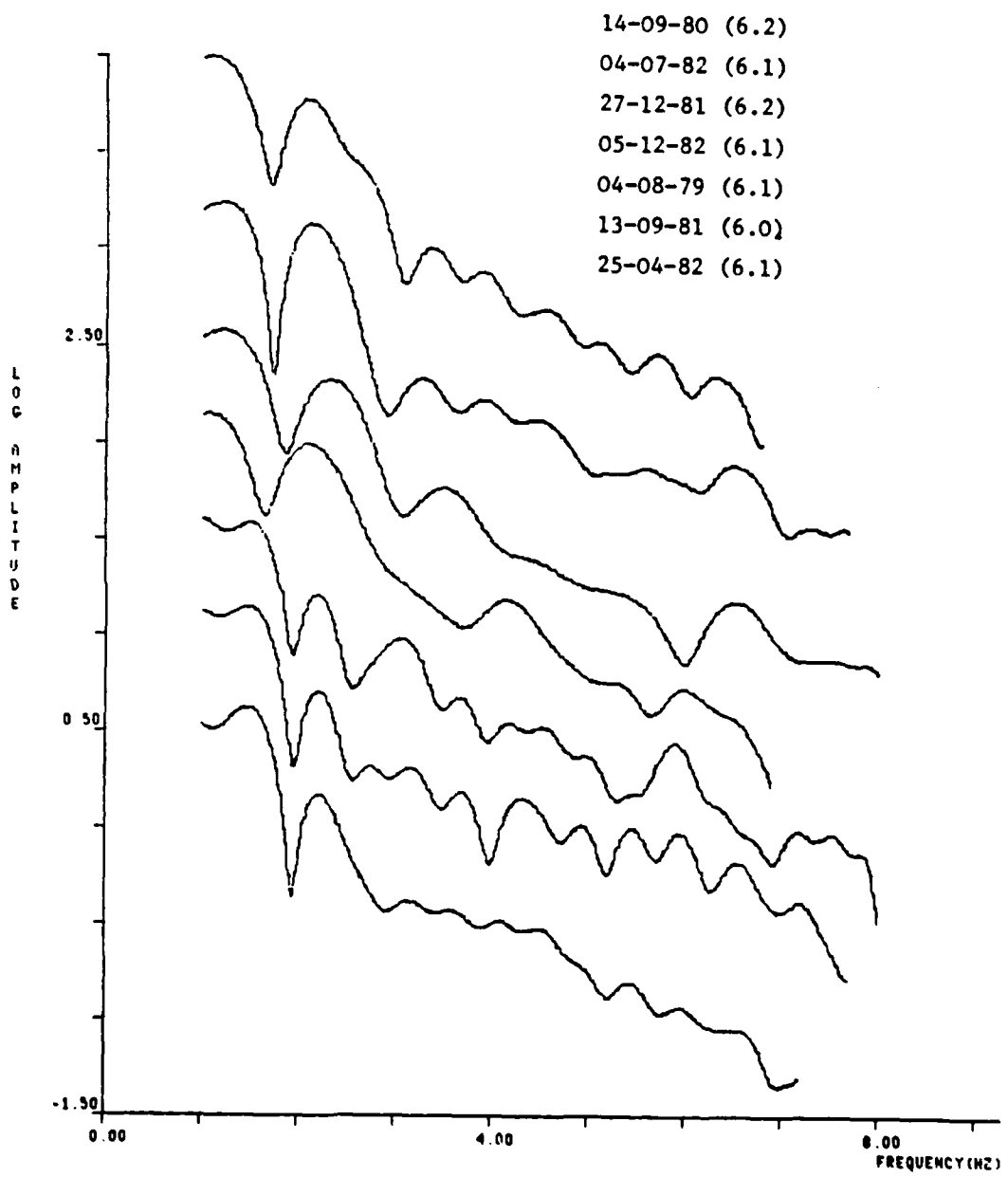


Figure A.3 GBA Recordings of Southwest Shagan River Explosions

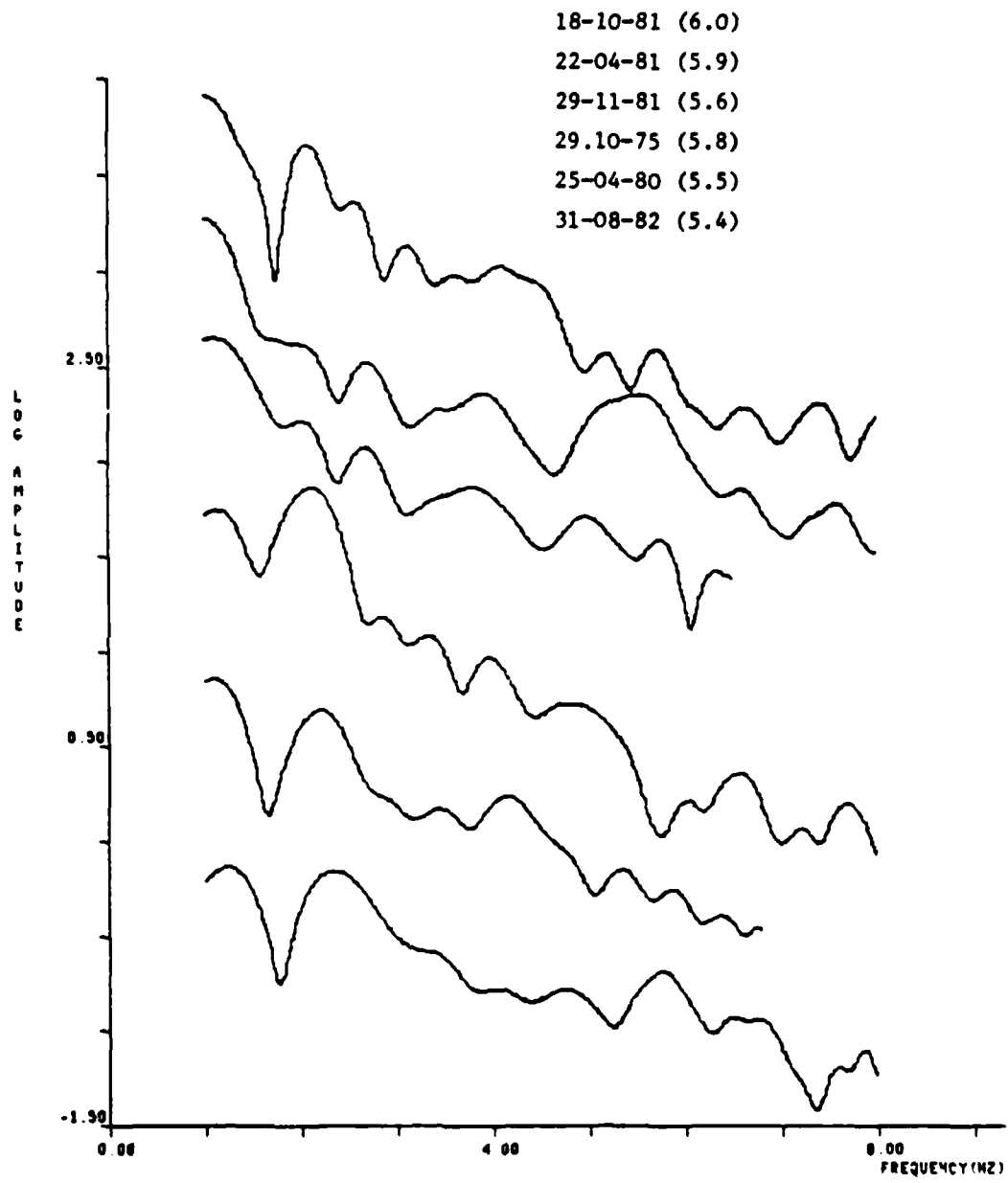


Figure A.3 (continued)

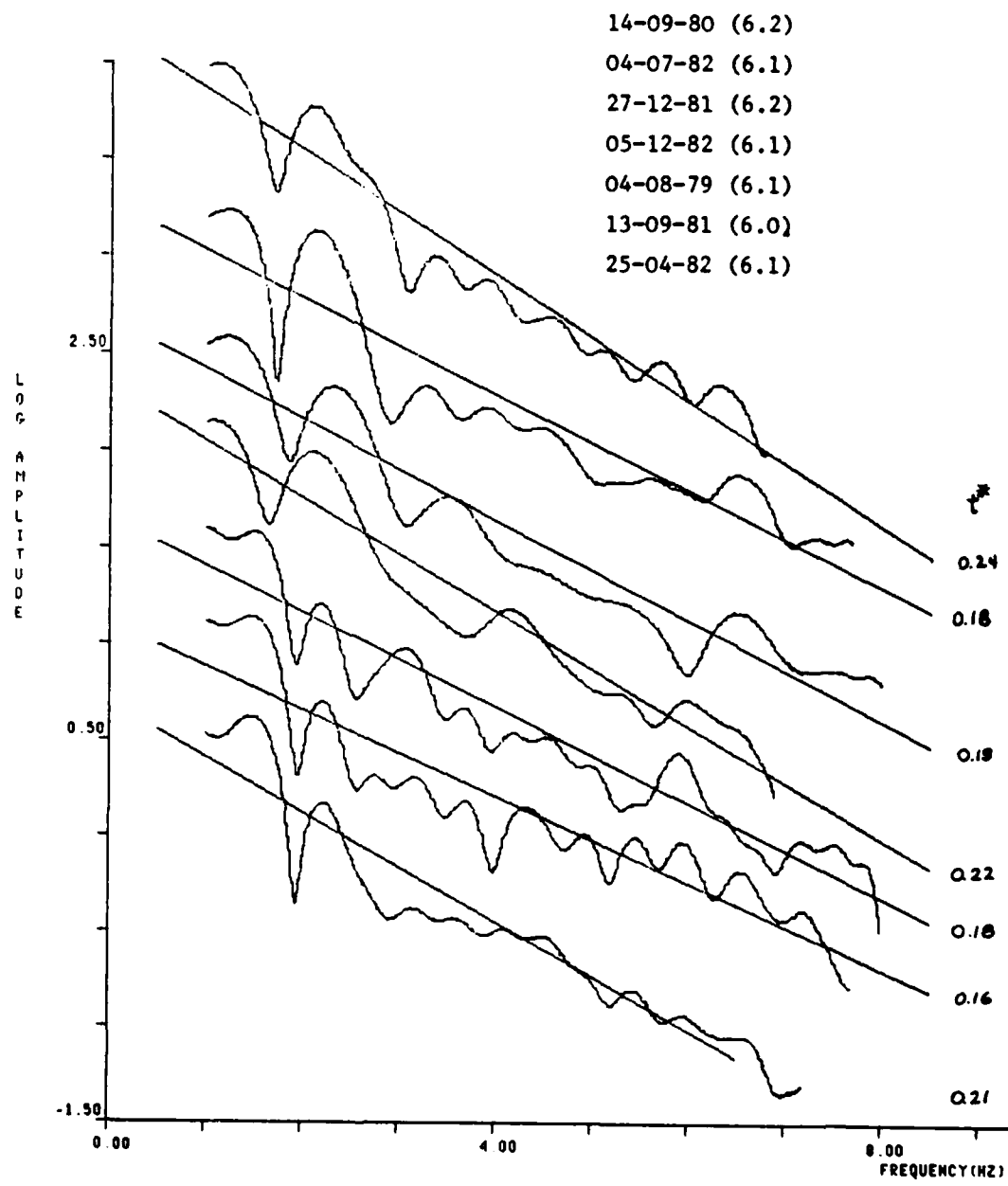


Figure A.3 (continued)

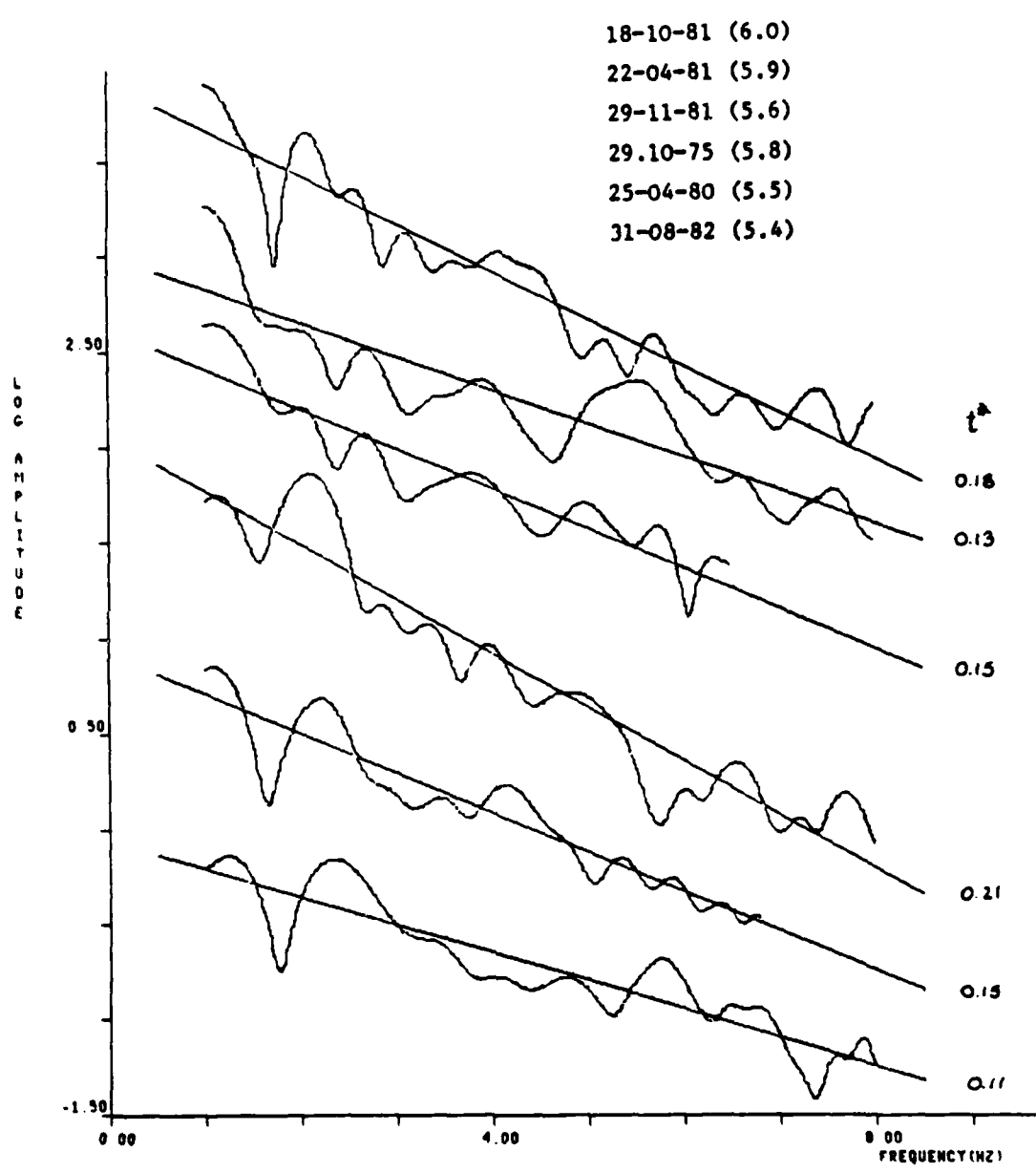


Figure A.3 (continued)

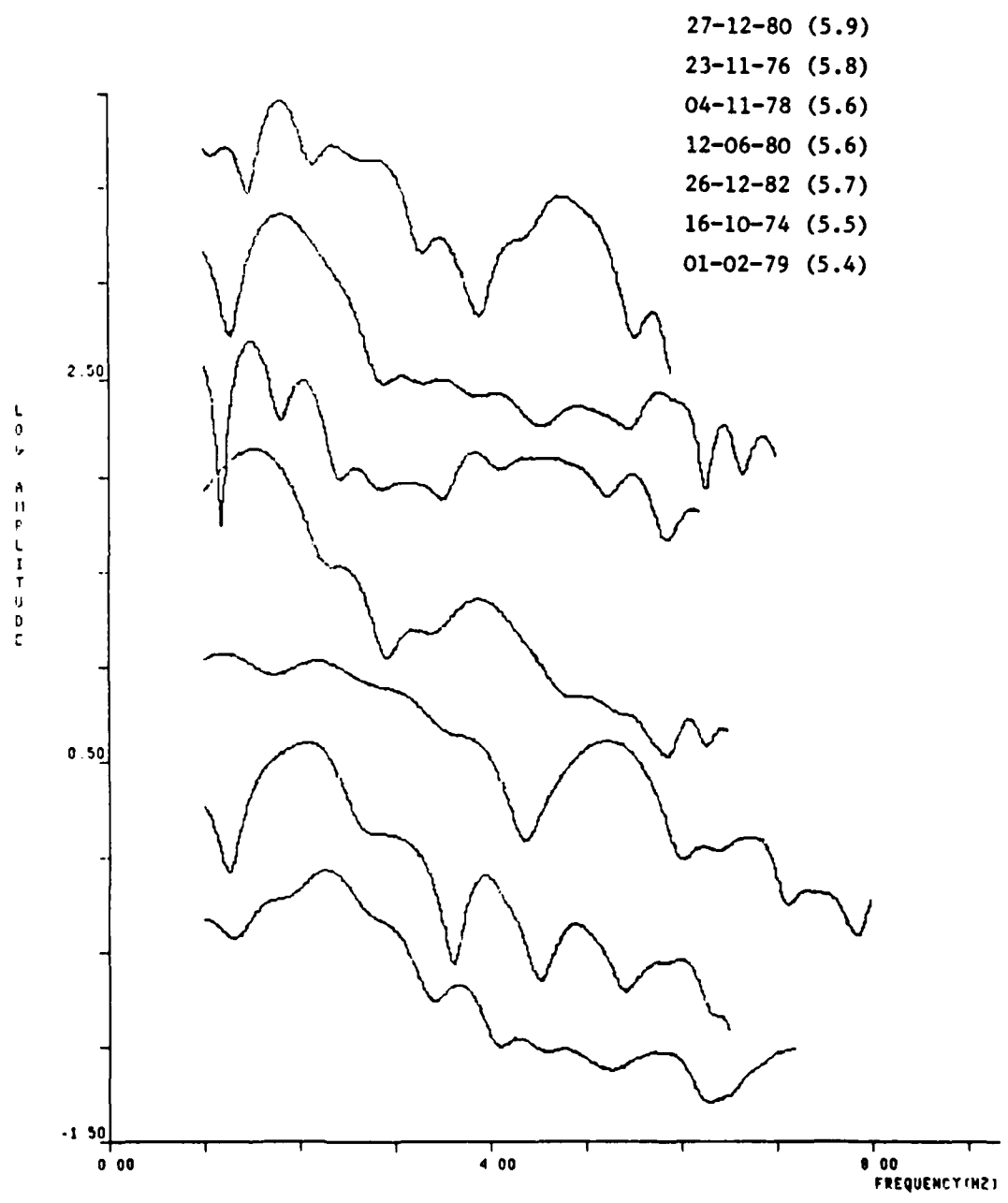


Figure A.4 GBA Recordings of Northeast Shagan River Explosions

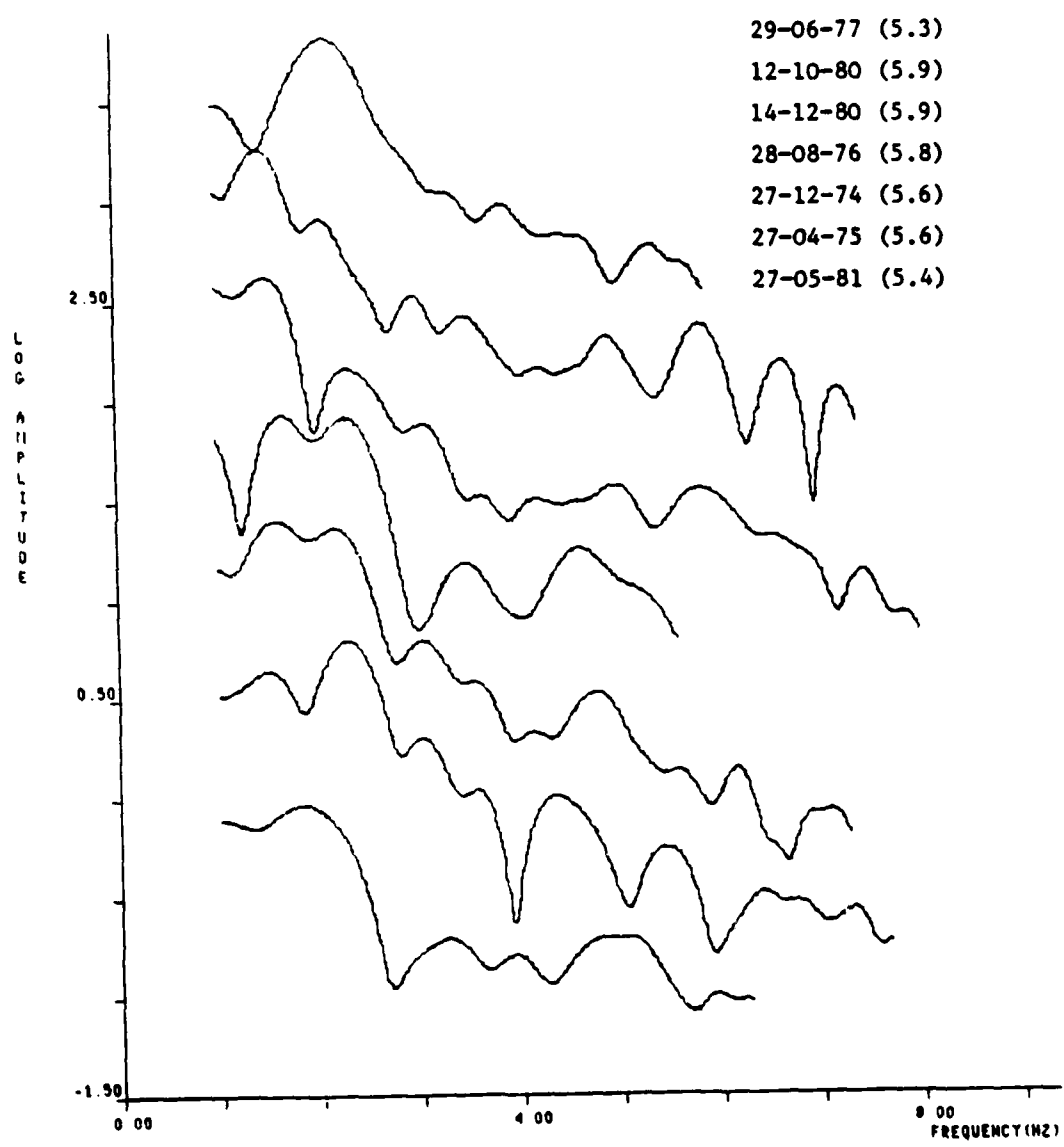


Figure A.4 (continued)

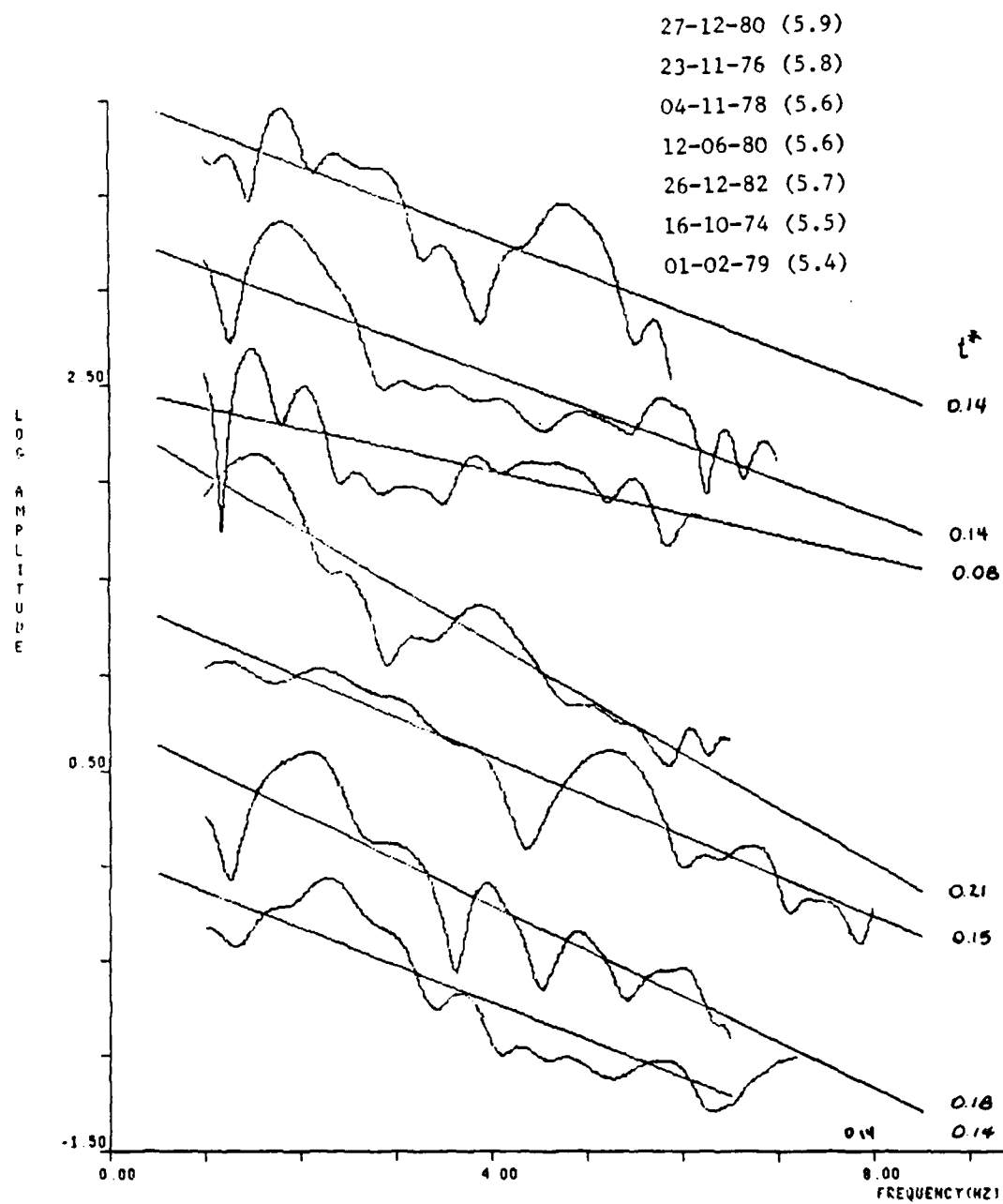


Figure A.4 (continued)

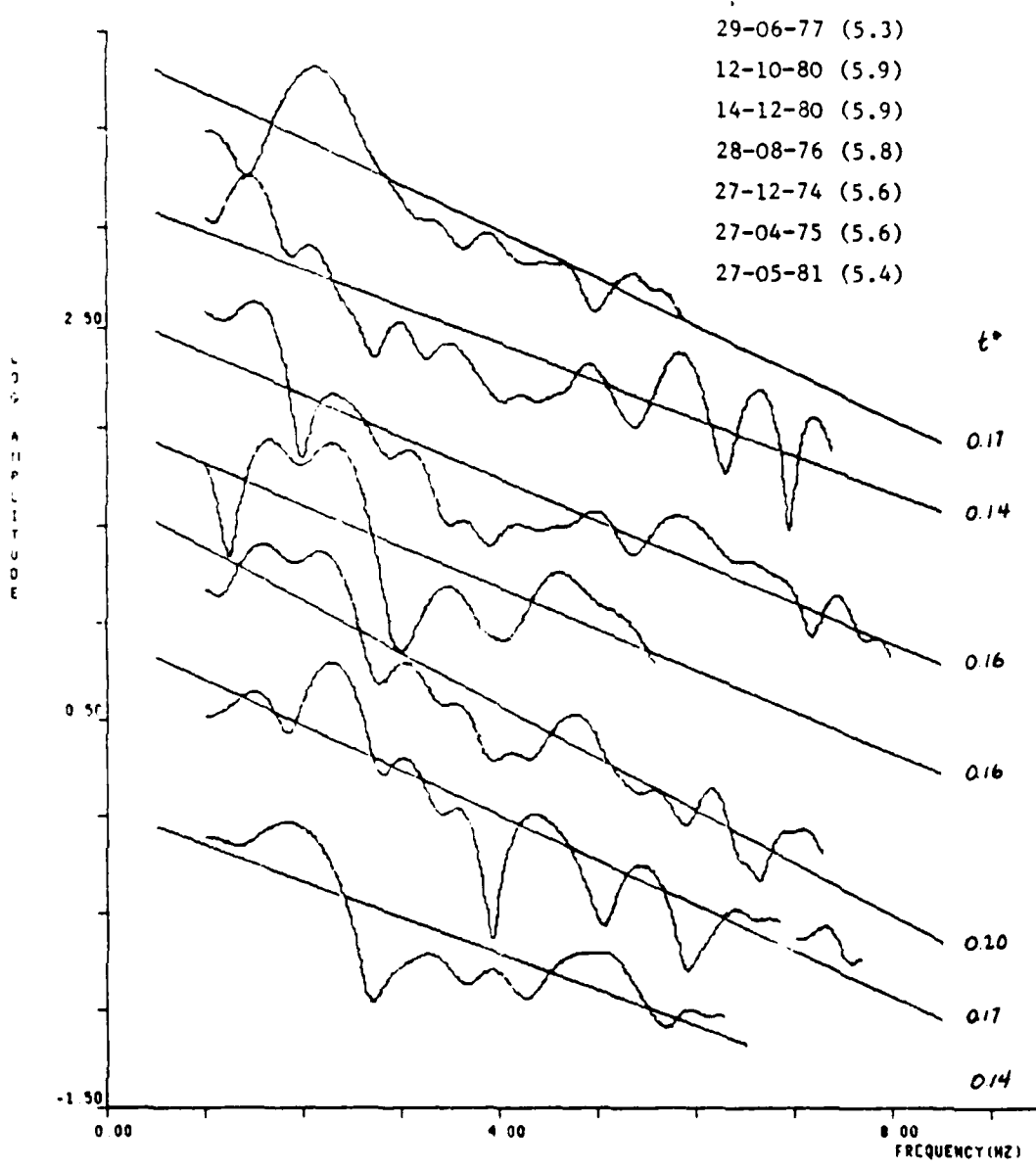


Figure A.4 (continued)

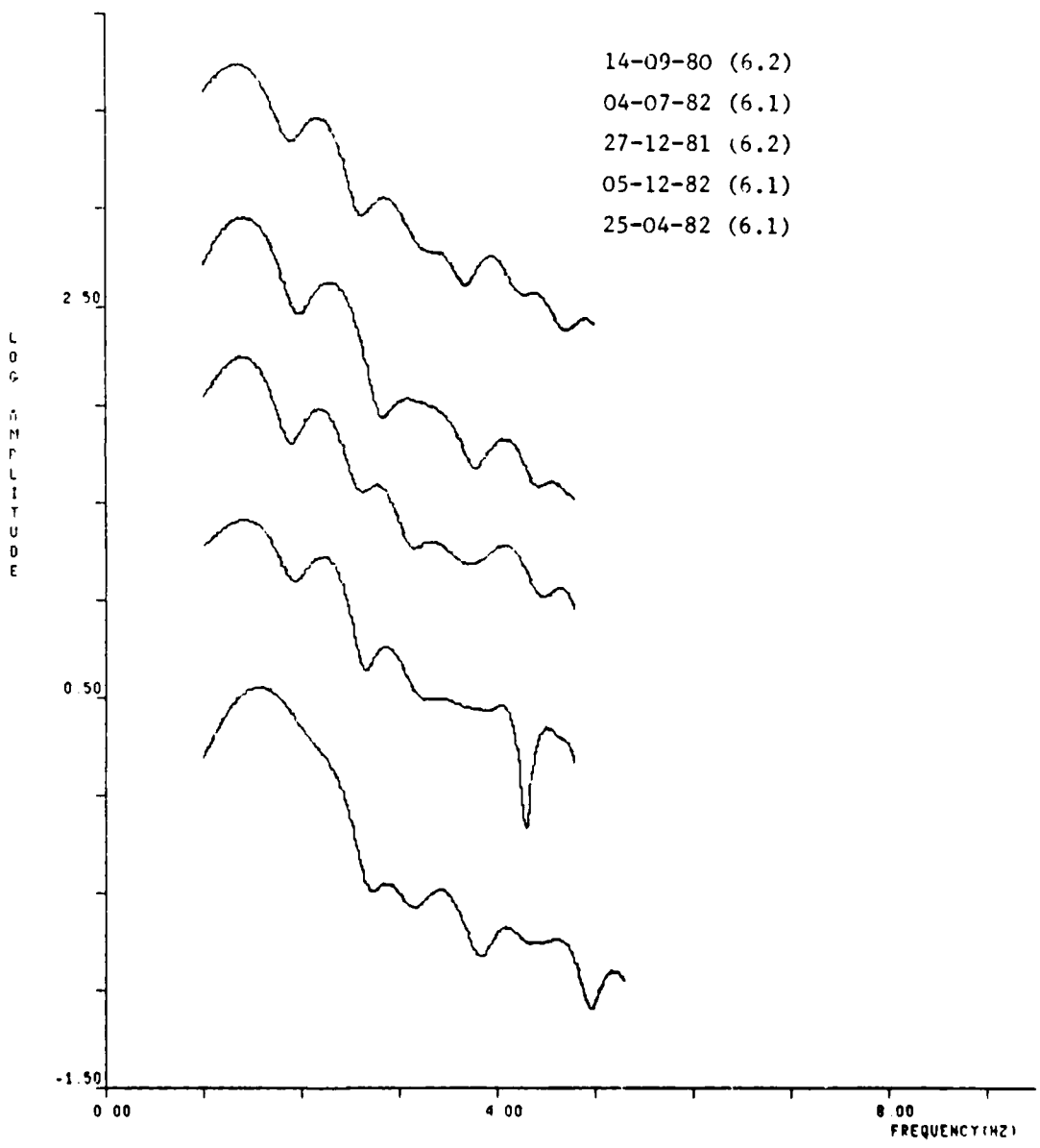


Figure A.5 GBA PcP Southwest Shagan River Explosions

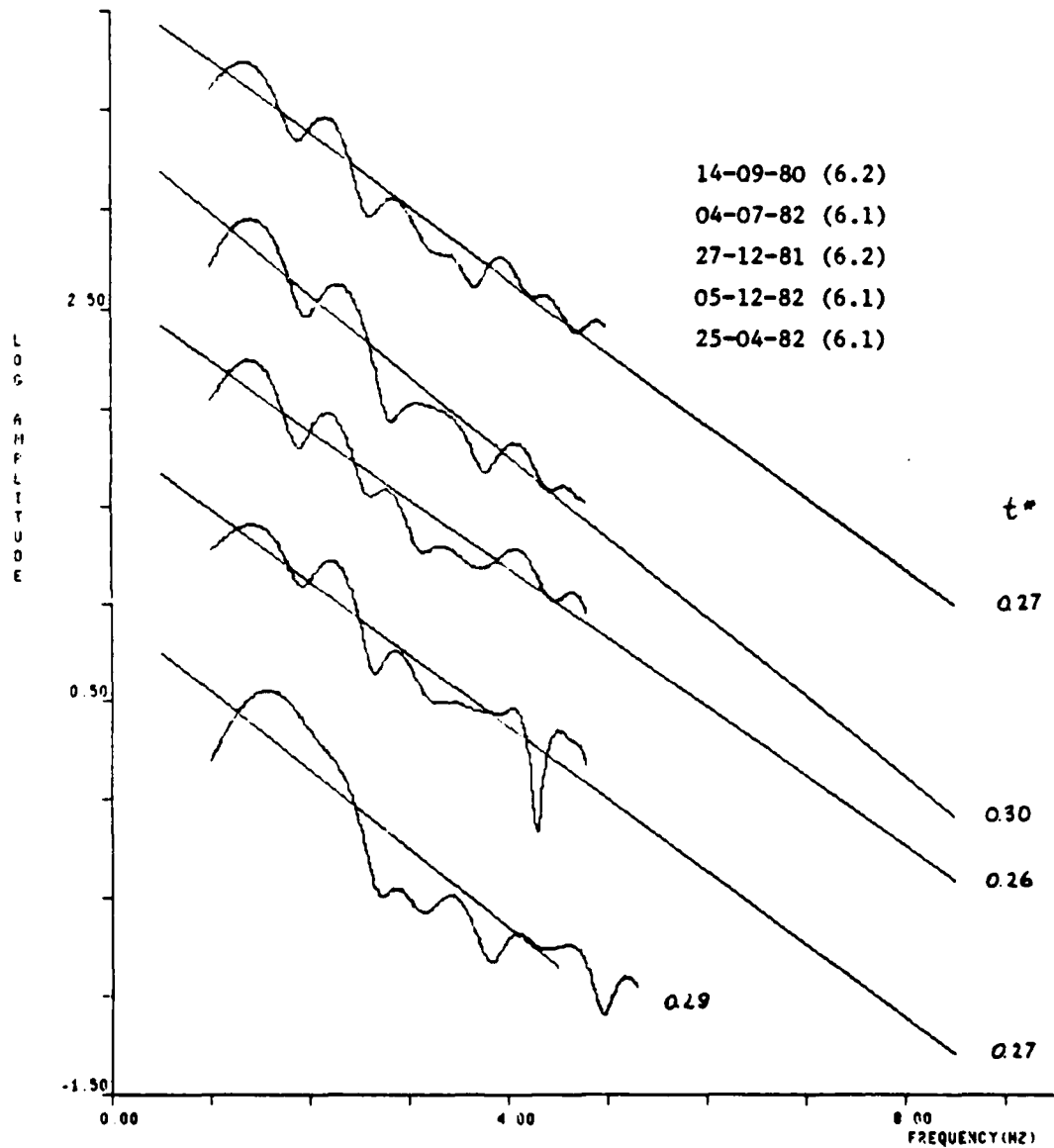


Figure A.5 (continued)

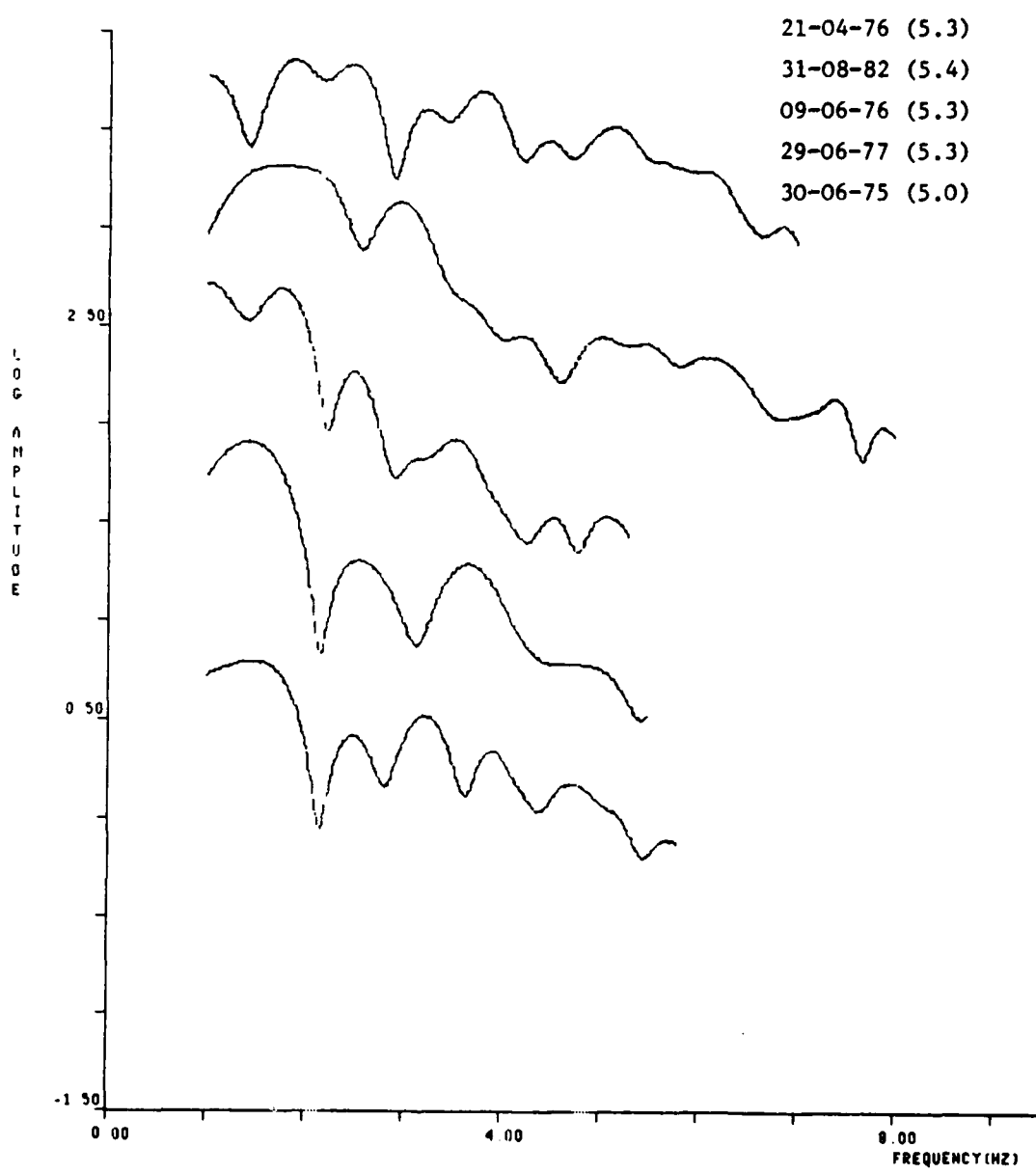


Figure A.6 YKA Recordings of Shagan River Explosions

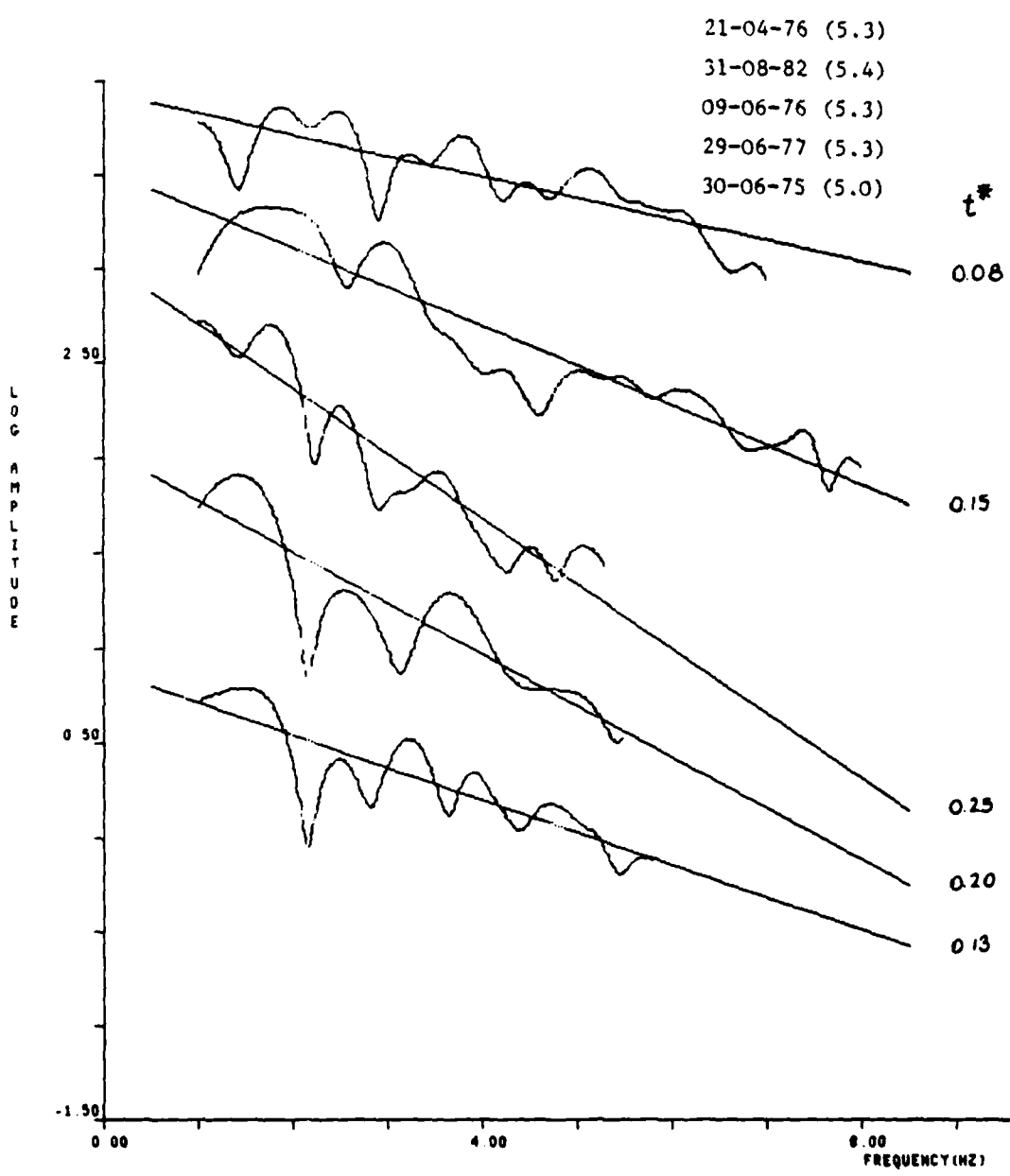


Figure A.6 (continued)

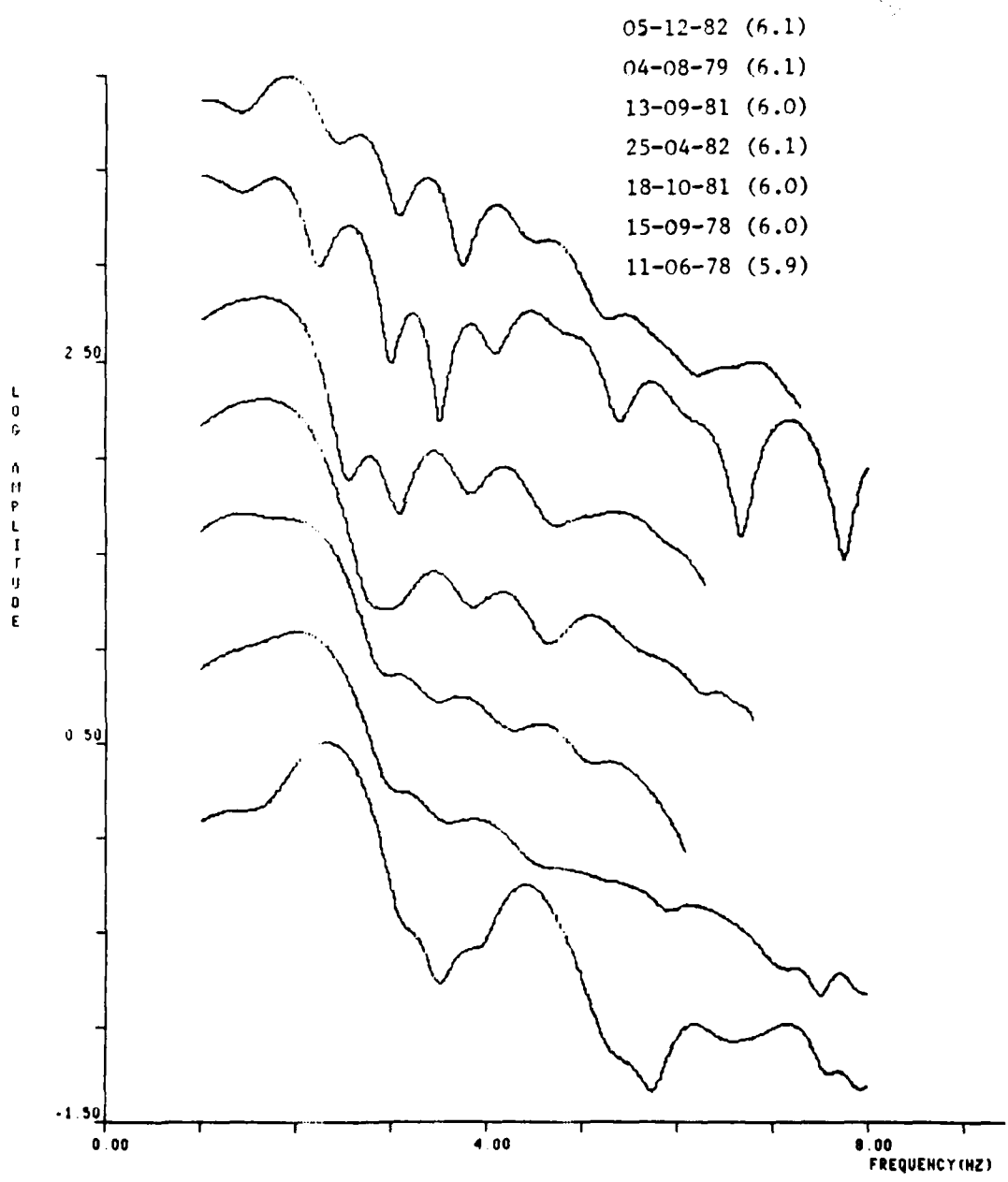


Figure A.7 WRA Recordings of Southwest Shagan River Explosions

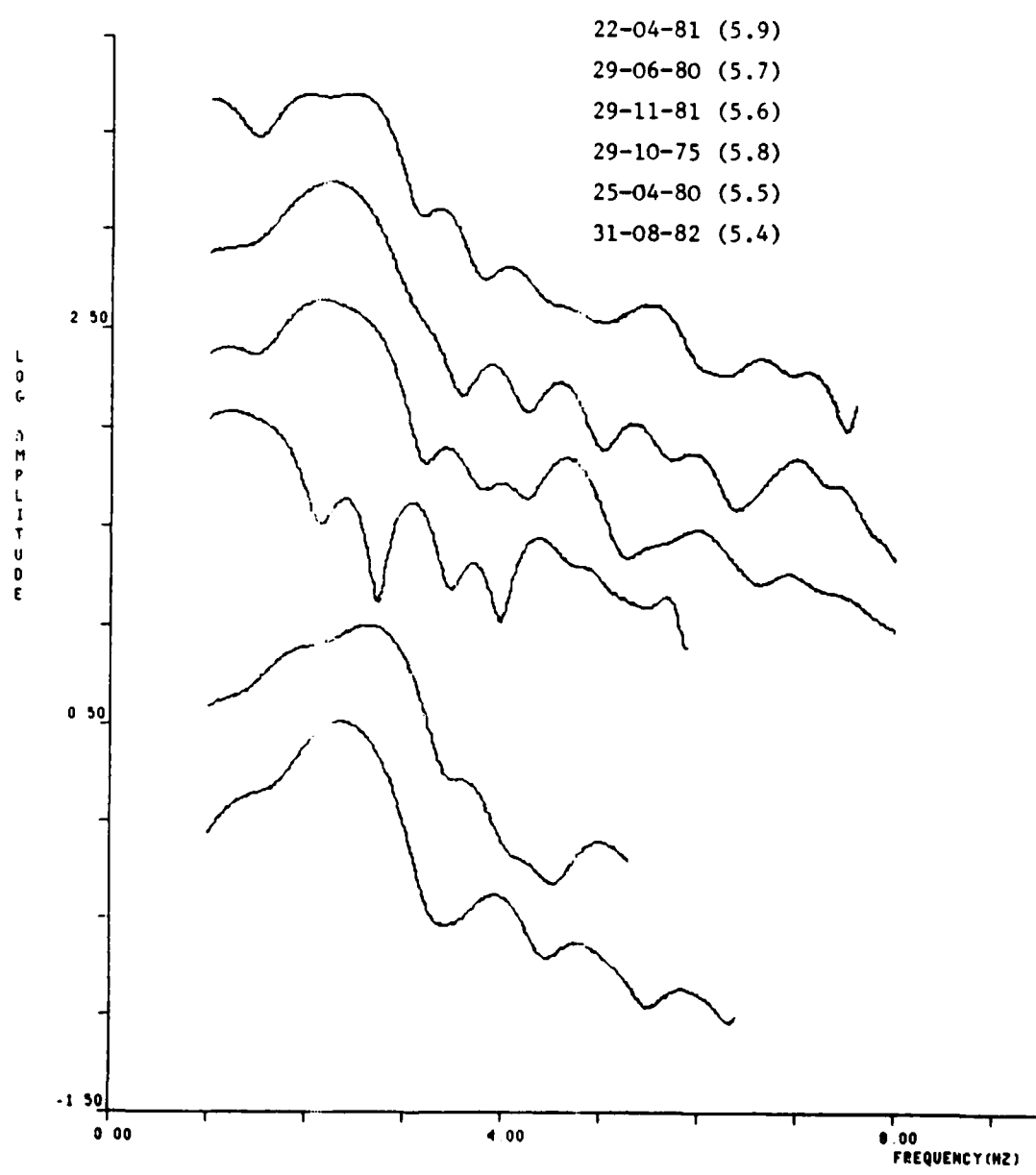


Figure A.7 (continued)

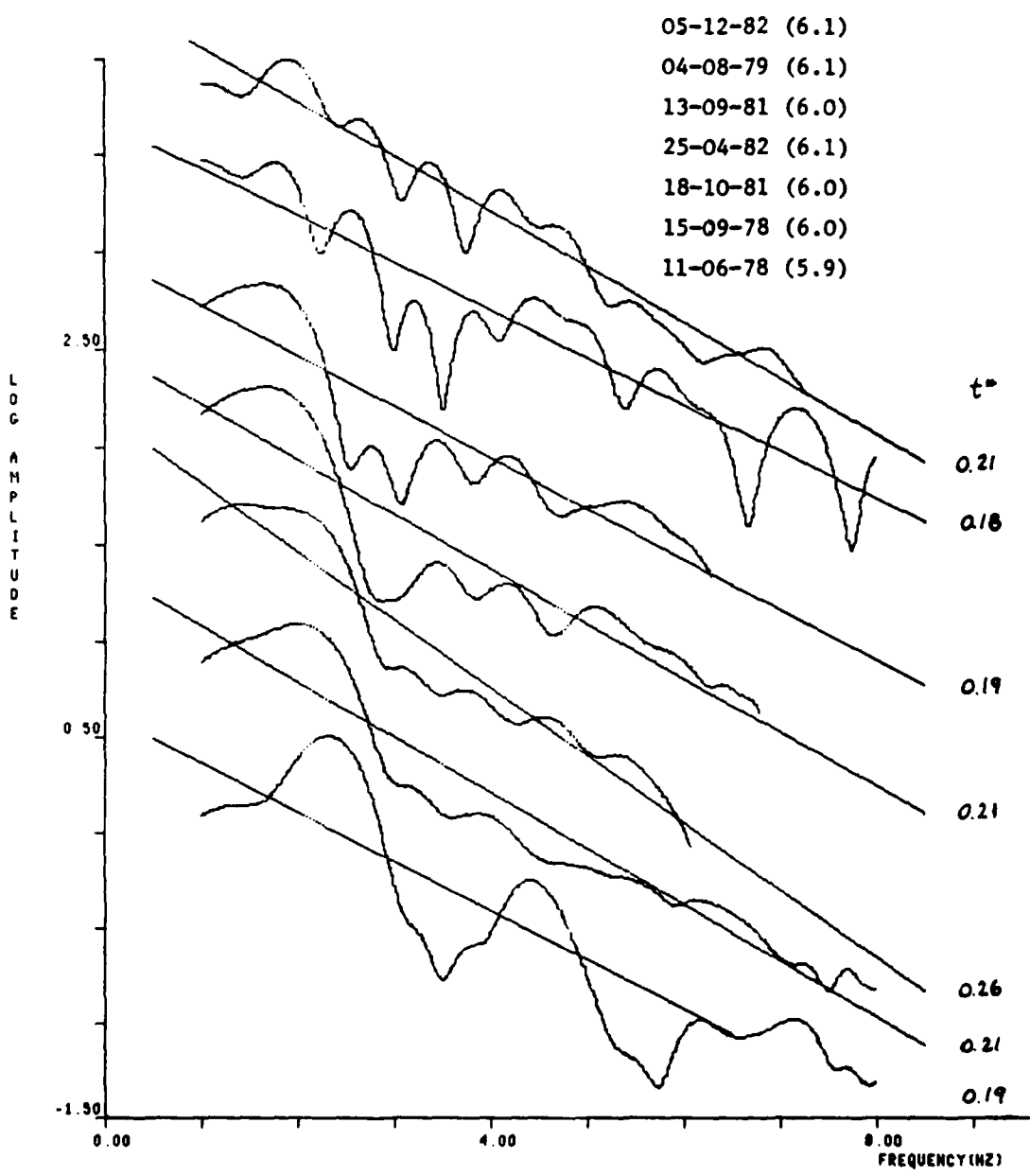


Figure A.7 (continued)

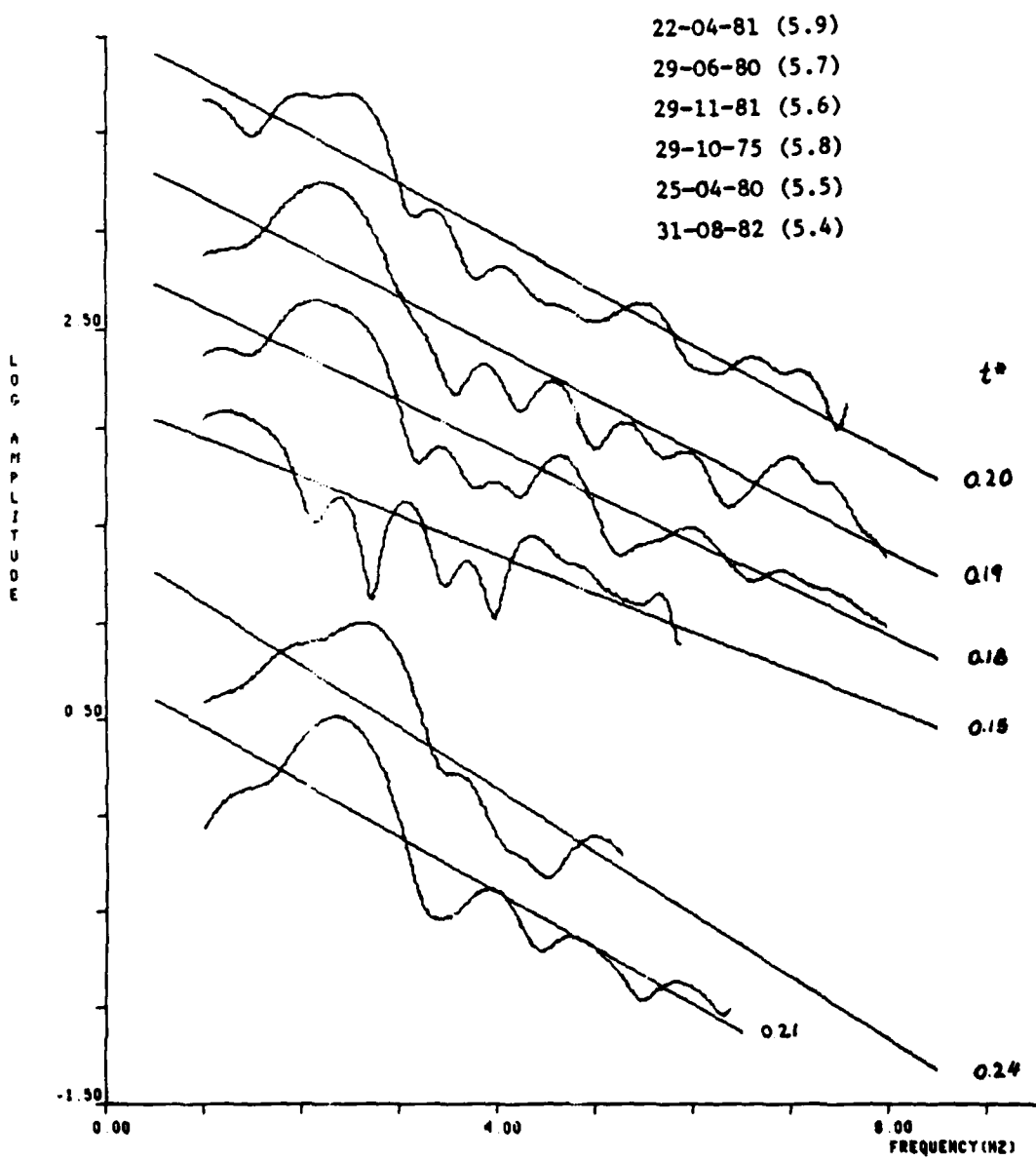


Figure A.7 (continued)

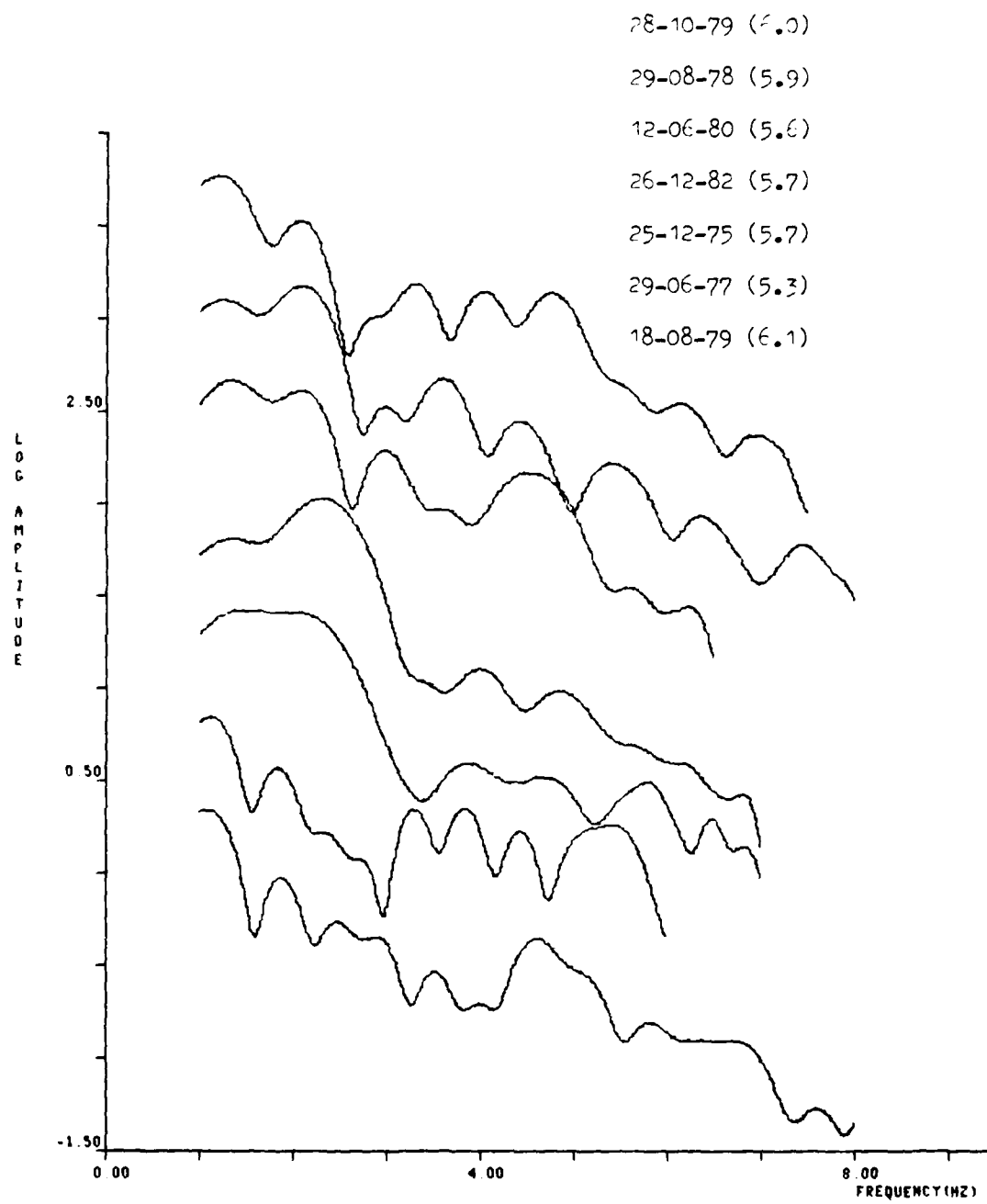


Figure A.8 WRA Recordings of Northeast Shagan River Explosions

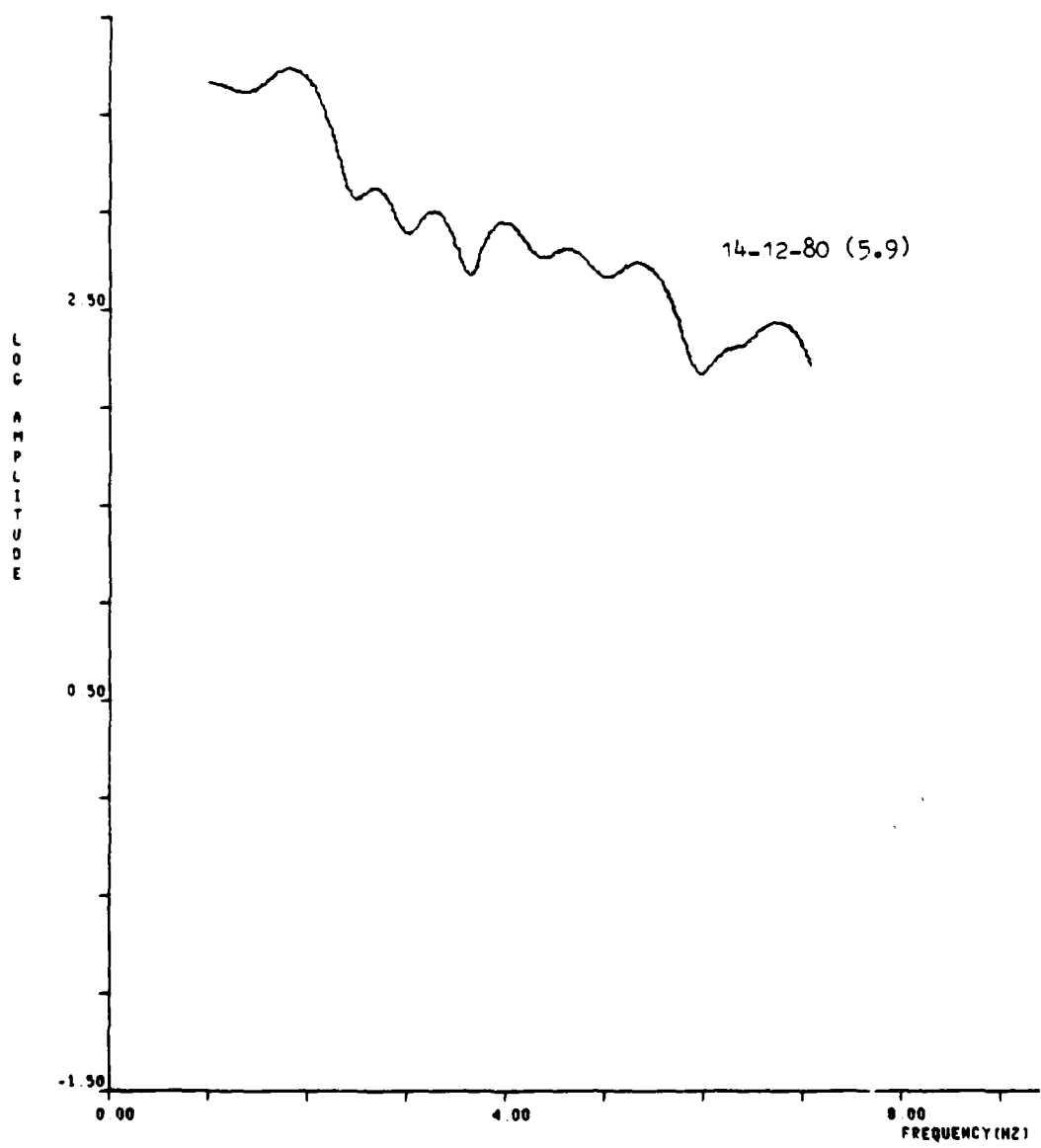


Figure A.8 (continued)

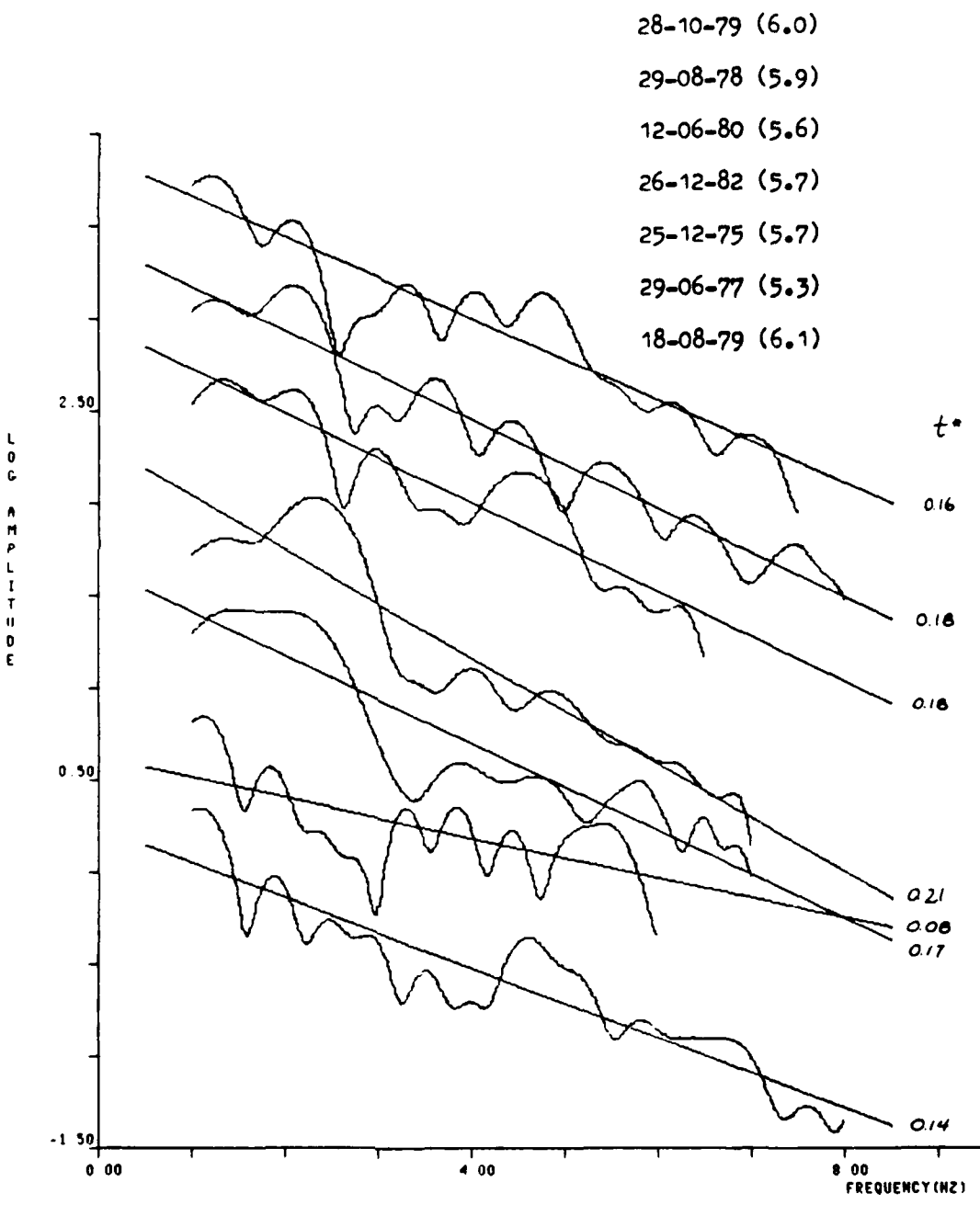


Figure A.8 (continued)

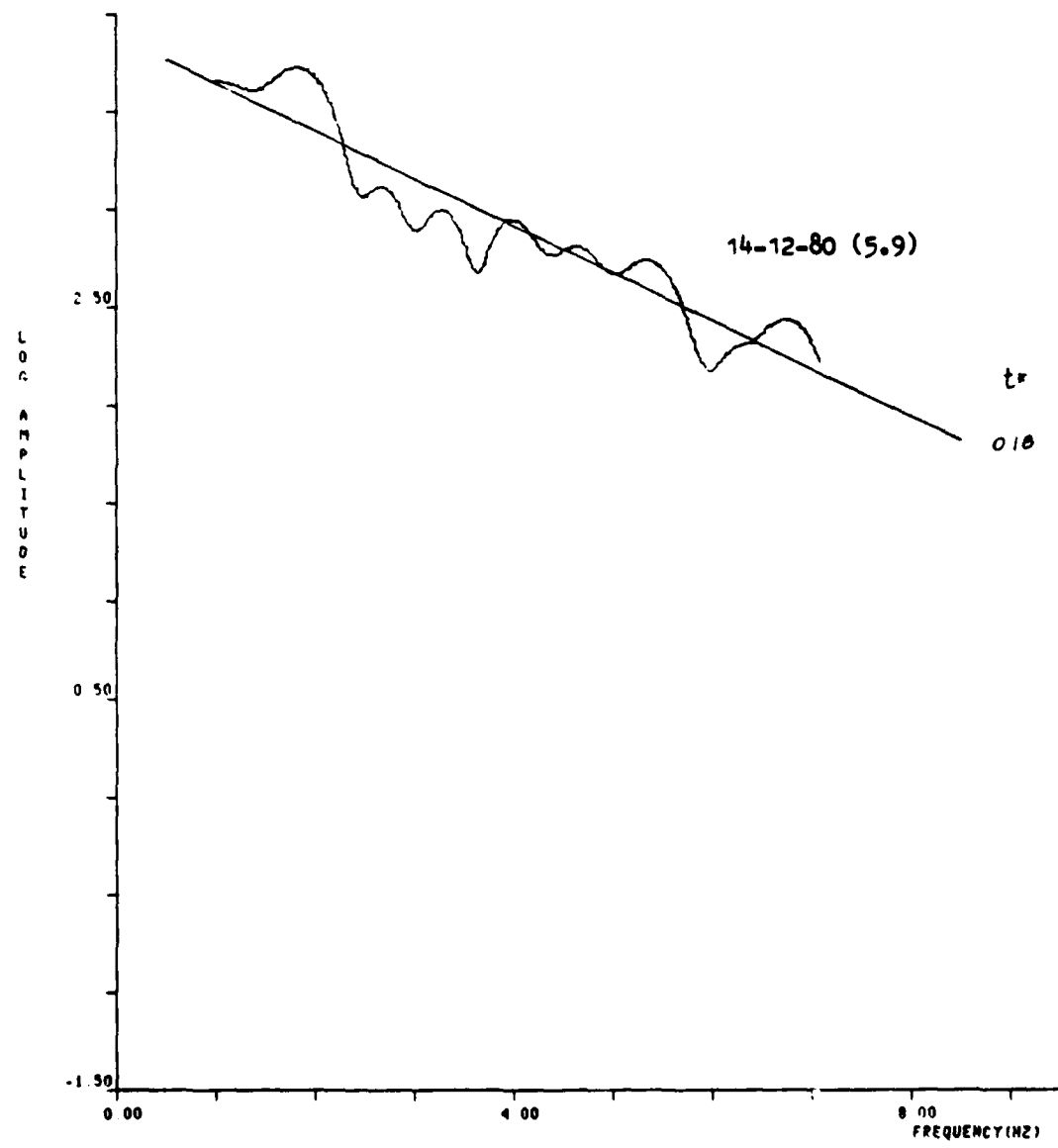


Figure A.8 (continued)

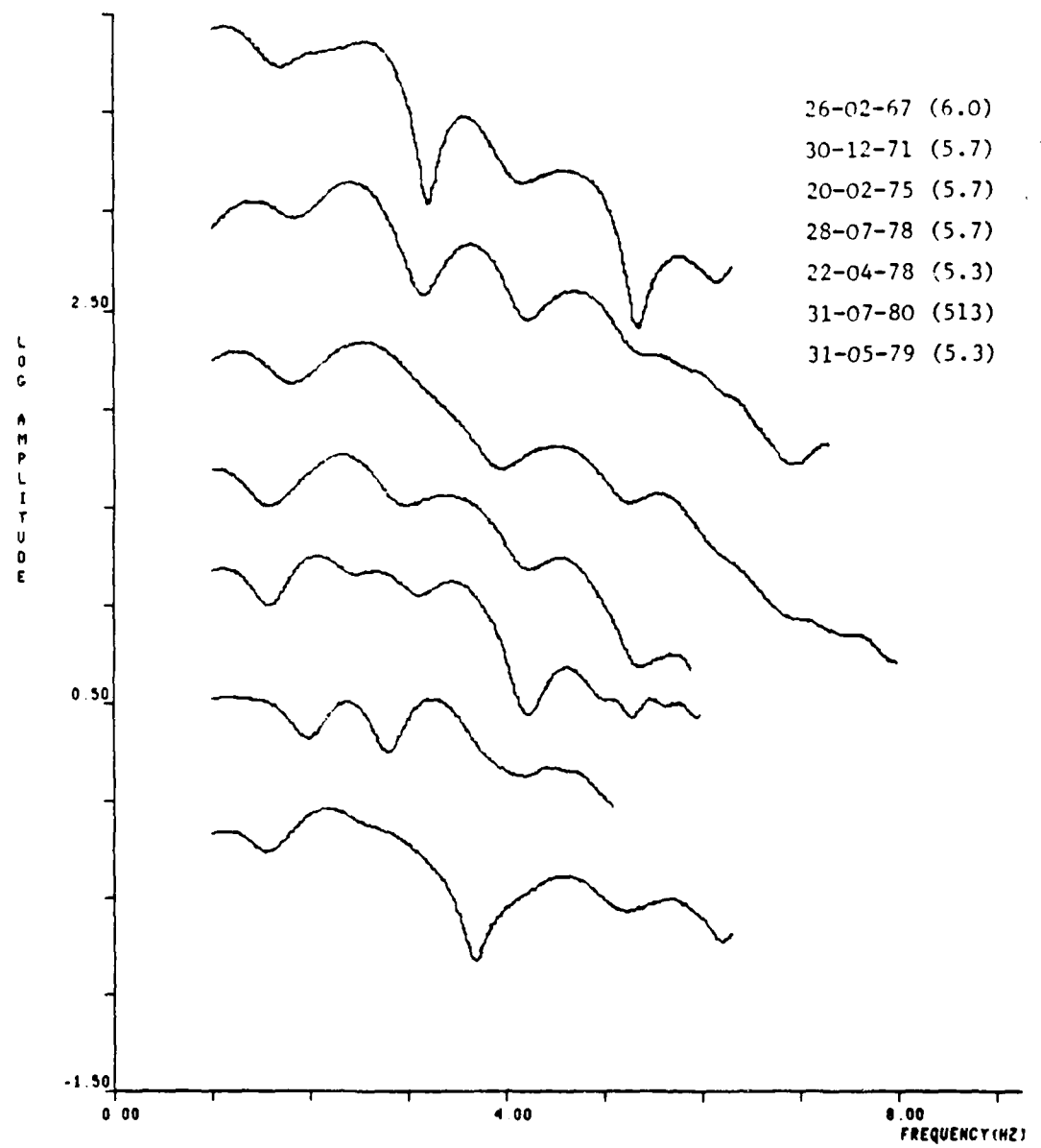


Figure A.9 EKA Recordings of Degelen Explosions

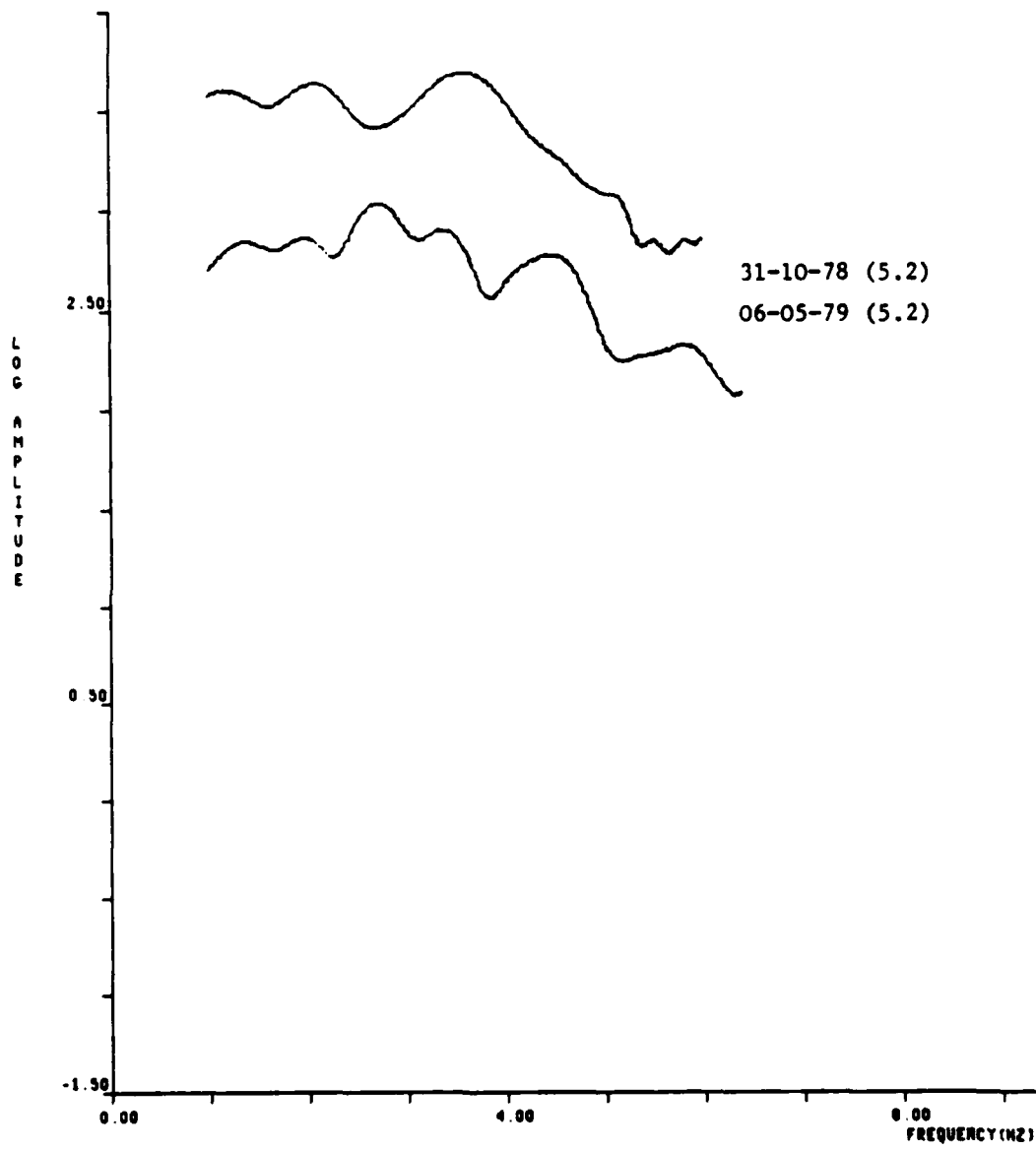


Figure A.9 (continued)

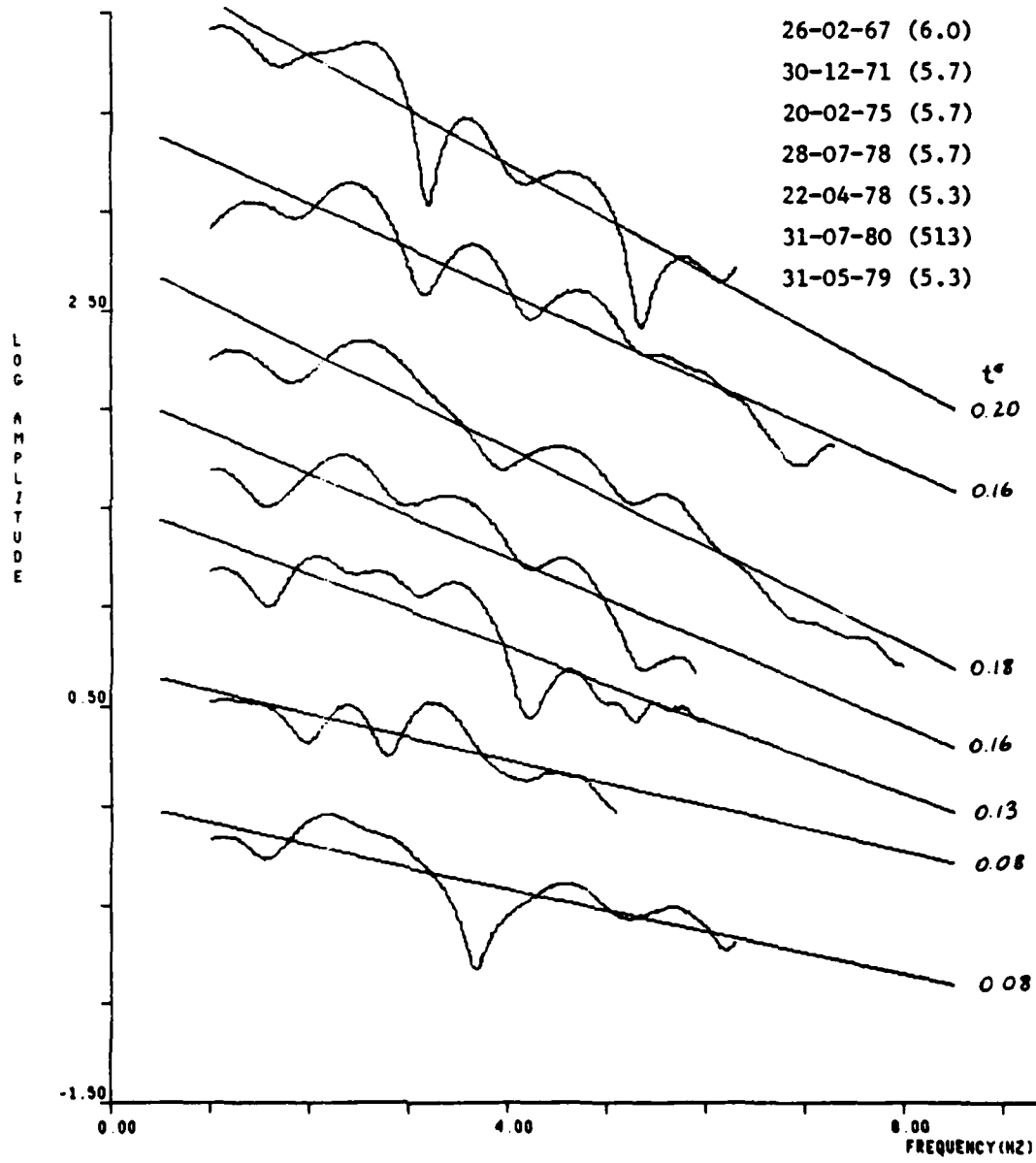


Figure A.9 (continued)

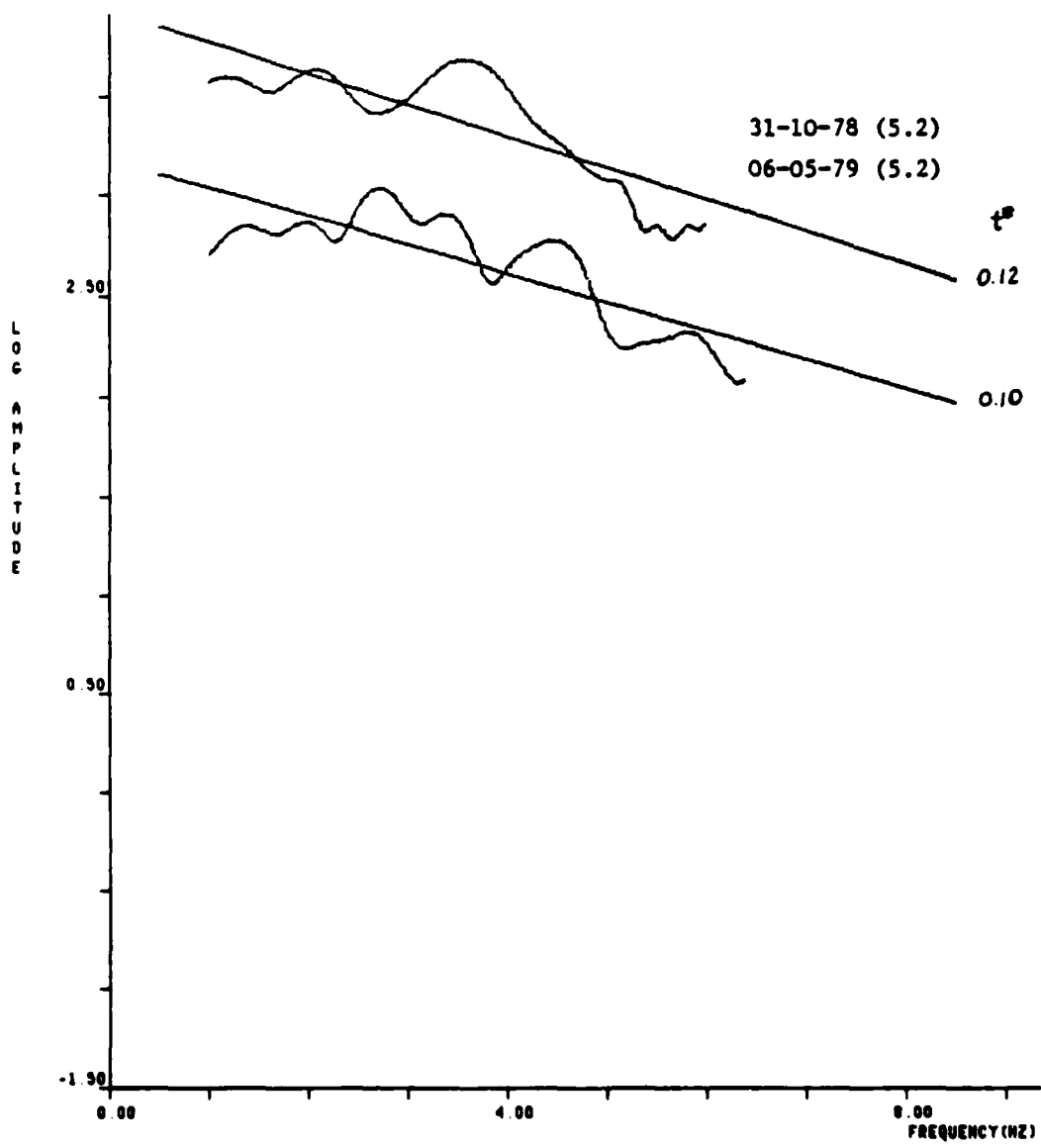


Figure A.9 (continued)

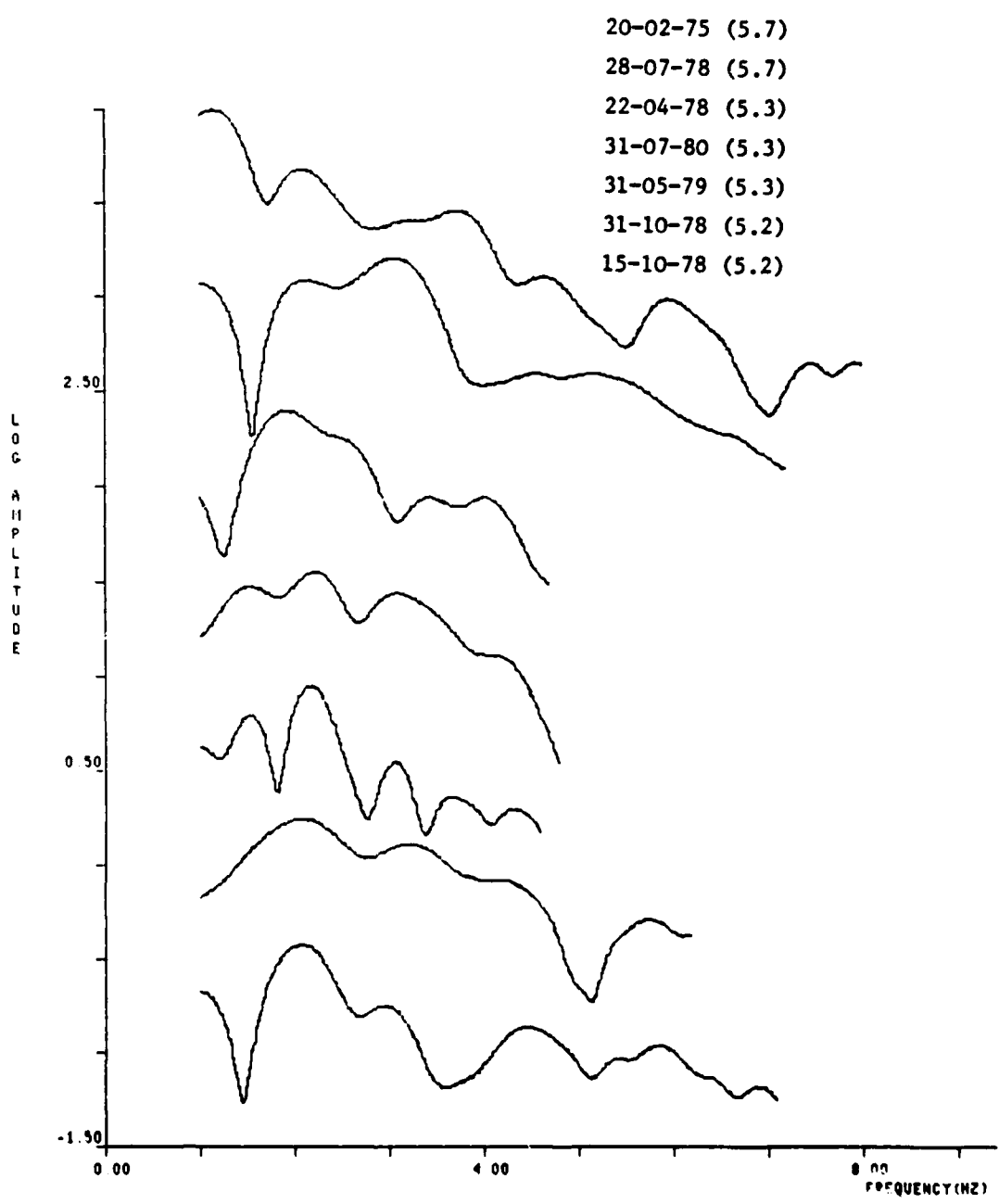


Figure A.10 GBA Recordings of Degelen Explosions

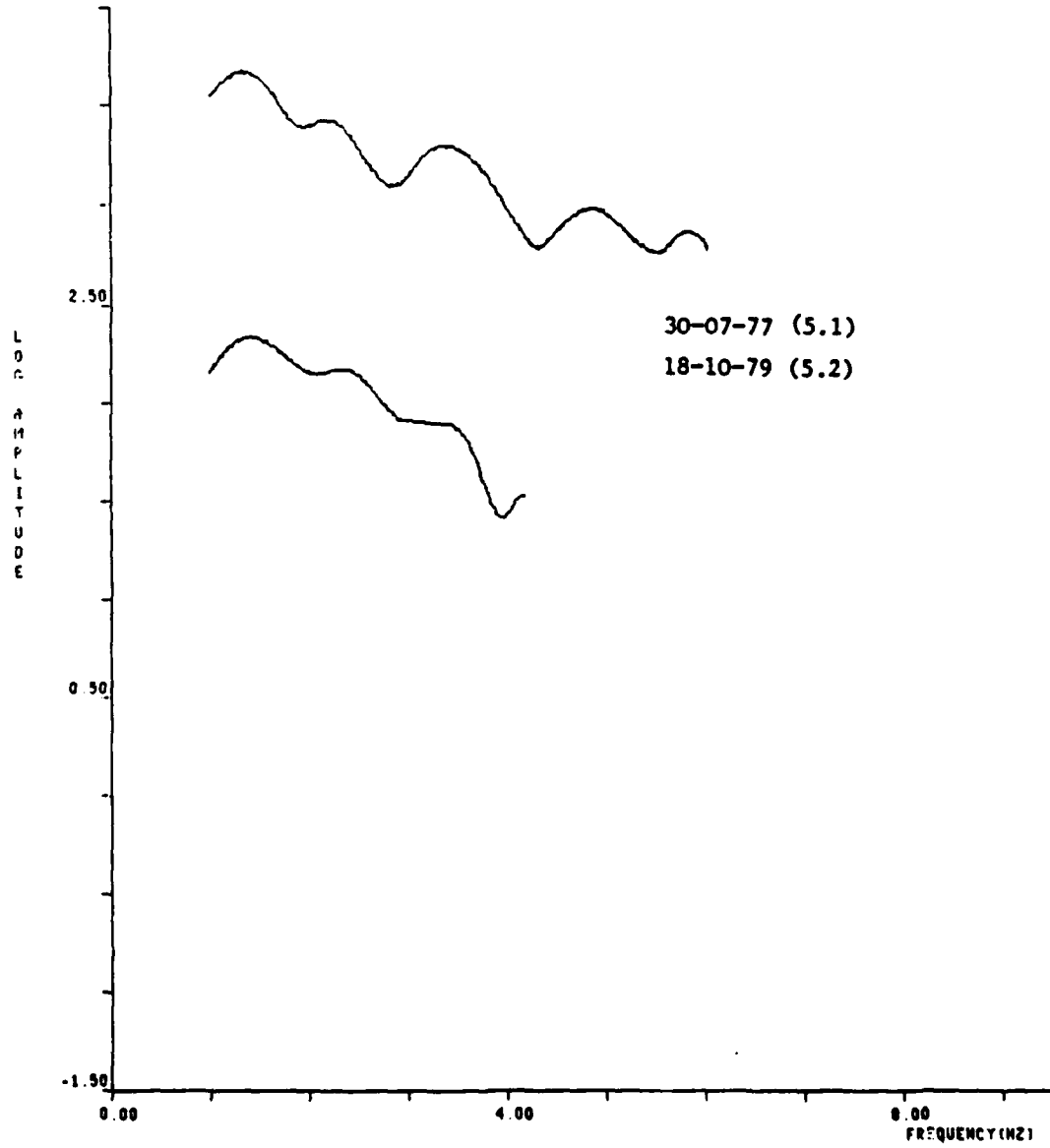


Figure A.10 (continued)

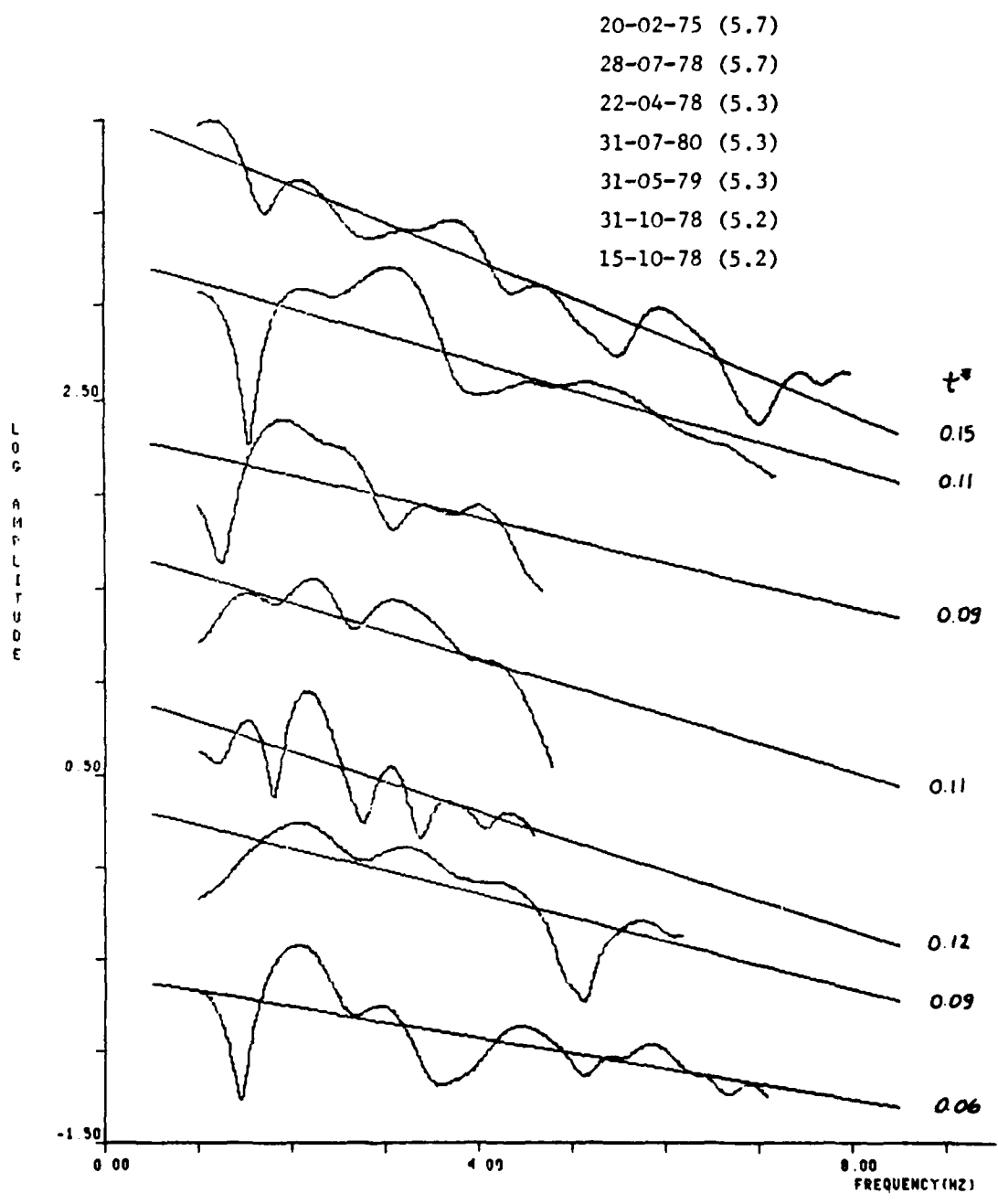


Figure A.10 (continued)

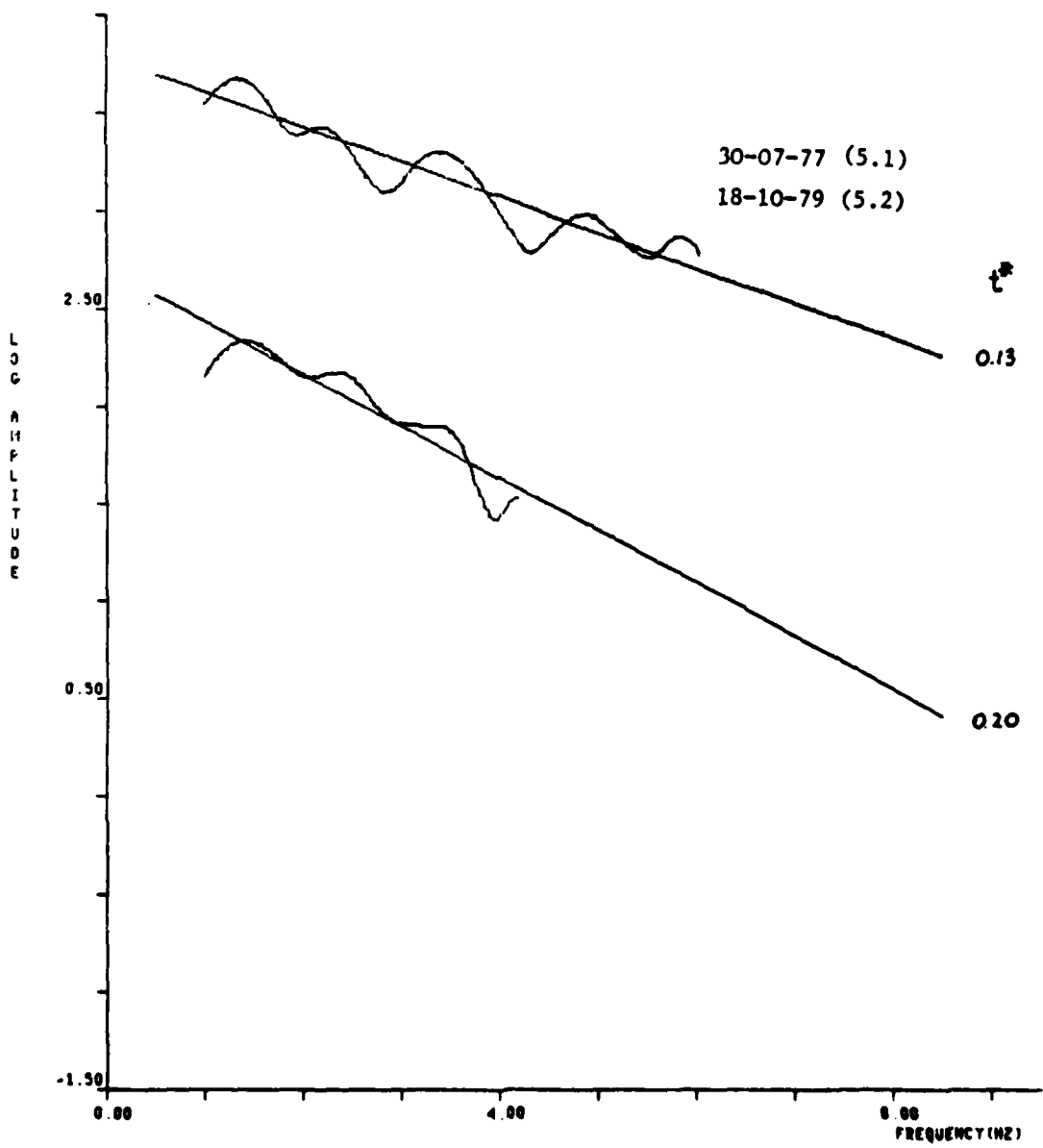


Figure A.10 (continued)

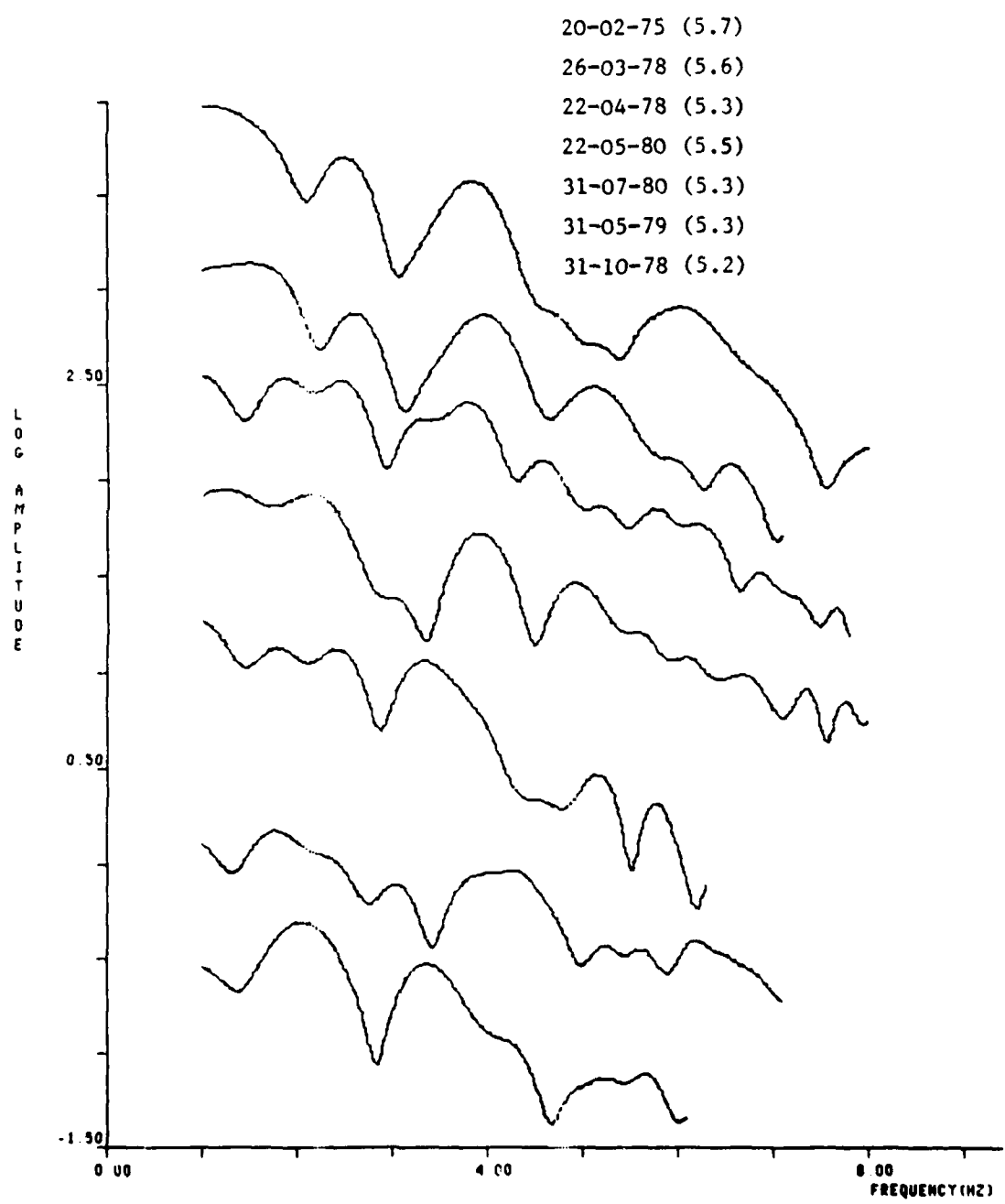


Figure A.11 YKA Recordings of Degelen Explosions

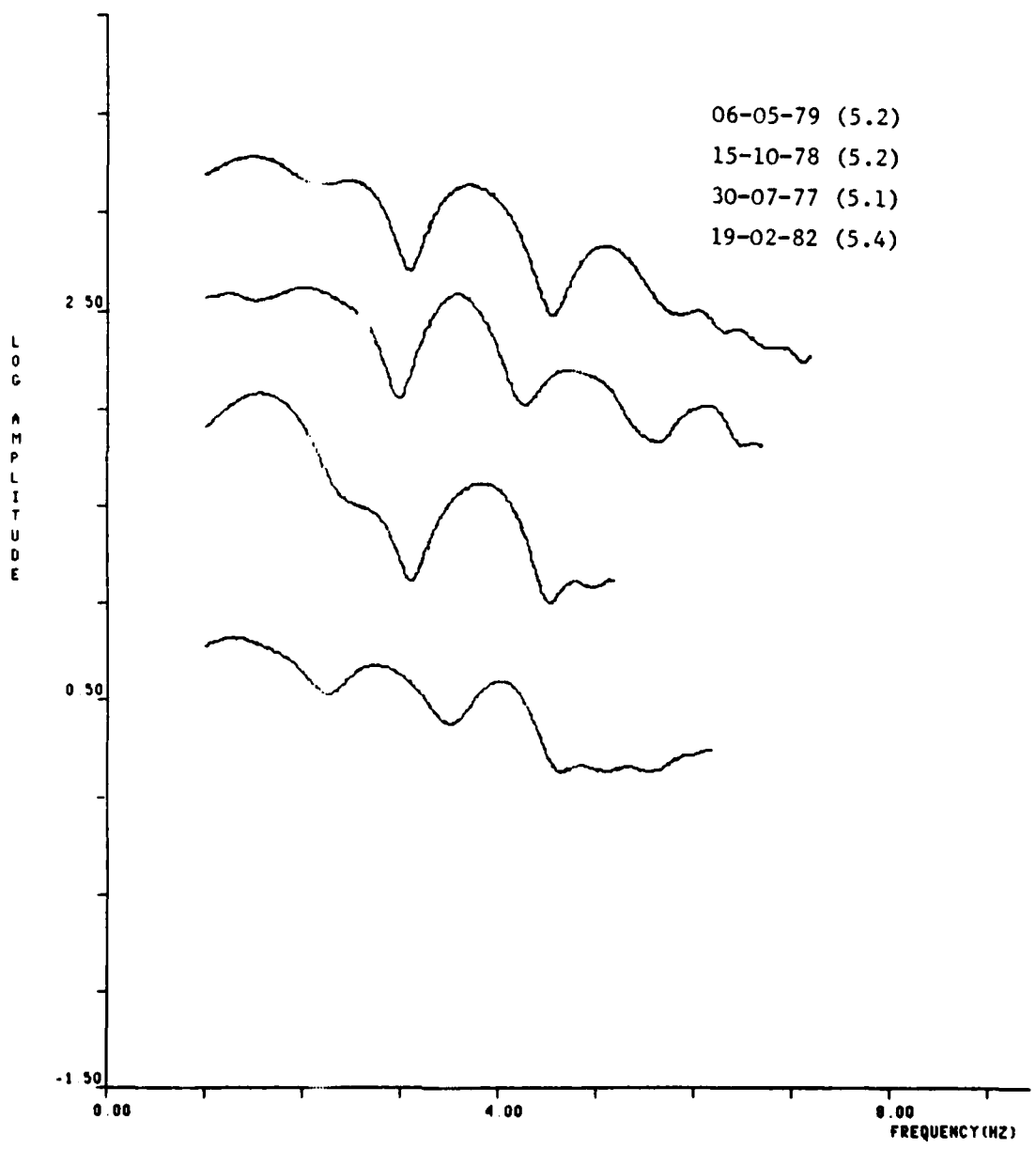
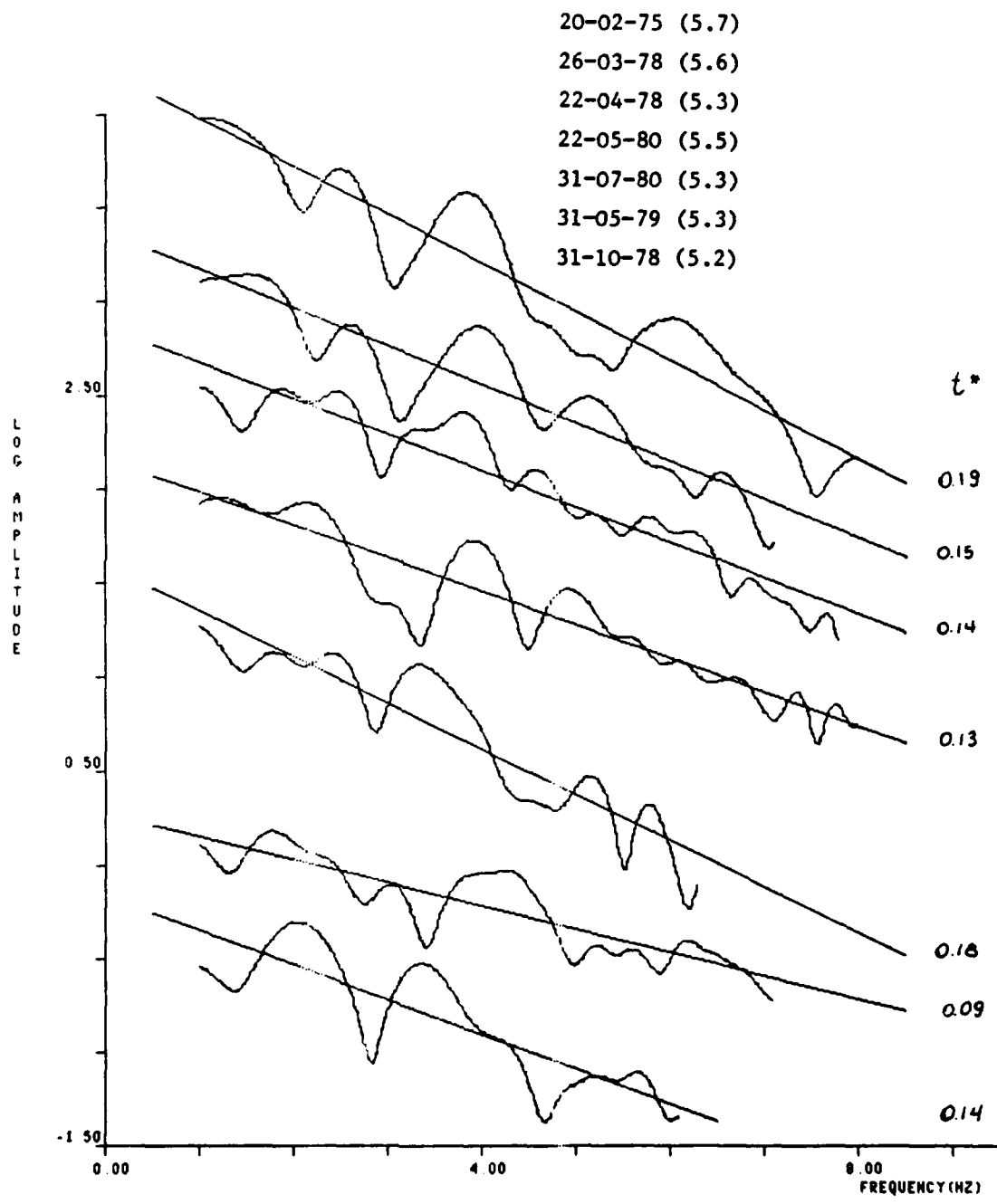


Figure A.11 (continued)



207 Figure A.11 (continued)

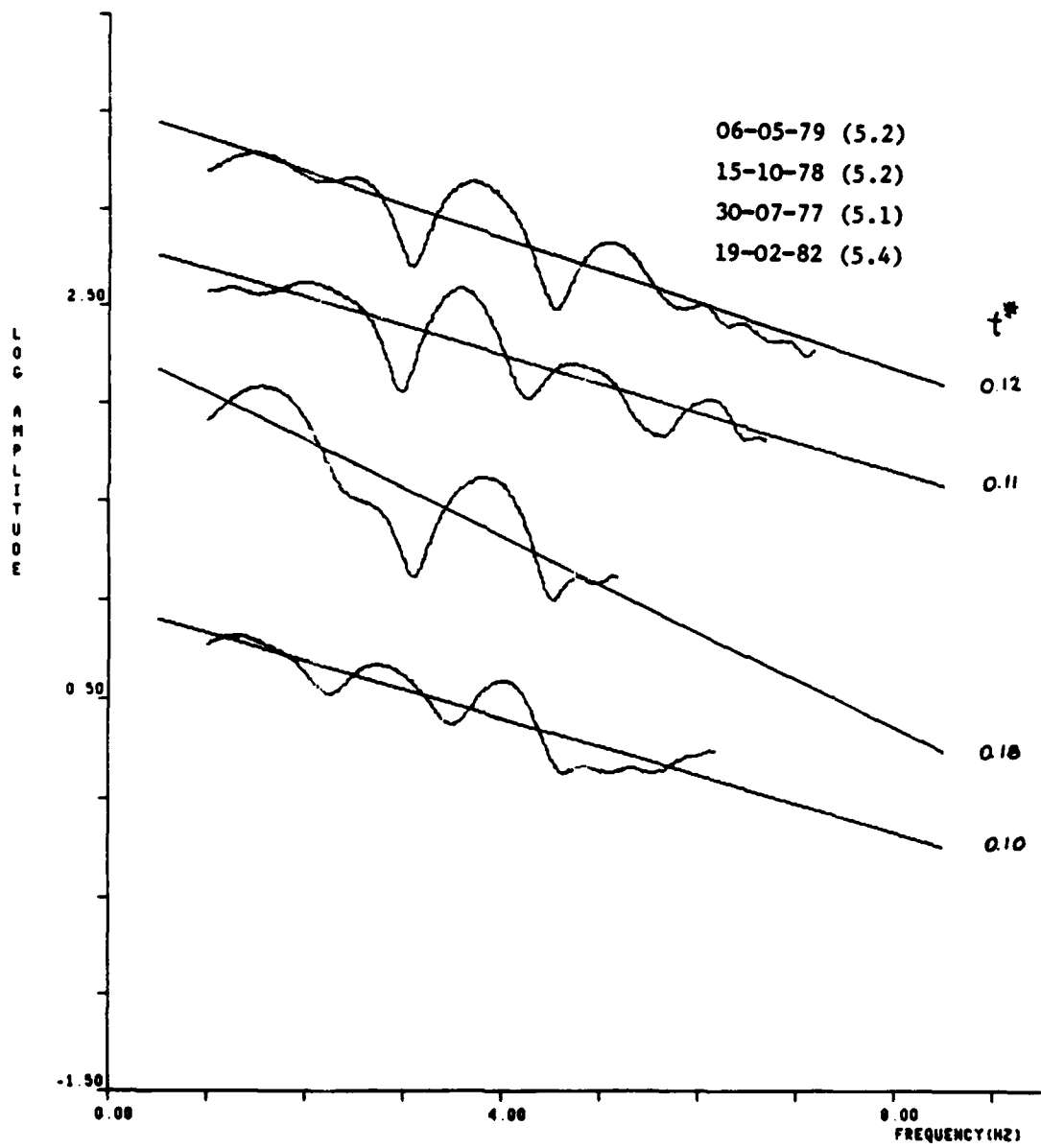


Figure A.11 (continued)

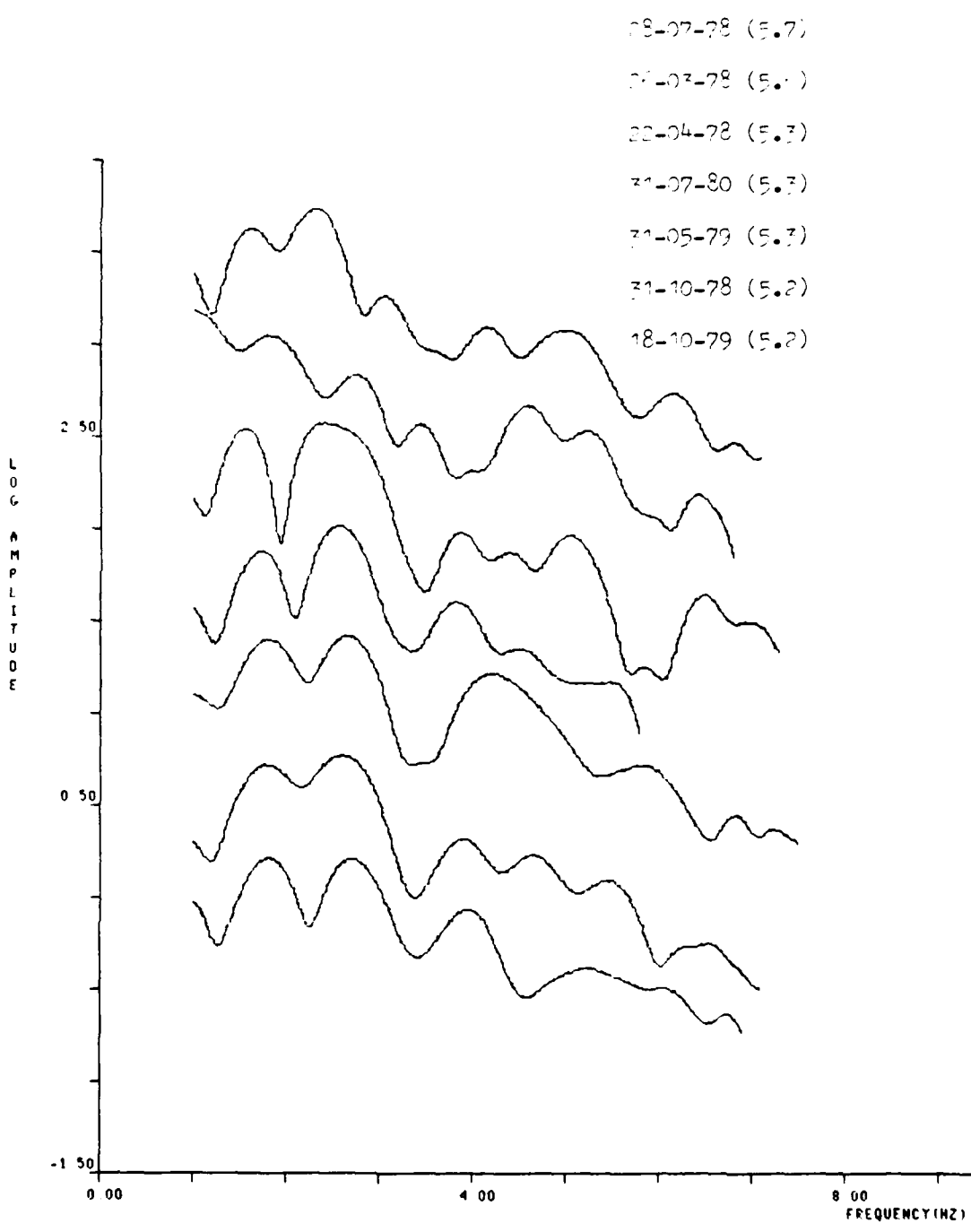


Figure A.12 WRA Recordings of Degelen Explosions

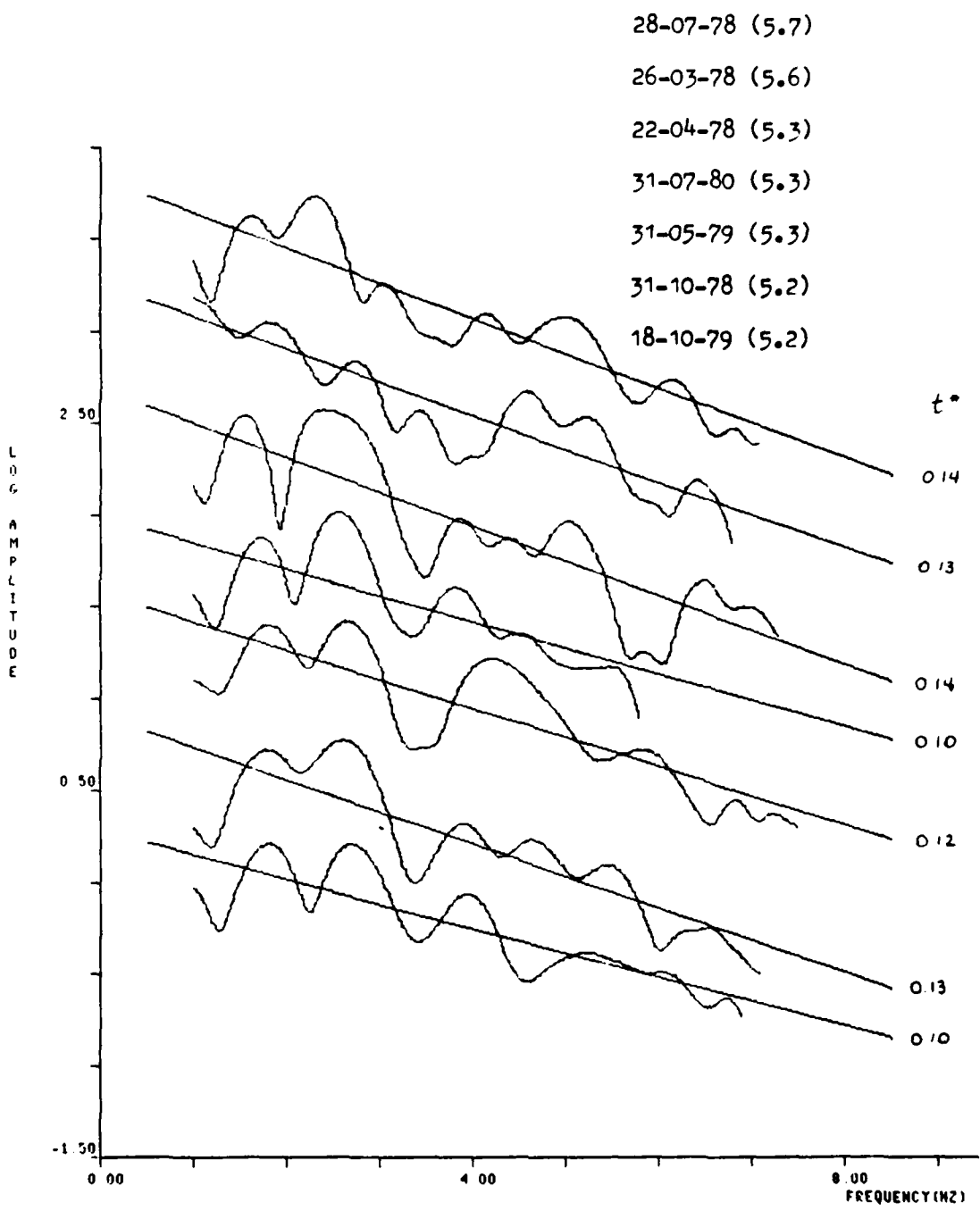


Figure A.12 (continued)

SECURITY CLASSIFICATION OF THIS PAGE (When Data Entered)

REPORT DOCUMENTATION PAGE		READ INSTRUCTIONS BEFORE COMPLETING FORM	
1. REPORT NUMBER SAI-84/1589	2. GOVT ACCESSION NO. <i>A142526</i>	3. RECIPIENT'S CATALOG NUMBER	
4. TITLE (and Subtitle) Q and Its Effect on Short Period P Waves From Explosions in Central Asia		5. TYPE OF REPORT & PERIOD COVERED Semi-Annual Technical Report July 1983 to February 1984	
6. PERFORMING ORG. REPORT NUMBER SAI - 84/1589		7. CONTRACT OR GRANT NUMBER/s DNA001-83-C-0383	
8. AUTHOR(s) Thomas C. Bache		9. PERFORMING ORGANIZATION NAME AND ADDRESS Science Applications, Inc. P. O. Box 2351, 1200 Prospect La Jolla, California 92038	
10. PROGRAM ELEMENT PROJECT TASK AREA & WORK UNIT NUMBERS DARPA Order 4858-Program Code 3D60/Program Element Code 61101E		11. CONTROLLING OFFICE NAME AND ADDRESS Defense Advanced Research Projects Agency 1400 Wilson Boulevard Arlington, VA 22209	
12. REPORT DATE April 1984		13. NUMBER OF PAGES 210	
14. MONITORING AGENCY NAME & ADDRESS (if different from Controlling Office)		15. SECURITY CLASS. (of this report) Unclassified	
15a. DECLASSIFICATION/DOWNGRADING SCHEDULE			
16. DISTRIBUTION STATEMENT (of this Report)			
17. DISTRIBUTION STATEMENT (of the abstract entered in Block 20, if different from Report)			
18. SUPPLEMENTARY NOTES			
19. KEY WORDS (Continue on reverse side if necessary and identify by block number) Attenuation      Body Wave Magnitude P Waves      Explosion Seismology			
20. ABSTRACT (Continue on reverse side if necessary and identify by block number) A detailed model for the attenuation of high frequency (1-8Hz) P waves is developed for the paths from the Soviet test site in eastern Kazakhstan to the sites of the four 20-element United Kingdom arrays. These short period arrays (Scotland, India, Canada and Australia) have been operated in an essentially constant configuration since the mid-1960's and are very well suited to high frequency spectral analyses. Event P wave spectra are computed by summing the power spectra (corrected for the noise power) from			

Continued from Block #20:

individual array elements, and the interpretation is based on very smooth average path spectra obtained by stacking spectra from many similar events. Effects of source differences, especially corner frequency variations, can be seen and taken into account. The attenuation model includes contributions from both intrinsic absorption and scattering. The absorption Q dominates at low frequencies and is strongly dependent on frequency on this band. The preferred model has  $t^*$  - 0.6 seconds at long period and frequency dependence characterized by a half-amplitude value ( $\tau_u$ ) of 0.05 to 0.1 seconds. The scattering is represented by an essentially frequency-independent  $t^*$  of about 0.1 seconds and has an important effect above 2.5 Hz. Differences in the phase spectrum for these two mechanisms for attenuation are important. A key conclusion is that regional attenuation variations are not represented very well by fitting frequency-independent  $t^*$  operators to P wave spectra in the 0.5 - 3.0 Hz band. Source spectrum variations can have a large biasing effect, as can the effect of frequency dependence of Q. The Q will be seriously overestimated if frequency dependence is present, but not included in the model.